

THEORETICAL STUDY OF THE ROTATIONALLY AND VIBRATIONALLY INELASTIC COLLISION DYNAMICS OF SMALL MOLECULES

by
Qianli Ma

A dissertation submitted to Johns Hopkins University in conformity with
the requirements for the degree of Doctor of Philosophy

Baltimore, Maryland
August, 2014

© 2014 Qianli Ma
All Rights Reserved

Abstract

Rotationally and vibrationally inelastic collision dynamics of several small molecules are investigated through *ab initio* calculations of potential energy surfaces (PESs) and time-independent close-coupling scattering calculations. The scattering resonances in the collision energy dependent rotationally inelastic cross sections of OH in collisions with He and Ne, and NH₃ in collisions with H₂ were computed and analyzed. Both shape and Feshbach resonances were identified and the prospects for experimentally observing scattering resonances using Stark decelerated beams of OH radicals were discussed. A new PES for the interaction between CH₃ with different umbrella displacements and a He atom were computed and the collisional vibrational relaxation of the ν_2 mode of CH₃ were studied. The vibrational relaxation rate constant was found to be two orders of magnitude smaller than the pure-rotational relaxation between two lower levels. Differential cross sections for the rotationally inelastic scattering of CH₃ and CD₃ with He, Ar, and H₂ were computed and compared with results of velocity map imaging experiments conducted by Orr-Ewing and coworkers. In general, good agreement was found between theory and experiment, confirming the accuracy of our theoretical approach. Also, new sets of PESs describing the interaction between OH and H₂ were computed, and bound-state calculations and scattering calculations were performed for this system. The computed dissociation energy of OH-*ortho*-H₂ complex and state-to-state cross sections of OH in collisions with H₂ are in excellent agreement with earlier experimental results.

Dissertation directed by: Professor Paul J. Dagdigian
The Johns Hopkins University

Dissertation committee member: Professor Harris J. Silverstone
The Johns Hopkins University

Dissertation committee member: Professor David R. Yarkony
The Johns Hopkins University

Guest dissertation committee member: Professor Millard H. Alexander
University of Maryland, College Park

Acknowledgments

I would like to sincerely thank my advisor, Dr. Paul J. Dagdigian. Paul has encouraged me to grow as an independent thinker by giving me the opportunity to tackle research problems in my own way, yet patiently offered assistance when I needed it.

I would like to thank Dr. Millard H. Alexander for his encouragement and guidance. His valuable assistance in some tough projects is greatly appreciated. I am also appreciative of the help from Dr. Jacek A. Kłos and other collaborators.

I would also like to thank other members of my dissertation committee, Dr. David R. Yarkony and Dr. Harris J. Silverstone, for their help in the course of my graduate study.

Finally, I would like to thank my parents for their continuous support.

Contents

List of Tables	ix
List of Figures	x
1 Introduction	1
1.1 Background	1
1.2 Time-Independent Quantum Scattering Calculations	4
1.2.1 The Close-Coupling Equations	4
1.2.2 Calculation of Experimental Observables	7
1.2.3 Solving the Close-Coupling Equations	8
1.2.4 Alternative Methods	9
1.3 Potential Energy Surfaces	10
1.3.1 <i>Ab initio</i> Calculation of Intermolecular Interactions	10
1.3.2 Creating Potential Energy Surfaces	13
1.4 Organization of the Dissertation	17
2 Scattering Resonances of OH($X^2\Pi$) in Collisions with He and Ne	20
2.1 Introduction	20
2.2 Scattering Calculations	23
2.3 Three-Dimensional OH-He Potential	24
2.4 OH-He Collisions	33
2.4.1 State-to-State Integral Cross Sections	33
2.4.2 Shape Resonances	35
2.4.3 Feshbach Resonances	38
2.5 OH-Ne Collisions	42
2.6 Discussion	45
2.7 Conclusions	49

3	Scattering Resonances of NH₃ in Collisions with H₂ and D₂	50
3.1	Introduction	50
3.2	Scattering Calculations	53
3.3	Potential Energy Surface	54
3.4	Results	57
3.4.1	Collisions between NH ₃ and <i>para</i> -H ₂	57
3.4.2	Collisions between NH ₃ and <i>ortho</i> - and Normal H ₂	65
3.4.3	Collisions between ND ₃ and H ₂	68
3.5	Discussion	69
4	Vibrational Relaxation of CH₃ in Collisions with He	72
4.1	Introduction	72
4.2	Potential Energy Surface	74
4.3	Scattering Calculations	80
4.4	Results	83
4.4.1	Rotationally Inelastic Collisions	83
4.4.2	Vibrationally Inelastic Collisions	86
4.4.3	Rate Constants for Vibrational Relaxation	90
4.5	Discussion	93
5	Rotational Inelastic Scattering of Methyl Radicals with He and Ar	96
5.1	Introduction	96
5.2	Method	99
5.2.1	Experimental Apparatus	99
5.2.2	Rotational Levels of CH ₃ and CD ₃	99
5.2.3	Initial State Distribution of CD ₃ and the REMPI Detection	100
5.2.4	Potential Energy Surface	101
5.2.5	Quantum Scattering Calculations	105
5.3	Results	106
5.3.1	DCSs for CD ₃ -He Collisions	106
5.3.2	DCSs for CH ₃ -He Collisions	109
5.3.3	DCSs for CD ₃ -Ar Collisions	110
5.4	Discussion	112
5.5	Conclusions	117
6	Rotationally Inelastic Scattering of Methyl Radicals with H₂ and D₂	119
6.1	Introduction	119

6.2	Method	122
6.2.1	Experimental Apparatus	122
6.2.2	Potential Energy Surface	122
6.2.3	Quantum Scattering Calculations	129
6.3	Results	131
6.3.1	Integral Cross Sections	131
6.3.2	Differential Cross Sections	133
6.4	Discussion	138
6.5	Conclusions	143
7	OH-H₂ Potential Energy Surfaces and Bound States	145
7.1	Introduction	145
7.2	Theory	148
7.2.1	Interaction Potential	148
7.2.2	Diagonal ($\Lambda' = \Lambda$) Matrix Elements	150
7.2.3	Off-Diagonal ($\Lambda' \neq \Lambda$) Matrix Elements	151
7.2.4	Restriction on ($l_1 + l_2 + l$)	151
7.2.5	Normalization	152
7.2.6	Adiabatic and Quasi-Diabatic Bases	152
7.2.7	Symmetry Restrictions	155
7.2.8	Limiting Geometries	155
7.3	Potential Energy Surfaces	156
7.3.1	MRCI Calculations	156
7.3.2	CCSD(T) Calculations	157
7.3.3	Fitting the Potential Energy Surfaces	158
7.3.4	Extrapolation of the Potential Energy Surfaces	160
7.3.5	Fitted Potential Energy Surfaces	162
7.4	Bound-state Calculations	172
7.4.1	Theory and Method	172
7.4.2	Results	173
7.5	Discussion and Conclusions	177
8	Rotationally Inelastic Scattering of OH and H₂	179
8.1	Introduction	179
8.2	Quantum Scattering Calculations	181
8.3	Collisions of OH with H ₂	181
8.3.1	OH-H ₂ Collisions at 595 cm ⁻¹ Collision Energy	181

8.3.2	Cold Collisions of OH with H ₂	184
8.4	Collisions of OH with D ₂	187
8.5	The Quality of the PESs	192
8.6	Conclusions	195
A	Theory on the OH-H₂ Potential Energy Surfaces, and Bound-State and Scat-	
	tering Calculations	196
A.1	Expansion of the Potential	196
A.2	Long-Range Multipole-Multipole Expansion of the PESs	201
A.3	Matrix Elements of the Potential in an OH-H ₂ Rotational Basis	203
	Bibliography	206
	Curriculum Vitae	220

List of Tables

7.1	Multipole moments of OH($X^2\Pi$) and H ₂	161
7.2	Predicted and experimental OH-H ₂ equilibrium separation (R_e) and dissociation energies for the OH-H ₂ complex	163
7.3	$J = 1/2$ bound levels (in cm ⁻¹) of OH-H ₂ for the CCSD(T) PESs	173
7.4	$J = 3/2$ bound levels (in cm ⁻¹) of OH-H ₂ predicted the CCSD(T) PESs .	174
7.5	The lower $J = 1/2$ and $3/2$ bound levels (in cm ⁻¹) of OH-H ₂ predicted the MRCI and MRCI-HS PESs	175
7.6	Predicted and experimental spectroscopic constants for the lowest bend-stretch level of the OH- <i>ortho</i> -H ₂ complex	177
8.1	Populations of the D ₂ rotational levels at various rotational temperatures	191
8.2	Comparison of the computed OH-H ₂ diagonal and off-diagonal potential at three intermolecular separations for the T-shaped geometry	193

List of Figures

2.1	Energies of the lower rotational levels of OH($X^2\Pi$)	24
2.2	Illustration of the coordinates defining the OH-He geometries	26
2.3	Contour plots of the A' surface of the 3D OH-He PES	29
2.4	Contour plots of the A'' surface of the 3D OH-He PES	30
2.5	Comparison between theoretical and experimental relative state-to-state cross sections for the inelastic scattering of OH ($X^2\Pi, j = 3/2, F_1, f$) radicals with He atoms	32
2.6	State-to-state integral cross sections vs. collision energy for transitions out of the OH $j = 3/2, F_1, f$ level in collisions with He	34
2.7	State-to-state integral and differential cross section of OH in collisions with He for the $j = 3/2, F_1, f \rightarrow j = 5/2, F_1, e$ transition	35
2.8	Plots of the OH-He adiabatic bender curves that correlate with the OH $j = 5/2, F_1, e$ level, obtained from close-coupling calculations.	36
2.9	Phase shifts as a function of collision energy for OH($j = 5/2, F_1, e$)-He collisions obtained from close-coupling adiabatic bender curves	37
2.10	Integral cross section vs. collision energy and differential cross sections for the $j = 3/2, F_1, f \rightarrow j = 1/2, F_2, f$ transition of OH in collisions with He	38
2.11	Partial cross sections vs. collision energy for the $j = 3/2, F_1, f \rightarrow j = 1/2, F_2, f$ transition of OH in collisions with He for total angular momentum $J \leq 11/2$	39
2.12	Collision lifetime $\Delta t^J(E)$ as a function of collision energy for the OH $j = 3/2, F_1, f \rightarrow j = 1/2, F_2, f$ transition in collisions with He	41
2.13	State-to-state inelastic scattering cross sections of OH ($X^2\Pi, j = 3/2, F_1, f$) radicals with Ne atoms as a function of the collision energy	42
2.14	Integral and differential cross section for the $j = 3/2, F_1, f \rightarrow j = 5/2, F_1, f$ transition of the collisions of OH radicals with Ne atoms	44

2.15	Inelastic scattering cross section for the $j = 3/2, F_1, f \rightarrow j = 3/2, F_1, e$ channel in collisions of OH radicals with He atoms convoluted with Gaussian energy distributions	46
3.1	Rotational level diagrams of <i>para</i> -NH ₃ and ND ₃ in the E nuclear spin modification	52
3.2	Comparison between the larger expansion coefficients $V_{l_1\mu_1l_2l}$ of the NH ₃ -H ₂ and ND ₃ -H ₂ potential energy surfaces	56
3.3	State-to-state integral cross section as a function of collision energy for transition from the 11- level of <i>para</i> -NH ₃ in collision with <i>para</i> -H ₂ in the $j = 0$ level	57
3.4	Partial cross sections as a function of collision energy for the 11- \rightarrow 11+ transition of <i>para</i> -NH ₃ in collisions with <i>para</i> -H ₂ in the $j = 0$ level	59
3.5	Adiabatic bender curves for the interaction between <i>para</i> -NH ₃ and <i>para</i> -H ₂ for the $J = 6, +$ parity partial wave	59
3.6	Contributions of various levels to the square of the scattering wave function of the $J = 6, +$ parity partial wave for the scattering of NH ₃ in the 11- initial state and <i>para</i> -H ₂ ($j = 0$)	61
3.7	Differential cross sections for the 11- \rightarrow 11+ transition in NH ₃ in collisions with <i>para</i> -H ₂ $j = 0$	62
3.8	Partial cross sections as a function of collision energy for the 11- \rightarrow 21+ transition of <i>para</i> -NH ₃ in collisions with <i>para</i> -H ₂ in the $j = 0$ level	63
3.9	Phase shifts as a function of collision energy for the collision between <i>para</i> -NH ₃ and <i>para</i> -H ₂	65
3.10	State-to-state integral cross sections as a function of collision energy for transitions from the 11- level of <i>para</i> -NH ₃ in collisions with <i>ortho</i> -H ₂ in the $j = 1$ level	66
3.11	Integral cross section as a function of collision energy for the 11- \rightarrow 11+ transition of NH ₃ in collision with <i>para</i> -, <i>ortho</i> -, and normal (1:3 <i>para:ortho</i>) H ₂	67
3.12	State-to-state integral cross sections as a function of collision energy for transitions from the 11- level of ND ₃ in collision with <i>para</i> -H ₂ ($j = 0$) . .	68
3.13	State-to-state integral cross section as a function of collision energy out of the 11- level of <i>para</i> -NH ₃ in collisions with <i>ortho</i> -D ₂ ($j = 0$)	70
3.14	State-to-state integral cross section as a function of collision energy out of the 00+ level of <i>ortho</i> -NH ₃ in collisions with <i>para</i> -H ₂ ($j = 0$)	71

4.1	Potential energy of CH ₃ as a function of the umbrella displacement Q . . .	76
4.2	Dependence of the vibrational coupling potential $V_{10}(R, \theta, \phi)$ of CH ₃ -He on the orientation of the He atom with respect to the CH ₃ molecule for an atom-molecule separation $R = 6$ bohr	78
4.3	Dependence of the larger expansion coefficients $V_{10}^{\lambda\mu}(R)$ on the CH ₃ -He separation R	79
4.4	Rotational levels for <i>ortho</i> and <i>para</i> CH ₃ in the $v = 0$ and $v = 1$ umbrella vibrational manifold	82
4.5	Larger state-to-state integral cross sections as a function of collision energy for rotational transitions out of the lowest <i>ortho</i> level of $v_2 = 1$ and $v_2 = 0$ CH ₃ in collisions with He	84
4.6	Bar plot of the cross sections for rotationally inelastic collisions of CH ₃ ($v_2 = 1$) in the 6_6^\dagger and 7_0^\dagger initial levels with He at a collision energy of 300 cm^{-1} .	85
4.7	Dependence upon the collision energy of the vibrational relaxation cross section for selected CH ₃ ($v = 1$) rotational levels in collisions with He . . .	87
4.8	Rotationally-summed vibrational relaxation cross sections at 300 cm^{-1} collision energy for different initial rotational levels n_k^\dagger of CH ₃ ($v_2 = 1$) in collisions with He	88
4.9	Bar plot of the integral cross sections for $v=1 \rightarrow 0$ ro-vibrationally inelastic scattering of <i>para</i> CH ₃ in the 5_1^\dagger and 5_3^\dagger levels through collision with He at a collision energy of 300 cm^{-1}	88
4.10	Dependence on the rotational and translational temperature of the rotationally-summed vibrational relaxation rate constant for CH ₃ ($v = 1$) in collisions with He upon the translational and rotational temperature .	91
5.1	Rotational energy level diagrams for the ground vibrational level of the \tilde{X}^2A_2'' electronic state of CH ₃ and CD ₃	100
5.2	Dependence of the CH ₃ -Ar potential energy (in cm^{-1}) on the orientation (θ, ϕ) at $R = 6.75 a_0$	103
5.3	Dependence of the larger expansion coefficients of the CH ₃ -Ar PES on the atom-molecule separation R	104
5.4	Integral cross sections for transitions out of the lowest CD ₃ levels of each nuclear spin symmetry in collisions with Ar at a collision energy of 440 cm^{-1}	105
5.5	DCSs for inelastic scattering of CD ₃ radicals by He at a collision energy of $440 \pm 35 \text{ cm}^{-1}$ into final rotational levels $n' = 2-4$	107

5.6	DCSs for inelastic scattering of CD ₃ radicals by He at a collision energy of 440 ± 35 cm ⁻¹ into final rotational levels $n' = 5-9$	108
5.7	DCSs for inelastic scattering of CH ₃ radicals by He at a collision energy of 425 ± 35 cm ⁻¹ into final rotational levels $n' = 2,3$	110
5.8	DCSs for inelastic scattering of CD ₃ radicals by Ar at a collision energy of 330 ± 25 cm ⁻¹ into final rotational levels $n' = 2,3$	111
5.9	DCSs for inelastic scattering of CD ₃ radicals by Ar at a collision energy of 330 ± 25 cm ⁻¹ into final rotational levels $n' = 4,5$	111
5.10	Theoretical state-to-state CH ₃ /CD ₃ -He inelastic DCSs out of the level $n_k = 1_1$ into levels with $n' = 4$	113
5.11	Theoretical state-to-state CD ₃ -Ar inelastic DCSs out of the level $n_k = 1_1$ into levels with $n' = 4$	114
5.12	Computed state-to-state differential and partial cross sections for the inelastic scattering of CD ₃ with He and Ar	114
5.13	Contour plots showing the variation of the CH ₃ -Ar and CH ₃ -He interaction energies averaged over ϕ on the plane containing the CH ₃ molecule .	116
5.14	Computed state-to-state differential and partial cross sections for the inelastic scattering of CD ₃ with He and Ar	117
6.1	Body-frame coordinate system to specify the geometry of the CH ₃ -H ₂ complex	122
6.2	Dependence of the larger expansion coefficients upon the CH ₃ -H ₂ separation R	128
6.3	Contour plots of the CH ₃ -H ₂ PES at $R = 6.5 a_0$	131
6.4	Integral cross sections for the collisions between CD ₃ and D ₂ at a collision energy of 640 cm ⁻¹	132
6.5	Newton diagrams for inelastic scattering of CD ₃ with D ₂ and H ₂	133
6.6	Experimental and theoretical DCSs for inelastic scattering of CD ₃ radicals by D ₂ at a collision energy of 640 ± 60 cm ⁻¹ into final rotational levels $n' = 2-4$	135
6.7	Experimental and theoretical DCSs for inelastic scattering of CD ₃ radicals by D ₂ at a collision energy of 640 ± 60 cm ⁻¹ into final rotational levels $n' = 5-7$	136
6.8	Experimental and theoretical DCSs for inelastic scattering of CD ₃ radicals by H ₂ at a collision energy of 680 ± 75 cm ⁻¹ into final rotational levels $n' = 2-4$	137

6.9	Experimental and theoretical DCSs for inelastic scattering of CD ₃ radicals by H ₂ at a collision energy of 680 ± 75 cm ⁻¹ into final rotational levels $n' = 5-8$	138
6.10	Computed state-to-state DCSs for inelastic scattering of CD ₃ , initially in the 1 ₀ rotational level, with D ₂ and H ₂	140
6.11	Computed state-to-state DCSs for inelastic scattering of CD ₃ from the 1 ₁ rotational level into various final rotational levels in collisions with D ₂ and He at a collision energy of 640 cm ⁻¹	141
7.1	The definition of the coordinate system describing the interaction between OH and H ₂	149
7.2	Root mean squares (RMS) as a function of intermolecular distance between the fitted potential and the <i>ab initio</i> OH-H ₂ potential	159
7.3	The diagonal OH-H ₂ potential V_d as a function of intermolecular distance for various θ_O with $\theta_H = 90^\circ$ and $\phi_H = 0^\circ$	162
7.4	Larger $B_{l_1 l_2 l}$ expansion coefficients for the diagonal OH-H ₂ potential V_d as a function of intermolecular distance R	164
7.5	Larger $F_{l_1 l_2 l}$ expansion coefficients for the off-diagonal OH-H ₂ potential V_o as a function of intermolecular distance R	165
7.6	Contour plots of the CCSD(T) OH-H ₂ V_d PES averaged over all orientations of H ₂ compared to the V_{sum} PES for OH-He and OH-Ne	167
7.7	Contour plots of the (left panel) CCSD(T) OH-H ₂ V_o PES averaged over the orientation of H ₂ in its $j = 0$ rotational level compared to the V_{diff} PES for OH-He and OH-Ne	168
7.8	Contour plots showing the variation of V_d and $ V_o $ for OH-H ₂ in the OH molecule frame.	169
7.9	Contour plots of the diagonal CCSD(T) OH-H ₂ potential V_d as a function of θ_O and θ_H	169
7.10	Contour plots of V_o of the CCSD(T) OH-H ₂ PES as a function of θ_O and θ_H	170
7.11	Contour plots showing the variation of OH-H ₂ V_o of the electrostatic interactions and the CCSD(T) PESs as a function of θ_O and θ_H	171
8.1	Experimental and theoretical cross sections for the scattering of OH($X^2\Pi$, $j = 3/2, F_1, f$) with “cold” <i>para</i> -H ₂ at 595 cm ⁻¹	182
8.2	Experimental and theoretical cross sections for the scattering of OH($X^2\Pi$, $j = 3/2, F_1, f$) with “cold” normal H ₂ at 595 cm ⁻¹	183

8.3	Experimental and theoretical cross sections for the scattering of OH($X^2\Pi$, $j = 3/2, F_1, f$) with “warm” <i>para</i> -H ₂ at 595 cm ⁻¹	184
8.4	Theoretical state-to-state integral cross section as a function of collision energy for transitions out of the OH $j_1 = 3/2, F_1, f$ level in collisions with H ₂ in the $j_2 = 0$ level	185
8.5	Theoretical state-to-state integral cross section as a function of collision energy for transitions out of the OH $j_1 = 3/2, F_1, f$ level in collisions with H ₂ in the $j_2 = 1$ level	187
8.6	State-to-state integral cross section as a function of collision energy for transition from the $j_1 = 3/2, F_1, f$ level of OH to other F_1 levels in collisions with D ₂	188
8.7	State-to-state integral cross section as a function of collision energy for transition from the $j_1 = 3/2, F_1, f$ level of OH to other F_2 levels in collisions with D ₂	189
8.8	Experimental and theoretical relative state-to-state inelastic scattering cross section of as a function of collision energy for transition out of the $j_1 = 3/2, F_1, f$ level of OH	190
8.9	Comparison of the theoretical state-to-state OH-H ₂ ($j_2 = 0$) integral cross section computed from potential energy surfaces generated using different monomer bond lengths	194

Chapter 1

Introduction

1.1 Background

The science of molecular collision dynamics studies the change in chemical properties of atoms and molecules during the collision process in a microscopic scale, and describes the relation between the properties of individual molecules and chemical kinetics [1]. The knowledge of collision dynamics is fundamental in understanding the connection between the intermolecular forces and the outcome of a collision process [2, 3]. It also permits us to model and to understand complex real-world kinetics systems in fields such as atmospheric chemistry [4], combustion chemistry [5], and astrophysics [6].

The interdependence between experiments and theory is characteristic to the study of collision dynamics [3]. The experimental observables, such as the probability of a collision (or scattering) event (usually in terms of cross sections) and rate constants, can only be measured for certain systems and/or internal state transitions. Moreover, these observables do not provide directly more fundamental properties such as the interaction between molecules. The theoretical studies, while being able to connect the intermolecular interaction with the experimental observables, require quality assessment in which the comparison with the experimental results is a critical part. A well tested theoretical method can also be used in predicting the behavior of new systems, and thus can either provide knowledge in properties difficult to measure, or guide the design of experiments.

Molecular collision processes can be categorized into three broad classes: the elastic collision in which kinetic energy is conserved, the inelastic collision in which there is a change of internal energy of the collision partners, and the reactive collision in which a chemical reaction happens [2]. This dissertation studies the inelastic collisions of atoms and small molecules. As compared to reactive collisions, fully-quantum dynamics calculations on inelastic collisions can be easier performed without significant approximation, which can provide insight into in the understanding of the quantum properties of molecules. Also, the inelastic collision dynamics can play a role in modeling kinetic systems, given the dependence of reaction rates on the internal states of reactants.

The crossed molecular beam experiment is the most powerful experimental tool in the study of molecular collision dynamics [7, 8]. In such experiments two beams of atoms or molecules are collided together, and the final products, including their angular and velocity distributions, can be measured. The experimental study of inelastic collisions is the most difficult of the three classes of collisions [3]. To measure the inelastic cross sections, the apparatus must at least be able to detect the quantum states of atoms or molecules. Ideally, the incident beam shall also have a high quantum purity in order to obtain the most useful information, the state-to-state cross sections. In addition, due to the densely spaced internal levels of molecules, useful information can only be obtained with relatively low and narrowly-distributed collision energies.

Significant improvements has been made to crossed molecular beam experiments since its original development by Herschbach and Lee [7]. On the detection of molecules, with the development of powerful tunable lasers, spectroscopic detection methods, such as the laser-induced fluorescence (LIF) and the resonance-enhanced multiphoton ionization (REMPI) techniques, have been widely used to measure state-resolved cross sections [8, 9]. On the beam preparation, supersonic molecular beam sources [10], and other techniques including laser photolysis, have been used in preparing a variety of molecular beams of stable molecules, as well as reactive intermediates. In certain cases, the electrically neutral

atomic and molecular beams can be further manipulated with appropriately designed inhomogeneous electromagnetic fields [11]. With these techniques, state-resolved cross sections or rate constants have been determined for a large number of systems and as a function of collision energy. Recent examples of such studies include the determination of fully state-resolved cross sections of the collision between OH and NO [12], and the observation of a scattering resonance,¹ which is a pure quantum phenomenon, in the collision between O₂ and H₂ [13].

The velocity map imaging (VMI) technique [14, 15] is another interesting development in crossed molecular beam experiments that allows the measurement of the angular resolved cross section (differential cross section, or DCS) [16–21]. The observation of state-resolved diffraction oscillations, which is another pure quantum phenomenon, in the collisions of NO with rare gas atoms by van de Meerakker and coworkers [22] is a recent example of successful experiments using the VMI technique.

Theoretical investigations of the collision dynamics of a molecular system can take two paths, by solving either the classical equations of motion with Newtonian mechanics, or by solving the Schrödinger equation using quantum mechanical methods [1]. Although in some study quasi-classical methods can provide insights to a system [23], fully quantum calculations are the standard for small molecules. In this dissertation we use the time-independent close-coupling method to study the collision dynamics. The details on such calculations are described in Sec. 1.2.

With either path, the study of collision dynamics requires a the potential energy surface (PES), or the intermolecular force as a function of the position of atoms. With modern computational techniques, accurate *ab initio* PESs are usually used for the inelastic scattering of small molecules. More information on creating the PESs is described in Sec. 1.3.1.

In this dissertation, the rotationally inelastic scattering of three molecules, OH,

¹Further discussions on scattering resonances can be found in Chapters 2 and 3.

NH₃, and CH₃, with rare gas atoms or the hydrogen molecule as the collision partner is studied. In addition, the vibrational relaxation of CH₃ in collisions with He is investigated. More background information and the organization of the dissertation is provided in Sec. 1.4. In addition, More specific information can be found in the “introduction” section of each following chapters.

1.2 Time-Independent Quantum Scattering Calculations

1.2.1 The Close-Coupling Equations

The time-independent close-coupling method is the most widely used fully quantum treatment of molecular inelastic scattering. The method was first introduced by Arthurs and Dalgarno [24], and is described further in a number of references [2, 25–27]. In this section we briefly review the equations of the close-coupling formalism, considering specifically the rotationally inelastic collision between two rigid molecules.

The Hamiltonian of the system of two molecules in a space-fixed coordination system can be written, in atomic units, as

$$\hat{H} = -\frac{1}{2\mu}\nabla_{\mathbf{R}}^2 + \hat{H}_{\text{int}} + V(\mathbf{R}, \Omega_{BS}, \Omega_{1B}, \Omega_{2B}), \quad (1.1)$$

where $\mu = m_1 m_2 / (m_1 + m_2)$ is the reduced mass of the two molecules, \mathbf{R} is the Jacobian vector pointing from molecule 1 to molecule 2, $\Omega_{BS} = (\phi, \theta, 0)$ is the relative orientation of \mathbf{R} to the chosen space frame, Ω_{1B} and Ω_{2B} are the orientation of the molecule-fixed frames with respect to the body-fixed frame, \hat{H}_{int} is the internal Hamiltonian of the two molecules, and V is the interaction energy. As a short-hand notation, we will use Ω to represent $(\Omega_{BS}, \Omega_{1B}, \Omega_{2B})$ in the rest of the section.

We write the full scattering wave function as the linear combination of angular basis

functions ϕ_i

$$\Psi_I(R, \Omega) = \frac{1}{R} \sum_i F_{iI}(R) \phi_i(\Omega), \quad (1.2)$$

where I and i are composite indices representing multiple quantum numbers representing an internal state (usually called a channel) of the system. The close-coupling basis function ϕ_i can be formulated by coupling the total angular momenta of the two molecules, j_1 and j_2 to form j_{12} , followed by vector coupling of j_{12} and the orbital angular momentum L to form the total angular momentum of the system J :

$$\phi_i(\Omega) = \sum_{m_1 m_2 m_{12} m_L} \langle j_1 m_1, j_2 m_2 | j_{12} m_{12} \rangle \langle j_{12} m_{12}, L m_L | J M \rangle | j_1 m_1 \rangle | j_2 m_2 \rangle | L m_L \rangle, \quad (1.3)$$

where $|j_1 m_1\rangle$ and $|j_2 m_2\rangle$ are the rotational wave function of the two molecules in their molecule frames, $|L m_L\rangle = Y_{L m_L}(\theta, \phi)$ is a spherical harmonic in the body-fixed frame, and $\langle j_1 m_1, j_2 m_2 | j m \rangle$ is a Clebsch-Gordan coefficient [28]. Depending on the nature of the molecules, the rotational wave functions may need quantum numbers other than j and m to describe and take different forms.

Such close-coupling basis functions are eigenfunctions of J . Since collision cannot induce the change of J , the Hamiltonian will be block diagonalized. Further, there is no coupling between channels whose internal wave functions have opposite total parity. Therefore we can solve the Schrödinger equation of the system independently for each J and parity (usually referred to as a partial wave).

Substitution of Eq. (1.2) into the time-independent Schrödinger equation of the system $\hat{H}\Psi(R, \Omega) = E\Psi(R, \Omega)$ gives

$$\left[-\frac{1}{2\mu} \nabla_R^2 + V(R, \Omega) + H_{\text{int}} - E \right] \sum_i F_{iI}(R) \phi_i(\Omega) = 0, \quad (1.4)$$

where E is the total energy of the collision system, including the internal energies of independent molecules and the relative translational energy (or collision energy E_c). Premulti-

plying the above equation by another close-coupling basis function $\phi_{i'}(\Omega)$ and integrating over Ω yields

$$\left[\frac{d^2}{dR^2} - \frac{L_{i'}(L_{i'} + 1)}{R^2} + k_i^2 \right] F_{i'I}(R) = \sum_i F_{ii}(R) \int \phi_j^*(\Omega) V(R, \Omega) \phi_i(\Omega) d\Omega, \quad (1.5)$$

where the squared wave vector k_i^2 equals

$$k_i^2 = 2\mu(E - \varepsilon_i), \quad (1.6)$$

with ε_i the internal rotational energy of channel i .

Equation (1.5) can be written in a matrix form [29]

$$\left[\mathbf{I} \frac{d^2}{dR^2} + \mathbf{W}(R) \right] \mathbf{F}(R) = 0, \quad (1.7)$$

where \mathbf{I} is an identity matrix, and

$$\mathbf{W}(R) = \mathbf{k}^2 - \mathbf{l}^2(R) - \mathbf{V}(R). \quad (1.8)$$

\mathbf{k} and \mathbf{l} are diagonal matrices with elements defined previously by k_i and L_i , respectively.

We now consider the boundary conditions for this collision system. Obviously, $\Psi_I(R, \Omega)$ shall vanish at a small R well inside the classical forbidden region. Asymptotically, $\Psi(R, \Omega)$ shall take the form of an incoming plane wave and outgoing waves to all the channels

$$\lim_{R \rightarrow \infty} \Psi_I(R, \Omega) \sim e^{ik_I z} \phi_I(\Omega) + \sum_{I'} \frac{e^{ik_{I'} R}}{R} \phi_{I'}(\Omega) f_{I'I}(\theta, \phi). \quad (1.9)$$

The quantity $f_{I'I}(\theta, \phi)$ is called the scattering amplitude. The squared scattering amplitude is the probability that the incident particles with internal states I will emerge in internal state I' and in a direction defined by θ and ϕ as a result of the collision.

1.2.2 Calculation of Experimental Observables

The differential cross section for a transition from state I to I' is given by

$$\frac{d\sigma_{I'I}(\theta, \phi)}{d\Omega} = \frac{k_{I'}}{k_I} |f_{I'I}(\theta, \phi)|^2, \quad (1.10)$$

and the integral cross section can be expressed as

$$\sigma_{I'I} = \int_0^{2\pi} \int_0^\pi \frac{d\sigma_{I'I}(\theta, \phi)}{d\Omega} \sin\theta d\theta d\phi. \quad (1.11)$$

In practice, it is most convenient to introduce the scattering matrix \mathbf{S} and match the asymptotic wave function to the boundary condition

$$\lim_{R \rightarrow \infty} F_{iI}(R) \sim \frac{1}{k_i^{1/2}} \left[\delta_{iI} e^{-ik_i R + \frac{L_I \pi}{2}} - S_{iI} e^{ik_i R - \frac{L_i \pi}{2}} \right]. \quad (1.12)$$

The scattering amplitudes for the transition between the initial rotational levels $j_1 m_1, j_2 m_2$ and the final levels $j'_1 m'_1, j'_2 m'_2$ of the collision partners can then be computed from

$$\begin{aligned} & f_{j_1 m_1 j_2 m_2 \rightarrow j'_1 m'_1 j'_2 m'_2}(\theta, \phi) \\ &= \sum_{JMLL'} \sum_{j_{12} j'_{12} m_{12} m'_{12} m'_L} k_{j_1 j_2}^{-1/2} k_{j'_1 j'_2}^{-1/2} i^{L-L'} \pi^{1/2} [J] ([L][j_{12}][j'_{12}])^{1/2} (-1)^{j_1 + j'_1 + j_2 + j'_2 + L + L' + j_{12} + j'_{12} + m'_L} \\ & \times \begin{pmatrix} j_1 & j_2 & j_{12} \\ m_1 & m_2 & -m_{12} \end{pmatrix} \begin{pmatrix} j_{12} & L & J \\ m_{12} & 0 & -M \end{pmatrix} \begin{pmatrix} j'_1 & j'_2 & j'_{12} \\ m'_1 & m'_2 & -m'_{12} \end{pmatrix} \\ & \times \begin{pmatrix} j'_{12} & L' & J \\ m'_{12} & m'_L & -M \end{pmatrix} T_{j_1 j_2 j_{12} L; j'_1 j'_2 j'_{12} L'}^J Y_{L' m'}(\theta, \phi), \end{aligned} \quad (1.13)$$

where $[x] = 2x + 1$, and $\mathbf{T} = \mathbf{I} - \mathbf{S}$ is called the transmission matrix, $(:::)$ is a Wigner 3- j symbol, and Y_{lm} is a spherical harmonic [28]. The integral cross section will take a simple

form

$$\sigma_{j_1 j_2 \rightarrow j'_1 j'_2} = \frac{\pi}{k_{j_1 j_2}^2} \sum_J (2J+1) \sum_{j_{12} j'_{12} L L'} \frac{1}{[j_1][j_2]} |T_{j'_1 j'_2 j'_{12} L'; j_1 j_2 j_{12} L}|^2, \quad (1.14)$$

The thermal rate constant for a transition $j_1 j_2 \rightarrow j'_1 j'_2$ can be computed from the integral cross section with [1]

$$k(T) = \frac{1}{k_B T} \left(\frac{8}{\pi \mu k_B T} \right)^{\frac{1}{2}} \int_0^\infty E_c \sigma_{j_1 j_2 \rightarrow j'_1 j'_2}(E_c) e^{-\frac{E_c}{k_B T}} dE_c, \quad (1.15)$$

where k_B is the Boltzmann constant, T is the temperature, E_c is the collision energy, and $\sigma_{j_1 j_2 \rightarrow j'_1 j'_2}(E)$ is the energy dependent integral cross section.

1.2.3 Solving the Close-Coupling Equations

Since the close-coupling equations emerge in a number of chemical dynamics problems, the algorithm of solving them has been of great interest prior to 1990. A couple extensive reviews on this topic has been published [25, 30]. In general, these equations can be solved with two approaches [25]: By solving the differential equations numerically (approximate-solution), and by approximate the potential matrix \mathbf{V} and solve the equations analytically (approximate-potential). The approximate-solution algorithms tend to be more efficient when the integration steps are small, and the approximate-potential algorithms allow larger steps while achieving acceptable accuracy.

For the rotationally inelastic scattering problems, the interaction potential is usually characterized by a strongly repulsive wall at small intermolecular separation R , followed by an attractive well and a slowly-changing, weak long-range interaction as R increases. the most efficient approach is to use an approximate-solution algorithm at short range, where \mathbf{V} changes dramatically with respect to the R , and an approximate-potential algorithm at moderate to long range, where a larger integration step could significantly reduce the computation cost while retaining good accuracy.

For the work described in this dissertation, the HIBRIDON suite of programs [31]

by Alexander *et al.* is used to solve the close-coupling equations. HIBRIDON combines a log-derivative algorithm [32, 33] at short range, and a locally adiabatic Airy function algorithm [29, 34, 35] at moderate to long range with variable R interval. The algorithm in HIBRIDON uses an “invariant embedding” [25] technique to improve the numerical stability. MOLSCAT [36], which is no longer under active development since 1994, is another popular program suite in solving the close-coupling equations.

Presently, a desktop computer can generally solve a coupled system with ~ 1000 channels within minutes. Although the actual investigation of a scattering system involves solving the close-coupling equations for a large number of partial waves and collision energies, these can be easily and almost evenly distributed to multiple nodes of a computer cluster without sophisticated parallel algorithms. We do note that solving the close-coupling equations requires matrix inversion in each step of propagation. For dense matrices, commonly used inversion algorithms scale approximately as $O(N^3)$. Therefore the work described in Chapters 4 and 6 involving partial waves with more than 5000 channels require a lot of computation power to solve.

Some of the scattering calculations described in chapters 2, 3, and 8 are also independently performed by Ad van der Avoird and coworkers at Radboud University Nijmegen. In their calculations a renormalized Numerov algorithm [37, 38] is used in solving the close-coupling equations. Comparison with the Nijmegen results provided an additional check on our calculations.

1.2.4 Alternative Methods

Many approximation methods exist for the inelastic scattering calculations. The most successful one is probably the coupled states, or centrifugal decoupling, approximation [39]. With this approximation, the l^2 matrix representing the centrifugal barrier in the close-coupling formalism is replaced by a constant matrix with an averaged orbital angular momentum. In this case, the close-coupling equations become block-diagonal in the index

which is the body-frame projection of the total angular momentum of the molecule, and the computation effort can be significantly reduced. While the coupled states approximation is unnecessary for relatively small systems investigated in this dissertation, using it can sometimes provide more insights of a system [40, 41].

One should also mention here that another approach to the quantum scattering calculations is the wave packet method, which solves the time-dependent Schrödinger equation. This approach has certain advantages over the conventional close-coupling method, particularly in that it scales more favorably to larger systems, and that the calculation does not need to be repeated for each collision energy. The wave packet method has been successfully applied to, for example, the ro-vibrational inelastic scattering between two H₂ molecules and their isotopomers [42, 43].

1.3 Potential Energy Surfaces

Theoretical studies of the dynamics in molecular collision starts with the PES describing the interaction between atoms and molecules. For the inelastic collisions of molecules, the PES is governed by the intermolecular interactions, with contributions from electron exchange, multipole-multipole electrostatic, induction, and dispersion. The power of modern computers has enabled the computation of potentials using accurate *ab initio* methods, which is almost exclusively used today for small molecules. Several excellent review articles exist on the computation of intermolecular interactions [44–46]. This section only describes briefly the theoretical methods relevant to the inelastic scattering calculations.

1.3.1 *Ab initio* Calculation of Intermolecular Interactions

The supermolecular approach [44] is most commonly used in dealing with intermolecular interactions between small molecules. In this approach the two-body interaction

is defined as

$$E_{\text{int}} = E_{AB} - E_A - E_B. \quad (1.16)$$

Despite of the simple formula, careful treatment is necessary to obtain high-quality PESs that could reasonably reproduce experimental cross sections and spectra.

To get the desired accuracy, a highly correlated *ab initio* method needs to be used in calculating the energies of the complex and the monomers. The coupled cluster method with single, double, and (perturbative) triple excitations [CCSD(T)] has been the golden standard for many systems, and is used in creating PESs through out this dissertation. In the coupled cluster method, the electronic wave function is defined as [47]

$$\Psi_{\text{CC}} = e^{\mathbf{T}}\Phi_0 = (1 + \mathbf{T} + \frac{1}{2}\mathbf{T}^2 + \frac{1}{6}\mathbf{T}^3 + \dots)\Phi_0, \quad (1.17)$$

where Φ_0 is a reference Hartree-Fock function, and $\mathbf{T} = \mathbf{T}_1 + \mathbf{T}_2 + \mathbf{T}_3 + \dots$ is the excitation operator. In the CCSD(T) method, \mathbf{T} is truncated to $\mathbf{T}_1 + \mathbf{T}_2$, and the contribution from triple excitations is treated perturbatively and added to the coupled cluster result. This method has been shown to incorporate more of the correlation energy than the likely more expensive configuration interaction method with single, double, and triple excitation (CISDT), and the fourth-order Møller-Plesset perturbation theory (MP4) [47].

In order to obtain accurate interaction energies, the basis sets for correlated calculations shall be able to provide a virtual orbital space capable of recovering the majority of correlation energy [48]. The suite of correlation-consistent polarized valence basis sets cc-pVnZ, and its augmented version aug-cc-pVnZ with diffuse functions added is most commonly used with CCSD(T) calculations. In the notation n is a cardinal number representing the quality of the basis sets (D for double-zeta quality, T for triple-zeta quality, etc.).

A significant advantage of the correlated-consistent basis sets is its convergence behavior in the correlation energy computed with basis sets with increasing n . However, the

convergence is usually painfully slow, and it is generally difficult to compute a whole PES with basis sets with higher than quadruple-zeta quality today. Several techniques exist to solve this problem. The most obvious one is to extrapolate the correlation energies obtained with basis sets of different n , usually to a n^{-3} dependence [48]. Another commonly used method is to add mid-bond functions [49, 50]. Most recently, explicitly correlated coupled cluster methods, in particular the approximation methods CCSD(T)-F12a/b developed by Werner and coworkers [51–53] have been proved to be cost-effective in creating accurate non-reactive PESs [54, 55]. However, these methods were found to give incorrect long range behaviors in certain cases [55].

The consideration of basis-set superposition error (BSSE) is crucial in modeling van der Waals interactions [47]. In the supermolecule model, when computing the energy of the complex E_{AB} using a finite basis set, the description of one molecule is improved by the basis functions of the other molecule (and vice versa). Such effect is absent when computing the energies of individual molecules. As a result, an artificial attractive contribution to the interaction energy known as the BSSE may arise. A most commonly used technique to solve this problem in CCSD(T) calculations is the counterpoise (CP) correction [56, 57], in which the basis functions of the other molecule are included in computing the energy of one molecule.

The CCSD(T) method is not suited for all bimolecular inelastic collision problems. One could expect that such a highly-correlated method not scale very well and cannot be used for large molecular systems. In some difficult problems, the method is found not accurate enough [58]. And more importantly, the CCSD(T) method is a single reference method that cannot be generally used for collisions involving a open shell molecule. These systems are governed by multiple PESs that are degenerate at large molecular separations due to the non-zero total electronic spin in the open shell molecule. In some systems, e.g. the collision of a $^2\Pi$ molecule and a structureless atom, the two degenerate states belong to different symmetry groups and the restricted open-shell CCSD(T) method

can be formally used. In other systems, the use of a multi-reference electronic structure method is required. To date, an accurate and general multi-reference method for the computation of intermolecular interactions is not present, and such multi-surface systems remain challenging in inelastic scattering calculations. A widely used method is the multi-reference configuration interaction (MRCI) method, on top of the complete active space multi-configuration self-consistent field (CASSCF) wave functions. However, the MRCI method is usually limited to double excitations (MRCISD) and cannot retrieve sufficient correlation energy. Usually the Davidson correction [59] is applied to improve the correlation energy, but the results are not on par with CCSD(T) ones. In addition, the MRCI method is not size-extensive and the simple CP correction [56, 57] of the BSSE is not applicable.

An alternative approach to compute intermolecular interactions is the symmetry-adapted perturbation theory (SAPT). In addition to the possibility of dealing with larger molecular systems, the SAPT method can provide directly the contribution to the intermolecular potential from different sources (electrostatic, dispersion, etc.) [46]. The SAPT method is considered less reliable than the supermolecular model in modeling small molecules since the accurate modeling of induction and dispersion interactions is extremely challenging. References [60–62] are some excellent review articles on SAPT.

1.3.2 Creating Potential Energy Surfaces

The accuracy of the PES is not totally governed by the accuracy of the *ab initio* calculations. In order to be used in scattering calculations, the computed interaction energies as a function of the internal degrees of freedom of the collision system need to be fitted to an analytical form. However, for more complicated systems the sampling of all internal degrees of freedom is difficult. For example, a diatomic–diatomic collision system will have 6 degrees of freedom, and a grid sampling 10 on each degree of freedom will have one million geometries. A commonly used approach when studying rotationally inelastic

collisions is to create reduced dimension PESs, usually by fixing the geometries of the individual molecules. It has been shown that a reduced-dimension PES computed using the monomer geometries averaged over ground-state vibrational wave function may provide a good approximation to the full-dimensional PES [63]. Even with this approach, PESs for the interaction between a polyatomic molecule and another molecule would still have too many degrees of freedom for a grid sampling. In that case, the random sampling of geometries, in combination of a Monte Carlo error estimator [64] to evaluate the sampling is a useful technique. The random sampling can also be used in creating full-dimensional PESs [65].

For close-coupling calculations of rotationally inelastic scattering, the interaction energy is usually evaluated on a grid of R and angles in body-fixed frame. The potential is then fitted in a form involving spherical harmonics or rotation matrices. Such fitting form allows us to take advantage of the angular momentum algebra to efficiently evaluate potential matrix [\mathbf{V} in Eq. (1.8)] elements. Below we provide a description of the equation used in fitting the PES.

We can approximately consider the interaction of the two molecules as the expectation value of the sum of electrostatic interactions between them

$$V = \langle \psi_1 \psi_2 | V | \psi_1 \psi_2 \rangle = \left\langle \psi_1 \psi_2 \left| \sum_{ij} q_i q_j r_{ij}^{-1} \right| \psi_1 \psi_2 \right\rangle, \quad (1.18)$$

where ψ_1 and ψ_2 are the electronic wave functions of the two molecules, q_i is the charge of particle i , and r_{ij} is the distance between particles i and j .

Following Eq. (34) of Ref. [66], we expand r_{ij}^{-1} in the spherical harmonic series

$$r_{ij}^{-1} = \sum_{l_1 l_2 l} A_{l_1 l_2 l}(r_i, r_j, R) \sum_{m_1 m_2 m} \langle l_1 m_1, l_2 m_2 | l m \rangle C_{l_1 m_1}(\hat{r}_i) C_{l_2 m_2}(\hat{r}_j) C_{l m}^*(\Omega_{BS}), \quad (1.19)$$

where \mathbf{r}_i and \mathbf{r}_j are coordinates of particles in the space frame, $\Omega_{BS} = (\phi, \theta, 0)$ is the orientation of the body frame with respect to the space frame, and $C_{lm}(\hat{r})$ is an unnormalized

spherical harmonic. If the interaction is purely electrostatic with non-penetrating charge distributions, we can restrict that $l = l_1 + l_2$. However, when induction and dispersion is considered, we should include lower values of l as well for a proper description [66, 67].

In practice, the rotational wave functions of molecules are described in their molecule-frame coordinates. We transform the spherical harmonics in Eq. (1.19) to molecule frames with [68]

$$C_{l_1 m_1}(\hat{r}_i) = \sum_{\mu_1} D_{m_1 \mu_1}^{l_1*}(\Omega_{1S}) C_{l_1 \mu_1}(\rho_i), \quad (1.20)$$

and

$$C_{l_2 m_2}(\hat{r}_j) = \sum_{\mu_2} D_{m_2 \mu_2}^{l_2*}(\Omega_{2S}) C_{l_2 \mu_2}(\rho_j), \quad (1.21)$$

where $\Omega_{1S} = (\bar{\phi}_1, \bar{\theta}_1, \bar{\chi}_1)$ and $\Omega_{2S} = (\bar{\phi}_2, \bar{\theta}_2, \bar{\chi}_2)$ are the relative orientation of the two molecule frames to the body frame. Hence r_{ij}^{-1} can be expanded as

$$\begin{aligned} r_{ij}^{-1} &= \sum_{l_1 l_2 l} A_{l_1 l_2 l}(\rho_1, \rho_2, R) \sum_{m_1 m_2 m} \langle l_1 m_1, l_2 m_2 | l m \rangle \\ &\times \sum_{\mu_1 \mu_2} D_{m_1 \mu_1}^{l_1*}(\Omega_{1S}) D_{m_2 \mu_2}^{l_2*}(\Omega_{2S}) C_{l m}^*(\Omega_{BS}) C_{l_1 \mu_1}(\rho_i) C_{l_2 \mu_2}(\rho_j). \end{aligned} \quad (1.22)$$

And it is formally correct to expand the potential as

$$V(\mathbf{R}, \Omega_{1S}, \Omega_{2S}) = \sum_{l_1 l_2 l \mu_1 \mu_2} B_{l_1 l_2 l \mu_1 \mu_2}(R) \mu_{l_1 l_2 l \mu_1 \mu_2}(\Omega_{1S}, \Omega_{2S}, \Omega_{BS}), \quad (1.23)$$

with the expansion coefficients

$$\begin{aligned} B_{l_1 l_2 l \mu_1 \mu_2}(R) &= \sum_{ij} \int \int \psi_1^*(\rho_1) \psi_2^*(\rho_2) A_{l_1 l_2 l}(\rho_i, \rho_j, R) C_{l_1 \mu_1}(\rho_i) C_{l_2 \mu_2}(\rho_j) \\ &\times \psi_1(\rho_1) \psi_2(\rho_2) d\rho_1 d\rho_2, \end{aligned} \quad (1.24)$$

and the angular basis

$$u_{l_1 l_2 l \mu_1 \mu_2}(\Omega_{1S}, \Omega_{2S}, \Omega_{BS}) = \sum_{m_1 m_2 m} \langle l_1 m_1, l_2 m_2 | l m \rangle D_{m_1 \mu_1}^{l_1*}(\Omega_{1S}) D_{m_2 \mu_2}^{l_2*}(\Omega_{2S}) C_{lm}^*(\Omega_{BS}). \quad (1.25)$$

Since V is actually independent of the choice of \hat{R} (or the space-fixed frame), in fitting the *ab initio* potential, we usually align the space-fixed frame to the body-fixed frame mentioned above. In this frame, only $m = 0$ terms will contribute to the potential. It follows that

$$u_{l_1 l_2 l \mu_1 \mu_2}(\Omega_{1S}, \Omega_{2S}, \Omega_{BS}) = \sum_{m_1} \langle l_1 m_1, l_2, -m_1 | l 0 \rangle D_{m_1 \mu_1}^{l_1*}(\Omega_{1S}) D_{-m_1, \mu_2}^{l_2*}(\Omega_{2S}). \quad (1.26)$$

Equation (1.26) can be further simplified if the system has extra symmetry. For example, if molecule 2 is a linear molecule in the $^1\Sigma$ state, its electronic wave function is cylindrically symmetric, $B_{l_1 l_2 l \mu_1 \mu_2}(R)$ will be zero unless $\mu_2 = 0$. When such symmetry properties are considered, Eq. (1.26) may be written in a slightly different form, such as expressing the angular dependence in terms of spherical harmonics.

The $B_{l_1 l_2 l \mu_1 \mu_2}$ expansion coefficients in Eq. (1.23) can be evaluated from fitting the *ab initio* potential, usually by a least-squares fit. Alternatively, we can use the orthogonal property of the angular basis in Eq. (1.26) and compute the expansion coefficients through numerical integration. The latter method requires that *ab initio* calculations be performed on an angular grid suitable for a numerical quadrature.

A converged scattering calculation usually requires an integration grid on R with a small spacing. Performing *ab initio* calculation of the interaction energies at each R is impractical and generally unnecessary. One can simply spline the fitted expansion coefficients over R to ensure a smooth variation. Another approach is to spline the *ab initio* interaction energies of each molecular orientation and fit them during the course of solving CC equations. In a study of the OH-HCl PESs Wormer *et al.* [69] claim that the

first approach is more efficient.

Solving the CC equations usually requires propagation to a large value of R , at which the interaction is weak that one can hardly describe it reliably with *ab initio* calculations. For systems dominated by multipole-multipole electrostatic interaction at long range, a distributed multipole analysis of the electron density of individual molecules from *ab initio* calculations [70, 71] can be performed, and the expansion coefficients can be expressed analytically at long range [69]. For other systems, larger expansion coefficients are usually extrapolated with a R^{-n} dependence, with n either fitted [72] or chosen according to the spherical harmonic expansion of electrostatic, induction, and dispersion forces [66, 73]. In either case, smaller expansion coefficients are usually damped to zero with a switching function.

Extrapolation of the PES to the classical forbidden region where the repulsive electron exchange interaction dominates is considered unreliable. Usually *ab initio* calculations are performed to R small enough (i.e., to an R at which the repulsive interaction energy is much larger than the collision energy) for a converged scattering calculation.

1.4 Organization of the Dissertation

In this dissertation the collisional dynamics of three small molecules, OH, NH₃, and CH₃ will be studied. OH and CH₃ are unstable free radicals that occur commonly in combustion, atmospheric processes and interstellar chemistry. These radicals usually play a key part in many chemical processes, and the study of the interaction between these species and other molecules will be important in understanding reaction mechanisms and energy transfer. Experimental and theoretical studies of the collision of free radicals have been extensively reviewed [9, 74, 75]. NH₃ is one of the most important interstellar molecule and the study of its collisional dynamics is of astrophysical importance [76–79].

The following chapters can be divided into three parts. The first part is primarily motivated to interpret crossed molecular beam experiments that can be carried out with a

Stark decelerator. This technique uses an inhomogeneous electronic field to manipulate molecular beams. It could help setting up molecular beam experiment with continuously varying collision energy and a narrow collision energy distribution. This in turn makes possible the observation of scattering resonances. Scattering resonances arises from short-lived quasibound states between the collision partners formed during the course of collision [80]. These resonances are very sensitive to PES's and are purely quantum effects.

This part contains two chapters. Chapters 2 and 3 describes the resonances in the state-to-state rotationally inelastic cross sections of the OH-He/Ne and the NH₃-H₂ systems, respectively. In these chapters we present and analyze the resonances in the two systems and discuss the requirements for observing them. We show that rich resonance structures exist in these systems, although the observation would require a very narrow collision energy distribution in a crossed molecular beam experiment. We hope these studies would help experimentalists in searching scattering resonances.

The second part of the dissertation describes our work on the CH₃ radical. Previously, the study of the inelastic collisions of a polyatomic free radical has been rare. Chapter 4 presents our investigations of the vibrational relaxation of CH₃ in collisions with He. This is, to our best knowledge, the first fully quantum study of state-resolved collisional ro-vibrational energy transfer of a polyatomic molecule.

Inspired by the theoretical work of our group [81], Orr-Ewing and co-workers at the University of Bristol performed a series of crossed molecular beam experiments measuring the differential cross sections (DCSs) of CH₃ and CD₃ in inelastic collisions with various partners. Chapters 6 and 5 describe respectively the joint theoretical and experimental study in the rotational energy transfer of methyl radicals in collisions with He, Ar, and H₂/D₂. In these studies, we computed new PESs for the corresponding systems and performed close-coupling calculations. The experimental and theoretical results are in good agreement, confirming the accuracy of our theoretical approach. The properties of the PESs and their connections to the propensities in the rotationally inelastic collision

process are also discussed.

The third part, including Chapters 7 and 8, presents our work on the PESs, bound-state, and scattering calculations of the OH-H₂ system. This work was motivated by a new experiment carried out in Berlin [82] measuring the fully state-resolved OH-H₂ integral cross sections as a function of collision energy. The calculation is theoretically challenging in that this is a two-surface problem and the Born-Oppenheimer approximation is broken down. In Chapter 7, we present two sets of OH-H₂ PESs, representing two approaches of tackling the problem: by direct computation of the non-adiabatic coupling, and by circumventing the problem through sampling only molecular geometries with certain symmetry properties. We also performed bound-state calculations and the results are in excellent agreement with earlier experimental results.

Finally in Chapter 8 we show the computed OH-H₂ rotationally inelastic collision cross sections and compare them with experimental results. While the agreement is reasonable, the cross sections of this system is very sensitive to the PESs. We also show extra *ab initio* calculations to justify our PESs, and discuss the discrepancy between theory and experiments.

Chapter 2

Scattering Resonances of OH($X^2\Pi$) in Collisions with He and Ne

This chapter contains long excerpts of a paper titled “Theoretical studies of the resonances in state-to-state rotationally inelastic scattering of OH($X^2\Pi$) with helium” by Koos B. Gubbels, Qianli Ma, Millard H. Alexander, Paul J. Dagdigian, Dick Tanis, Gerrit C. Groenenboom, Ad van der Avoird, and Sebastiaan Y. T. van de Meerakker, originally published on *J. Phys. Chem.* [83], and is presented with permission of the American Institute of Physics.

The new OH–He potential energy surface, described in Sec. 2.3, was created by our collaborators at Radboud University Nijmegen. The scattering calculations described in this chapter were performed by both groups individually.

2.1 Introduction

Measurements of state-to-state cross sections provide important tests of the reliability of computed potential energy surfaces (PESs) describing the interaction of atoms and molecules [84]. Cross sections for collision-induced rotational transitions are sensitive to the anisotropy of the PES. Since non-bonding interactions are relatively weak, the magnitudes of the cross sections are mostly sensitive to the repulsive part of the PES, except at very low collision energies. An alternative, spectroscopic approach to gaining

information on PESs is the determination of the energies of the bound levels of van der Waals complexes of the collision partners [85, 86]. The energies of the bound levels are mainly sensitive to the attractive part of the PESs. As we go up higher in the manifold of these weakly bound levels, the energies of these levels eventually become higher than the dissociation energy of the complex, and such levels are quasi-bound. These quasi-bound levels are often described as resonances and can be thought of as a distortion of the continuum in the collision energy dependence of state-to-state cross sections [2]. In inelastic scattering, resonances are called shape or orbiting resonances when the quasi-bound levels involve monomer levels that are the same as in the initial or final level of the collision-induced transition, or Feshbach resonances when they involve different monomer states [2, 84]. Due to their sensitivity to the PES, resonances can reveal important information on the PES [87, 88]. So far, however, resonant structures in scattering cross sections have been experimentally observed only in exceptional cases [13, 89–92].

The crossed molecular beam technique has been an extremely useful tool for the determination of state-to-state cross sections, both integral and differential, as well as their dependence upon the collision energy [93]. The recently developed Stark deceleration technique, taking advantage of the interaction of polar molecules with time-varying electric fields, has allowed continuous tuning of the beam velocity [11]. This has facilitated measurements of the collision energy dependence of state-to-state integral cross sections down to energies of 70 cm^{-1} [94]. Moreover, the velocity spread in such decelerated beams is much smaller than in conventional molecular beams. Thus far, an energy resolution of $\geq 13 \text{ cm}^{-1}$ has been achieved for collisions of OH radicals with rare gas atoms [94–96]. This resolution is mainly limited by the velocity and angular spread of the atomic collision partner, and is too low to experimentally resolve scattering resonances. A recent study has shown that the energy resolution can be improved significantly by an appropriate choice of the beam velocities and interaction angle [97]. When these measures are put into practice in the laboratory, collision energy resolutions can be obtained that may enable

the observation of scattering resonances.

Atom-molecule collisions are the simplest type of collision process in which rotationally inelastic transitions can be observed. Early calculations [98, 99] on rotationally inelastic scattering of N_2 molecules with He atoms have shown that resonances occur at low collision energies, but the experimental verification of these predictions was not yet possible. Collisions of $\text{OH}(X^2\Pi)$ with rare gases have emerged as paradigms of scattering of an open-shell molecule with an atom [94, 96, 100–105]. The OH–rare gas systems are good candidates for the observation and analysis of resonances in rotationally inelastic collisions because the collision energy can be reduced by Stark deceleration of the OH beam. Since $\text{OH}(X^2\Pi)$ is an open-shell molecule with orbital degeneracy, the collision dynamics is governed by two PESs [106], and interesting multi-state dynamics can occur. Of particular interest for the study of resonances are the OH–He and OH–Ne systems, since the dissociation energies of these systems are smaller than the rotational level spacings of the OH radical. The resonance features associated with the various rotational levels are therefore well separated. The shallow van der Waals wells support only one or two stretch vibrational levels [107], resulting in a rather simple, yet interesting, analysis of the resonances. Shape resonances in OH–He collisions were previously analyzed by Dagdigian and Alexander [104] in a study of elastic depolarization. Bound states of the OH–He complex have been investigated spectroscopically by Han and Heaven, who identified complex features as scattering resonances in $\text{OH}(A)$ –He [108].

Here, we present a detailed and precise study of scattering resonances in the OH–He and OH–Ne systems, in order to develop insight into the nature and strength of the resonances and to assist in the experimental search for such scattering resonances. For the OH–He system, we have calculated new three dimensional potential energy surfaces. The collision energy dependence of the relative state-to-state integral scattering cross sections that are derived from these potentials compares more favorably with recent experiments [96] than the results from previous calculations. For the correct assessment

of the resonances, the calculations are performed on a very fine grid of collision energies, and particular care is taken to converge the calculations to avoid numerical artifacts to be interpreted as resonant structures.¹

We characterize the resonances with various techniques, including the adiabatic bender model [40, 109] and collision lifetime analysis [110]. We investigate how the differential cross section for several transitions changes as the collision energy is scanned through the resonances, and observe dramatic effects.

This chapter is organized as follows: The details of the scattering calculations are briefly presented in Section 2.2. In Section 2.3 we describe the new three-dimensional (3D) PESs that are developed for OH-He. Section 2.4 describes our calculations on the state-to-state scattering cross sections in OH-He collisions. A detailed analysis of shape and Feshbach resonances is given. Section 2.5 presents similar results for the OH-Ne system. A discussion of the prospects for observing these resonances in crossed beam experiments using a Stark decelerator, by either recording the integral or the differential cross sections, follows in Sec. 2.6.

2.2 Scattering Calculations

The theory of scattering between a molecule in a $^2\Pi$ electronic state and a structureless atom is well established [106]. The interaction can be described by two PESs corresponding to states of A' and A'' symmetries. For OH-He, we have constructed new PESs, which are explained in Sect. 2.3, while for OH-Ne, we used the PESs by Sumiyoshi *et al.* [111] Close-coupling calculations were performed both with the HIBRIDON suite of programs [31], and with a second independent scattering program for open-shell diatom-

¹In HIBRIDON the RCUT parameter allows one to drop channels which are open asymptotically but closed at RCUT. A reasonable large RCUT would reduced the number of channels significantly while obtaining accurate cross sections. However, in cases where the collision energy lies near (either above or below) the threshold for one (or more) channels (in other words near the point where a particular asymptotic state just becomes energetically allowed), accuracy may be lost by dropping channels. In this work (and all other scattering calculations presented in this dissertation), this channel-dropping mechanism was not applied.

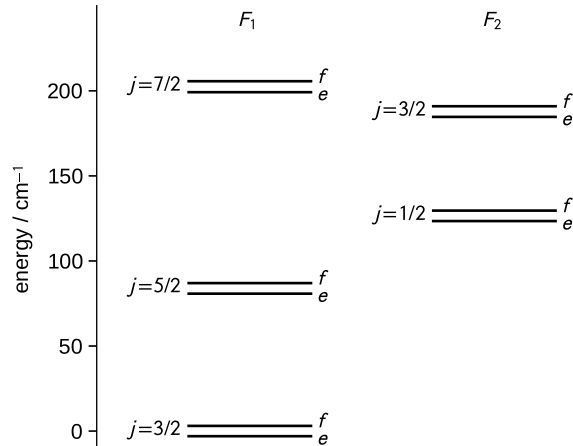


Figure 2.1: Energies of the lower rotational levels of OH($X^2\Pi$). The Λ -doublet splitting is exaggerated for clarity. The initial level for all scattering calculations is the $j = 3/2, F_1, f$ level.

atom scattering described in Ref. [112]. Care was taken to independently check the results with the two scattering programs and to converge the cross sections. For OH-He the maximum total angular momentum was $J = 100.5\text{--}140.5$, depending on the collision energy, and the channel basis consisted of all rotational levels of OH with $j \leq 6.5$, while for OH-Ne the channel basis consisted of all rotational levels with $j \leq 7.5$. In this paper, we calculate cross sections from fully converged close-coupling calculations in order to study resonances in inelastic collisions between low-lying rotational states of the OH radical. For reference, the energies of the lower rotational levels of OH($X^2\Pi$) are displayed graphically in Fig. 2.1.

2.3 Three-Dimensional OH-He Potential

A crucial role in the scattering calculations is played by the interaction potential. In Ref. [112] a detailed experimental and theoretical study of inelastic scattering between OH radicals and the rare gas atoms He, Ne, Ar, Kr and Xe was performed. The theoretical results in that study were shown to be in excellent agreement with experimentally measured inelastic cross sections. The agreement between theory and experiment was, although still very good, the worst for the OH-He system. It was believed that this was due to the quality

of the PES, since for the OH–He system a smaller basis set was used in the calculations than for the other systems. For this reason, we construct here a new potential for the OH–He system. We note that in Ref. [112] the experimental resolution was unfortunately not yet high enough to observe resonances.

In trying to improve the agreement with the experimental results, we first constructed new 2D PESs for OH–He collisions. This was done by enhancing the basis set for the coupled-cluster calculations of the interaction energy from the augmented triple-zeta correlation-consistent basis set (AVTZ) used by Lee *et al.* [107] to the quintuple-zeta basis set (AV5Z). We computed the interaction energies with the open-shell single and double excitation coupled cluster method with perturbative triples as implemented in the MOLPRO package [113]. The interaction energies were evaluated for 288 geometries on a two-dimensional grid with 12 Gauss-Legendre points in the Jacobi-angle θ . The OH bond length was fixed at the vibrationally averaged distance of $r_0 = 1.8502 a_0$, whereas Lee *et al.* used the equilibrium distance r_e . The relevant geometry is illustrated in Fig. 2.2. We included midbond orbitals ($3s, 3p, 2d, 1f, 1g$) with the exponents of Ref. [49]. These midbond functions were centered on the vector \mathbf{R} that connects the He atom and the center-of-mass of the OH molecule, at a distance from the helium atom that is half the distance of the helium atom to the nearest atom of the OH molecule. Also the counterpoise correction of Boys and Bernardi was applied [56]. The grid of atom-molecule separations consisted of 18 points ranging from $R = 3 a_0$ to $9 a_0$ at short range and 6 points on an approximately logarithmic scale up to $25 a_0$ at long range.

As mentioned before, two potential energy surfaces belonging to states of A' and A'' symmetry are involved in the OH–rare-gas atom scattering. The average V_s and half-difference V_d of these potentials can be expanded in Racah normalized spherical harmonics

to damp these five long-range terms in the short range with $\beta = 0.6 a_0^{-1}$. In the short range ($R < 5.5 a_0$), the expansion coefficients $v_{l,0}(R)$ were fitted to an exponential, namely

$$v_l^{\text{sr}}(R) = s_l e^{-\alpha_l R}. \quad (2.4)$$

The difference between the *ab initio* interaction energies and the analytic long range and short range functions was fitted with a reproducing kernel Hilbert space (RKHS) method [116]. The RKHS parameter m was chosen such that the RKHS fit would decay faster than the leading long-range term for each l . The RKHS smoothness parameter was set to 2. For the expansion coefficients of the difference potential, $v_{l,2}(R)$, no analytic short range and long range fit was performed, so that everywhere the RKHS method was used. Using the described procedure, we obtained an accurate fit to the *ab initio* points. More details of the fit can be found from the supporting material of Ref. [83], where we provide a FORTRAN 77 code for the two-dimensional AV5Z potential.

We found that the absolute minimum of the fitted potential is located at $\theta = 68.7^\circ$, $R = 5.69 a_0$ on the A' PES, corresponding to an interaction energy of $V_{A'} = -29.8 \text{ cm}^{-1}$. The minimum potential energy values for $\theta = 0^\circ$ and $\theta = 180^\circ$ were found at $R = 6.56 a_0$ and $R = 6.09 a_0$, giving rise to $V_{A'/A''} = -27.1 \text{ cm}^{-1}$ and $V_{A'/A''} = -21.6 \text{ cm}^{-1}$, respectively. For comparison, we also mention the values obtained by Lee *et al.* [107], who found that the absolute minimum of their potential was located at $\theta = 68.6^\circ$, $R = 5.69 a_0$ for A' symmetry, with an interaction energy of $V_{A'} = -30.0 \text{ cm}^{-1}$. The minimum values for $\theta = 0^\circ$ and $\theta = 180^\circ$ were found at $R = 6.54 a_0$ and $R = 6.09$, giving rise to $V_{A'/A''} = -27.1 \text{ cm}^{-1}$ and $V_{A'/A''} = -21.8 \text{ cm}^{-1}$, respectively. The two potentials are seen to give very similar results for the local and global minima. Moreover, using the new AV5Z potential for scattering calculations, we found only a very slight improvement in the agreement with the experimental data.

Therefore, we tried to improve the PES further by taking the vibrational motion of

the OH radical into account. To this end, we computed the interaction energies of the OH-He system on a three-dimensional grid. At short and intermediate range we used a step size of $\Delta R = 0.25 a_0$ for $3 a_0 \leq R \leq 12.5 a_0$ and $\Delta r = 0.25 a_0$ for $0.75 a_0 \leq r \leq 4.5 a_0$. For the angle θ we used an equidistant grid of 16 points including 0 and 180° with a spacing of $\Delta\theta = 12^\circ$. At long range we used 4 equidistant points between $14 a_0 \leq R \leq 20 a_0$, while we used a step size of $\Delta r = 0.5 a_0$ for $0.75 a_0 \leq r \leq 4.25 a_0$. The distance $r = 4.5 a_0$ was also included in the long-range fit. For the angle θ we used an equidistant grid of 9 points with a spacing of $\Delta\theta = 22.5^\circ$. On this grid we computed the interaction energies with a triple-zeta basis set (AVTZ) and using midbond orbitals with geometry-dependent exponents [117]. Especially for large r and small R , the electronic structure calculations did not always converge. Then, we obtained the energy for the corresponding grid point by means of interpolation or extrapolation from neighbouring grid points.

To perform the fit of the sum interaction potential V_s , we proceed in the following way. We represent the potential as a sum of three terms, namely

$$V_s(R, \theta, r) = V_s^{\text{sr}}(R_a, \theta_a, r) + V_s^{\text{sr}}(R_b, \theta_b, r) + V_s^{\text{lr}}(R, \theta, r), \quad (2.5)$$

where the different coordinates are defined in Fig. 2.2. This representation is convenient because the coordinates of the first and second term of Eq. (2.5) are ideally suited to describe the short-range behavior near the H and O atom, respectively, while the coordinates of the third term are convenient to describe the long-range behavior. The short-range terms are fitted by

$$V_s^{\text{sr}}(R_i, \theta_i, r) = \sum_{l=0}^{l_{\text{max}}^i} e^{-\beta_i R_i} P_l(\cos \theta_i) s_l^{(i)} + \sum_{l=0}^{l_{\text{max}}^i} \sum_{k=0}^{k_{\text{max}}^i} \sum_{n=0}^{n_{\text{max}}^i} R_i^n e^{-\beta_i R_i} P_l(\cos \theta_i) r^k e^{-\alpha_i r^3} s_{lnk}^{(i)}, \quad (2.6)$$

where $i = a, b$, while $P_l(x)$ are Legendre polynomials corresponding to the functions

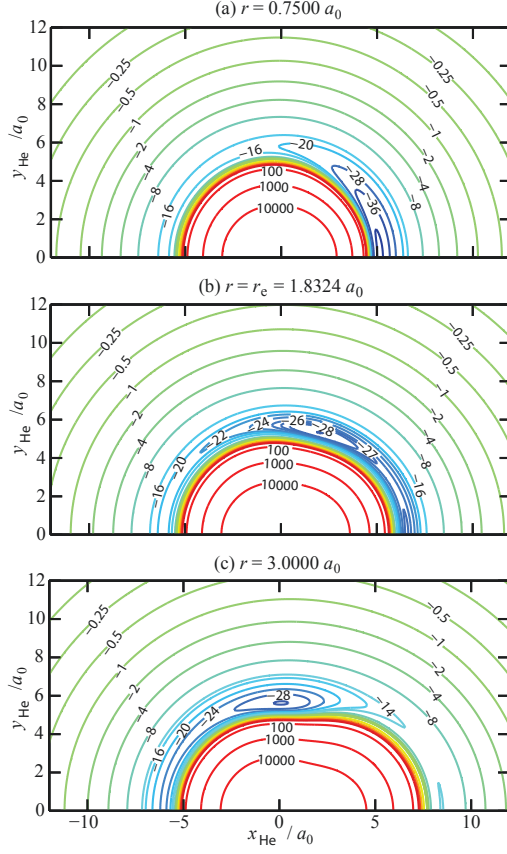


Figure 2.3: A' potential energy surface. The OH radical lies on the horizontal axis, with the center-of-mass of the molecule at the origin. The O atom lies left of the origin, the H atom to the right. For each geometry of the complex, defined by the OH bond length r and the position $(x_{\text{He}}, y_{\text{He}})$ of the He atom, the interaction energy is calculated, resulting in contours with the unit of cm^{-1} . The three plots differ in the OH bond length, namely in panel (a) we have $r = 0.75 a_0$, in panel (b) $r = 1.8324 a_0$, and in panel (c) $r = 3.00 a_0$.

$C_{l,0}(\theta, 0)$ of Eq. 2.1. We used the values $l_{\text{max}}^0 = 1$, $n_{\text{max}}^a = 3$, $k_{\text{max}}^a = 8$, $l_{\text{max}}^a = 7$, $n_{\text{max}}^b = 3$, $k_{\text{max}}^b = 8$ and $l_{\text{max}}^b = 5$. The long range term is fitted by

$$V_s^{\text{lr}}(R, \theta, r) = \sum_{n=6}^{13} \sum_{l=0}^{n-4} \frac{f_n(\beta R)}{R^n} P_l(\cos \theta) c_{nl}(r), \quad (2.7)$$

where f_n is the damping function of Eq. (2.3). Nonzero values of c_{nl} occur only for even values of $l + n$, and then they are given by

$$c_{nl}(r) = c_{nl}^0 + \sum_{k=0}^3 r^k e^{-\alpha_n r^3} c_{nlk}. \quad (2.8)$$

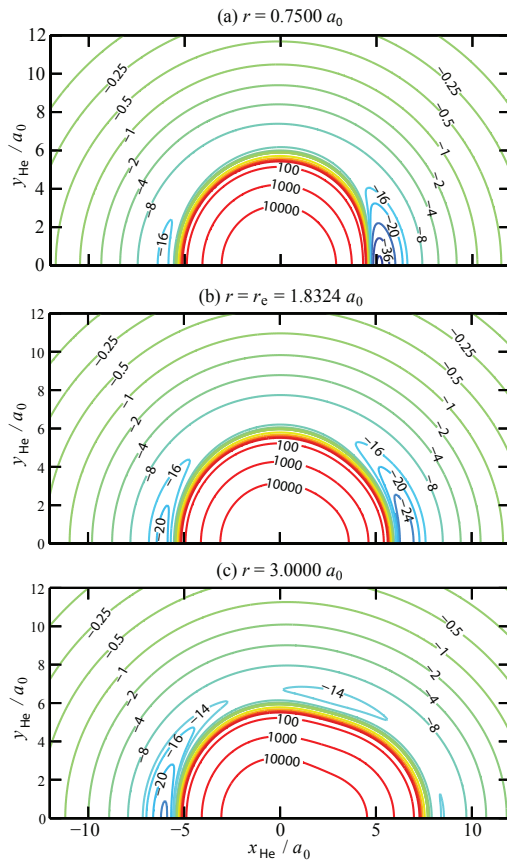


Figure 2.4: A'' potential energy surface. The OH radical lies on the horizontal axis, with the center-of-mass of the molecule at the origin. The O atom lies left of the origin, the H atom to the right. For each geometry of the complex, defined by the OH bond length r and the position $(x_{\text{He}}, y_{\text{He}})$ of the He atom, the interaction energy is calculated, resulting in contours with the unit of cm^{-1} . The three plots differ in the OH bond length, namely in panel (a) we have $r = 0.75 a_0$, in panel (b) $r = 1.8324 a_0$, and in panel (c) $r = 3.00 a_0$.

We use two different values for α_n , namely $\alpha_n = \alpha_{\text{I}}$ for $6 \leq n \leq 9$, and $\alpha_n = \alpha_{\text{II}}$ for $10 \leq n \leq 13$. For the difference potential V_{d} similar fit functions are used, only now the Legendre polynomials $P_l(x)$ are replaced by associated Legendre functions $P_l^2(x)$ corresponding to the Racah spherical harmonics $C_{l,2}(\theta, 0)$ of Eq. (2.1), so that all sums start with $l = 2$. Moreover, we use $l_{\text{max}}^0 = 2$, $n_{\text{max}}^a = 5$, $k_{\text{max}}^a = 5$, $l_{\text{max}}^a = 6$, $n_{\text{max}}^b = 5$, $k_{\text{max}}^b = 4$ and $l_{\text{max}}^b = 6$. The linear and the nonlinear fit parameters were determined by minimizing a weighted least-squares error.

By evaluating the analytic representation of the potential on the *ab initio* grid, we were able to compare the fitted energy values with the *ab initio* values. We found that

we only obtained a reliable fit for OH bond lengths $r \leq 3 a_0$. At smaller values of R the largest relative error of an analytic value compared to an *ab initio* value for $r \leq 3 a_0$ was 6.67% for the sum potential and 1.10% for the difference potential. At large R , again considering only $r \leq 3 a_0$, the largest relative error was 3.23 % for the sum potential and 3.32% for the difference potential. We also calculated the average relative error, which for the sum potential was 0.32% at short range and 0.49% at long range, while for the difference potential it was 0.04% in the short range and 0.90% in the long range. In Fig. 2.3, we show two-dimensional contour plots of the fitted OH-He A' PES for $r = 0.75 a_0$, $r = 1.8324 a_0$ and $r = 3.00 a_0$, while in Fig. 2.4 the same plots are shown for the fitted A'' PES. For the equilibrium bond length $r_e = 1.8324 a_0$, our fit of the 3-dimensional potential is in very close agreement with the PES of Lee *et al.* [107], as it should, since both PESs were calculated with the same *ab initio* method using the same basis set. The absolute potential energy minimum for $r = 1.8324 a_0$ is located at $\theta = 69.2^\circ$, $R = 5.69 a_0$ for A' symmetry, leading to an interaction energy of $V_{A'} = -30.0 \text{ cm}^{-1}$. The minimum values for $\theta = 0^\circ$ and $\theta = 180^\circ$ were found at $R = 6.55 a_0$ and $R = 6.09$, giving rise to $V_{A'/A''} = -27.2 \text{ cm}^{-1}$ and $V_{A'/A''} = -21.7 \text{ cm}^{-1}$, respectively.

To use the three dimensional potential for scattering, we started with the three-dimensional AVTZ potential, and then subtracted the values of this potential at $r = r_0$ and added the two-dimensional potential calculated for $r = r_0$ at the AV5Z level. This implies that the dependence of the intermolecular potential on the most relevant coordinates for the scattering calculation, namely R and θ , is computed at the AV5Z level for $r = r_0$, while the variation of the potential with the OH bond length r is taken into account at the AVTZ level. We solved for the OH vibrational motion in the full 3D potential generated by taking the intermolecular potential energy $V(R, \theta, r)$ and adding the free OH monomer potential $V_{\text{OH}}(r)$ [118]. For fixed R and θ this leads to an effectively one-dimensional problem that can be easily solved by standard numerical methods, such as the discrete variable representation based on sinc-functions (sinc-DVR) [119]. Taking the resulting

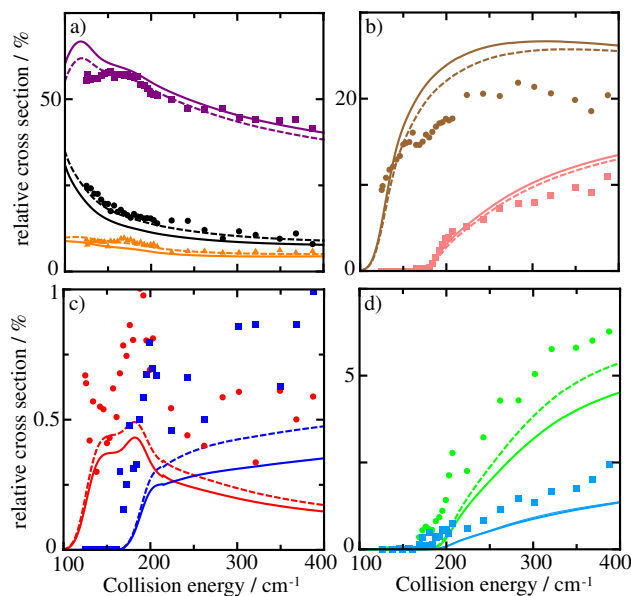


Figure 2.5: Relative state-to-state inelastic scattering cross sections of OH ($X^2\Pi, j = 3/2, F_1, f$) radicals with He atoms. On the vertical axes of the plots, 100 % refers to the total inelastic cross section. The experimental data points are shown as dots, while the theoretically calculated cross sections calculated by Lee *et al.* are included as solid curves, and the results with the adiabatic potential as dashed curves. Relative cross sections for inelastic collisions populating the (a) $j = 3/2, F_1, e$ (black), $j = 5/2, F_1, e$ (purple), and $j = 5/2, F_1, f$ (orange) states; (b) the $j = 1/2, F_2, e$ (brown) and $j = 3/2, F_2, f$ (pink) states; (c) the $j = 1/2, F_2, f$ (red) and $j = 3/2, F_2, e$ (blue) states; (d) the $j = 7/2, F_1, e$ (green) and $j = 7/2, F_1, f$ (cyan) states.

ground state energy for each R and θ and subtracting the $v = 0$ monomer vibrational energy in the absence of the He atom then results in an adiabatic two-dimensional PES. We found, actually, that this adiabatic potential is very similar to the “diabatic” potential obtained by first calculating the lowest vibrational state of OH in the monomer potential $V_{\text{OH}}(r)$ and then averaging the interaction potential $V(R, \theta, r)$ over this ground state. The two methods are expected to give similar results since the vibrational levels of OH are well separated in energy, so that the weak OH–He interaction gives only a slight admixture of the higher vibrational states of OH.

The inelastic OH–He cross sections with OH initially in the $j = 3/2, F_1, f$ level were calculated with the adiabatic potential. The results are shown in Fig. 2.5, where the experimental data of Ref. [112] is also shown, as well as the scattering results obtained with the potential of Lee *et al.* [107]. The theoretical data are convoluted with the experimental

energy resolution. To this end a Gaussian energy distribution is taken with a standard deviation that is a function of the energy. The value of the standard deviation ranges from 24 cm^{-1} at low collision energies to 59 cm^{-1} at the highest collision energies. We note that the relative cross sections are plotted, rather than the absolute cross sections, because these relative cross sections are the quantities experimentally measured. More details can be found in Refs. [94, 112]. We see from Fig. 2.5 that the overall the agreement with experimental data has improved noticeably with the adiabatic potential.

2.4 OH–He Collisions

2.4.1 State-to-State Integral Cross Sections

For OH–He collisions, the state-to-state scattering cross sections were calculated with the adiabatic potential described in the previous section. In Fig. 2.6, the energy dependence of the state-to-state integral cross sections for several transitions out of the $j = 3/2, F_1, f$ level of OH are shown. This level, which is the higher Λ -doublet component of the ground rotational level (see Fig. 2.1), can be selected with the Stark decelerator since it is low-field seeking in an inhomogeneous electric field [94]. The cross sections are computed on a very fine grid of energies to be able to study resonant features in detail.

Away from the resonances, these results are in good agreement with those previously reported by Kłos *et al.* [102]. As noted by these authors, there is a propensity for transitions preserving the total parity. The cross sections are found to be smaller for transitions with large energy gaps. The initial and final levels of the two transitions shown in Fig. 2.6(a) have a rather large energy separation ($> 100 \text{ cm}^{-1}$), and the total parity is inverted during the transitions. Hence, the cross sections for these transitions are small.

Resonances can be observed in Fig. 2.6 near the collision energies corresponding to thresholds for excitation of the OH radical to higher rotational and spin-orbit levels. Both shape resonances, which appear right above the threshold energies for the final

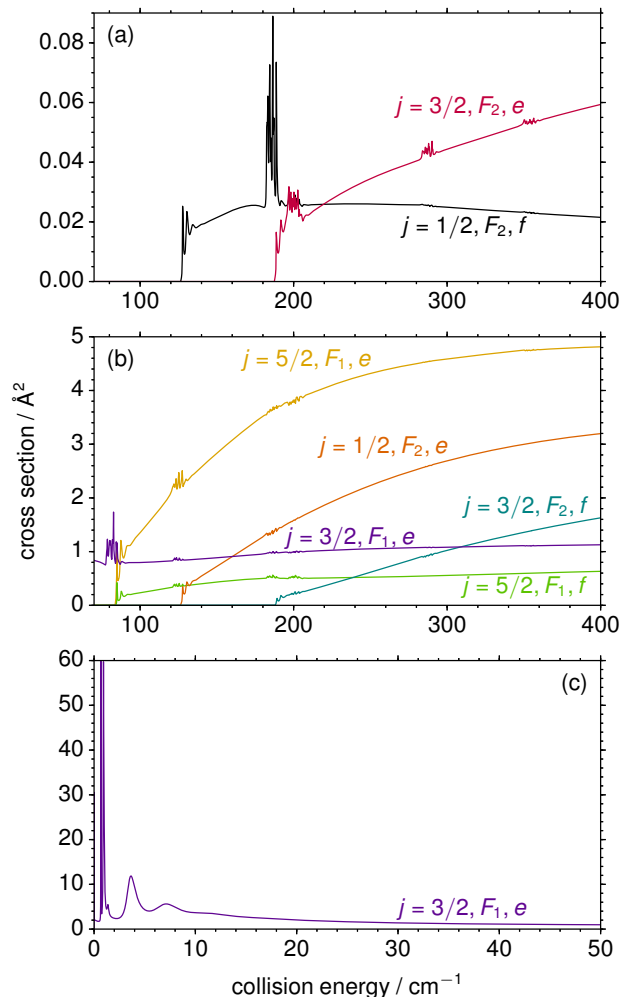


Figure 2.6: State-to-state integral cross sections vs. collision energy for transitions out of the OH $j = 3/2, F_1, f$ level in collisions with He. The final levels are indicated for each transition for which the cross section is plotted.

levels, and Feshbach resonances, which appear near the energies where higher rotational levels than the considered outgoing channel become open, are present. Except for the $j = 3/2, F_1, f \rightarrow j = 3/2, F_1, e$ and the $j = 3/2, F_1, f \rightarrow j = 1/2, F_2, f$ transitions, the Feshbach resonances are not significant compared with the background continuum. The $j = 3/2, F_1, f \rightarrow j = 3/2, F_1, e$ transition dominates at low collision energies and also gives rise to shape resonances with cross sections peaking above 10 \AA^2 . However, these shape resonances occur at collision energies of only a few wavenumbers.

In the following subsections, we analyze the shape resonances in the $j = 3/2, F_1, f \rightarrow$

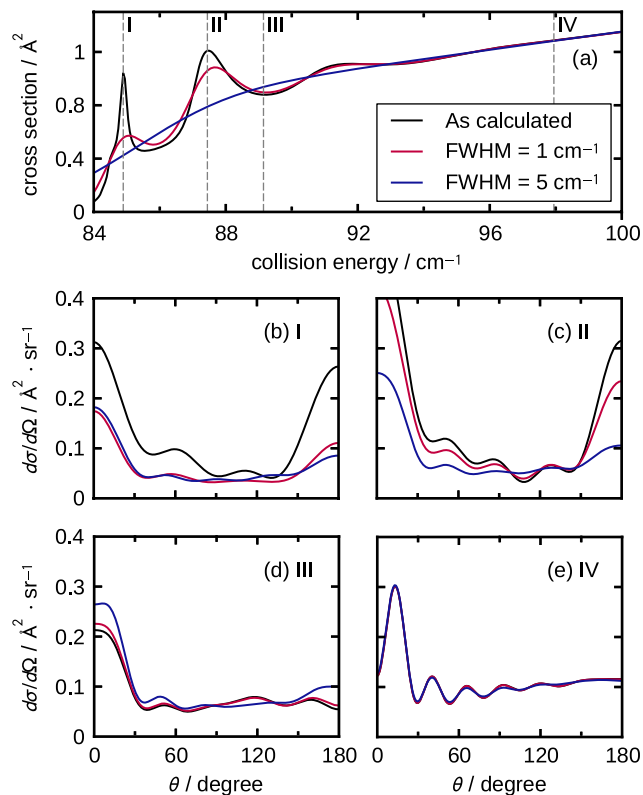


Figure 2.7: (a) State-to-state integral cross sections vs. collision energy for the $j = 3/2, F_1, f \rightarrow j = 5/2, F_1, e$ transition of OH in collisions with He (black line), and the integral cross section convoluted with Gaussian energy distributions of FWHM of 1 and 5 cm^{-1} (red and blue lines, respectively). (b)–(e) Differential cross sections $d\sigma/d\Omega$ of the above transition at several energies marked as dashed lines with Roman numerals in (a), together with the differential cross sections convoluted with Gaussian energy distributions as in (a).

$j = 5/2, F_1, e$ transition and the Feshbach resonances in the $j = 3/2, F_1, f \rightarrow j = 1/2, F_2, f$ transition. The former transition has a large cross section; the latter transition exhibits strong resonances that show the largest enhancement compared to the background.

2.4.2 Shape Resonances

Shape resonances result from quasi-bound states of the van der Waals complex formed by the collision partners at energies just above the threshold for the final level. All integral cross sections plotted in Fig. 2.6 display shape resonances. In this subsection we analyze the shape resonances associated with the $j = 3/2, F_1, f \rightarrow j = 5/2, F_1, e$ transition since it has a large integral cross section. Figure 2.7(a) displays these resonances on an expanded

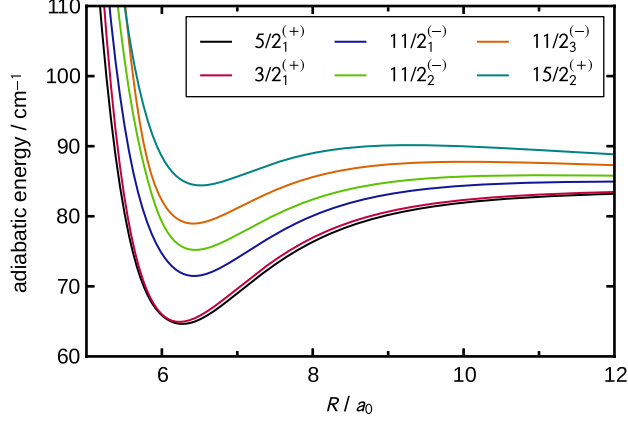


Figure 2.8: Plots of the OH-He adiabatic bender curves that correlate with the OH $j = 5/2, F_1, e$ level, obtained from close-coupling calculations. Curves are labeled with $J_n^{(p)}$, where J , p , and n are the total angular momentum, the total parity of the scattering wavefunction, and the cardinal index, respectively.

energy scale. Several maxima, with increasing peak width vs. energy, can be observed, as was also previously found [104] for OH-He and other He-molecule systems [81, 87, 120].

To gain more insight, we employ the adiabatic bender model [40, 109] to analyze the shape resonances. The method is similar to the previous analysis of OH-He collisions by Dagdigian and Alexander [104], except that we used a close-coupling channel basis instead of a coupled-states one. The full Hamiltonian with the inclusion of Coriolis coupling and only the radial nuclear kinetic energy excluded is diagonalized as a function of R . The eigenvalues define a set of adiabatic bender potential energy curves, which are labeled by the total angular momentum J , the total parity p of the scattering wavefunction, and the cardinal index n of the eigenvalue. In this paper, we will use the symbol $J_n^{(+)}$ and $J_n^{(-)}$ to label close-coupling adiabatic bender curves with $p = +1$ and $p = -1$, respectively.

Figure 2.8 shows several adiabatic bender curves that correlate with the OH $j = 5/2, F_1, e$ level. The curves marked with $5/2_1^{(+)}$ and $3/2_1^{(+)}$ are the two lowest lying adiabatic bender curves, each of which supports only one bound stretch level, with energies of 77.47 cm^{-1} and 78.15 cm^{-1} , respectively. As J and n increase, the curves move up in energy and the well depths become smaller. As a consequence, some of the bound levels become quasi-bound, and for the high lying curves (for example, the $15/2_2^{(+)}$ curve shown

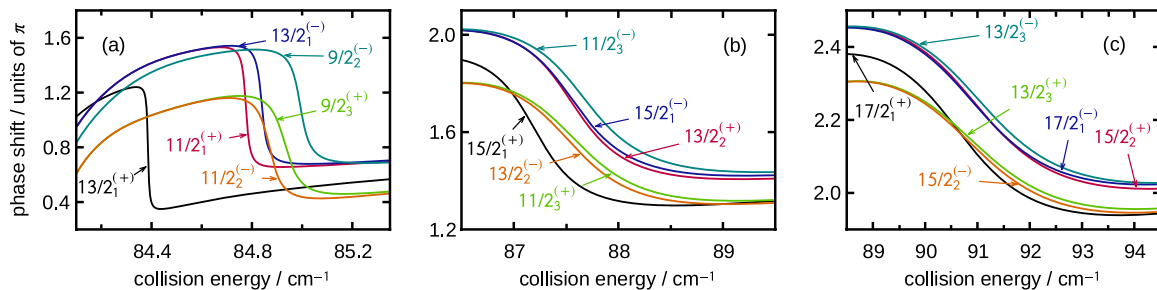


Figure 2.9: Phase shifts as a function of collision energy for OH($j = 5/2, F_1, e$)-He collisions, obtained from close-coupling adiabatic bender curves described in the text and shown in Fig. 2.8. Curves are labeled with $J_n^{(p)}$, where J , p , and n are the total angular momentum, the total parity of the scattering wavefunction, and the cardinal index, respectively.

in Fig. 2.8) the wells are too shallow to support any quasi-bound levels.

To compute the energies of the shape resonances, we treat the adiabatic bender curves in conventional one-dimensional scattering problems and calculate the phase shift. We should be able to observe rapid changes by π , signifying resonances, in the collision energy dependence of phase shift [2]. Fig. 2.9 shows the phase shift as a function of collision energy for all the adiabatic bender curves that have such a feature. We see from Fig. 2.9 that resonances in six adiabatic bender curves contribute to each of the three peaks shown in Fig. 2.7(a) (labeled as I, II, and III), which occur at 84.8, 87.6 and 91 cm^{-1} , respectively. The resonance features in Fig. 2.7(a) and Fig. 2.9 match well both in energy and width. Note that in order to distinguish the phase shift in different adiabatic bender curves, Fig. 2.9(b) and (c) do not show the whole range of the resonances, and thus the resonant changes in phase shift shown are less than π .

It is also interesting to compare the differential cross sections for collision energies on and off a resonance. Figures 2.7(b)–(e) display differential cross section for several energies marked in Fig. 2.7(a) with Roman numerals. The center of the two major peaks are marked as I and II, while III and IV correspond to non-resonant energies. We observe significant backward scattering for energies I and II, likely because of an increased time delay of collision due to the formation and decay of quasi-bound levels of the van der Waals complex. Backward peaks are insignificant for energies III and IV. We will further discuss

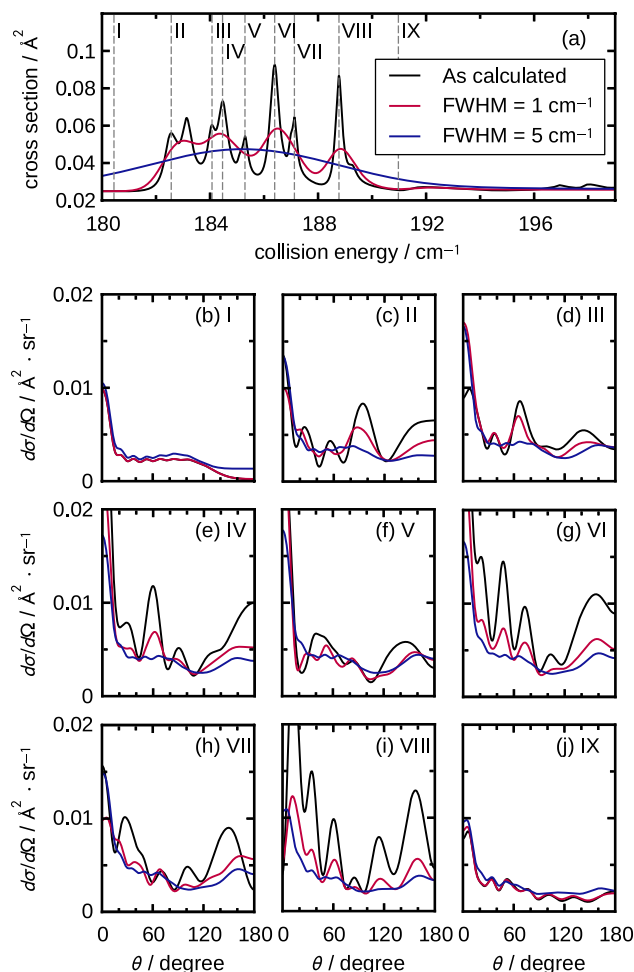


Figure 2.10: (a) State-to-state integral cross section vs. collision energy for the $j = 3/2, F_1, f \rightarrow j = 1/2, F_2, f$ transition of OH in collisions with He (black line), and the integral cross section convoluted with Gaussian energy distributions with FWHM of 1 (red line) and 5 cm^{-1} (blue line). (b)–(j) Differential cross sections $d\sigma/d\Omega$ of the above transition at several energies marked as dashed lines and Roman numerals in (a), together with the convoluted differential cross sections with Gaussian energy distribution as in (a).

this topic in the next subsection.

2.4.3 Feshbach Resonances

In Feshbach resonances, quasi-bound levels of the collision complex associated with a given rotational level dissociate to yield the molecule in a lower-energy rotational level. We consider here Feshbach resonances associated with the $j = 3/2, F_1, f \rightarrow j = 1/2, F_2, f$ transition. This transition was chosen for detailed study since the resonance features show

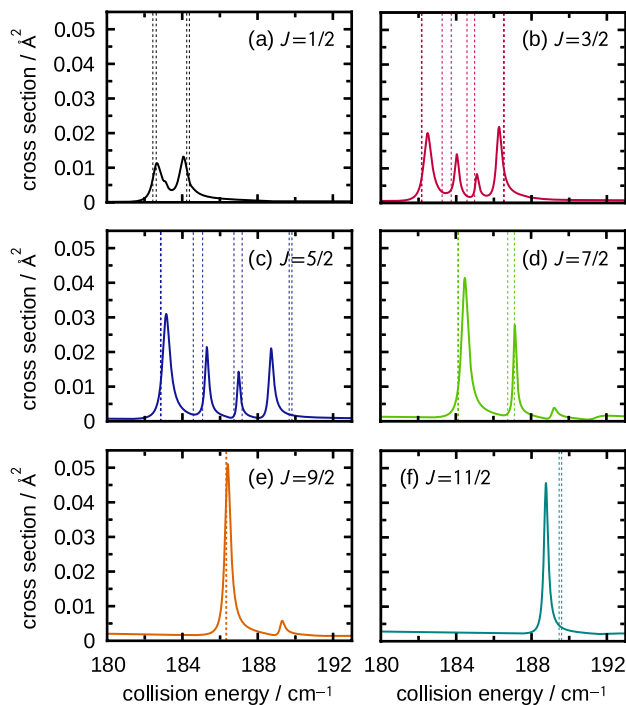


Figure 2.11: Partial cross sections vs. collision energy for the $j = 3/2, F_1, f \rightarrow j = 1/2, F_2, f$ transition of OH in collisions with He for total angular momentum $J \leq 11/2$. The dotted vertical lines denote the computed energies of the van der Waals stretch levels supported by the close-coupling adiabatic bender curves.

a *ca.* 4-fold increase over the continuum background (see Fig. 2.6). Figure 2.10(a) displays these resonances on an expanded energy scale.

It is seen that a rich set of Feshbach resonances exists in a collision energy range of several cm^{-1} below the energetic threshold for opening of the $F_2, j = 3/2$ level at 188 cm^{-1} . Figure 2.11 displays the contribution to the integral cross section for the $j = 3/2, F_1, f \rightarrow j = 1/2, F_2, f$ transition from various values of the total angular momentum J (partial cross sections). The individual partial cross sections exhibit one or more peaks, and their energies shift toward higher collision energy as J increases. For $J \geq 13/2$, no significant resonances can be found in the energy dependence of partial cross sections.

We performed an adiabatic bender analysis similar to that described in subsection 2.4.2. We calculated adiabatic bender potentials by diagonalizing the Hamiltonian expressed in a close-coupling channel basis. Since all possible values of l (the orbital angular momentum of the van der Waals complex) are included in the channel basis, there are

multiple adiabatic bender curves for each value of J . These adiabatic bender curves look similar to those shown in Fig. 2.8 and are not plotted here. The energies of the van der Waals stretch levels supported by these curves were derived using a fixed step-size discrete variable representation (DVR) method [121, 122]. To treat levels that might be quasi-bound, an infinite barrier was placed at the maximum of the centrifugal barrier on each adiabatic bender potential. For curves associated with large J , this approximation will lead to calculated energies higher than they should be and could lead to significant error. These computed energies are shown as dotted lines in Fig. 2.11. There is a reasonable match between the energies of the resonances and of the bend-stretch levels, especially for small J .

Fig. 2.10(b)–(j) display the differential cross section for the OH $j = 3/2, F_1, f \rightarrow j = 1/2, F_2, f$ transition at several energies marked on Fig. 2.10(a) with Roman numerals. The energies at I and IX are not at a resonance, and the differential cross sections show little backward scattering, while II – IV correspond to resonance energies, for which some backward scattering can be observed. The shapes of the differential cross sections are quite different at resonance energies compared to collision energies away from the resonances.

A simple way to analyze the resonances and to qualitatively explain backward scattering appearing in differential cross sections is to calculate the collision lifetime, which is the difference between the time that the collision partners spend in each other's neighborhood with and without the interaction [110, 123, 124]. For a direct comparison with the partial cross sections shown in Fig. 2.11, we compute the collision lifetime from initial state γ to final state γ' for individual total angular momenta J , defined as

$$\Delta t_{\gamma\gamma'}^J(E) = \text{Re} \left[-i \hbar \sum_{l,p,l',p'} \delta_{pp'} \left(S_{\gamma,\gamma',l,l'}^J \right)^* \frac{dS_{\gamma,\gamma',l,l'}^J}{dE} \right] \quad (2.9)$$

where l, p and l', p' denotes the orbital angular momentum and parity of initial and final levels, respectively, and $S_{\gamma,\gamma',l,l'}^J$ denotes S -matrix elements for total angular momentum J from close-coupling calculations. The lifetimes vs. J for the $j = 3/2, F_1, f \rightarrow j = 1/2, F_2, f$

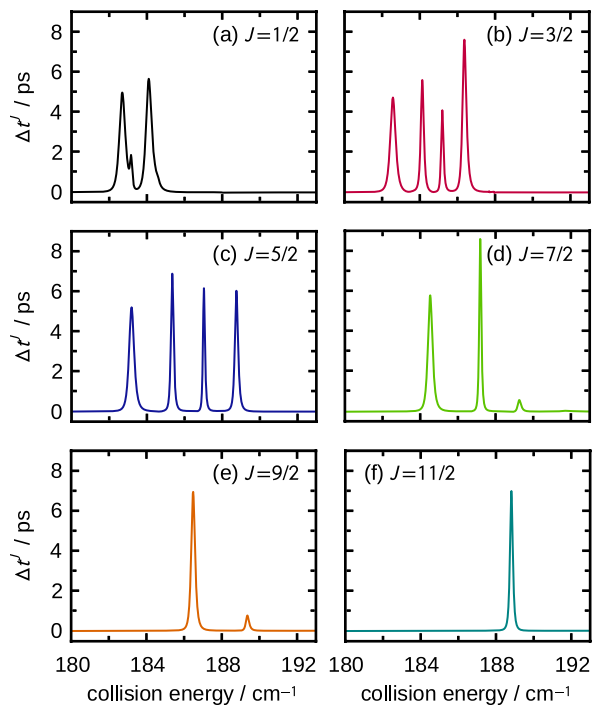


Figure 2.12: Collision lifetime $\Delta t^J(E)$ as a function of collision energy for the OH $j = 3/2, F_1, f \rightarrow j = 1/2, F_2, f$ transition in collisions with He, as defined in Eq. (2.9) of the text, for total angular momenta $J = 1/2 - 11/2$.

transition are plotted in Fig. 2.12. Clearly, the resonance peaks in Fig. 2.11 are well reproduced, with collision lifetimes of a few picoseconds. The most intense resonance peak lies at 186.4 cm^{-1} , which was largely due to the $J = 9/2$ partial cross section. From Fig. 2.12 we see that the corresponding lifetime is about 6 ps. We can compare this collision lifetime with the rotational period of the OH–He van der Waals complex. We estimate the rotational constant of the complex to be 0.32 cm^{-1} from the expectation value of $1/R^2$ computed with the wave function obtained from the DVR method on the lowest lying $J = 9/2$ adiabatic binder curve. This corresponds to a rotational period 14.9 ps, assuming $l = 3$.

We thus conclude that the collision lifetime has the same order of magnitude as the rotational period of the OH–He complex. It is therefore not surprising to observe significant backward scattering at some resonance energies. At off-resonance energies the collision lifetime will be $\ll 1 \text{ ps}$, which is much smaller than the OH–He rotational period.

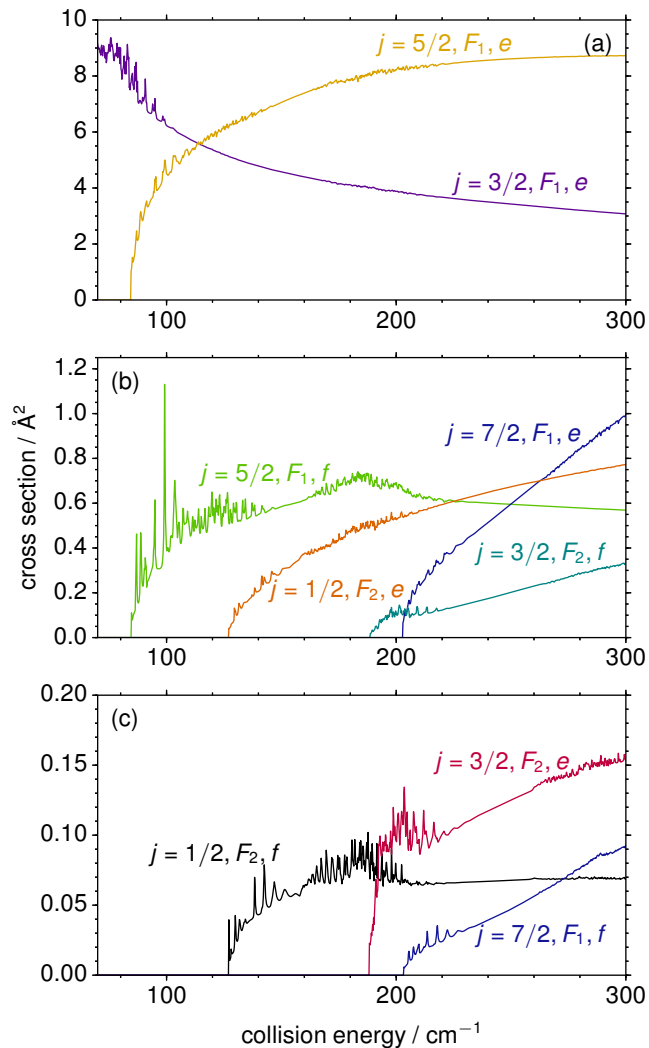


Figure 2.13: State-to-state inelastic scattering cross sections of OH ($X^2\Pi$, $j = 3/2, F_1, f$) radicals with Ne atoms as a function of the collision energy. The final states of the transitions are labelled on the curves.

Hence, backward scattering is expected to be barely observable.

2.5 OH–Ne Collisions

To describe the interaction between OH and Ne, we used the PES of Sumiyoshi *et al.* [111]. This PES was calculated using an explicitly correlated, spin-unrestricted coupled-cluster approach [UCCSD(T)-F12b] with a quintuple-zeta basis set (AV5Z). Although Sumiyoshi *et al.* calculated a three-dimensional potential, we used in Ref. [112] their

interaction potential evaluated at the equilibrium distance $r_e = 1.832 a_0$ for the scattering calculations, so that no effect of the OH vibrational motion was included. In that reference it was shown that this procedure already gives excellent agreement between theory and high-precision scattering experiments for OH–Ne collisions. Since we found in Section 2.3 that the vibrational motion of OH can be of quantitative influence, we also calculated an adiabatic potential from the three-dimensional potential of Sumiyoshi *et al.* in the same way as we did for OH–He. The resulting adiabatic potential was found to improve slightly the excellent agreement with the experimental results for the scattering of OH and Ne. In the present study, we use the adiabatic potential throughout and compute the cross sections on a much finer grid than in the study by Scharfenberg *et al.* [112] in order to study scattering resonances. In Fig. 2.13 we show the energy dependence of state-to-state integral cross sections for collisions of the OH radical with Ne atoms, where the OH radicals are initially in the $j = 3/2, F_1, f$ level. Overall, the behavior of the inelastic cross sections as a function of energy is rather similar to what was observed for the OH–He system in Section 2.4. For example, we again observe a propensity for transitions preserving the total parity. However, in the OH–Ne system none of the channels appears to have particularly strong Feshbach resonances, as was the case for the $j = 3/2, F_1, f \rightarrow j = 1/2, F_2, f$ transition of the OH–He system. The most pronounced resonant features observed for OH–Ne collisions are shape resonances in the $j = 3/2, F_1, f \rightarrow j = 5/2, F_1, f$ transition. In Fig. 2.14 we show these shape resonances in more detail.

Looking closely at Fig. 2.14, we see several resonance peaks that correspond to an increase in the cross section by about a factor of two compared to the nonresonant energies. A relatively strong resonance occurs at a collision energy of 99.23 cm^{-1} ; this resonance increases the cross section by a factor of four compared to the background. The latter resonance is indicated by the Roman numeral V. The main contributions to this resonance originate from partial cross sections with total angular momenta of $J = 37/2$ and $J = 39/2$. In Fig. 2.14, we also show the differential cross sections for several energies

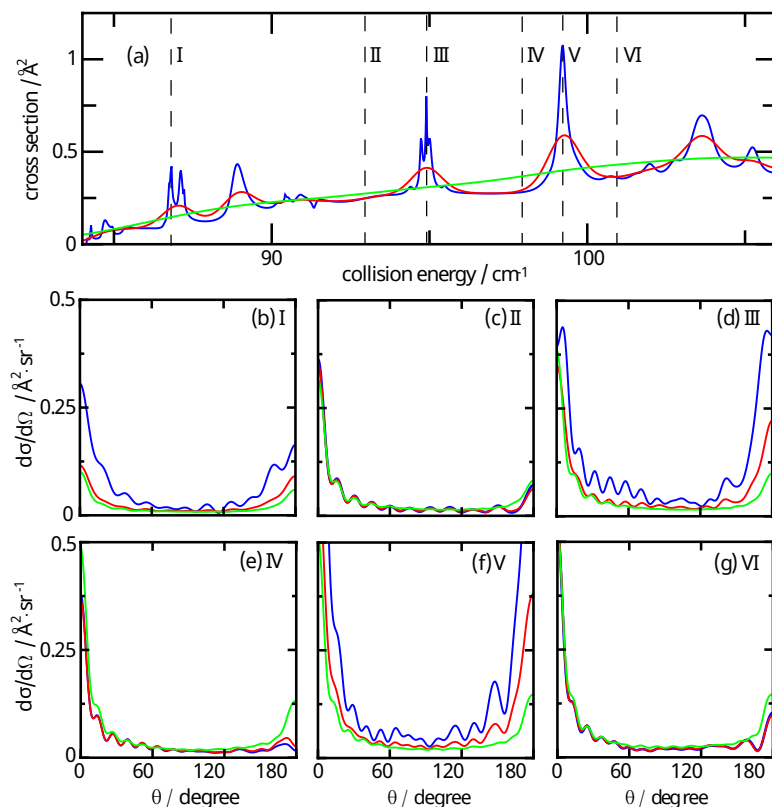


Figure 2.14: (a) Integral cross section for collisions of OH radicals with Ne atoms as a function of the collision energy. The initial state of the OH radical is the $j = 3/2, F_1, f$ state and the final state is the $j = 5/2, F_1, f$ state. The blue curve shows the theoretical results without any convolution, the red curve shows the integral cross section convoluted with a Gaussian energy distribution having a FWHM of 1 cm^{-1} , while for the green curve a FWHM of 5 cm^{-1} was used. At the collision energies designated with the Roman numerals I-VI, differential cross sections were calculated, shown in panels (b) to (g). Again the blue curves are not convoluted, while for the red curves a FWHM of 1 cm^{-1} was used, and for the green curves a FWHM of 5 cm^{-1} . At the scattering resonances (I, III and V), strong backscattering is observed.

that are marked by Roman numerals in panel (a). For the resonances at collision energies of $86.83, 94.90$ and 99.23 cm^{-1} , the cross sections are shown in the panels (b), (d) and (f). In these plots, large amplitudes for backscattering are observed. To compare, the differential cross sections were also calculated away from the resonances at the energies $93.00, 98.00$ and 101.00 cm^{-1} , and the results are shown in the panels (c), (e) and (g). In the case of nonresonant scattering, the observed backscattering is significantly reduced. The differential cross sections at these resonances look similar to those at the shape resonances for the $j = 3/2, F_1, f \rightarrow j = 5/2, F_1, e$ transition of the OH-He system (see Fig. 2.7), where

also an increase in backscattering was found. With a measurement of the differential cross sections, the strong increase and decrease in the backscattering might help in experimentally identifying the shape resonances at 94.90 and 99.23 cm^{-1} . However, we note that one must be careful with identifying the backscattering signal with resonances in the cross section. Namely, in Fig. 2.14(a) also less pronounced resonances are seen, and not all of them have such a strong backscattering signal as the strongest resonances I, III and V. Moreover, closer to the threshold of the $j = 3/2, F_1, f \rightarrow j = 5/2, F_1, e$ transition significant backscattering is observed away from the resonances.

2.6 Discussion

The experimental observation of resonance structures as discussed in this paper would comprise a very detailed test for the calculated PESs and scattering calculations on these PESs. The Stark deceleration technique provides a source of state-selected molecules with a tunable velocity and narrow velocity distribution. This technique enables state-to-state scattering experiments in which the collision energy can be precisely tuned over a wide range with a high collision energy resolution. Yet, the observation of scattering resonances requires an energy resolution that has not yet been achieved in this type of experiments. In this section, we analyze the collision energy resolution required to observe resonance features in either the state-to-state integral or the differential cross sections for OH-He and OH-Ne collisions. We discuss the requirements on the beam velocity and angular distributions, and discuss the feasibility of obtaining these distributions.

Referring back to Figs. 2.7, 2.10, and 2.14, the most prominent resonance structures are found for OH-He in the $j = 3/2, F_1, f \rightarrow j = 3/2, F_1, e$, $j = 3/2, F_1, f \rightarrow j = 5/2, F_1, e$ and the $j = 3/2, F_1, f \rightarrow j = 5/2, F_2, f$ transitions. For OH-Ne collisions the $j = 3/2, F_1, f \rightarrow j = 5/2, F_1, f$ channel is of most relevance. To simulate what would be observed in a molecular beam scattering experiment, the integral cross sections in Figs. 2.7, 2.10, and 2.14 are convoluted with Gaussian collision energy distributions of

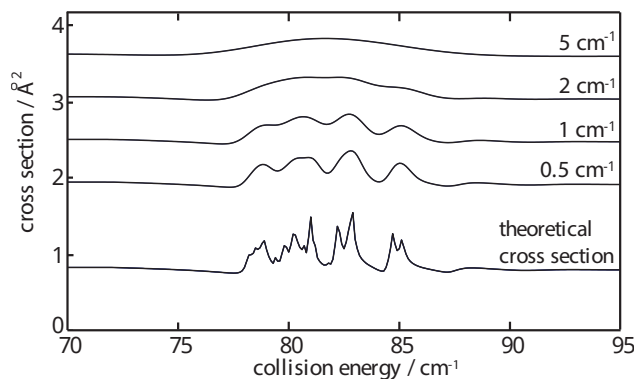


Figure 2.15: Inelastic scattering cross section for the $j = 3/2, F_1, f \rightarrow j = 3/2, F_1, e$ channel in collisions of OH radicals with He atoms, showing Feshbach resonances that correspond to the opening of the $j = 5/2, F_1$ rotational levels of OH. The theoretical curve is convoluted with Gaussian energy distributions with FWHM of 0.5 cm^{-1} , 1 cm^{-1} , 2 cm^{-1} , and 5 cm^{-1} . The upper four curves have been given a vertical offset for reasons of clarity.

1 and 5 cm^{-1} full width at half maximum (FWHM). In Fig. 2.15, the resonance structure at collision energies around 85 cm^{-1} for the $j = 3/2, F_1, f \rightarrow j = 3/2, F_1, e$ channel in OH–He collisions is shown. This scattering channel displays a number of Feshbach resonances, corresponding to the opening of the $j = 5/2, F_1$ channels, that are grouped within a relatively narrow range of collision energies. The theoretical curve is convoluted using 0.5 , 1 , 2 , and 5 cm^{-1} (FWHM) energy distributions. We will use this scattering channel as a benchmark to establish the energy resolution required in the experiments to observe signatures of scattering resonances. Scattering resonances are partially resolved for energy resolutions of $\leq 1 \text{ cm}^{-1}$. When a resolution between 1 and 2 cm^{-1} is achieved, some of the resonance structure is resolved, while for resolutions of 5 cm^{-1} , most of the resonance structure has disappeared. In these cases, at best only a broad peak is observed in the integral cross section.

For given beam velocity and angular spread, the collision energy distribution is a function of the collision energy; the highest resolutions are obtained for the lowest collision energies. We can estimate the beam parameters required to reach collision energy distributions of $\leq 2 \text{ cm}^{-1}$ at a collision energy of 85 cm^{-1} for collisions of Stark-decelerated OH radicals with He atoms, i.e., to (partially) resolve the scattering resonances shown

in Fig. 2.15. We assume a beam intersection angle of 45° and choose the velocities of the He and OH beams such that the relative velocity vector is perpendicular to the He atom velocity vector. In this geometry, the collision energy distribution is almost independent of the He atom beam velocity spread [97]. A collision energy of 85 cm^{-1} is reached for He and OH velocities of 790 m/s and 1120 m/s , respectively. In the chosen geometry, the most critical parameter that determines the collision energy resolution is the distribution in beam intersection angles $\Delta\phi$. If we assume extremely well collimated beams such that $\Delta\phi = 10 \text{ mrad}$ (corresponding to 0.6°), a velocity spread of the OH radicals of 5 m/s results in a collision energy resolution of 1.9 cm^{-1} .

Experimentally, the most challenging requirement is the angular spread of both beams. Multiple collimation slits for both the OH and He beams are required to reach the required angular spreads. The required He atom velocity can be obtained using a cryogenic source that is maintained at a temperature of 60 K , and the required OH velocity can be produced using the Stark decelerator. The required velocity spread for the OH radicals can be obtained using the Stark decelerator, either by choosing the appropriate phase angle in the decelerator [11], or by additional phase-space manipulation techniques [125]. For the OH-Ne system, even more stringent requirements apply to the beam distributions due to the higher reduced mass for this system. Beam speeds of 664 m/s and 470 m/s for the OH radical beam and Ne atom, respectively, will result in a collision energy of 85 cm^{-1} using a beam crossing angle of 45° . For the velocity and angular distributions used above for OH-He, a collision energy distribution of 2.1 cm^{-1} is obtained.

The signatures of scattering resonances can also be inferred from differential cross sections. State-to-state differential cross sections can be measured using the velocity map imaging technique, that provides the full angular and velocity distribution of the scattered molecules. Alternatively, information on the differential cross section may be obtained via Doppler profile measurements of the scattered molecules. The backward scattered components that appear in the differential cross sections when a resonance is accessed

offers interesting prospects to reveal the existence of resonances. As the collision energy is tuned over a group of scattering resonances, the presence of these resonances can in principle be inferred from the measured product flux at backward scattering angles. In Figs. 2.7, 2.10, and 2.14, the differential cross sections are shown at collision energies near and at the resonances, convoluted with Gaussian collision energy distributions of 1 and 5 cm^{-1} full width at half maximum (FWHM). In particular for the $j = 3/2, F_1, f \rightarrow j = 5/2, F_1, f$ channel in OH-Ne, a significant scattering intensity at backward scattering angles remains, even for a collision energy resolution as high as 5 cm^{-1} . In the integral cross section, no signature of the scattering resonances is observable at these energy resolutions. In these cases, it may be favorable to experimentally explore the existence of resonances via measurements of differential cross sections instead of integral cross sections.

The examples treated above show that collision energy resolutions in the 1–2 cm^{-1} range, although very challenging experimentally, should allow for the observation of both shape and Feshbach resonances in the integral cross sections for inelastic collisions between OH radicals and He or Ne atoms. The OH radical is an excellent candidate in these experiments, as a sensitive detection scheme, appropriate for ion imaging, has recently been developed for this species [126]. In addition, the relatively large rotational spacing of the molecular levels results in a molecular beam pulse with less initial population in excited rotational states, and therefore a packet of Stark-decelerated OH radicals with a high state purity. This facilitates the sensitive and background free detection of scattering products and enables the implementation of beam collimators that improve the angular and velocity spreads of the beams at the cost of particle densities. The disadvantage of the large rotational spacing, however, is the relatively high energies of the energetic thresholds for inelastic scattering, and corresponding relatively high collision energies at which scattering resonances appear. In this respect, the inelastic scattering of OD radicals or ND_3 molecules with He and Ne atoms will be interesting candidates for studying scattering resonances as well, reducing the energy for the lowest lying threshold to 42 cm^{-1} and 14

cm^{-1} , respectively. To reach a collision energy resolution $\leq 2 \text{ cm}^{-1}$ at these energies will relax the requirements on the velocity and angular spreads of both beams.

2.7 Conclusions

We have presented detailed calculations on scattering resonances in the rotationally inelastic scattering of OH radicals with He and Ne atoms. For OH-He, we have developed new 3D *ab initio* potential energy surfaces, and the inelastic scattering cross sections that are derived from these surfaces compare favorably with recent experiments. We have identified numerous scattering resonances, of both the shape and Feshbach types, in the integral cross sections. We have analyzed these resonances using the adiabatic bender model and computed collision lifetimes. We observe dramatic changes in the differential cross sections at the resonances, showing in selected cases a forward-backward peaking of the scattered flux. The analysis of scattering resonances presented here will be indispensable in the experimental search for such resonances in, for instance, crossed beam scattering experiments using Stark-decelerated molecular beams. To experimentally observe signatures of resonances in the integral cross sections and to partially resolve individual resonances, a collision energy resolution of $\leq 2 \text{ cm}^{-1}$ is required. Obtaining energy resolutions $\leq 2 \text{ cm}^{-1}$ mainly requires highly collimated molecular beams, which appears challenging. Alternatively, signatures of scattering resonances may be found in the differential cross sections. The selective detection of scattered molecules at backward scattering angles may facilitate the identification of resonances if the collision energy resolution is not sufficient to resolve them in the integral cross sections.

Chapter 3

Scattering Resonances of NH₃ in Collisions with H₂ and D₂

This chapter contains long excerpts of an unpublished manuscript titled “Resonances in rotationally inelastic scattering of NH₃ and ND₃ with H₂” by Qianli Ma, Ad van der Avoird, Paul J. Dagdigian, Millard H. Alexander, and Sebastiaan Y. T. van de Meerakker.

3.1 Introduction

The resonance is one of the most interesting phenomena in molecular scattering and has been of great interest to both experimentalists and theoreticians [2, 84, 127, 128]. In inelastic scattering, a resonance originates from a quasibound level produced during the course of a collision [80, 129], and usually appears as a distortion of the continuum in the collision energy dependence of cross sections [2]. The resonances are called shape or Feshbach resonances, depending on whether the quasibound level is associated with the same monomer levels as the initial or final levels of the collision-induced transition [84].

An accurate potential energy surface (PES) is the foundation for the theoretical study of the dynamics in a collision system. Unlike the bound state of the van der Waals complex of the collision partners that depends mostly upon the attractive part of the PES, the quasibound levels are sensitive to both the repulsive and the attractive part of the PES. Due to this sensitivity, the measurement of scattering resonances can provide a strong validation

of the PES [87, 88]. The PES can then be reliably used in further theoretical investigations of the system and in calculating the rate coefficients and other useful quantities difficult or impossible to measure.

The observation of scattering resonances requires low collision energies with high energy resolution in crossed molecular beam experiments, as well as a high state purity of the collision partners [55, 83, 130]. In a few studies, scattering resonances have been observed in collisions between atoms [89–91], and in the reactive $F + HD \rightarrow HF + D$ system [92]. Recently, Chefdeville *et al.* observed both shape and Feshbach resonances in the inelastic scattering of O_2 by H_2 [13]. In that experiment, the authors used Even-Lavie pulsed valves [131] to cool the molecular beams and were able to measure the cross sections of the $n = 1, j = 0 \rightarrow n = 1, j = 1$ transition of O_2 in collision with *para*- H_2 at collision energies between 3.7 and 20 cm^{-1} . To our best knowledge, this work is the only unambiguous observation of resonances in inelastic scattering of molecules to date.

For molecules having dense rotational level structure (such as the Λ -doublets of OH and the inversion doublets of NH_3), and/or multiple nuclear spin symmetry, cooling down the molecular beam alone cannot produce a beam with a dominant population in the lowest level. For these molecules, the Stark deceleration technique [11, 94] can be a promising tool in producing cold molecular beams for the measurement of scattering resonance since it can also act as a state selector. Inspired by this technique, our groups have investigated theoretically the resonances in the OH-He/Ne and the NH_3 -He systems using state-of-the-art PESs [55, 83]. We have illustrated that both these systems show significant shape and Feshbach resonances. The observation of the resonances in these systems would require a $\sim 1 \text{ cm}^{-1}$ resolution in the collision energy, which is very challenging at present.

Rotationally inelastic scattering of NH_3/ND_3 with H_2 has received considerable interest in the past [72, 132–136], primarily because of its astrophysical importance [76–79]. These studies mostly focused on collisions out of the ground rotational level of *para*- NH_3 , which is not suitable for Stark deceleration. Strong resonance peaks do appear

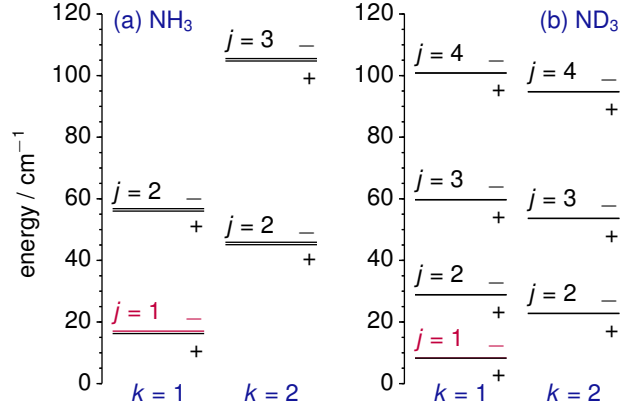


Figure 3.1: Rotational level diagrams of (a) *para*-NH₃ and (b) ND₃ (*E* nuclear spin modification). The level 11— can be selected with a Stark decelerator and is labeled in red. The inversion doublets of ND₃ cannot be distinguished in the diagram due to the small inversion splitting.

in the computed energy dependence of state-to-state cross sections (Fig. 2 for Ref. [72]).

In the present work, we study in detail the resonances in the state-to-state cross sections of NH₃ and ND₃ out of the rotational state suitable for Stark deceleration (11—, see Sec. 3.2 for the notation of the rotational levels) in collisions with H₂, using the PES computed by Maret *et al.* [72]. We will show that this system has strong and broad resonance peaks along with relative large state-to-state cross sections, and these resonances are particularly suitable for crossed molecular beam studies.

This chapter is organized as follows: In Sec. 3.2 we briefly present the theory for rotationally inelastic scattering between a symmetric top and a ¹Σ molecule, and describe our scattering calculations. In Sec. 3.3 we introduce the PESs we used in our calculations. We present in Sec. 3.4 our results on the scattering resonances and show that they are shape or Feshbach resonances. We also analyze the resonances using various techniques, including the adiabatic bender model [40, 109] and the scattering wave function analysis [55]. A discussion in Sec. 3.5 concludes the chapter.

3.2 Scattering Calculations

We label the rotational levels of the NH_3 and ND_3 symmetric top molecules with the notation $j k \pm$, where j is the total angular momentum of the molecule, k is the projection of j on the C_3 axis, and \pm is the umbrella inversion symmetry. Similar to the methyl radicals discussed in detail in Chapter 5, the NH_3 and ND_3 molecules have respectively two (*para* and *ortho*) and three (E , A_1 , and A_2) nuclear spin modifications that do not interconvert during inelastic scattering. The initial level suitable for Stark deceleration (11 --) belongs to the *para* or E nuclear spin symmetry, which includes all rotation levels with k not a multiple of 3. For reference, we show in Fig. 3.1 the lower rotational levels of *para*- NH_3 and ND_3 (E nuclear spin symmetry).

The quantum theory of inelastic collisions between a symmetric top molecule and a molecule in a $^1\Sigma$ electronic state can be found in Chapter 6 and several previous papers [133–135, 137]. As in these studies, we approximate the inversion doublets wave functions of NH_3/ND_3 as a combination of rigid rotor wave functions with $|j k m \varepsilon\rangle = 2^{-1/2}[|j k m\rangle + \varepsilon |j k, -m\rangle]$. The umbrella inversion symmetry equals to $-\varepsilon(-1)^j$. Previous investigations of the inelastic scattering in the NH_3/ND_3 -He systems [55, 138] showed that this approximation gives excellent relative cross sections by comparison with a more elaborate model including the umbrella vibration–inversion coordinate.

Close-coupling calculations were performed both with the HIBRIDON suite of programs [31] and with a second independent scattering program described in Ref. [112]. Care was taken to independently check the results with the two scattering programs and to converge the cross sections. We include in the close-coupling channel basis all *para* rotational levels of NH_3 with $j \leq 6$, or E rotational levels of ND_3 with $j \leq 7$. For the collision with *para*- H_2 , the $j = 0$ and $j = 2$ levels of H_2 are included; for *ortho*- H_2 , only the $j = 1$ level is included. The maximum total angular momentum in the calculations was $J = 20$, which gives inelastic cross sections converged to at least 0.1 \AA^2 for total energies $<$

70 cm⁻¹. For NH₃, we adopted rotational constants $B = 9.9402$ cm⁻¹ and $C = 6.3044$ cm⁻¹. while for ND₃ we used $B = 5.1420$ cm⁻¹ and $C = 3.1170$ cm⁻¹. We assume the inversion splitting is the same for all inversion doublets and equals to 0.7903 and 0.053 cm⁻¹ for NH₃ [139] and ND₃ [140, 141], respectively.

3.3 Potential Energy Surface

In describing the interaction between NH₃ and H₂ we use a coordinate system defined in Ref. [135]. In this system the Jacobian vector \mathbf{R} lies along the space-fixed frame z axis, and the rotations from the molecule frames of NH₃ and H₂ to this space-fixed frame are defined by the Euler angles $(0, -\theta_1, -\phi_1)$ and $(\phi_2, \theta_2, 0)$, respectively. The interaction potential can be expanded either in a “space-frame expansion”

$$V(R, \theta_1, \phi_1, \theta_2, \phi_2) = \sum_{l_1 l_2 l \mu_1} V_{l_1 l_2 l \mu_1}(R) \sum_{m_1} \langle l_1 m_1, l_2, -m_1 | l 0 \rangle \times D_{m_1 \mu_1}^{l_1*}(0, -\theta_1, -\phi_1) D_{-m_1, 0}^{l_2*}(\phi_2, \theta_2, 0), \quad (3.1)$$

or a “body-frame expansion”

$$V(R, \theta_1, \phi_1, \theta_2, \phi_2) = \sum_{l_1 l_2 l \mu_1} V_{l_1 l_2 \mu_1 m_1}(R) \times D_{m_1 \mu_1}^{l_1*}(0, -\theta_1, -\phi_1) D_{-m_1, 0}^{l_2*}(\phi_2, \theta_2, 0). \quad (3.2)$$

In the above equations, $V_{l_1 l_2 l \mu_1}$ and $V_{l_1 l_2 \mu_1 m_1}$ are expansion coefficients, $\langle l_1 m_1, l_2, -m_1 | l 0 \rangle$ is a Clebsch-Gordan coefficient, and $D_{m \mu}^l$ are rotation matrices [28]. Another frequently adopted angular expansion of the PES [142] uses a different set of angles to define the orientation of the molecules, but is practically equivalent to the space-frame expansion above.

For the collision between NH₃ with H₂, we used a CCSD(T)/aug-cc-pVDZ PES with

corrections from CCSD(T)/CBS calculations created by Maret *et al.* [72]. We obtained from the authors the potential fitted both in Eq. (3.1) and Eq. (3.2), and used both in our scattering calculations. Because the sensitivity of resonances to the PES, the two expansions give slightly different resonance structures. Given that the fitted potential using Eq. (3.1) has smaller root mean squares (RMS) compared with the *ab initio* potential when similar numbers of terms in the two angular expansions are used and the evaluation of coupling matrix elements is easier with Eq. (3.1), we recommend using the space-frame expansion of the PES in scattering calculations.

To describe ND₃-H₂ collisions, the NH₃-H₂ PES needs to be modified because the center of mass is at a different location in NH₃ and ND₃. We define the shift of the center of mass as δ_{COM} . From the NH₃ geometry used in computing interaction energies in Ref. [72] ($r_{\text{NH}} = 1.9512 a_0$, $\angle_{\text{HNN}} = 107.38^\circ$), we calculate that $\delta_{\text{COM}} = 0.088530 a_0$.

The *ab initio* calculation for the NH₃-H₂ potential was performed on a grid of 29 R 's, and the same set of 3000 and 1000 orientations for each R were used for the CCSD(T)/aug-cc-pVDZ and CCSD(T)/CBS calculations, respectively. To obtain a set of ND₃-H₂ interaction energies suitable for developing a PES, we compute for each of the θ_1 used in the NH₃-H₂ calculation a corresponding θ'_1 for ND₃-H₂ by

$$\theta'_1 = \arccos \frac{R'^2 + \delta_{\text{COM}}^2 - R^2}{2\delta_{\text{COM}}R'}, \quad (3.3)$$

where R' are the intermolecular distance chosen to fit the ND₃-H₂ PES, and R is the corresponding intermolecular distance for NH₃-H₂ calculated from

$$R = -\delta_{\text{COM}} \cos \theta_1 + \sqrt{R'^2 - \delta_{\text{COM}}^2 \sin^2 \theta_1}. \quad (3.4)$$

These equations were obtained from trigonometric considerations.

We used these relations to transform the orientations $(\theta_1, \phi_1, \theta_2, \phi_2)$ for NH₃-H₂ to $(\theta'_1, \phi_1, \theta_2, \phi_2)$ for ND₃-H₂ for each R' (from the same R grid used in the NH₃-H₂

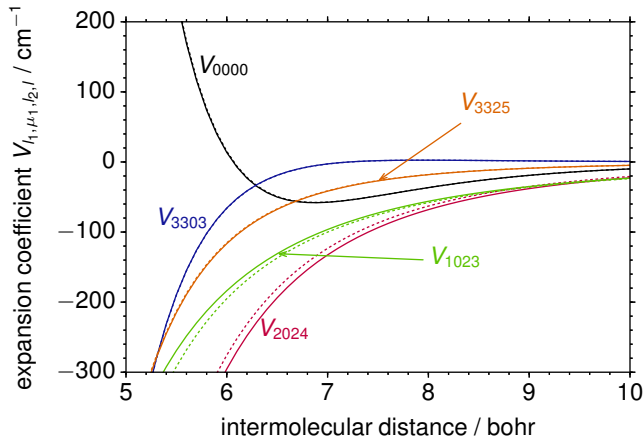


Figure 3.2: Comparison between the larger expansion coefficients $V_{l_1, \mu_1, l_2, l}$ (as defined in Eq. (8) of Ref. [137]) as a function of intermolecular distance R , of the $\text{NH}_3\text{-H}_2$ PES described in Ref. [135] (dashed lines) and the $\text{ND}_3\text{-H}_2$ PES described in the present work (solid lines).

calculations), and estimated the interaction energy for that geometry by splining the R dependence of $\text{NH}_3\text{-H}_2$ interaction energies at this orientation. We then fit the $\text{ND}_3\text{-H}_2$ interaction energies using the same technique as in described in Ref. [72] to obtain a PES.

Figure 3.2 shows the comparison of the larger angular expansion coefficients as a function of R between the original $\text{NH}_3\text{-H}_2$ PES and the fitted $\text{ND}_3\text{-H}_2$ PES. We see that the two PESs are quite similar, with three of the five larger expansion coefficients virtually identical and the other two showing slight differences. This is not unreasonable given the small shift in the COM. The two expansion coefficients showing differences have significant contributions from multipole-multipole electrostatic interactions, with V_{1023} associated with the NH_3/ND_3 -dipole- H_2 -quadrupole interaction, and V_{2024} the quadrupole-quadrupole interaction [66].

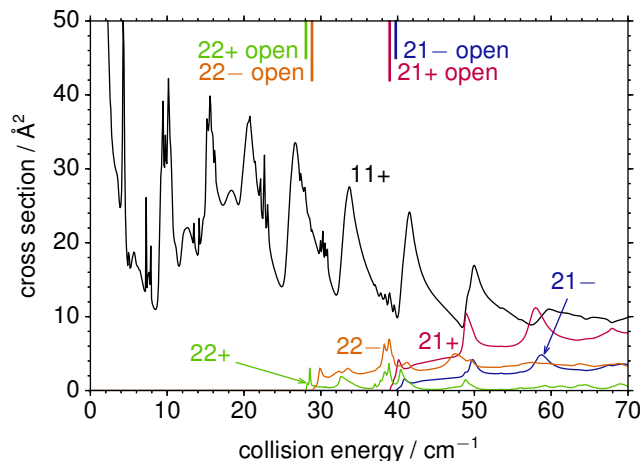


Figure 3.3: State-to-state integral cross section as a function of collision energy for transition from the 11– level of *para*-NH₃ in collision with *para*-H₂ in the $j = 0$ level. The final levels are indicated for each transition for which the cross section is plotted.

3.4 Results

3.4.1 Collisions between NH₃ and *para*-H₂

Overview of the Resonances

We first show in Fig. 3.3 the energy dependence of the state-to-state integral cross sections for transitions from the 11– initial level at collision energies below 70 cm⁻¹. At these energies, H₂ cannot be collisionally excited. In this energy range, the transition between the inversion doublets (11– → 11+) dominates and shows rich resonance structure, with both broad and sharp peaks. Because of the deep well of the NH₃–H₂ PES ($D_e = 267$ cm⁻¹ [72]), we do not observe clearly groups of resonances associated with the opening of a particular channel, as appears in molecule–rare gas systems [55, 83]. We will show in Sec. 3.4.1 that the resonances seen in Fig. 3.3 are indeed Feshbach resonances. The broad peaks of a few wavenumbers in width and intensity more than 3 times the background inelastic cross sections are particularly promising for observation in a crossed beam experiment.

The 11– → 21+ transition also shows several resonances with magnitudes double the background cross section. As will be analyzed in Sec. 3.4.1, these are shape resonances

originating from the quasibound states associated with the final level $21+$. Similar to the $11- \rightarrow 21+$ transition, the $11- \rightarrow 21-$ transition also has a few shape resonances at similar collision energies, though smaller in magnitude. The resonances in the $11- \rightarrow 22\pm$ transitions have contributions from both shape and Feshbach resonances caused by the quasibound states associated with the $21\pm$ levels.

The relative magnitudes of the state-to-state cross sections are significantly different for the $\text{NH}_3\text{-H}_2$ and $\text{NH}_3\text{-He}$ systems. In particular, the transition to the $21+$ level is much stronger when the collision partner is H_2 . This can partly be explained with the differing anisotropies of the PESs. In collisions of NH_3 with $\text{H}_2(j=0)$, the V_{1001} and V_{3003} terms directly couple the $11-$ and $21+$ levels, while V_{2002} term directly couples the $11-$ and $21-$ levels. These three coefficients in the $\text{NH}_3\text{-H}_2$ PES are comparable in magnitude at moderate to large intermolecular distances. For the $\text{NH}_3\text{-He}$ PES, the V_{10} and V_{30} terms have significantly smaller magnitudes than the V_{20} term (see Fig. 3 of Ref. [55]), giving rise to smaller $11- \rightarrow 21+$ cross sections. Further, with $\text{H}_2(j=2)$ in the close-coupling channel basis, expansion terms with $l_2 > 0$ can affect the cross sections. Such anisotropies are absent from the $\text{NH}_3\text{-He}$ system.

Feshbach Resonances in the $11- \rightarrow 11+$ Transition

To understand the resonances in the $11- \rightarrow 11+$ transition, we plot in Fig. 3.4 the contributions to the integral cross section (partial cross sections) from each partial wave, distinguished by the total angular momentum J and the parity. We can observe several series of resonance structures consisting peaks of similar shape and shifting to higher collision energies as J increases. We expect that peaks within a given series are resonances arising from quasibound states associated with a same rotational level of NH_3 . As J increases, the corresponding orbital angular momentum L increases, which leads to a higher centrifugal barrier and a higher quasibound state energy.

To investigate the origin of the resonances, we performed an adiabatic bender analysis

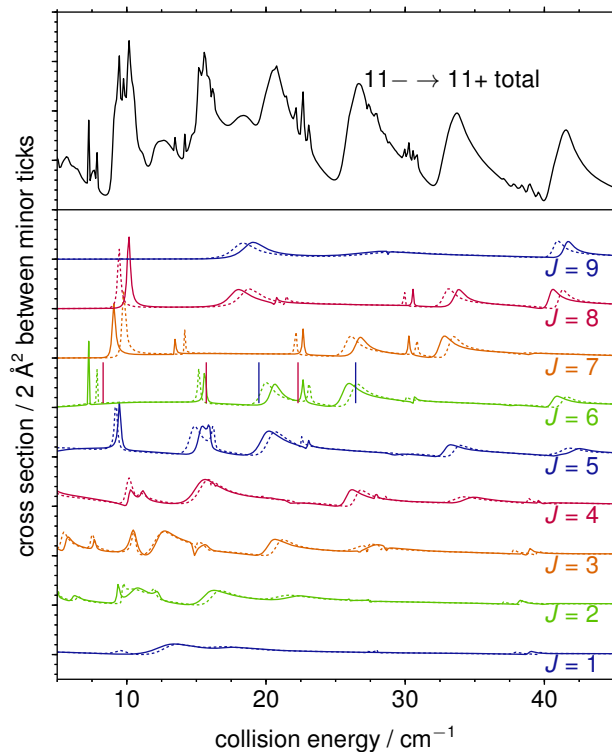


Figure 3.4: Partial cross sections as a function of collision energy for the $11- \rightarrow 11+$ transition of *para*-NH₃ in collisions with *para*-H₂ in the $j = 0$ level. Solid lines represent the cross sections for + parity, and dotted lines - parity for the given total angular momentum J . The red and blue vertical lines on the $J = 6$, + parity partial cross sections show the stretch level energies of the adiabatic bender curves (shown in Fig. 3.5) associated to the $22\pm$ and $11\pm$ levels of NH₃, respectively.

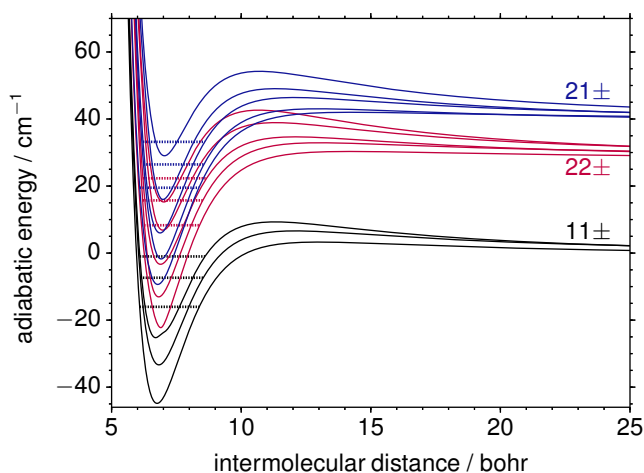


Figure 3.5: Adiabatic bender curves for the interaction between *para*-NH₃ and *para*-H₂ for the $J = 6$, + parity partial wave. The line colors indicate the asymptotic inversion doublet associated with the curves (the assignment is only approximate due to avoided crossings between curves). Quasibound states are shown as dotted horizontal lines. The zero of energy is the asymptotic energy of the $11-$ level of NH₃ and the $j = 0$ level of H₂.

similar to that described in Sec. 2.4.3. Here, we diagonalize the Hamiltonian exclusive of the nuclear kinetic energy for a given partial wave to obtain adiabatic bender curves. The energies of the van der Waals stretch levels supported by those curves are computed using a discrete variable representation (DVR) method [121, 122].

We display the derived adiabatic bender curves and quasibound level energies for the $J = 6, +$ parity partial wave in Fig. 3.5 as an example. We see that the stretch levels supported by the adiabatic bender curves associated with the NH_3 $22\pm$ levels, at 8.30, 15.71, and 22.30 cm^{-1} (red vertical lines in Fig. 3.4), are in reasonable agreement with the positions of the sharp resonance peaks that appear on the energy dependence of partial cross sections for this partial wave (the upper solid green curve in Fig. 3.4). The two lower stretch levels associated with the NH_3 $21\pm$ levels, 19.49 and 26.44 cm^{-1} (blue vertical lines in Fig. 3.4), agree with the positions of the broad resonance peaks. These results suggest that both the sharp and broad resonance peaks shown in Fig. 3.4 are Feshbach resonances, with the sharp peaks originating from quasibound states associated with the NH_3 $22\pm$ level and the broad peaks from the $21\pm$ level.

One of the adiabatic bender curves in Fig. 3.5 has a bound stretch level at 33.18 cm^{-1} , at which no resonance appears in Fig. 3.4. A close look reveals that this adiabatic bender curve has avoided crossings with other curves, including those associated with a different NH_3 level. This is an example of the limitations of the adiabatic bender model. Near an avoided crossing, the scattering wave function would change dramatically, and the separation of radial and angular functions, as assumed in the adiabatic bender model, would no longer be a good approximation. Such a phenomenon is analogous to nonadiabatic effects [143] in electronic structure theory. As shown in Fig. 3.5, the $\text{NH}_3\text{-H}_2$ adiabatic bender curves have well depths comparable or greater than the rotational level separation, and the adiabatic bender analysis is particularly vulnerable to these avoided crossings.

An alternative method of studying the Feshbach resonances is to examine the contributions to the radial scattering wave functions by the close-coupling channels originating

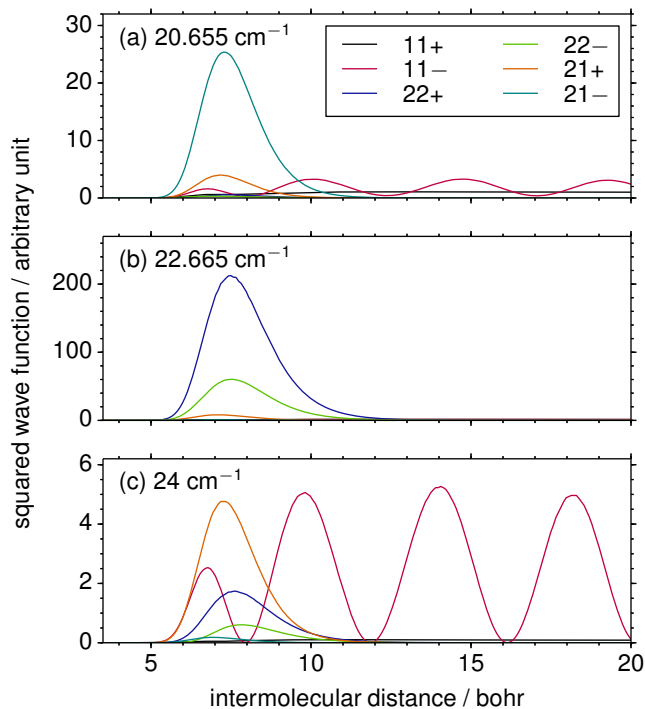


Figure 3.6: (a)–(c) Contributions of various levels to the square of the scattering wave function of the $J = 6$, + parity partial wave for the scattering of NH_3 in the $11-$ initial state and *para*- H_2 ($j = 0$). The initial state corresponds to $L = 6$ asymptotically. Collision energies are labeled on each panel.

from various monomer rotational levels [55]. We plot in Fig. 3.6 such contributions to the squared scattering wave function of the $j = 6$, + parity partial wave at three collision energies. We note that each NH_3 rotational level may give rise to several channels with different orbital angular momentum L , and we have summed up their contributions.

The three energies considered in Fig. 3.6 are close to each other, but the scattering wave functions are quite different. Fig. 3.6(a) corresponds to a collision energy where a broad resonance peak occurs. We see clearly the $21-$ channels has a dominating amplitude in the region of the van der Waals well, showing that the broad resonance peak is a Feshbach resonance associated with the $21-$ level of NH_3 . Fig. 3.6(b) represents a collision energy at which there is a sharp resonance peak. The major contributors to the scattering wave functions here are the $22+$ and $22-$ channels, and those channels are responsible for this Feshbach resonance. Fig. 3.6(c) shows the scattering wave functions at an off-

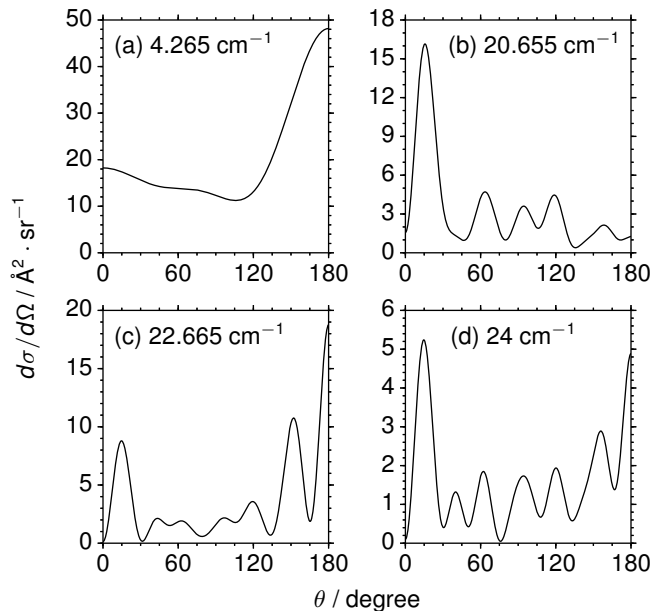


Figure 3.7: Differential cross sections for the $11- \rightarrow 11+$ transition in NH_3 in collisions with *para*- H_2 $j = 0$ at several collision energies, labeled on each panel.

resonance energy, and we see the magnitudes of the wave functions are small and there is no dominating channel.

We see that the two techniques for analyzing the resonances agree on the origin of the resonances. The scattering wave function analysis, while slightly more computationally demanding, does not suffer from avoided crossings in the adiabatic bender analysis. We performed the wave function analysis on other major resonance peaks and found that these are primarily Feshbach resonances. We conclude that the broad resonance peaks arise from the $21\pm$ levels of NH_3 , and the sharp peaks from the $22\pm$ levels. How these two levels lead to different widths and magnitudes of the Feshbach resonances remains unclear. We do note that the $11- \rightarrow 21\pm$ transitions have larger cross sections than the $11- \rightarrow 22\pm$ transitions, despite a larger energy gap. This indicates a stronger coupling between $11-$ and $21\pm$ levels.

We also computed the differential cross sections (DCSs) at several resonance and off-resonance energies; these are shown in Fig. 3.7. The pattern of increased backward scattering at energies close to a resonance, as we found for the OH/NH_3 -rare gas systems

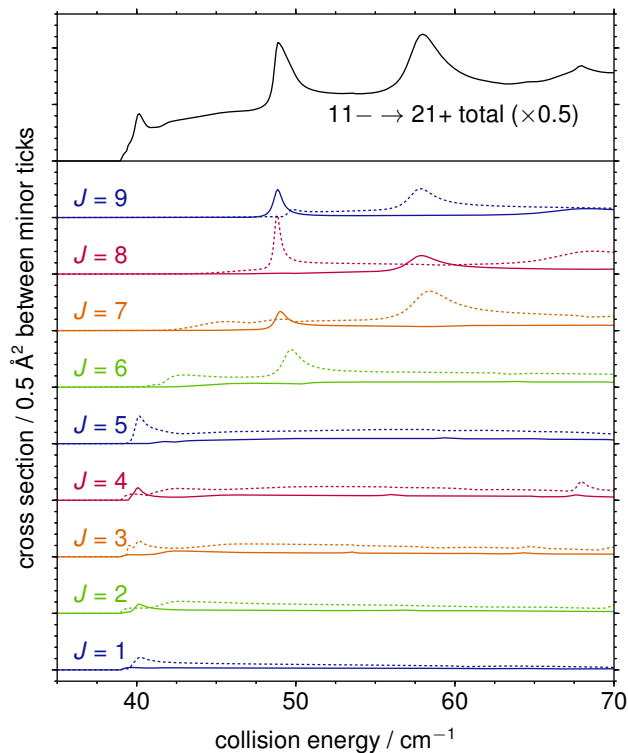


Figure 3.8: Partial cross sections as a function of collision energy for the $11- \rightarrow 21+$ transition of *para*- NH_3 in collisions with *para*- H_2 in the $j = 0$ level. Solid lines represent the cross sections for + parity, and dotted lines — parity for the given total angular momentum J .

[55, 83], is less clear for $\text{NH}_3\text{-H}_2$ collisions. Figures 3.7(a) and (c) show DCSs at energies close to sharp resonance peaks, and we see significant backward scattering as expected. Backward scattering is even dominating at a collision energy of 4.265 cm^{-1} , corresponding to the first sharp resonance peak shown in Fig. 3.3. Figures 3.7(b) and (d) correspond to energies at which there is a broad peak, and an off-resonance energy, respectively. Surprisingly, we see strong backward scattering at the off-resonance energy but not the near-resonance energy. We do note that the differential cross sections are not from the $J = 6$, + parity partial wave alone and there are significant contributions and interferences involving other partial waves.

Shape Resonances in the $11^- \rightarrow 21^+$ Transition

In this section we analyze the resonance structure shown in the energy dependent $11^- \rightarrow 21^+$ cross section. Although not as dramatic as the resonances in the $11^- \rightarrow 11^+$ transition, the resonances in this transition have a relatively simple structure, and these moderately broad resonance peaks at slightly higher collision energies may facilitate the observation of resonances in molecular beam experiments.

We first show the partial cross sections for this transition in Fig. 3.8. We see the contribution to the resonance peaks is quite different from those shown in Fig. 3.4. Namely, each of the three peaks at collision energies of $\sim 40, 50,$ and 60 cm^{-1} has contributions from several partial waves. The three peaks have increasing width as the energy increases. These are typical characteristics of a shape resonance [83, 104, 120]. This resonance structure, however, is distinguished from that observed in the $\text{NH}_3\text{-He}$ and OH-He systems by the rapid increasing background cross section and the large spacing between resonance peaks. The large spacing is a direct consequence of the small reduced mass of the system and large centrifugal barriers.

To confirm the origin of these resonances, we again applied the adiabatic bender model used in Sec. 3.4.1. The adiabatic bender curves look similar to those shown in Fig. 3.5 and are not shown here. After computing the adiabatic bender curves, we treat them as in a conventional one-dimensional scattering problem and compute the phase shift as a function of collision energy. A rapid increase of the energy dependent phase shift by π indicates a scattering resonance [2]. We plot in Fig. 3.9 the phase shifts for all adiabatic bender curves associated with the 21^+ level with $6 \leq J \leq 9$ that give rise to such changes in phase shift. We see clearly for each of the curve shown in Fig. 3.9 that the energy dependent partial cross section for the corresponding partial wave (Fig. 3.8) shows a resonance peak at a similar collision energy. Further, the widths of the resonances match those for the change of phase shift by π . This confirms that the resonances in the $11^- \rightarrow 21^+$ transition are shape resonances caused by quasibound states associated with

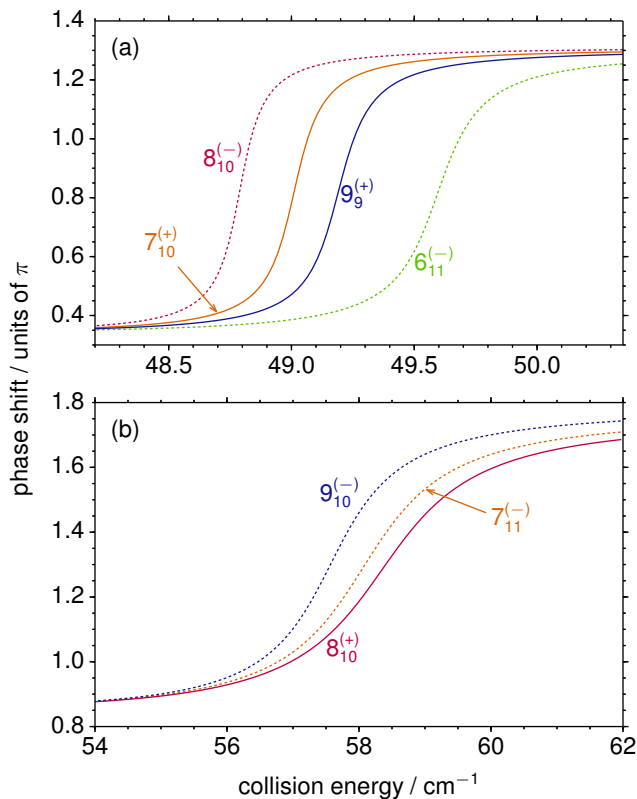


Figure 3.9: Phase shifts as a function of collision energy for the collision between *para*-NH₃ and *para*-H₂, obtained from close coupling adiabatic bender curves that correlate asymptotically with NH₃ 21+ - H₂ $j = 0$. The curves are labeled with $J_n^{(\pm)}$, where J , (\pm) , and n are the total angular momentum, the total parity of the scattering wave function, and the cardinal index, respectively. Only curves with $6 \leq J \leq 9$ that show a rapid increase of phase shift by π are plotted. The colors and line shapes of the curves match those for the corresponding partial waves in Fig. 3.8.

the final level of the transition.

We note that there are four rotational levels below the 21+ level and the adiabatic bender curves related to that level have large cardinal indices. There are many avoided crossings between the adiabatic bender curves that makes such phase shift analysis difficult and inaccurate. For this particular case, we found such analysis satisfactory.

3.4.2 Collisions between NH₃ and *ortho*- and Normal H₂

We show in Fig. 3.10 the collision energy dependence of the state-to-state cross sections out of the 11- level of NH₃ in collisions with *ortho*-H₂ in the $j = 1$ rotational level. We see the 11- \rightarrow 11+ transition dominates at the collision energies considered, and

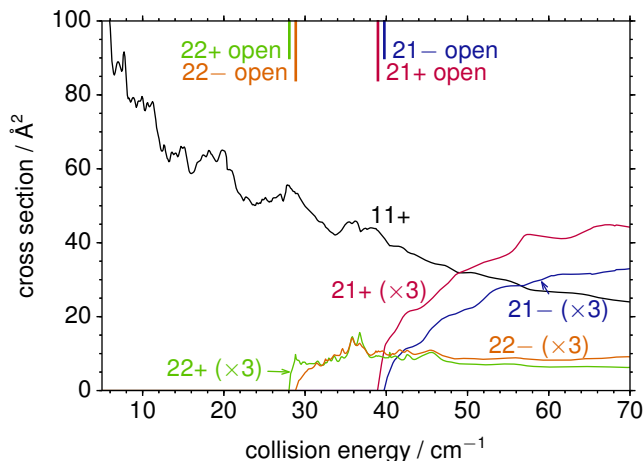


Figure 3.10: State-to-state integral cross sections as a function of collision energy for transitions from the 11– level of *para*-NH₃ in collisions with *ortho*-H₂ in the $j = 1$ level. The final levels are indicated for each transition for which the cross section is plotted. The cross sections to the 21± and 22± levels are multiplied by 3 for clarity.

the cross section for this transition is considerably larger than the corresponding transition for collision with H₂ $j = 0$, displayed in Fig. 3.3. Unlike H₂ $j = 0$, the $j = 1$ level can polarize as it approaches the collision partner; the form of the $j = 1$ rotational wave function allows access to regions of the PES that are anisotropic in θ_2 and ϕ_2 (or $l_2 > 0$). Only $l_2 = 0$ terms in the angular expansion [see Eq. (3.1)] of the PES directly couple channels in collisions with H₂ $j = 0$, while many of the larger expansion coefficients have $l_2 > 0$. A similar enhancement in cross sections for collisions of *ortho*-H₂, as compared to those for *para*-H₂ has also been found in other molecule–H₂ inelastic collisions [144, 145].

We also see that the energy-dependent 11– → 11+ cross section plotted in Fig. 3.10 displays many, overlapping resonances. This contrasts with the much smaller number of mostly resolved resonances seen for collision of H₂ $j = 0$ (Fig. 3.3). The binding energy for NH₃–H₂($j = 1$) is expected to be much larger than for NH₃–H₂($j = 0$) since the PES for the former includes $l_2 > 0$ terms in the PES. This is similar to other molecule–H₂ systems in which the binding energy of the complex is significantly lower in energy for *ortho*-H₂ than for *para*-H₂ [146–150]. Thus, there are more bound, and quasi-bound, levels associated with NH₃–H₂($j = 1$) than with NH₃–H₂($j = 0$), and the resonance structure

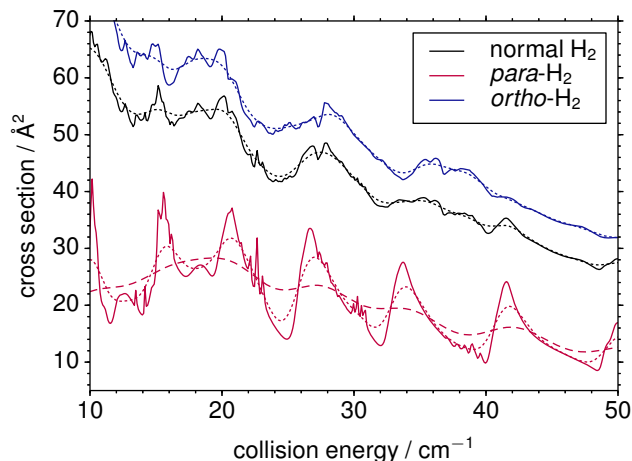


Figure 3.11: Integral cross section as a function of collision energy for the $11- \rightarrow 11+$ transition of NH_3 in collision with *para*-, *ortho*-, and normal (1:3 *para:ortho*) H_2 . Computed cross sections (solid lines), and cross sections convoluted with Gaussian energy spread of FWHM of 2 cm^{-1} (dotted lines) and 5 cm^{-1} (dashed lines, only for NH_3 -*para*- H_2) are plotted.

in the cross section for the $11- \rightarrow 11+$ transition is much more complicated for collision with H_2 $j = 1$ than for $j = 0$. We have not carried out a detailed analysis of the resonances seen in Fig. 3.10.

The shape resonances in the cross sections for the $11- \rightarrow 21\pm$ transitions in collision with H_2 $j = 1$ are small in magnitude relative to the non-resonant background, as compared to those when H_2 $j = 0$ is the collision partner. For the $11- \rightarrow 22\pm$ transitions, the shape and Feshbach resonances associated with the $21\pm$ levels overlap and are small in magnitude (see Fig. 3.10). We expect that the resonances in these transitions would be difficult to observe in crossed beam experiments.

Normal hydrogen has an *ortho* to *para* ratio of 3:1. We plot in Fig. 3.11 the cross section for the NH_3 $11- \rightarrow 11+$ transition in collision with *para*-, *ortho*-, and normal H_2 . Because of the larger nuclear spin statistical weight and the larger cross section, the resonance structures for NH_3 -normal H_2 (black lines in Fig. 3.11) is almost the same as for NH_3 -*ortho*- H_2 (blue lines in Fig. 3.11).

To estimate the feasibility of observing these resonances in molecular beam experiments, we plot also in Fig. 3.11 the cross sections for the $11- \rightarrow 11+$ transition of NH_3 in

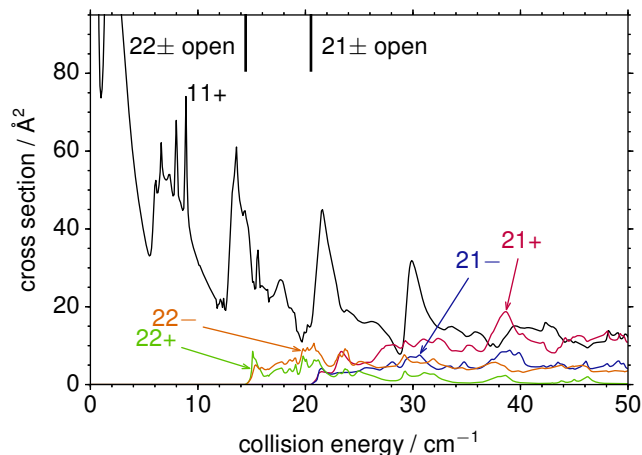


Figure 3.12: State-to-state integral cross sections as a function of collision energy for transitions from the 11⁻ level of ND₃ in collision with *para*-H₂ ($j = 0$). The final levels are indicated for each transition for which the cross section is plotted.

collisions with *para*-, *ortho*-, and normal H₂, convoluted with Gaussian collision energy spreads of two different widths. We see that with a 2 cm⁻¹ energy resolution, the sharp resonance peaks disappear, but the broad resonance peaks are still resolved. However, with an energy spread of 5 cm⁻¹, only relatively weak oscillatory structures corresponding to the broad resonance peaks are left. Such structures would be difficult to observe in experiments.

The best prospect for observing resonances in NH₃-H₂ collisions is with *para*-H₂. When *ortho*-H₂ or normal H₂ is the collision partner, only two broad peaks are prominent, but the magnitudes of these peaks are relatively small compared with the background non-resonance cross sections.

3.4.3 Collisions between ND₃ and H₂

The ND₃ molecule has a smaller inversion splitting, and is easier to manipulate with a Stark decelerator. Accordingly, we investigate resonances in ND₃-H₂ collisions in this subsection. We present in Fig. 3.12 state-to-state integral cross sections as a function of collision energy for transitions from the 11⁻ level of ND₃ in collisions with *para*-H₂ $j = 0$. We notice that there are dramatic resonance structures in the cross section for

the $11- \rightarrow 11+$ transition. Similar to the *para*-NH₃-*para*-H₂ system, the broad peaks are Feshbach resonances associated with the $21\pm$ levels of NH₃, while the sharp peaks are Feshbach resonances associated with the $22\pm$ levels. Although the NH₃-H₂ and ND₃-H₂ PESs are quite similar, the ND₃ rotational levels are more closely spaced. As a result, the ND₃ $22\pm$ and $21\pm$ levels become open at a lower collision energies; this in turn lowers the energies of the quasibound levels associated with these levels relative to the energy of the initial $11-$ level. It is therefore reasonable to see the resonance peaks appear at lower collision energies. Also, two higher inversion doublets, $32\pm$ and $31\pm$, open at ~ 45 and ~ 51 cm⁻¹, respectively. Quasibound states associated with these levels also give rise to weaker resonance peaks in the plotted collision energy range, making the resonance structure more complicated.

The propensities for various transitions are generally the same for NH₃-H₂ and ND₃-H₂, consistent with the similarity of the PESs. However, the resonances in the $11- \rightarrow 21\pm$ and $11- \rightarrow 22\pm$ transitions of ND₃ show significant overlap and would be difficult to observe cleanly in crossed beam experiments. We will not show a detailed analysis of these resonances here.

3.5 Discussion

In this chapter, we have presented calculations and analysis of resonances in rotationally inelastic scattering of NH₃ and ND₃, in the $11-$ initial level, with H₂ $j = 0$ and $j = 1$. The large width of many resonances and relatively large resonance contributions to the cross sections, particularly for the $11- \rightarrow 11+$ transition of NH₃ or ND₃ with *para*-H₂, make the observation of resonances in this system very promising in molecular beam experiments. The observation of multiple resonance peaks in these systems requires a ~ 2 cm⁻¹ collision energy resolution in a crossed beam experiment. While the requirement is comparable with that for the OH-He/Ne and NH₃-He systems [55, 83], the resonances in the present system are more prominent, and the cross sections are larger.

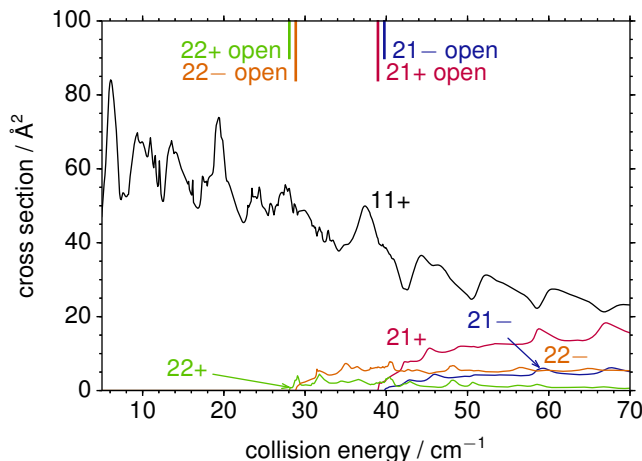


Figure 3.13: State-to-state integral cross section as a function of collision energy out of the 11– level of *para*-NH₃ in collisions with *ortho*-D₂ ($j = 0$). The final levels are indicated for each transition for which the cross section is plotted.

In addition to H₂, we have also considered D₂ as the collision partner. We found in this case that the resonance structures are complicated, with significant overlapping between resonances associated with different asymptotic rotational levels. (The energy dependence of the cross sections are plotted in Fig. 3.13). The reduced mass of NH₃-D₂ is almost twice that of NH₃-H₂. Thus, the zero-point energy of the former complex would be smaller, and the NH₃-D₂ would support more bound and quasi-bound levels, including some levels with stretch quantum number greater than 0. Consequently, Feshbach resonances arising from quasi-bound levels associated with higher NH₃ levels will appear at a lower energy and overlap significantly. In addition, the experimental method for *ortho*→*para* conversion of H₂ to form clean samples of H₂ $j = 0$ does not work well for D₂. For these reasons, D₂ is not an ideal candidate for the study of resonances in this system.

The ground level (00+) of NH₃ is not suitable for Stark deceleration. Nevertheless, we find that NH₃-H₂ cross sections for transitions from that level, particularly for the 00+ → 10+ transition, also display interesting resonance structures with both broad and sharp resonance peaks. Their energy-dependent cross sections are presented in Fig. 3.14.

The resonances in inelastic scattering have strong connections to the PES of the given system. The current study uses a PES developed by Maret *et al.* [72]. The *ab initio*

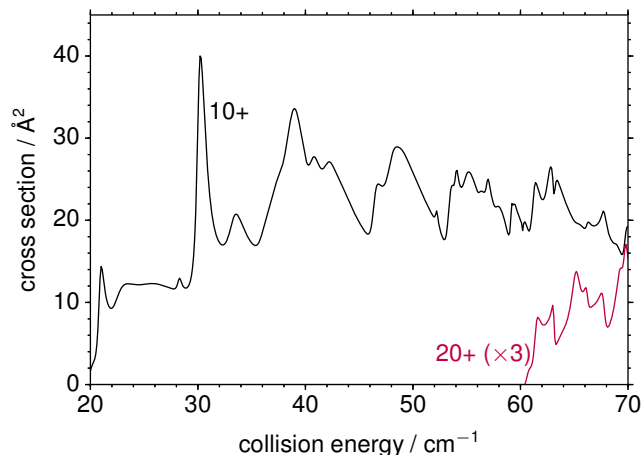


Figure 3.14: State-to-state integral cross section as a function of collision energy out of the $00+$ level of *ortho*- NH_3 in collisions with *para*- H_2 ($j = 0$). The final levels are indicated for each transition for which the cross section is plotted. The $00+ \rightarrow 20+$ cross sections are multiplied by 3 for clarity.

calculations for the reference PES are only at CCSD(T)/aug-cc-pVDZ level, and those for the correction PES are extrapolated from CCSD(T)/aug-cc-pVDZ and CCSD(T)/aug-cc-pVTZ calculations. To check the accuracy of the PES, we have performed CCSD(T)-F12a calculations [51, 53] with the aug-cc-pVTZ basis using Molpro [151] for 3000 geometries at $R = 5 a_0$ and fitted the interaction energies using the same angular expansion as the Maret *et al.* PES. We found that all the ten expansion coefficients with the largest absolute values differ by less than 1% from those in the Maret *et al.* PES. Therefore, we believe the PES used in this study has good accuracy for the computation of cross sections and resonance structures.

Chapter 4

Vibrational Relaxation of CH₃ in Collisions with He

This chapter contains long excerpts of a paper titled “Theoretical study of the vibrational relaxation of the methyl radical in collisions with helium” by Qianli Ma, Paul J. Dagdigian, and Millard H. Alexander, originally published on *J. Chem. Phys.* [152], and is presented with permission of the American Institute of Physics.

4.1 Introduction

Collisional vibrational energy transfer is fundamental to many processes in chemistry, including thermalization of non-equilibrium vibrational state distributions and relaxation of energized molecules in unimolecular reactions. Modern laser methods have revolutionized the experimental study of vibrational energy transfer [153–159]. Theoretical calculations, both quantum scattering calculations and semiclassical trajectory studies, can predict cross sections and rate constants for vibrationally inelastic collisions. In the case of collisions of diatomic molecules with atoms, fully quantum scattering calculations with all degrees of freedom have been carried out only for a few exemplary systems [122, 160–163].

Theoretical studies of collisional vibrational energy transfer have emphasized the study of the relaxation of highly energized polyatomic molecules because of the role of this process in unimolecular reactions. Examples are the work by Lendvay, Schatz, and Harding on the relaxation of SO₂ by Ar [164], the work of Oref and Bernshtein on

benzene–Ar and azulene–Ar [165, 166], and the work of several groups on the relaxation of pyrazine in collisions with CO and CO₂ [167, 168]. Because of the large number of ro-vibrational levels that are energetically accessible, there have been few quantum scattering calculations on ro-vibrational relaxation of polyatomic molecules. Only by eliminating the rotational degrees of freedom, and using approximate models such as the infinite-order-sudden approximation, have earlier authors been able to model collisional vibrational relaxation of polyatomics. Examples include a colinear quantum model by Schatz and Lendvay [169] in treating CS₂–He vibrational energy transfer, a breathing sphere approximation by Ivanov, Grebenshchikov, and Schinke [170] on O₃–Ar, zero-impact parameter calculations by Christoffel and Bowman [171] on HCN/HNC–Ar, time-dependent wave packet calculations by Valero and Kroes [172], and vibrational close-coupling, infinite-order sudden quantum-scattering calculations by Clary *et al.* [173, 174].

Our focus here is the relaxation of the umbrella vibrational motion of the methyl radical, with full retention of the rotational degrees of freedom. Several experimental studies of the collisional vibrational relaxation of the methyl radical have been reported [175–179]. In some cases, vibrational relaxation was investigated while determining the nascent internal state distribution of methyl radicals, either CH₃ or CD₃, produced in photolysis or chemical reaction [176, 180–183]. In a previous study, our group carried out a theoretical investigation of purely rotationally inelastic collisions of the methyl radical with He [81]. In that study, a potential energy surface (PES) for the interaction of CH₃ with He was computed using a restricted open-shell coupled-cluster method with inclusion of all single, double, and (perturbatively) triple excitations [RCCSD(T)]. The geometry of the CH₃ radical was held fixed at the planar trigonal lowest-energy structure [81, 184]. Full close-coupling quantum scattering calculations were then carried out to determine state-to-state integral cross sections, as well as thermal rate constants, for rotational energy transfer.

The methyl radical has four vibrational modes. The lowest-frequency mode (at 606.5

cm^{-1}) is the ν_2 out-of-plane bending mode [185], usually referred as the “umbrella” mode. Here we extend our earlier work [81] to the ro-vibrational relaxation of the ν_2 mode. The umbrella mode has been found to be excited in methyl formed in the photolysis of methyl halides and in some chemical reactions producing methyl [176, 177, 180–183, 186]. The lowest-frequency mode is often considered to be the “gateway” for the overall collisional relaxation of a molecule [187].

This chapter is organized as follows: Section 4.2 describes construction of a 4-dimensional PES to describe the interaction of a methyl radical undergoing umbrella vibrational motion with a He atom, and, then, the averaging over the vibrational coordinate in a given ν_2 level. Section 4.3 describes the level structure of CH_3 and the technical details of the scattering calculation. In Sec. 4.4 we report calculated cross sections and rate constants, and analyze the dynamics of the relaxation of the $\nu_2 = 1$ umbrella vibrational mode. The other vibrational modes of CH_3 are assumed to remain in their ground state. A discussion and comparison with experimental results concludes the paper.

4.2 Potential Energy Surface

We employ the body-frame coordinate system shown in Fig. 1 of Ref. [81] to describe the location of the He atom relative to the methyl radical. The center of mass of CH_3 is located at the origin, with the z axis defining the C_3 symmetry axis. The x axis lies along one of the C–H bonds. The orientation of the He atom with respect to the center-of-mass of CH_3 is described by the spherical polar coordinates R , θ , and ϕ . Following the study by Yamada, Hirota, and Kawaguchi [188] of the ν_2 bands of methyl, the umbrella vibrational coordinate Q is defined as the perpendicular distance of the carbon atom from the plane containing the three hydrogen atoms.

As in our earlier study of pure rotational energy transfer in CH_3 [81], to determine the PES we used restricted coupled-cluster calculations with full inclusion of single and double excitations and the perturbative inclusion of triplet excitations [189–191]. We used

the aug-cc-pVQZ correlation-consistent basis sets [192], with the addition of bond functions [49, 50] located at the mid-point of the Jacobian vector \mathbf{R} . A counterpoise correction [57] was used to correct for basis-set superposition error. All *ab initio* calculations were done with the Molpro 2010.1 suite of programs [113].

The CH₃-He PES was computed on a four-dimensional (R , θ , ϕ , and Q) grid delimited by 19 values of R [R (in bohr) = 3.5–10 in steps of 0.5; 11, 12, 13, 15 and 20], 10 values of θ [θ = 0–90° in steps of 10°], 7 values of ϕ [ϕ = 0–60° in steps of 10°], and 11 values of Q [Q (in bohr) = –0.94–0.94 in steps of 0.094]. For $\theta = 90^\circ$ only points with non-negative Q are unique and for $\theta = 0^\circ$ all values of ϕ are equivalent. Interaction energies for other values of (θ, ϕ) can be obtained by symmetry. The total number of (nonequivalent) nuclear geometries is 12711.

From these points, we obtain three-dimensional (R , θ , ϕ) vibrationally averaged PESs by integrating over the vibrational wave functions $\chi_v(Q)$ of the umbrella mode (which we assume to be real), namely

$$V_{v,v}(R, \theta, \phi) = \int \chi_v(Q) V(R, \theta, \phi, Q) \chi_v(Q) dQ \quad (4.1)$$

where Q designates the umbrella coordinate. Even when constrained to C_{3v} symmetry, as the CH₃ molecule bends out of planar geometry the C–H bond length increases significantly, a manifestation of the transition from $s p^2$ to $s p^3$ hybridization [193]. To account for this effect, in the determination of the wave functions for the CH₃ vibrational motion we used an umbrella potential obtained by similar CCSD(T) calculations with, at each value of Q , minimization of the energy with respect to the C–H bond length. The importance of a proper description of the C–H stretch is illustrated by Fig. 4.1, which shows the comparison of the CH₃ umbrella potential from our *ab initio* calculation with a C–H bond length fixed at the equilibrium planar value and varying at each Q , and that derived from experiment by Yamada, Hirota, and Kawaguchi [188]. The agreement with

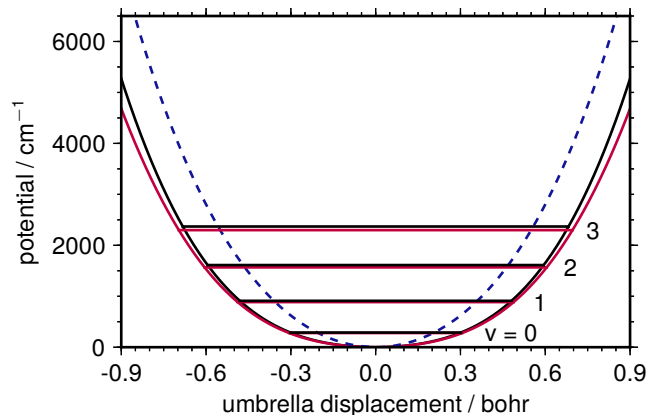


Figure 4.1: Potential energy of CH_3 as a function of the umbrella displacement Q . The red line shows the experimentally derived curve of Yamada, while the black line shows the potential from our *ab initio* calculations with optimized C-H bond length for each umbrella displacement as described in the text. The blue dashed line shows the potential calculated with a fixed C-H bond length of 2.037 bohr. The horizontal lines indicate the positions of the lower experimental (red) and calculated (black) vibrational levels.

experiment is far better when the C-H bond length is allowed to relax.

A simplified treatment restricts the motion of the three H nuclei to the Q coordinate, with the Hamiltonian

$$\hat{H} = -\frac{1}{2\mu_u} \frac{d^2}{dQ^2} + V_u(Q), \quad (4.2)$$

where $V_u(Q)$ is the umbrella potential described in the previous paragraph, and the reduced mass is [188]

$$\mu_u = 3m_{\text{H}}m_{\text{C}}/(3m_{\text{H}} + m_{\text{C}}). \quad (4.3)$$

As shown in Fig. 4.1, the calculated energies of the lower ν_2 levels estimated with our umbrella potential energy curve match well with experiment. The calculated $\nu_2 = 1 \leftarrow 0$ band origin is 623.02 cm^{-1} , This differs by less than 3% from the experimental value of 606.45 cm^{-1} [188].

The positions of the levels and the ν_2 wave functions determined by this one-dimensional treatment agree extremely well with the predictions based on a more rigorous treatment of the umbrella motion [194], developed in the study of the $\text{NH}_3\text{-Ar}$ van der Waals complex. In this work, the kinetic energy term in the Hamiltonian for umbrella

motion is expressed through a moment of inertia that depends on the inversion (umbrella) coordinate.

We follow Green [195] in expanding each vibrationally-integrated $V_{v'v}(R, \theta, \phi)$ potential energy surface (with $v', v \leq 3$) in terms of spherical harmonics

$$V_{v'v}(R, \theta, \phi) = \sum_{\lambda\mu} V_{v'v}^{\lambda\mu}(R) (1 + \delta_{\mu 0})^{-1} \left[Y_{\lambda\mu}(\theta, \phi) + (-1)^\mu Y_{\lambda, -\mu}(\theta, \phi) \right]. \quad (4.4)$$

Equation (4.4) can be equivalently written as

$$V_{v'v}(R, \theta, \phi) = \sum_{l_1 \mu_1 \geq 0} V_{v'v}^{\lambda\mu}(R) (2 - \delta_{\mu 0}) \left(\frac{2\lambda + 1}{4\pi} \right)^{\frac{1}{2}} d_{\mu 0}^\lambda(\theta_1) \cos \mu \phi. \quad (4.5)$$

where $d_{m'm}^j(\theta)$ is a reduced rotation matrix and is real. Since the umbrella motion preserves C_3 symmetry, the angular expansion coefficients $V_{v'v}^{\lambda\mu}(R)$ vanish except when μ is a multiple of 3 [81]. Further, the interaction potential has the additional symmetry

$$V(R, \theta, \phi, Q) = V(R, \pi - \theta, \phi, -Q), \quad (4.6)$$

and the symmetry of the wave function for the umbrella mode with respect to reflection through $Q = 0$ is equal to the parity of the vibrational quantum number. It follows that

$$\begin{aligned} & \int \chi_{v'}(Q) V(R, \pi - \theta, \phi, Q) \chi_v(Q) dQ \\ &= (-1)^{v+v'} \int \chi_{v'}(Q) V(R, \theta, \phi, Q) \chi_v(Q) dQ \end{aligned} \quad (4.7)$$

With Eqs. (4.4) and (4.7), and the fact that $Y_{\lambda\mu}(\pi - \theta, \phi) = (-1)^{\lambda+\mu} Y_{\lambda\mu}(\theta, \phi)$, we conclude that the only non-vanishing expansion coefficients are those for which

$$(-1)^{\lambda+\mu} = (-1)^{v+v'}. \quad (4.8)$$

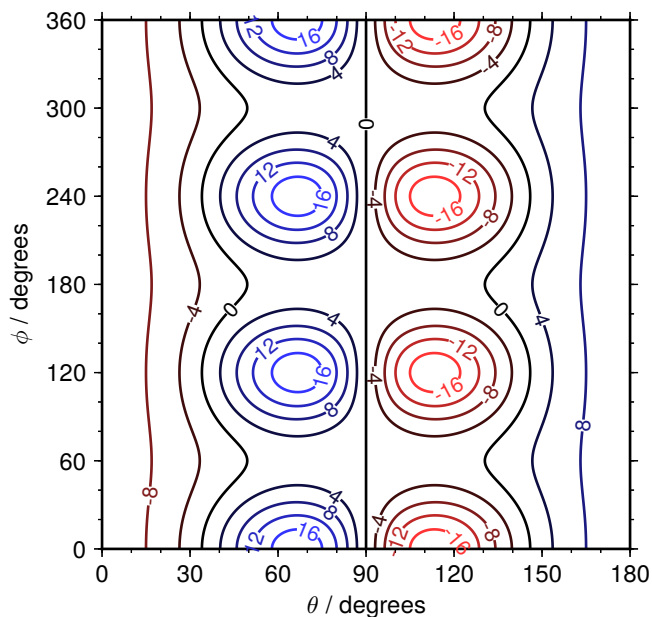


Figure 4.2: Dependence of the vibrational coupling potential $V_{10}(R, \theta, \phi)$ of $\text{CH}_3\text{-He}$ defined in Eq. (4.1) on the orientation (θ, ϕ) of the He atom with respect to the CH_3 molecule for an atom-molecule separation $R = 6$ bohr.

In the angular expansion of the $\text{CH}_3(v)\text{-He}$ PES we included 12 terms with $\mu = 0, 3, 6, 9$, and $\lambda \leq 9$ for even $\lambda + \mu$ and $\lambda \leq 10$ for odd $\lambda + \mu$. The choice of λ and μ is also constrained by Eq. (4.8).

Figure 4.2 presents a contour plot of the V_{10} coupling PES at $R = 6$ bohr. To assess the quality of the fit, we note that the root mean square deviation of the fit to the $V_{1,0}$ coupling potential at $R = 6$ bohr is 0.516 cm^{-1} . The V_{10} PES is antisymmetric about $\theta = 90^\circ$, because of the differing symmetries of the $v = 0$ and 1 wave functions with respect to reflection through $Q = 0$. As a consequence, there is no isotropic term in this expansion of the PES, since $\lambda = 0, \mu = 0$ does not satisfy Eq. (4.8) for coupling between an even and odd v vibrational level. The overall sign of this off-diagonal coupling depends on the relative phases of the $v = 0$ and $v = 1$ umbrella wave functions and is arbitrary. The results of the scattering calculations will be invariant with this choice of the phase provided that a consistent set of vibrational wave functions is used to compute all the off-diagonal coupling PESs. We can also see that the coupling potential is roughly $1/8$ of the magnitude

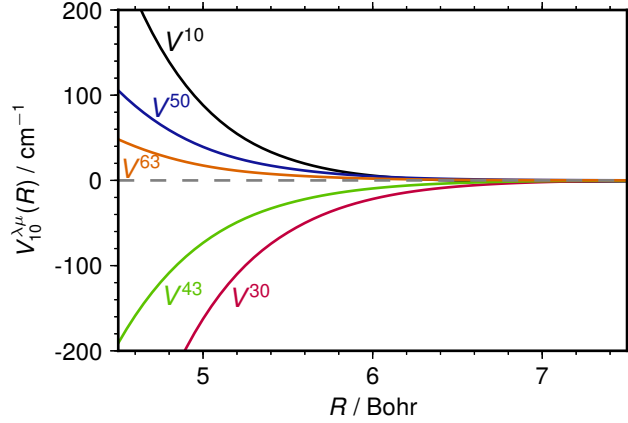


Figure 4.3: Dependence of the larger expansion coefficients $V_{10}^{\lambda\mu}(R)$ [defined in Eq. (4.4)] on the CH_3 -He separation R . The gray dashed line indicates zero.

of the $v = 0$ vibrationally elastic CH_3 -He PES [$V_{00}(R, \theta, \phi)$] at the same atom-molecular separation (see Fig. 3 of Ref. [81]), depending on the helium location considered.

To investigate further the anisotropy of the coupling potential, we present in Fig. 4.3 the dependence on the atom-molecule separation R of the larger angular expansion coefficients $V_{10}^{\lambda\mu}(R)$ for the $v = 0-1$ coupling. Under thermal conditions, the range of R accessible is governed by the isotropic term in the vibrationally-diagonal PES, V_{vv}^{00} . This can be easily estimated from Fig. 4 of Ref. [81]. Over this range of R , V^{10} , V^{30} , and V^{43} are the largest anisotropic terms in the V_{10} PES. The dependence of these three terms on θ and ϕ is

$$V_{10}^{10}(R, \theta, \phi) \sim Y_{1,0}(\theta, \phi) \sim \cos \theta. \quad (4.9)$$

$$V_{10}^{30}(R, \theta, \phi) \sim Y_{3,0}(\theta, \phi) \sim 5 \cos^3 \theta - 3 \cos \theta, \quad (4.10)$$

and

$$V_{10}^{43}(R, \theta, \phi) \sim [Y_{4,3}(\theta, \phi) + Y_{4,-3}(\theta, \phi)] \sim \cos \theta \sin^3 \theta \cos 3\phi. \quad (4.11)$$

The first term reflects the antisymmetry, with respect to θ of the V_{10} PES, which is due (as we have mentioned) to the differing parities of the $v = 0$ and $v = 1$ vibrational levels.

The second term reflects the line of maxima at $\theta \sim 65^\circ$ and minima at $\theta \sim 115^\circ$. The third term reflects the localization of these extrema at $\phi = 0^\circ, 120^\circ, 240^\circ$ and 360° .

The anisotropy of the V_{10} vibrational coupling potential is very different from that of the vibrationally-diagonal V_{00} PES which governs collision-induced rotational energy transfer within a vibrational manifold, discussed in Ref. [81]. The largest anisotropic term of the V_{00} PES is V_{00}^{33} , which depends on both θ and ϕ . As we will see in Sec. 4.4, this difference ultimately leads to very different propensity rules for rotational transitions in vibrationally inelastic collisions.

We have determined all the $\text{CH}_3(v_2)$ vibrational coupling PESs for $v, v' \leq 3$. We will give a brief description of these terms here. First, we consider the vibrationally-diagonal $v = v' \geq 1$ PESs which govern pure rotational transitions of $\text{CH}_3(v \geq 1)$ with He. These averaged PESs show little difference with the V_{00} PES, but are increasingly less repulsive as v increases when θ approaches 0° or 180° . This corresponds to approach of the He atom from below or above the CH_3 plane containing the CH_3 molecule.

The anisotropy of the V_{21} PES is similar to that of the V_{10} PES, discussed above, although the magnitude of the potential is slightly larger. Thus, we could expect similar rotational propensities for $v = 1 \rightarrow 2$ as compared to $v = 0 \rightarrow 1$ transitions. The V_{20} PES is much smaller ($\sim 1/10$) than those for $\Delta v = \pm 1$ coupling. This V_{20} PES has a small isotropic V_{20}^{00} term, while the major contribution to the anisotropy comes from the V_{20}^{40} , V_{20}^{53} , and V_{20}^{22} terms. However, since the magnitude of V_{20} is so small, we anticipate that $\Delta v = \pm 2$ vibrationally-inelastic collisions will be induced by successive $\Delta v = \pm 1$ coupling. Contour plots, as well as the dependence upon R of the expansion coefficients for the coupling PESs described above, are available in the supplementary material of Ref. [152].

4.3 Scattering Calculations

Based on the PES described in the preceding section we have carried out full close-coupling calculations to compute cross sections and rate constants for CH_3 $v = 1 \rightarrow 0$

ro-vibrational relaxation.

Since we treat the CH₃ molecule as a symmetric top regardless of the value of the umbrella displacement Q , we can express the rotational part of the wave function as [195]

$$|nkm\varepsilon\rangle = [2(1 + \delta_{k0})]^{-1/2} (|nkm\rangle + \varepsilon |n, -km\rangle), \quad (4.12)$$

where n is the rotational angular momentum, and k and m are the the body-frame and the space-frame projections, respectively, of n . The symmetry index ε is restricted to $+1$ for $k = 0$, but can take on values of ± 1 for $k > 0$. Although the methyl radical has a total electronic spin of $S = 1/2$, the spin-rotation and hyperfine interactions are very small [196]. Consequently, as in our earlier treatment of pure rotational energy transfer in collisions of CH₃ with He [81], we will neglect the spin of CH₃ in our treatment of the dynamics.

The nuclear permutation symmetry of the three protons imposes a further restriction: the overall wave function, including the vibrational wave function for the umbrella motion, must be antisymmetric with respect to permutation of the hydrogen nuclei. The *ortho*-labelled nuclear spin modification includes projection levels with k equal to a multiple of 3 (*i.e.* $k = 0, 3, 6, \dots$), and $\varepsilon = (-1)^{n+v}$ [81, 197, 198]. In particular, for $k = 0$ the only possible value of ε is $+1$, hence levels with $(-1)^{n+v} = -1$ are absent in the $k = 0$ stack. The *para* levels include all rotational levels with k not a multiple of 3 (*i.e.* $k = 1, 2, 4, 5, 7, 8, \dots$), and both values (± 1) are allowed for ε . Thus, there are roughly four times as many *para* levels as *ortho* ones. The nuclear statistical weights of the *ortho* and the *para* levels are 4 and 1, respectively.

Figure 4.4 presents a level diagram for the low-lying $v = 0$ and 1 rotational levels. The rotational energies were computed using a rigid rotor symmetric top Hamiltonian. The rotational constants for the individual umbrella-mode vibrational levels and their energies are taken from spectroscopic studies [188, 199]. We used these ro-vibrational energies

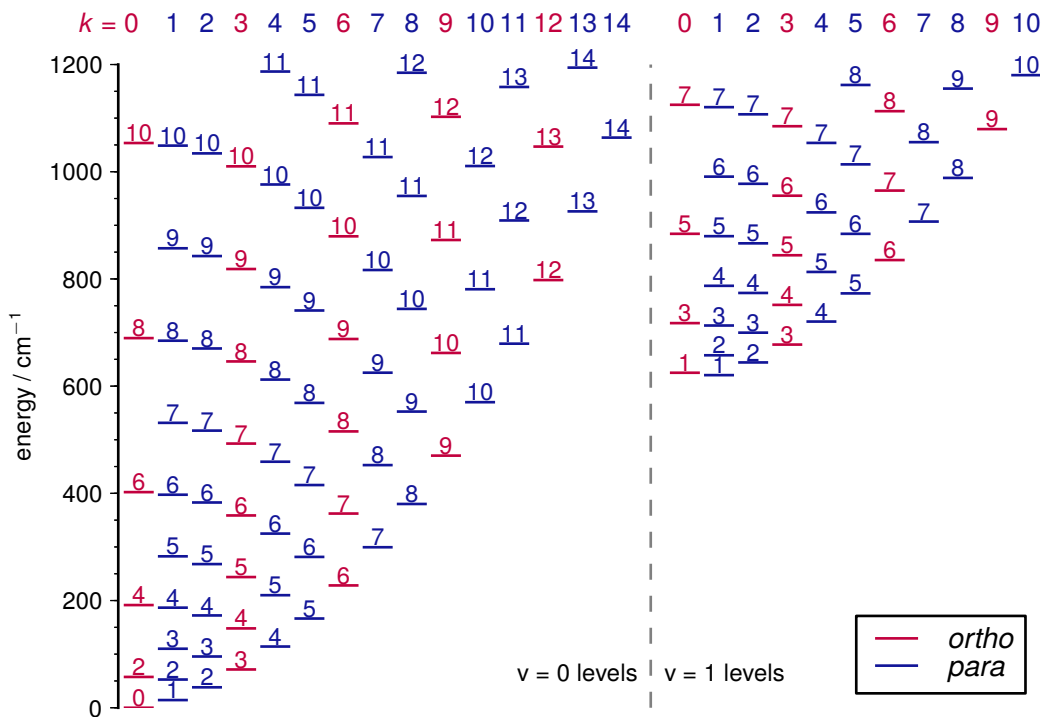


Figure 4.4: Rotational levels for *ortho* (red) and *para* (blue) CH₃ in the $v = 0$ and $v = 1$ umbrella vibrational manifold with energies less than 1200 cm^{-1} . Each level is labelled with its rotational quantum number n . The body-frame projection quantum number k appears at the top of each column. Note that for $k = 0$ only rotational levels with parity equal to $(-1)^k$ are present.

in our scattering calculations. For simplicity, we will designate the v, n ro-vibrational levels as n_k for $v = 0$ and n_k^\dagger for $v = 1$. Since we will not consider explicitly transitions into or out of levels with $v > 1$, we do not need to introduce a simplified notation for the ro-vibrational levels with $v > 1$.

The HIBRIDON suite of programs [31] was employed to compute the vibrationally elastic and inelastic cross sections. In the investigation of rotationally inelastic, but vibrationally elastic, scattering, we include only rotational channels in the particular vibrational manifold of interest, following procedures described in Ref. [81]. For rotationally inelastic scattering in vibrational manifold v , we used the vibrationally averaged PES [$v' = v$ in Eq. (4.1)].

We then treat scattering inelastic in both the rotational and umbrella degrees of freedom of CH₃. Because the state-to-state vibrationally inelastic cross sections were on

the order of 10^{-3} \AA^2 or even smaller, we wanted to ensure a precision of better than $\sim 10^{-5} \text{ \AA}^2$. To do so, we expanded the channel basis to include all ro-vibrational levels up to a specified maximum energy. At the highest energy considered (2500 cm^{-1}), the basis included all $v \leq 3$ rotational levels with energy less than 3650 cm^{-1} , and all total angular momenta $J \leq 150.5$. The calculations for *ortho* and *para* CH_3 at this energy required 3141 and 6291 channels, respectively.

As might have been anticipated, long-range collisions are too weak to promote vibrational relaxation. Consequently, the maximum total angular momentum J required for convergence is much smaller than that for purely rotationally inelastic collisions.

4.4 Results

4.4.1 Rotationally Inelastic Collisions

In our earlier study of purely rotationally inelastic scattering of $\text{CH}_3(v=0)$ by He [81], we found a strong propensity for $\Delta k = \pm 3$ transitions, a consequence of the large V_{00}^{33} term in the expansion of the coupling potential. We first consider here the effect of the CH_3 umbrella vibration on the PES for collision-induced rotational transitions. The vibrationally averaged PES for CH_3 [$V_{00}(R, \theta, \phi)$, see Figs. S1 and S2 of the supplementary material of Ref. [152]] is very similar to the rigid CH_3 -He PES reported in Ref. [81], except for a slightly less repulsive interaction at $\theta \sim 0^\circ$ or 180° . The cross sections computed with the vibrationally averaged PES are virtually identical (within 1%) with those obtained with the rigid CH_3 -He PES. Thus, inclusion of the CH_3 umbrella motion affects little the dynamics of rotationally inelastic but vibrationally elastic collisions.

The $\text{CH}_3(v=1)$ -He PES [$V_{11}(R, \theta, \phi)$, see Figs. S3 and S4 of the supplementary material of Ref. [152]] is very similar to both the rigid and V_{00} PESs. However, the rotational level structure in $v=1$ CH_3 is slightly different than that for $v=0$, because in the $k=0$ stack only even n rotational levels are allowed for $v=0$ but only odd n for $v=1$

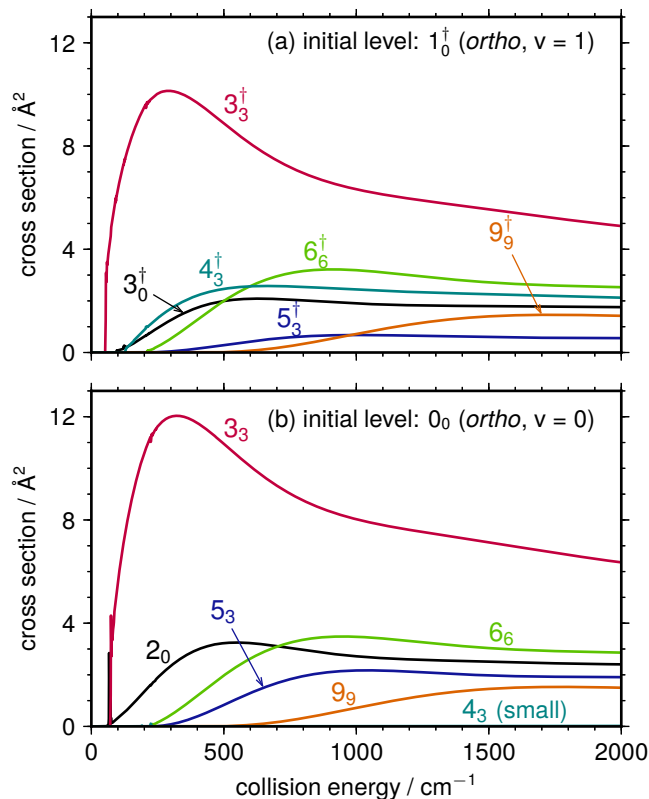


Figure 4.5: Larger state-to-state integral cross sections as a function of collision energy for rotational transitions out of the lowest *ortho* level of (a) $v_2 = 1$ and (b) $v_2 = 0$ CH_3 in collisions with He. The final levels are labeled on each curve.

(see Sec. 4.3).

To illustrate the effect of the difference in the rotational structure of the $v = 0$ and $v = 1$ vibrational manifolds, we show in Fig. 4.5 the collision energy dependence of the state-to-state cross sections for rotational transitions out of the 1_0^\dagger level and the 0_0 level of CH_3 , the lowest rotational levels in each manifold. The two panels of Fig. 4.5 are quite similar, most noticeably the energy dependence of the large cross sections for transitions to the $n = 3, k = 3$ state. However, we observe that the cross section for the $1_0^\dagger \rightarrow 3_3^\dagger$ transition is about 20% smaller than that for the $0_0 \rightarrow 3_3$ transition. Additionally, the cross section for the $1_0^\dagger \rightarrow 4_3^\dagger$ transition is much larger than that for $0_0 \rightarrow 4_3$. These differences are a direct consequence of the changes in the rotational level structure. The largest angular expansion coefficient for the $v = 1$ averaged PES (V_{11}^{33}) couples the ground 1_0^\dagger level with

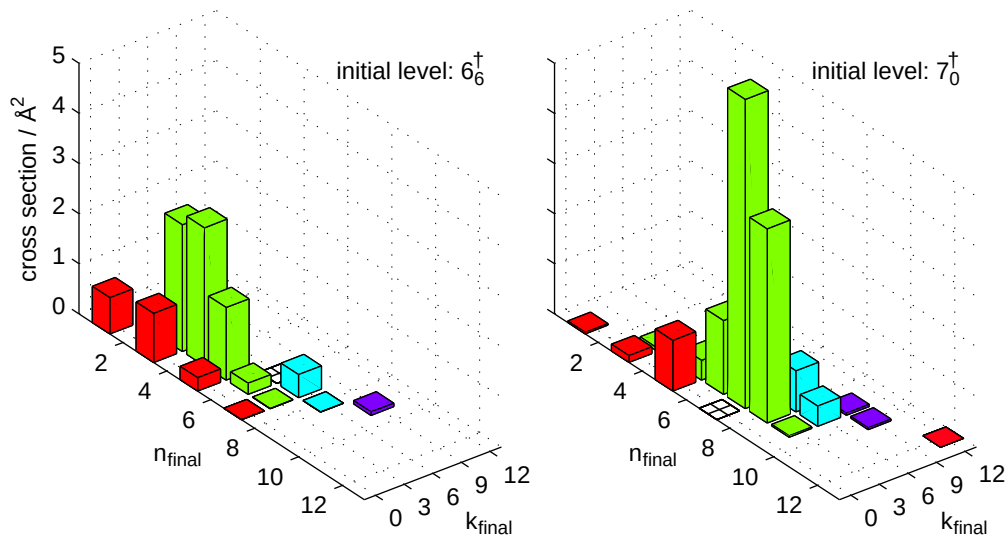


Figure 4.6: Bar plot of the cross sections for rotationally inelastic collisions of $\text{CH}_3(v_2 = 1)$ in the 6_6^\dagger and 7_0^\dagger initial levels with He at a collision energy of 300 cm^{-1} . The initial levels are denoted by crossed white squares.

two levels, 3_3^\dagger and 4_3^\dagger . For $\text{CH}_3(v = 0)$, the comparable term (V_{00}^{33}) couples the ground 0_0 level only with the 3_3 level. Although, the V_{11}^{33} term couples the 1_0^\dagger level with both the 3_3^\dagger and 4_3^\dagger levels, the energy gap for the transition to the latter state is larger (Fig. 4.4). Consequently, we see in Fig. 4.5(a) that the $1_0^\dagger \rightarrow 3_3^\dagger$ cross section is larger than the $1_0^\dagger \rightarrow 4_3^\dagger$ cross section.

Figure 4.6 shows the final-state distributions for collisions out of two *ortho* levels of $\text{CH}_3(v = 1)$ at a collision energy of 300 cm^{-1} . The two levels are chosen so that Fig. 4.6 is comparable to Fig. 8 in Ref. [81]. The largest cross sections out of the 6_6^\dagger level involve $\Delta k = -3$, while those out of 7_0^\dagger , $\Delta k = +3$. These transitions result from direct coupling between the initial and final levels by the dominant V_{11}^{33} term. The change in level structure of the $k = 0$ stack does not significantly affect the $\Delta k = \pm 3$ collisional propensity. The cross sections for transitions out of the 7_0^\dagger level are significantly larger than those for transitions out of the 6_6^\dagger level. This result is consistent with what we found for rotationally elastic transitions out of the 6_6 and the 6_0 levels for rigid CH_3 [81]. The transitions out of the 6_6^\dagger level to the 4_3^\dagger and 3_3^\dagger levels have larger energy gaps than the transitions out of the 7_0^\dagger level to the 7_3^\dagger and 8_3^\dagger levels, and the latter set of transitions are coupled more strongly by

the dominant V_{11}^{33} term (see Sec. V.A of Ref. [81]).

As we have seen here, the differing parities of the non-vanishing rotational levels in $k = 0$ stack of the $v = 0$ and $v = 1$ vibrational manifolds (Fig. 4.4) is responsible for differences in the rotationally inelastic scattering of *ortho*-CH₃ in these two vibrational manifolds. In contrast, for the *para* nuclear spin modification the level structure in $v = 0$ and $v = 1$ is very similar. Consequently, the rotationally inelastic scattering of *para*-CH₃ in these two vibrational manifolds is very similar (not shown here) to that of rigid *para*-CH₃, shown in Ref. [81].

4.4.2 Vibrationally Inelastic Collisions

We now consider $v = 1 \rightarrow 0$ ro-vibrational relaxation of CH₃. Since the number of levels is quite large, we first present results for the rotationally-summed vibrational relaxation cross sections, defined as

$$\sigma_{n_k}^{\text{vib}} = \sum_{n'k'} \sigma_{n_k^\dagger \rightarrow n'k'} \quad (4.13)$$

Here the sum extends over all energetically accessible rotational levels in the ground vibrational level.

We plot in Fig. 4.7 the collision energy dependence of these rotationally-summed vibrational relaxation cross sections for a number of *ortho* and *para* rotational levels, representing a range of values of n and k . We observe similar magnitudes of the cross sections for *ortho* and *para* levels with similar n and k , for example the *ortho* 7_0^\dagger and *para* 7_1^\dagger levels. However, the vibrational relaxation cross sections have a different collision energy dependence than the cross sections for collision-induced rotational transitions. The former show a roughly linear increase with collision energy. Because of the large vibrational energy spacing, collisions at low energy are close to the adiabatic limit, so that the cross section for vibrational relaxation will be small [2]. As the collision energy increases, the

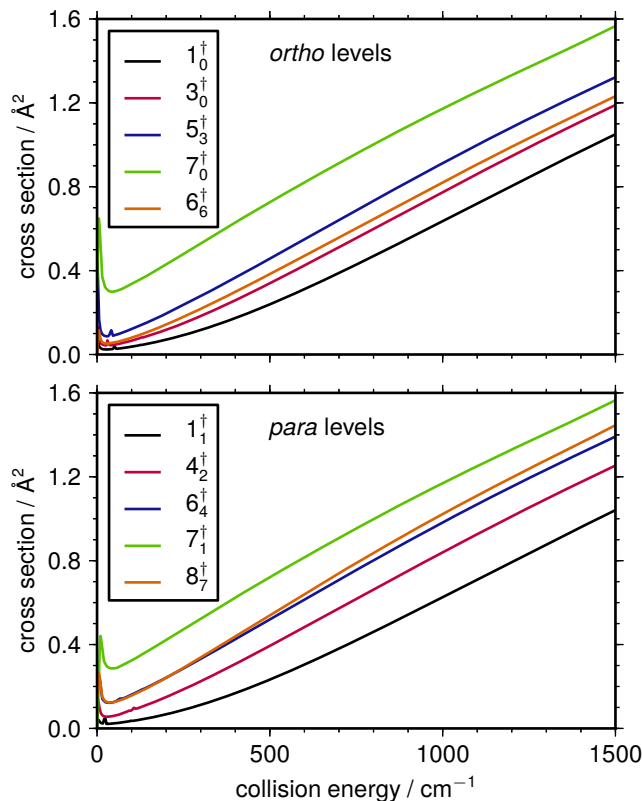


Figure 4.7: Dependence upon the collision energy of the vibrational relaxation cross section defined in Eq. (4.13) for selected $\text{CH}_3(v=1)$ rotational levels in collisions with He. The initial levels (*ortho* levels: upper panel; *para* levels: lower panel) are labeled.

degree of nonadiabaticity increases, with a corresponding growth in the cross section, which appears as an approximately linear dependence upon the collision energy.

A particularly interesting feature in Fig. 4.7 is the large variation in the vibrational relaxation cross sections for different initial rotational levels. To visualize better the dependence on initial level of the vibrational relaxation cross section, we plot in Fig. 4.8 these cross sections for a large range of rotational levels in $v=1$ at a collision energy of 300 cm^{-1} . We observe, except, perhaps, for the highest rotational level considered, an increase as the degree of rotational excitation increases, and, for a given n , a decrease as the body-frame projection k of n increases. This qualitative behavior appears to be unchanged for collision energies greater than $\sim 200 \text{ cm}^{-1}$.

To probe this dependence in more detail, as well to investigate the role of angular

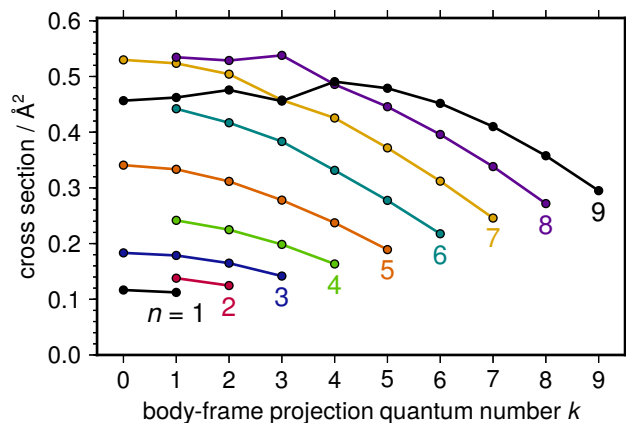


Figure 4.8: Rotationally-summed vibrational relaxation cross sections [defined in Eq. (4.13)] at 300 cm^{-1} collision energy for different initial rotational levels n_k^\dagger .

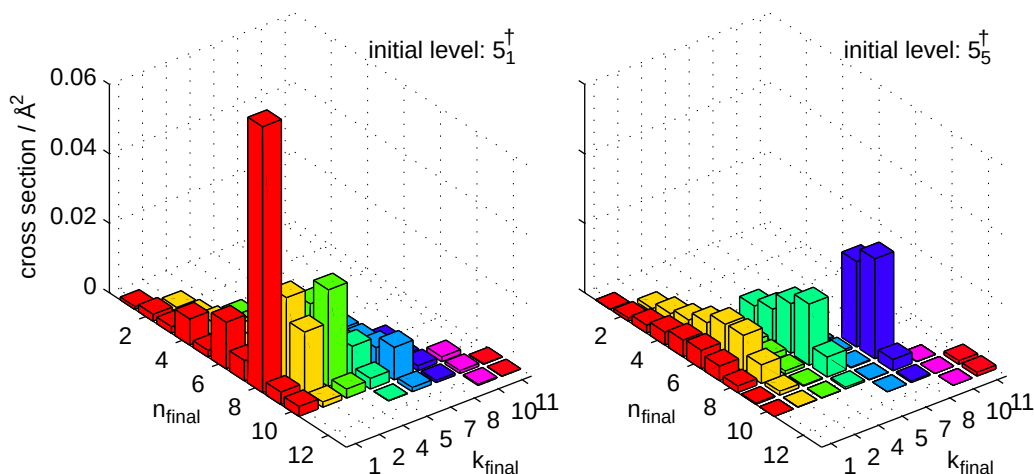


Figure 4.9: Bar plot of the integral cross sections for $v=1 \rightarrow 0$ ro-vibrationally inelastic scattering of *para* CH_3 (k not a multiple of 3) in the 5_1^\dagger and 5_5^\dagger levels through collision with He at a collision energy of 300 cm^{-1} .

momentum in vibrational relaxation, we present in Fig. 4.9 a bar plot of the state-to-state cross sections at 300 cm^{-1} collision energy for ro-vibrationally inelastic transitions out of two exemplary initial levels of *para*- CH_3 , 5_1^\dagger and 5_5^\dagger . Although these levels have the same n , their vibrational relaxation cross sections at 300 cm^{-1} differ by $\sim 50\%$ (see Fig. 4.8).

As in the case of purely rotationally inelastic transitions within the $v = 0$ manifold [81], there appear strong propensities in the rotational distribution of the scattered molecules. In the pure rotational case, we interpreted these in terms of the strength of the coupling between the initial and final states and the magnitude of the energy gap.

Interpretation is more complicated for the propensities revealed in the much less efficient rovibrational transitions seen in Fig. 4.9. Certainly, the large magnitude of the $5_1^\dagger \rightarrow 8_1$ cross section seen in the left panel can be attributed to the dominance of the V_{10}^{30} term in the expansion of the coupling potential. However, the cross section for the $5_5^\dagger \rightarrow 8_5$ transition, which is similarly coupled by the V_{10}^{30} term, is much smaller. This may partially due to the slightly larger energy gap for the $5_5^\dagger \rightarrow 8_5$ transition compared to that for $5_1^\dagger \rightarrow 8_1$. We found that the strength of coupling, estimated from the magnitude of the matrix elements of the V_{30}^{10} term of the potential in body frame, is significantly larger for the $5_1^\dagger \rightarrow 8_1$ transition. However, it is only within the first Born approximation that one can unambiguously correlate the size of a cross section to the magnitude of the potential matrix element between the initial and final state. Here, the weak vibrationally-inelastic coupling between a given n_k^\dagger and $n_{k'}$ level will be at least partially masked by the very strong, purely rotational couplings in both the $v = 1$ and $v = 0$ vibrational manifolds.

Finally, we examine the n dependence of the vibrational relaxation cross section. For a given value of k , this cross section generally increases with increasing n (see Fig. 4.8). The variation in the energy gap for important state-to-state transitions is an important factor contributing to this n dependence. As an example, we consider levels in the $k = 1$ stack. As discussed above, the $n_1^\dagger \rightarrow (n + 3)_1$ transitions coupled by V_{10}^{30} term make significant contributions to the vibrational relaxation cross sections for levels in this stack. For these transitions the energy gaps starts at -434 cm^{-1} for $n = 1$, decreases to -256 cm^{-1} for $n = 4$, -9 cm^{-1} for $n = 8$, and changes sign for $n = 9$ ($+54 \text{ cm}^{-1}$). This trend of decreasing energy gaps is in good agreement with the n dependence of the total cross section. Also, for low-lying rotational levels, a Δn , Δk transition coupled by the V_{10}^{30} or V_{10}^{43} term generally has a smaller energy gap as the initial rotational angular momentum n increases. As we will discuss in Sec. 4.4.3, high-energy rotational levels where the relaxation efficiency does not correlate as straightforwardly with the energy gap are unlikely to be populated significantly at room temperature and below.

4.4.3 Rate Constants for Vibrational Relaxation

Rate constants for vibrational relaxation at a given translational temperature T_t for individual $\text{CH}_3(v = 1)$ rotational levels were computed from the collision energy dependence of the vibrational relaxation cross sections [1]:

$$k_{n_k}^{\text{vib}}(T_t) = \left[\frac{8}{\pi \mu (k_B T_t)^3} \right]^{1/2} \int_0^\infty E_c \sigma_{n_k}^{\text{vib}}(E_c) e^{-E_c/k_B T_t} dE_c, \quad (4.14)$$

where k_B is the Boltzmann constant.

The computed relaxation rate constants for different initial levels at $T_t = 298 \text{ K}$ range from $\sim 3 - 9 \times 10^{-12} \text{ cm}^3 \text{ molecule}^{-1} \text{ s}^{-1}$. A table of these state-resolved rate constants is presented in Table SI of the supplementary material of Ref. [152]. The relative dependence on initial rotational and projection quantum number is strikingly similar to that of the vibrational relaxation cross sections at a collision energy of 300 cm^{-1} (see Fig. 4.8 and Fig. S9 of the supplementary material of Ref. [152]). This similarity is consistent with the parallel energy dependence of the vibrational relaxation cross section from different initial levels (see Fig. 4.7).

The thermal (averaged over initial rotational levels and summed over final rotational levels) vibrational relaxation rate constant for a thermal distribution of rotational levels in vibrational manifold v is given by

$$k^{\text{vib}}(T_t, T_r) = \frac{\sum_{n,k} g_{n_k} \omega_{n_k} k_{n_k}^{\text{vib}}(T_t) e^{-E_{n_k}/k_B T_r}}{\sum_{n,k} g_{n_k} \omega_{n_k} e^{-E_{n_k}/k_B T_r}} \quad (4.15)$$

where T_r is the rotational temperature, and g_{n_k} , ω_{n_k} , and E_{n_k} are the rotational degeneracy, nuclear statistical weight, and energy, respectively, of the level n_k . Although all the quantum numbers refer here to $v = 1$, for simplicity we have suppressed the dagger superscripts. As discussed in Sec. 4.3, there are roughly four times as many *para* levels as

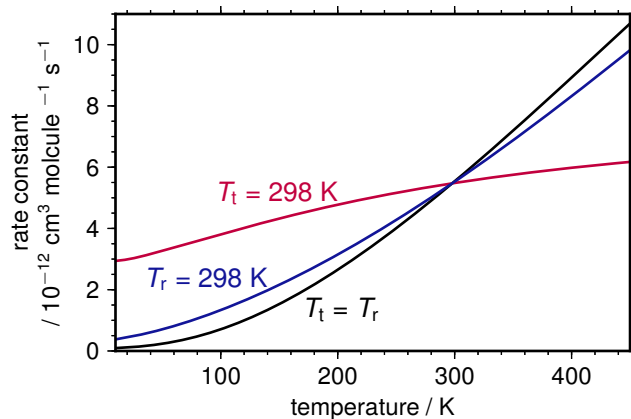


Figure 4.10: Dependence on the rotational and translational temperature of the rotationally-summed vibrational relaxation rate constant for $\text{CH}_3(v=1)$ in collisions with He upon the translational and rotational temperature. The black line assumes equal translational and rotational temperature ($T_t = T_r$); the red line assumes $T_t = 298$ K as T_r is varied; and the blue line assumes $T_r = 298$ K while T_t is varied. The rate constants at selected temperatures are also listed in Table SII of the supplementary material.

ortho levels. In contrast, the nuclear statistical weights w_{n_k} favor the *ortho* levels. These two preferences thus cancel each other out so that the thermal vibrational relaxation rate constants are similar in size for the two nuclear spin modifications.

In evaluating the thermally averaged vibrational rate constant in Eq. (4.15), we included all levels with $E_{n_k} \leq 1900 \text{ cm}^{-1}$ (see Fig. 4.4). For levels of higher energy, convergence of the integral over translational energy in Eq. (4.14) requires calculations at total energies so large that the number of channels required renders the calculations computationally infeasible with available computational resources. However, exploratory calculations confirm that levels with internal energies greater than 1900 cm^{-1} will make only a small contribution to the vibrationally inelastic rate constants at room temperature. Our calculated room-temperature ($T_t = T_r = 298 \text{ K}$) thermally-averaged vibrational $v = 1 \rightarrow 0$ relaxation rate constant equals $5.4 \times 10^{-12} \text{ cm}^3 \text{ molecule}^{-1} \text{ s}^{-1}$. We estimate that we can compute the thermally vibrational relaxation rate constant with reasonable accuracy (*ca.* 10%) within our model up to temperatures less than or equal to 450 K.

We have computed the temperature dependence of the thermal vibrational rate constant [Eq. (4.15)] under various assumptions about the translational and rotational

temperatures. Figure 4.10 displays these calculated rate constants. For relaxation in a cell where $T_t = T_r$, the rate constant increases monotonically with temperature.

To investigate the effects of translational and rotational temperatures separately, we also show the dependence of the thermal vibrational relaxation rate constants upon either the rotational or translational temperature with the other fixed at 298 K. As the translational temperature increase, the distribution of collision energies shifts to higher values. Since the vibrational relaxation cross sections for individual $\text{CH}_3(v_2 = 1)$ rotational levels increase almost linearly with collision energy (see Fig. 4.7), the vibrational relaxation cross section with T_r fixed at 298 K is seen in Fig. 4.10 to increase significantly with the translational temperature. The temperature dependence is nearly the same as when both temperatures are assumed equal. This implies that the collision energy dependence of the vibrational relaxation cross section, summed over final rotational quantum number is very similar. This is indeed the case (Fig. 4.7).

By contrast, the vibrational rate constant obtained with T_t fixed at 298 K has a much weaker dependence on the rotational temperature. We see that the low-temperature limit of this rate constant equals $\sim 3 \times 10^{-12} \text{ cm}^3 \text{ molecule}^{-1} \text{ s}^{-1}$, or approximately the room-temperature rate constants for the lowest rotational levels (see Fig. 4.14). Some numerical values of the rate constants shown in Fig. 4.10 are listed in Table SII of the supplementary material of Ref. [152].

To determine precise rate constants at sub-Kelvin temperatures, where the presence of resonances makes the energy dependence of the cross sections irregular, would require a finer grid in energy than we have used. At temperatures higher than $\sim 500 \text{ K}$, the determination of precise rate constants will require cross sections at even higher total energy and the inclusion of more vibrational levels in the channel basis, beyond the range of currently feasible quantum close-coupling calculations.

4.5 Discussion

In this study, we have extended earlier calculations [81] of the $\text{CH}_3\text{-He}$ PES to include multiple values of the umbrella coordinate (ν_2). Subsequent averaging over products of vibrational wave functions for the umbrella mode allowed us to determine state-to-state relaxation cross sections between the first-excited and ground umbrella states of CH_3 . The dominant anisotropies in the PES which couples these two vibrational manifolds are anti-symmetric with respect to reflection in the CH_3 plane and have a large three-fold repulsive anisotropy due to the equilateral positioning of the three H atoms. These two anisotropies give rise to a strong propensity for collision-induced ro-vibrational transitions involving $\Delta k = 0, \pm 3$. Additionally the vibrational relaxation cross sections are found to have a strong dependence on the degree of rotational excitation of the $\nu_2 = 1$ vibrationally excited CH_3 , as well as on the body-frame orientation of the initial rotational level. Preferential ro-vibrational relaxation occurs for molecules that are cartwheeling ($k = 0$) rather than pinwheeling ($k \sim \pm n$) with respect to the principal axis of the molecule.

We predict a room-temperature rate constant for relaxation of the $\nu_2 = 1$ vibrational level of $5.4 \times 10^{-12} \text{ cm}^3 \text{ molecule}^{-1} \text{ s}^{-1}$ (see Sec. 4.4.3). This is almost two orders of magnitude smaller than the rate constants for rotational relaxation within both the $\nu_2 = 0$ and 1 vibrational manifolds, which equal $\sim 2.0 \times 10^{-10} \text{ cm}^3 \text{ molecule}^{-1} \text{ s}^{-1}$ for the lower rotational levels (see Sec. 4.4.1 and Ref. [81]). The overall anisotropy of the $\text{CH}_3\text{-He}$ interaction is changed little upon excitation of the umbrella mode. Thus the coupling between different vibrational states of the umbrella mode is weak, compared to the coupling within a vibrational manifold.

Several experimental investigations have addressed the collisional vibrational relaxation of CH_3 . Callear and van den Bergh [175] (CvB) followed the concentration of the ground vibrational level of methyl through UV absorption after broadband flash photolysis of $\text{Hg}(\text{CH}_3)_2$. They estimated that 85% of the radicals are formed vibra-

tionally excited and determined a room-temperature vibrational relaxation rate constant of $8(\pm 2) \times 10^{-13} \text{ cm}^3 \text{ molecule}^{-1} \text{ s}^{-1}$ for collisions with He. They suggested that this relaxation corresponds to the collisional decay of the umbrella-excited levels.

Baughcum and Leone [177] investigated the internal excitation of the CH_3 radical in the 248 nm photolysis of $\text{Hg}(\text{CH}_3)_2$ and deduced that it possessed considerable ν_2 and ν_3 excitation. They also determined the nascent vibrational state distribution of ν_3 levels. Donaldson and Leone [178] employed infrared fluorescence detection to investigate relaxation of $\text{CH}_3(\nu_3)$ levels in collisions with He. For this process they determined a relaxation rate constant of $2.6(\pm 0.5) \times 10^{-13} \text{ cm}^3 \text{ molecule}^{-1} \text{ s}^{-1}$.

Rudolph, Hall, and Sears [179] measured vibrational relaxation rate constants of CD_3 produced in the 193 nm photolysis of acetone- d_6 and compared these with the corresponding rate constants for CH_3 . They observe that the collisional filling of the CD_3 ground vibrational level in the photodissociation of acetone- d_6 is significantly slower than the corresponding filling [175] of CH_3 in the photodissociation of $\text{Hg}(\text{CH}_3)_2$. It is expected [187] that the $V \rightarrow R, T$ relaxation probabilities should increase as the energy of the lowest excited level decreases. Since the lowest vibrational level in the perdeuterated isotopomer is lower in energy, we expect that relaxation of CD_3 would be faster, contrary to the reported relaxation measurements. This could be due to differences in the ro-vibrational spacings in the two isotopomers or to the role of $V \rightarrow V$ relaxation in the experiment, where higher umbrella levels are produced initially.

Our computed room-temperature rate constant for the collisional relaxation of CH_3 in collisions with He is significantly larger than the relaxation rate constant reported by CvB [175]. The discussion in the preceding two paragraphs raises the possibility that the measurement of CvB does not pertain specifically to the relaxation of $\text{CH}_3(\nu_2 = 1)$. In addition, our neglect of zero-point motion in the other vibrational degrees in methyl, and the neglect of vibrational inelasticity associated with all modes except for the umbrella motion, could introduce some error. In particular, since the $\nu_4 = 1$ vibrational level lies

only 790 cm^{-1} above the $\nu_2 = 1$ vibrational level, excitation of the $\nu_4 = 1$ level could occur at the higher collision energies which contribute to the relaxation rate constant for $\text{CH}_4(\nu_2)$.

To our knowledge, there have been no prior investigations, either quantum or classical, of state-resolved ro-vibrational relaxation of a polyatomic. We have demonstrated here that it is now possible to carry out high quality quantum simulations of the ro-vibrational relaxation of CH_3 (or, for that matter, other small hydride radicals). We encourage new studies of the relaxation of the umbrella mode in this molecule, to test the accuracy of these theoretical simulations. Also, our work can serve as a valuable benchmark for the calibration of more approximate treatments of the dynamics of ro-vibrational relaxation.

Chapter 5

Rotational Inelastic Scattering of Methyl Radicals with He and Ar

This chapter contains excerpts of a paper titled “Rotationally inelastic scattering of CD_3 and CH_3 with He: comparison of velocity map-imaging data with quantum scattering calculations” by Ondřej Tkáč, Alan G. Sage, Stuart J. Greaves, Andrew J. Orr-Ewing, Qianli Ma, Paul J. Dagdigian, and Millard H. Alexander, originally published on *Chem. Sci.* [200] under a Creative Commons Attribution 3.0 Unported License.

This chapter contains excerpts of an unpublished manuscript titled “Rotationally inelastic scattering of methyl radicals with Ar and N_2 ”, by Ondřej Tkáč, Qianli Ma, Martin Stei, Andrew J. Orr-Ewing, and Paul J. Dagdigian.

The experimental work described in this chapter was carried out by our collaborators at the University of Bristol.

5.1 Introduction

The methyl radical (CH_3) is a planar symmetric top molecule of particular interest in combustion chemistry [5, 201], material chemistry [202, 203], and astrophysics [204–207]. The study of the interaction between CH_3 and other atoms or molecules could extend our knowledge of molecular interactions beyond the well documented atom-diatomic molecule interactions.

The inelastic scattering of labile free radicals using molecular beams and laser spectroscopic techniques was reviewed in the mid 1990's [9, 74, 208]. However, considerable advances have been made since then using methods such as ion imaging [14] and velocity map imaging (VMI) [15] with laser spectroscopic detection of the final levels. Most of these experimental studies have concentrated on scattering dynamics of diatomic radicals, with spectroscopic probes used to measure state-resolved integral cross sections (ICSs), and more recently differential cross sections (DCSs). The most extensively studied free radicals have been NO [18, 23, 209–221] and OH [96, 97, 100, 103, 222–226], the latter because of its important role in atmospheric chemistry, astrochemistry and combustion. Sarma *et al.* [227] recently used VMI to obtain fully quantum-state-specified product angular distributions for OH scattered by He and Ar.

Nevertheless, measurements of DCSs for inelastic scattering of free radicals other than NO and OH are rare, and to the best of our knowledge have not been reported for reactive radicals larger than these diatomics. Macdonald and Liu [228, 229] and Lai *et al.* [230] examined the inelastic scattering of the linear triatomic NCO radical with He and Ar, respectively, but concentrated on ICSs for spin-orbit conserving and spin-orbit changing collisions. ICSs have also been reported for rotationally inelastic collisions of NH₂ with He [231]. Greater attention has been paid to the inelastic scattering of closed-shell triatomic and polyatomic molecules, as illustrated by determinations of DCSs for scattering of ammonia [232–234] and deuterated ammonia [17] with rare gases and molecular hydrogen, and for water with helium [20] and hydrogen [21].

Along with advances in experimental techniques, there have been many quantum scattering calculations of ICSs, and also DCSs, employing high-quality potential energy surfaces (PESs). These have mostly concerned collisions of diatomic and stable polyatomic molecules [19–21, 96, 97, 100, 103, 214, 217, 220, 223–226, 232]. A recent article by Dagdigian [27] reviewed collisional energy transfer calculations for small hydrocarbon intermediates, and highlighted computational studies of integral cross sections (ICSs) for

collisions of methylene (CH_2) [235, 236] and methyl radicals [81, 152]. The pathways for energy transfer in collisions of a polyatomic are more complicated than for collisions of a diatomic molecule. There is only one type of anisotropy in an atom-diatom interaction, namely the difference in interaction energy for end-on vs. side-on approach. By contrast, for collisions of a nonlinear polyatomic molecule there are two types of anisotropies, corresponding to approach of the collision partner in or perpendicular to the molecular plane.

Dagdikian and Alexander [81] recently used quantum scattering calculations to investigate rotational energy transfer of methyl in collisions with a helium atom through quantum scattering calculations on a computed PES. This PES was calculated with a coupled-cluster method that includes all single and double excitations, as well as perturbative contributions of connected triple excitations [RCCSD(T)]. Because of the anisotropy of the PES due to the repulsion of the He atom by the three H atoms on methyl, a strong propensity was found for $\Delta k = \pm 3$ transitions, where k is the body-frame projection of the rotational angular momentum n .

In the present work, DCSs for collisions of CH_3 and CD_3 with He and Ar are experimentally determined through the use of crossed molecular beam (CMB) and VMI methods. The measured DCSs are compared with quantum scattering calculations that use a previously published CH_3 -He PES [81, 152], and a newly-computed CH_3 -Ar PES. Comparison between experiment and theory at the level of state-resolved DCSs critically tests the influence of both short-range repulsive and long-range attractive intermolecular interactions. Anticipating this comparison, excellent agreement is found between the measured and computed state-to-state DCSs, thus providing important confirmation on the accuracy of the computed PESs. We also compare the ICSs and DCSs for the collision of CD_3 with He and Ar, and discuss the connection between the PESs and scattering dynamics.

This chapter is organized as follows: Sections 5.2.2 and 5.2.3 present, respectively,

a brief description of the rotational levels of CH₃ and CD₃, specifically the different nuclear spin modifications, and the spectroscopic intricacies of the detection scheme. Section 5.2.4 describes the details in creating the CH₃-Ar PES. Section 5.2.5 describes the close-coupling scattering calculations. Sections 5.3.1–5.3.3 present and compare the measured and theoretical cross sections for the CD₃-He, CH₃-He, and CD₃-Ar collisions, respectively. Discussion and conclusions sections then follow.

5.2 Method

5.2.1 Experimental Apparatus

Measurement of DCSs for the inelastic scattering of CD₃ with He and Ar used a compact crossed molecular beam apparatus with VMI. Details of the apparatus and the analysis of the experimental images is described in Ref. [200] and will not be shown here.

5.2.2 Rotational Levels of CH₃ and CD₃

In this subsection, we briefly describe the rotational levels of the CH₃ and CD₃ radicals, and their nuclear spin symmetries. The rotational energies for the lower levels of CH₃ and CD₃ are plotted in Fig. 5.1 and are described below. The methyl radical is an oblate symmetric top, with rotational quantum numbers n and body-frame projection k . Because the three H(D) atoms are equivalent, the ground vibronic state of CH₃ has two nuclear spin modifications, labelled *ortho* and *para* [81]. The *ortho* levels have nuclear spin symmetry A_1 and include rotational levels for which k is a multiple of 3 ($k = 0, 3, 6, \dots$). In particular, the rotational levels with $k = 0$ and odd n do not exist for the ground vibronic state. The *para* levels have nuclear spin symmetry E and include all rotational levels for which k is not a multiple of 3 ($k = 1, 2, 4, 5, \dots$).

There are three nuclear spin modifications in CD₃. The A_1 nuclear spin functions are those with rotational levels with $k = 0$ and odd n and with levels for which k is a

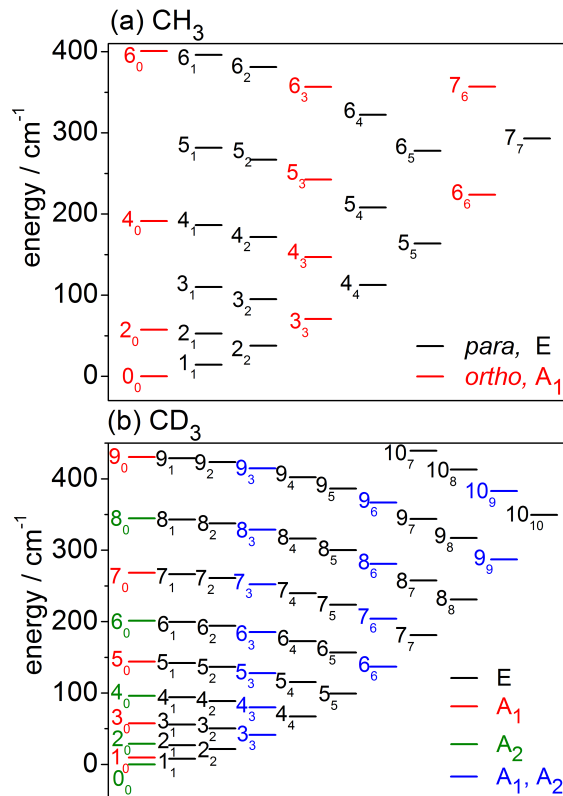


Figure 5.1: Rotational energy level diagrams for the ground vibrational level of the \tilde{X}^2A_2'' electronic state of (a) CH_3 and (b) CD_3 . Levels are labelled by n and (subscript) k . The color coding identifies the different nuclear spin modifications.

multiple of 3. The A_2 nuclear spin functions correspond to rotational levels with even n and $k = 0$, and also with levels for which k is a multiple of 3. Thus, rotational levels with $k = 3, 6, \dots$ are doubly degenerate (A_1 and A_2). Finally, the E nuclear spin functions include all levels for which k is not a multiple of 3.

5.2.3 Initial State Distribution of CD_3 and the REMPI Detection

(2 + 1) REMPI detection of inelastically scattered CD_3 or CH_3 radicals used the well-established scheme of excitation via the 0_0^0 band of the $4p^2A_2'' \leftarrow \tilde{X}^2A_2''$ transition [237, 238]. Determination of rotational level populations in the incident radical beam required comparison of experimental REMPI spectra with spectra simulated using the PGOPHER program [239]. The simulation incorporated the effects of nuclear spin

statistics of the three equivalent H or D atoms. The procedures used are described in the supplementary materials of Ref. [200]. The distribution of methyl radicals in the beam correspond to a rotational temperature of ~ 15 K, and relative populations of the rotational levels were presented in Table 1 of Ref. [200]. The ro-vibrational levels of the excited electronic state are predissociated, resulting in broader linewidths and poorer detection efficiencies for the CH₃ isotopologue than for CD₃. Therefore, the work presented here concentrates on the inelastic scattering of CD₃.

The REMPI spectral lines for methyl are resolved in the n rotational quantum number, but not in the k projection quantum number, and the k projection levels of a given n contribute differently to different Δn spectroscopic branches. We denote the unresolved n_{k_1}, n_{k_2}, \dots levels associated with a particular spectroscopic transition by $n_{k_1 k_2 \dots}$ and recognize that these levels all contribute to the measured DCSs. The relative contributions of the different k levels were determined by PGOPHER calculation of 2-photon line strength factors.

5.2.4 Potential Energy Surface

Since the center of mass of methyl is at the carbon atom, a same PES can be used for the scattering calculations of CH₃-He/Ar and CD₃-He/Ar. For the collisions of methyl with He, a previously computed PES [81] was used. For the collisions with Ar, we created a new *ab initio* PES. The details of this PES is presented below.

Similar to the treatment of CH₃-He, we describe the geometry of the CH₃-Ar rigid rotor complex by three coordinates, the intermolecular separation R , and two angles θ and ϕ . The two angles corresponds to the polar and azimuthal angle of the position of Ar in the CH₃ molecule-fixed frame.¹ This coordinate system is illustrated in Fig. 1 of Ref.

¹The theory for the rotationally inelastic collision of a symmetric top and a linear molecule in $^1\Sigma$ state described in Chapter 6 can also be applied for the present system. This is achieved by ignoring the θ_2 and ϕ_2 coordinates, and setting $l_2 = 0$. The variables, R , θ , and ϕ in this work is equivalent to R , θ_1 , and ϕ_1 defined in Chapter 6, respectively.

[81]. As in the CH₃-He case, the potential can be expanded with²

$$V(R, \theta, \phi) = \sum_{l_1, \mu_1 \geq 0} V_{l_1 \mu_1}(R) \left[Y_{l_1 \mu_1}(\theta, \phi) + (-1)^{\mu_1} Y_{l_1, -\mu_1}(\theta, \phi) \right]. \quad (5.1)$$

The three-fold symmetry of CH₃ requires that μ_1 be a multiple of 3, and the planar geometry of CH₃ requires that $l_1 + \mu_1$ be even [81].

We performed the explicitly correlated restricted coupled-cluster calculations with inclusion of single, double, and (perturbative) triple excitations [RCCSD(T)-F12a] [51–53] for the CH₃-Ar PES. We employed the augmented correlation-consistent basis set aug-cc-pVTZ (aVTZ) [240, 241]. A counterpoise correction was applied to correct for basis-set superposition error [56, 57]. All calculations were carried out with the MOLPRO 2012.1 suite of programs [151]. To check the accuracy of the *ab initio* calculations, we performed additional calculations on 10 random orientations each at 7 atom-molecule distances. We found the RCCSD(T)-F12a/aVTZ method gives interaction energies closer to the CBS limit [extrapolated from conventional RCCSD(T) calculations with the aVDZ, aVTZ, and aVQZ basis sets] at short to moderate R compared with the RCCSD(T)/aVQZ calculation with a mid-bond function [49, 50] added to the basis set. In addition, the former method is less computationally demanding.

The CH₃-Ar interaction energies were determined on a three-dimensional grid. The R grid includes 33 R 's (3.5 to $9a_0$ in steps of $0.25a_0$, 9.5, 10, 11, 12, 13, 14, 15, 16, 18, and $20a_0$). The θ grid contains 11 values from 0° to 90° defined by $\cos \theta = 0$ to 1 in steps of 0.1. The ϕ grid contains 7 values ranging from 0° to 60° in steps of 10° . The total number

²Equation (5.1) can be written alternatively, in terms of the reduced rotation matrix [28], as

$$V(R, \theta, \phi) = \sum_{l_1 \mu_1 \geq 0} V_{l_1 \mu_1}(R) (2 - \delta_{\mu_1, 0}) \left(\frac{2l_1 + 1}{4\pi} \right)^{\frac{1}{2}} d_{\mu_1, 0}^{l_1}(\theta_1) \cos \mu_1 \phi.$$

It can be shown that the relation between the V coefficients and the B coefficients defined in Chapter 6 is given by

$$B_{l_1 \mu_1}(R, \theta_1, \phi_1) = \pi (1 + \delta_{\mu_1, 0}) V_{l_1 \mu_1}(R, \theta_1, \phi_1).$$

The above equation is only valid for the collisions between a symmetric top and a structureless atom.

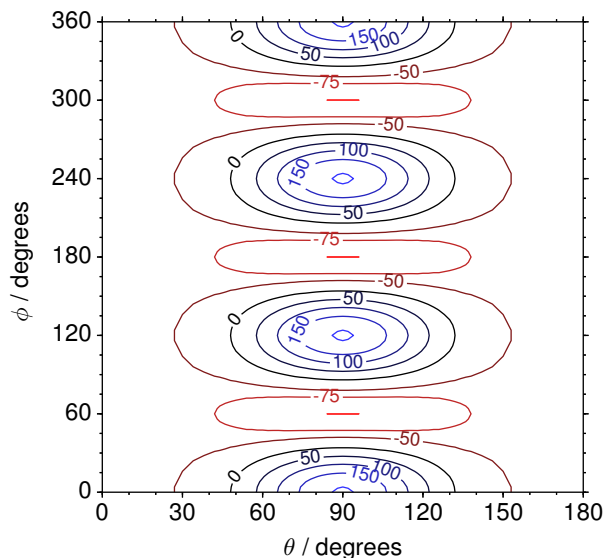


Figure 5.2: Dependence of the CH₃-Ar potential energy (in cm⁻¹) on the orientation (θ, ϕ) at $R = 6.75 a_0$.

of geometries for which the interaction potential was computed was 2541. For all the computations, C-H bond length is fixed at $r_0 = 1.078 \text{ \AA}$, which is the equilibrium bond length from CCSD(T)/aug-cc-pVQZ calculations [81].

In fitting the PES, we used all symmetry-allowed (l_1, μ_1) terms with $l_1 \leq 12$. The *ab initio* points were fitted with this 19-term angular basis using the least-squares method. The quality of the fit is good. For all $R > 4.5 a_0$, the RMS of the fit is less than 1% of the absolute value of *ab initio* interaction energies averaged over the 77 orientations. At long range, the four larger terms B_{00} , B_{33} , B_{20} , and B_{40} are extrapolated to AR^{-n} , with A and n determined from the fitted coefficients at $R = 18 a_0$ and $20 a_0$. The n obtained for the four terms are 6.36, 6.29, 7.92, and 7.35, respectively. The expansion coefficients for the isotropic term is much larger (by at least 20 times, at $R = 20 a_0$) than other terms at large R . $R^{-6.36}$ dependence is a reasonable approximation to the isotropic term of the dispersion interaction ($c_6 R^{-6} + c_8 R^{-8} + \dots$ [73]), confirming that the CCSD(T)-F12a interaction energies have a reasonable long-range behavior. All other terms were damped to zero beyond $R = 20 a_0$. The fitted coefficients was switched to long range ones with a switching function centered at $R = 18 a_0$ to ensure their smoothness over R .

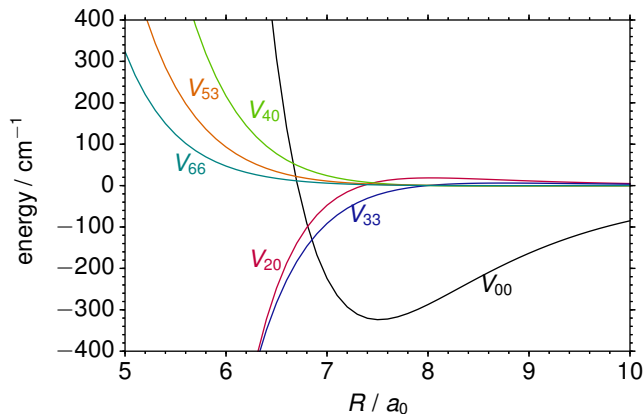


Figure 5.3: Dependence of the larger expansion coefficients v_{l_1, μ_1} [defined in Eq. (5.1)] on the CH₃-Ar separation R .

Figure 5.2 shows a contour plot of the PES at $R = 6.75 a_0$. Similar to the CH₃-He PES (Fig. 3 in Ref. [81]), the CH₃-Ar PES has a three-fold symmetry about ϕ , with maximum repulsion at orientation near the location of the hydrogen atoms. The potential is most attractive when Ar is in the plane of CH₃ bisecting a C-H-C angle. The global minimum of the CH₃-Ar PES is at $R = 7.13 a_0$, $\theta = 90^\circ$, $\phi = 60^\circ$, with a dissociation energy $D_e = 120.1 \text{ cm}^{-1}$. Different from the CH₃-He PES, at $R = 6 a_0$ the CH₃-Ar potential is repulsive for all orientations. The latter PES has a global minimum at a smaller R ($6.52 a_0$) with a much smaller D_e (27.0 cm^{-1}) [81].

We show in Fig. 5.3 a plot of the larger expansion coefficients V_{l_1, μ_1} as a function of the CH₃-Ar separation. Similar to the CH₃-He PES (Fig. 4 of Ref. [81]), the isotropic V_{00} term dominates at moderate to long range, and the V_{33} and V_{20} terms are largest isotropic terms at short to moderate range. In fact, the anisotropic properties of the two PESs are almost identical. The major difference lies at the larger magnitudes of the expansion coefficients (or stronger interactions), and slightly larger atom-molecule separation at which the minimum in the V_{00} term occurs, for the CH₃-Ar PES.

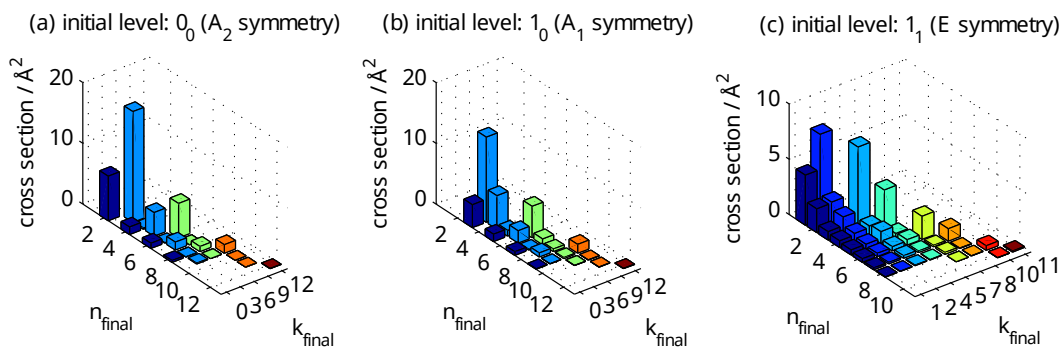


Figure 5.4: Integral cross sections for transitions out of the lowest CD_3 levels of each nuclear spin symmetry in collisions with Ar at a collision energy of 440 cm^{-1} .

5.2.5 Quantum Scattering Calculations

We used the HIBRIDON suite of programs [31] to carry out fully quantum, close-coupling, state-resolved differential cross sections for collisions of methyl with He and Ar. Rotational energies of CD_3 were computed with a rigid rotor symmetric top Hamiltonian using spectroscopic studies by Sears *et al.* [242]. Spin-rotation splitting and hyperfine splittings were ignored. Rotational levels whose energies were less than 1100 cm^{-1} for $\text{CH}_3\text{-He}$, and 1000 cm^{-1} for $\text{CH}_3\text{-Ar}$ were included in the channel basis, and the calculations included total angular momenta $J \leq 130\hbar$. The convergence of the cross sections were carefully checked.³ Since the CH_3/CD_3 incident beam contained several rotational levels, and the k quantum number is not resolved in REMPI spectra, the computed DCSs were weighted over initial levels with $n \leq 3$ according to a Boltzmann distribution described in Sec. 5.2.3 and over final levels according to the 2-photon line strengths factor for the given detection line.

For a comparison with the ICSs of the $\text{CD}_3\text{-Ar}$ and $\text{CD}_3\text{-He}$ collisions, we present in Fig. 5.4 computed state-resolved ICSs for transitions out of the 0_0 (A_2 nuclear spin symmetry), 1_0 (A_1 symmetry), and 1_1 (E symmetry) levels of CD_3 in collisions with Ar at a collision energy of 440 cm^{-1} . We notice the propensities of the transitions are almost identical to that for the $\text{CD}_3\text{-He}$ collisions (Fig. 5 of Ref. [243]). For both 0_0 and 1_0 initial

³The $\text{CD}_3\text{-Ar}$ system has a much larger reduced mass than $\text{CD}_3\text{-He}$. The integration steps in solving the CC equations need to be smaller for the former system to get converged cross sections.

levels, the largest cross section is found for the transition to the 3_3 level, and for the 1_1 initial level to the 2_2 and 4_4 levels. All these transitions are directly coupled by the V_{33} term of the PES. Comparing with the $\text{CD}_3\text{-He}$ PES, the relative magnitude of the V_{20} term is slightly larger in the $\text{CD}_3\text{-Ar}$ PES. However, we do not observe significant changes in the relatively small cross sections for $\Delta k = 0$ transitions, enabled by V_{20} and other $\mu_1 = 0$ terms. The larger $\text{CD}_3\text{-Ar}$ ICSs shown in Fig. 5.4 are approximately twice the $\text{CD}_3\text{-He}$ ICSs for the same transition. This is consistent with the stronger interaction between CD_3 and Ar.

5.3 Results

5.3.1 DCSs for $\text{CD}_3\text{-He}$ Collisions

The $\text{CD}_3\text{-He}$ collision energy was calculated to be $440 \pm 35 \text{ cm}^{-1}$, from the measured beam velocities. Figure 5.5 displays the determined DCSs for final levels $n' = 2\text{-}4$, while Fig. 5.6 presents the DCSs for $n' = 5\text{-}9$. In both figures, the unresolved k' projections are specified for each n' -resolved DCS. Also shown in Figs. 5.5 and 5.6 are theoretical DCSs. The experimental DCSs are not shown for $\theta < 30^\circ$ for final levels with $n' = 2$ and 3 and for $\theta < 20^\circ$ for final levels with higher n' because of contributions to these angles from unscattered radicals in the parent beam, as discussed above. The calculated DCSs show pronounced diffraction oscillations in this strongly forward scattered region. Unfortunately, even with greater initial state purity the angular resolution of the experiments would be insufficient to resolve these structures clearly. The experimental angular resolution is limited by the velocity and angular spreads of the two molecular beams. For the current experiments on the $\text{CD}_3\text{-He}$ system, this angular resolution ranges varies from 3 to 16° depending on the scattering angle.

For quantitative comparison with the theoretical calculations, the experimental angular distributions are normalized by scaling the experimental value at a 90° scattering

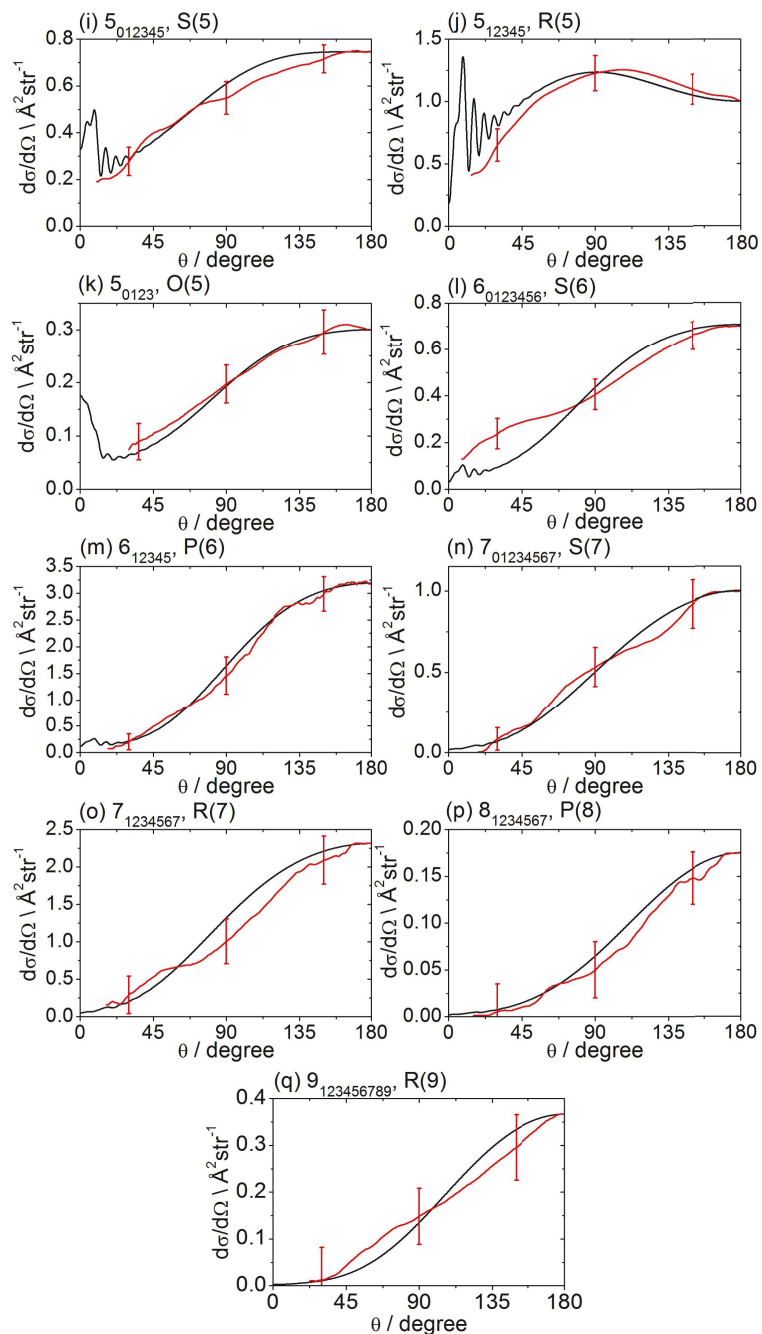


Figure 5.6: DCSs for inelastic scattering of CD_3 radicals by He at a collision energy of $440 \pm 35 \text{ cm}^{-1}$ into final rotational levels $n' = 5-9$. The REMPI line employed for detection is indicated, along with the range of k' projection levels contributing to the scattering. Red curves: DCSs determined from the measured images; black curves: theoretical DCSs. The method of normalization of the experimental DCSs is described in the main text.

angle for levels with $n' \leq 4$, or 180° for higher n' states, to match the theoretical value at that angle. These choices correspond to angles with adequate experimental signal levels. The error bars associated with the experimental DCSs were determined by combining the standard deviation determined from comparison of several (typically 3) measured images for a single final state with the uncertainty introduced by application of the density-to-flux transformation. The latter factor was quantified by comparing DCSs extracted from the two halves of the image separated by the relative velocity vector (which should be symmetric after perfect transformation). The theoretical DCSs reproduce satisfactorily all the features of the measured DCSs to within the experimental uncertainty. The n' -dependent DCSs are a sensitive probe of both attractive and repulsive parts of the potential. The near quantitative agreement for all final n' levels confirms the high quality of the calculated *ab initio* PES [81] and to the accuracy of the close-coupling treatment of the scattering dynamics.

5.3.2 DCSs for CH₃–He Collisions

The collision energy of $425 \pm 35 \text{ cm}^{-1}$ for inelastic scattering of CH₃ radicals (seeded in excess Ar) with He is the same as for the scattering of CD₃ by He. The spectroscopic lines for CH₃ are also not resolved in the k projection quantum number, although the spacings between the lines detecting different k levels of the same n are larger than for CD₃. In addition, the CH₃ REMPI transitions are more broadened by predissociation of the intermediate Rydberg state, which lowers the detection efficiency. Consequently, velocity map images for CH₃ scattering were recorded only for the three strongest spectroscopic lines.

The DCSs derived from the density-to-flux transformation and normalized to the theoretical DCSs are presented in Fig. 5.7. In two of the panels in Fig. 5.7, experimental DCSs derived from images accumulated on different days are compared. We see that these DCSs lie almost entirely on top of each other, which demonstrates excellent reproducibility.

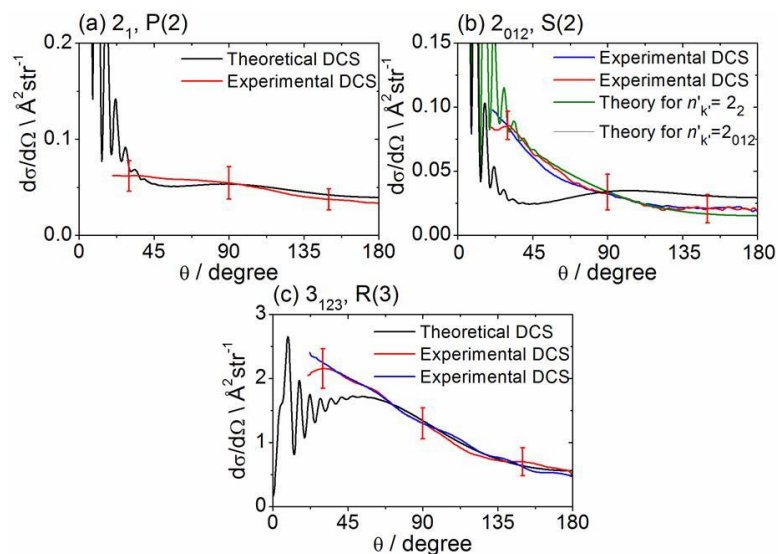


Figure 5.7: DCSs for inelastic scattering of CH_3 radicals by He at a collision energy of $425 \pm 35 \text{ cm}^{-1}$ into final rotational levels $n' = 2, 3$. The REMPI line employed for detection is indicated, along with the range of k' projection levels contributing to the scattering. Panels (b) and (c) also compare experimental DCSs for repeat measurements made on different days to demonstrate the reproducibility of the experimental determinations.

Figure 5.7 also compares these experimental DCSs with theoretical calculations. There is an agreement for the $n'_{k'} = 3_{123}$ and 2_1 final levels, except for small angle scattering. However, the experimental DCS for scattering into $n'_{k'} = 2_{012}$ does not agree with the comparable theoretical DCS, computed under the assumption that the probe laser excites all three k' projection levels. Careful examination of the 2-photon transition wavenumbers reveals that these lines are separated by more than their widths. If we assume that the $k' = 2$ level was preferentially excited, then we obtain good agreement of the computed DCS [green curve in Fig. 5.7(b)] with the experimental DCS.

5.3.3 DCSs for CD_3 -Ar Collisions

Higher mass of Ar atom and lower velocity of the Ar beam with respect to He results in smaller mean collision energy $E_{\text{col}} = 330 \pm 25 \text{ cm}^{-1}$. The derived DCSs are shown in Figs. 5.8 and 5.9 where they are compared with theoretical DCSs from the close-coupling scattering calculations. For quantitative comparison with the theoretical calculations, the

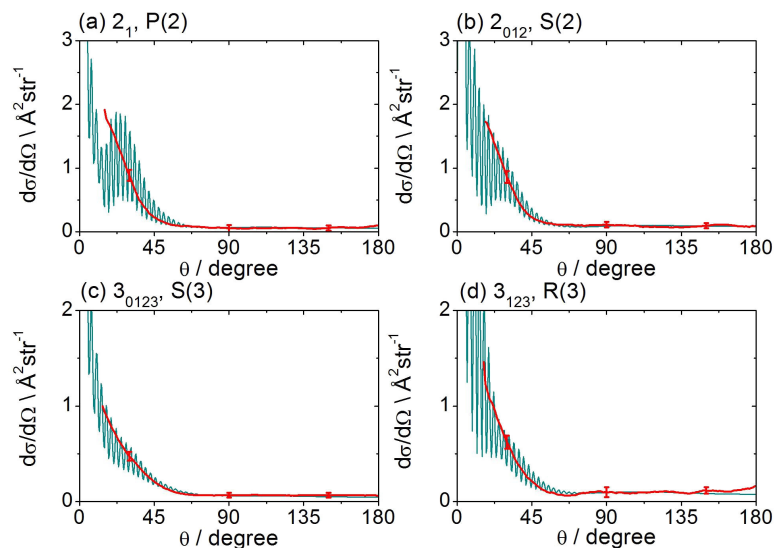


Figure 5.8: DCSs for inelastic scattering of CD₃ radicals by Ar at a collision energy of 330 ± 25 cm⁻¹ into final rotational levels $n' = 2, 3$. Red curves: DCSs determined from the measured VMI images; cyan curves: theoretical DCSs. The REMPI line employed for detection is indicated.

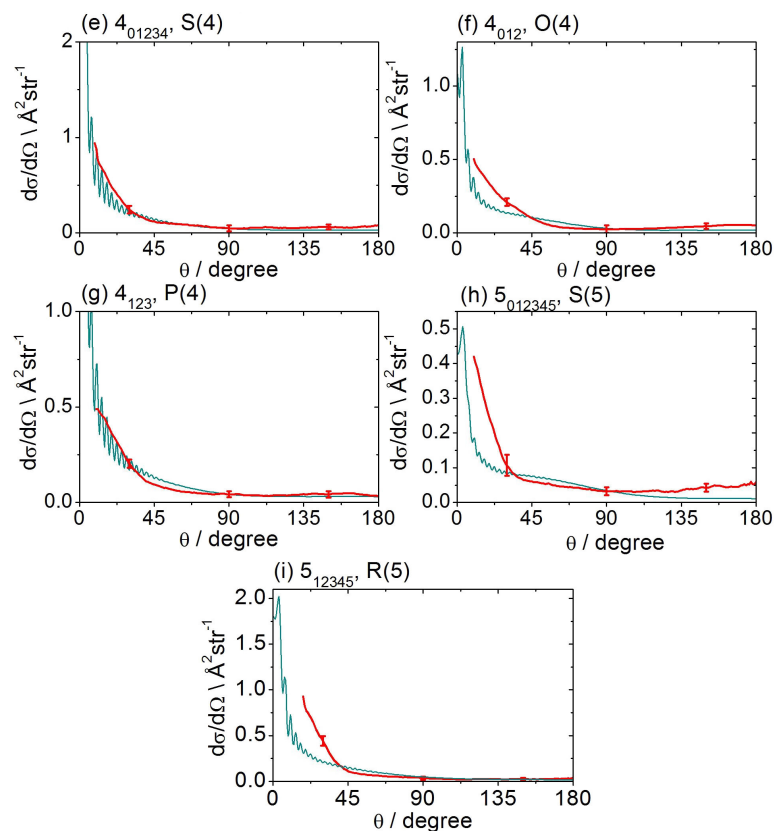


Figure 5.9: DCSs for inelastic scattering of CD₃ radicals by Ar at a collision energy of 330 ± 25 cm⁻¹ into final rotational levels $n' = 4, 5$. Red curves: DCSs determined from the measured VMI images; cyan curves: theoretical DCSs. The REMPI line employed for detection is indicated.

experimental DCSs were normalized by scaling the experimental value at a scattering angle of 90° to match the theoretical value at the same angle. The CD_3 molecules are almost exclusively scattered into the angular region $\theta \leq 60^\circ$ in collisions with Ar for all measured final levels with final rotational angular momentum up to $n' = 5$.

5.4 Discussion

The agreement between the experimental and theoretical DCSs for scattering of methyl with He and Ar lends considerable confidence to the quality of the theoretical treatment outlined in Secs. 5.2.4 and 5.2.5. We can therefore derive insights into the scattering dynamics not only from comparison with experiment, but also by analysis of the calculated, fully state resolved DCSs.

For the collision of both CD_3 and CH_3 with He, the angular distributions for transitions into $n' = 2-4$ (averaged over k') where the degree of translational to rotational energy transfer is small peak in the forward hemisphere, whereas those with $n' \geq 5$ (i.e., intermediate to large energy transfer) are predominantly sideways and backwards scattered. For the collision of CD_3 with He, the degree of backward scattering increases steadily with increasing n' , and hence with Δn , because the initial levels of CD_3 populated have mostly $n = 1$ (Table 1 of Ref. [200]). When Ar is the collision partner, CD_3 molecules are almost exclusively scattered into the angular region $\theta \leq 60^\circ$. The weak sideways and backward scattering is slightly enhanced for larger Δn collisions.

Similar behaviour is observed in the inelastic scattering of atoms such as He with diatomic molecules [19, 244, 245], and reveals that low impact parameter collisions are necessary for large changes in the rotational angular momentum. Classically, the rotational angular momentum of the molecule is induced by a torque that acts on the molecule for the duration of the collision [187]. The magnitude of the torque is proportional to the gradient of the intermolecular potential, which is largest at short range.

There are subtle differences in the shapes of the DCSs obtained for CD_3 detection in

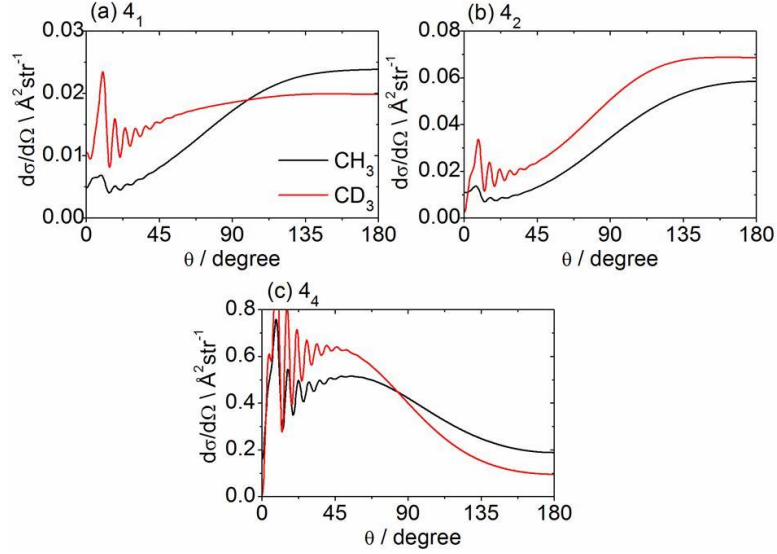


Figure 5.10: Theoretical state-to-state CH_3/CD_3 -He inelastic DCSs out of the level $n_k = 1_1$ into levels with $n' = 4$, at a collision energy of 4400 cm^{-1} .

a single n' level via different spectroscopic transitions. For example, the DCSs for $n' = 4$, obtained from measurements using the S(4), P(4) and O(4) REMPI lines, for both CD_3 -He (Fig. 5.5) and CD_3 -Ar (Fig. 5.9), differ slightly in shape. The three transitions probe respectively k' projections 0-2, 1-3, and 0-4. Changes in the scattering dynamics leading to population of different k' sub-levels for a given n' level can be explored by examination of the true state-to-state DCSs obtained from the QM scattering calculations. Figures 5.10 and 5.11 compare the computed DCSs for CD_3/CH_3 -He and CD_3 -Ar, respectively, for scattering from the initial state $n_k = 1_1$ into the $n' = 4$, $k' = 1, 2$ and 4 final levels. While the DCSs show significant variation with k' when He is the collision partner, such variation is more subtle for the CD_3 -Ar system.

We now compare the difference in the collision dynamics between the CD_3 -He and CD_3 -Ar systems. Figure 5.12 shows computed DCSs for inelastic scattering of CD_3 out of the $n_k = 1_0$ initial level into 3_3 and 5_0 final levels with both Ar and He as collision partners at the same collision energy of 440 cm^{-1} . We find the computed DCSs for the CD_3 -Ar system at a collision energy of 440 cm^{-1} are not much changed from those obtained 330 cm^{-1} . This is not unreasonable considering the steep repulsive wall in the

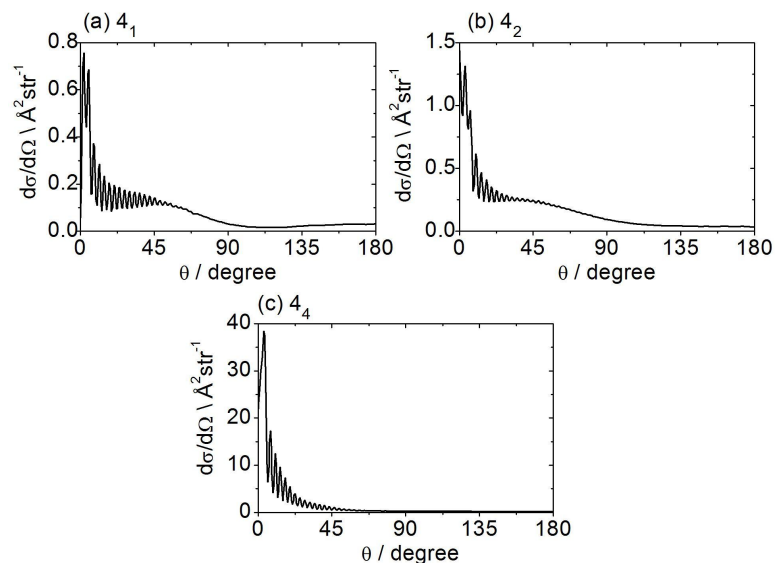


Figure 5.11: Theoretical state-to-state CD_3 -Ar inelastic DCSs out of the level $n_k = 1_1$ into levels with $n' = 4$, at a collision energy of 330 cm^{-1} .

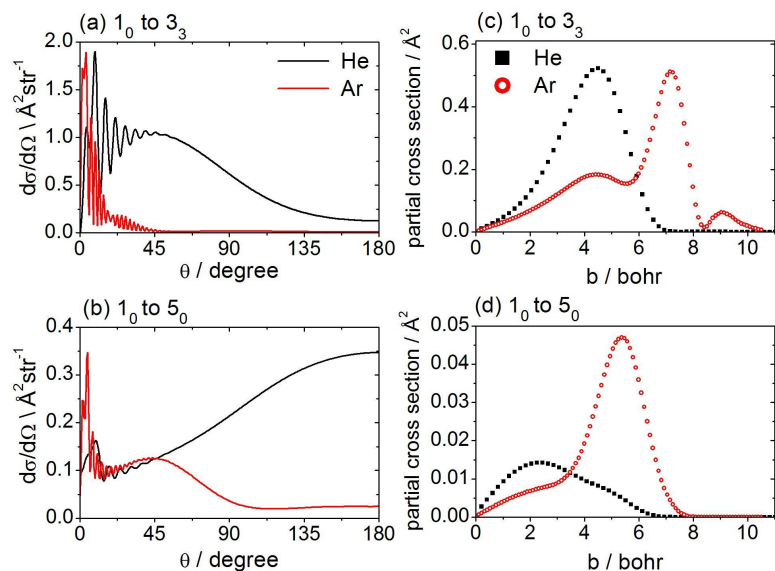


Figure 5.12: (a)-(b) Computed state-to-state DCSs and (c)-(d) corresponding partial cross sections for inelastic scattering of CD_3 out of the 1_0 rotational level into 3_3 and 5_0 final levels in collisions with Ar and He at a collision energy of 440 cm^{-1} . The DCSs for CD_3 -Ar were normalized to the same maximum value as the CD_3 -He DCS.

CH_3 -Ar PES.

We see from Fig. 5.12 that the spacings of the diffraction oscillation evident at small scattering angles are smaller for the CD_3 -Ar system than for CD_3 -He because of the larger mass of the collider Ar and the larger impact parameter [22]. In a simplified hard-

sphere model, the spacing of the differential oscillations $\Delta\theta$ in atom-molecular collisions is approximately given by $\pi/(kb)$ [246], where k is the wavenumber and would be smaller for a collision system with a larger reduced mass under a same collision energy.

The most striking difference between the CD_3 -Ar and CD_3 -He DCSs is the much greater propensity for forward scattering for the former. Indeed scattering into angles $\theta < 90^\circ$ dominates the measured and computed DCSs, whereas for collisions of CD_3 with the lighter He atoms the scattering extended across the full range of angles up to 180° , as demonstrated in Fig. 5.12(a), and peaked in the sideways or backward directions for $n' \geq 4$ [Fig. 5.12(b)]. The origin of these differences lies in the PESs that governs the scattering dynamics.

To better visualize the differences between the CH_3 -He and CH_3 -Ar PESs, we plot in Fig. 5.13 the dependence of the potential averaged over θ upon R and ϕ , shown as contours on the plane containing the CH_3 molecule. In the plots, a C-H bond is aligned with the positive direction of the x axis. The green contour corresponds to the 440 cm^{-1} , which equals to the collision energy. From Fig. 5.13 we see that the CH_3 -Ar PES has a steeper repulsive wall. Also, we can see from Fig. 5.13 that the CH_3 -Ar PES is more attractive at larger atom-molecule separation (the global minima for the CH_3 -He and CH_3 -Ar PESs are 27 and 120 cm^{-1} , respectively), and the gradient of the potential in the attractive regions of the PES is larger. This indicates that the attractive forces will be stronger for this heavier, more polarizable collider than for the methyl radical-He system. In addition, the duration of a collision is longer for the heavier Ar collider, because of the smaller relative velocity than for light He. The transfer of the angular momentum is classically directly proportional to the duration of the collision and to the gradient of the potential [247]. Consequently, the long-range attractive parts of the CD_3 -Ar PESs will be more important for changing the CD_3 rotational angular momentum than for the CD_3 -He system. Glancing collisions at large impact parameters that sample the attractive part of the potential can induce significant changes in the rotational angular momentum

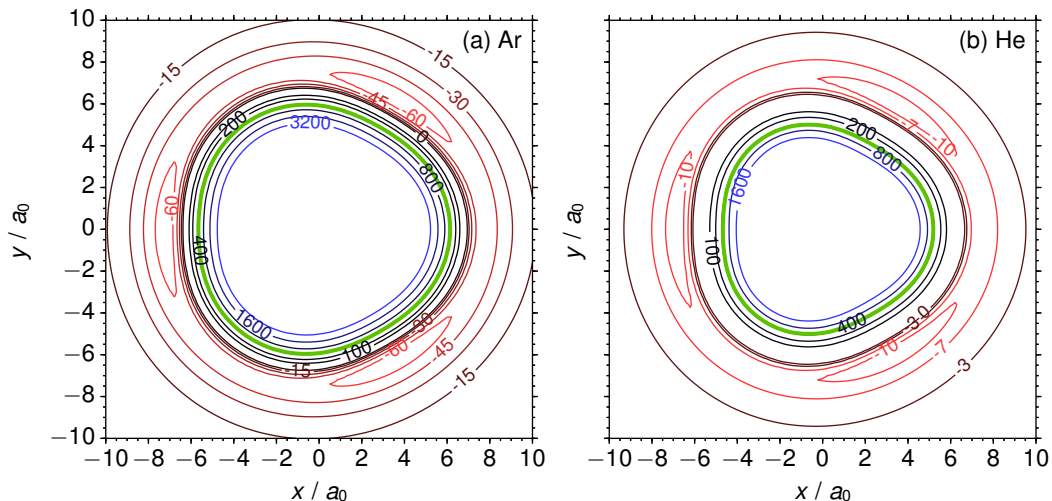


Figure 5.13: Contour plots showing the variation of the (a) CH₃-Ar and (b) CH₃-He interaction energies averaged over ϕ on the plane containing the CH₃ molecule. The PESs for CH₃-Ar and CH₃-He were described in Sec. 5.2.4 and Ref. [81], respectively. The green contour represents 440 cm⁻¹, which is the collision energies used in this work comparing the CH₃-Ar and CH₃-He DCSs.

and contribute to the small-angle scattering. Collisions of CD₃ with He are dominated by repulsive interactions and have relatively broad DCSs.

Figure 5.12(c, d) compare partial cross sections for 1₀ to 3₃ and 5₀ transitions for both collision partners. The partial cross sections (PCSs) report the contributions to the ICS from each value of J . Since the initial and final rotational quantum numbers n and n' of the transitions are small compared with the orbital angular momentum L , we can compute the classical impact parameters b assuming $L \approx J$. Thus the PESs give information about the range of b contributing to a particular transition. The inelastic scattering occurs to much larger impact parameters for Ar as a collision partner than for He: the maxima in the PCSs for the 1₀ to 5₀ transition occur for $b = 2.3 a_0$ and $5.5 a_0$ for He and Ar, respectively.

It is interesting to inquire whether two distinct $n_k \rightarrow n'_{k'}$ transitions for CD₃-Ar and He that happen to occur over the same range of impact parameters lead to similar DCSs. Figure 5.14 shows computed state-to-state DCSs and the corresponding PCSs for one such example. In this case, the 1₀ → 3₃ transition for CD₃-He and the 10 → 6₃ transition for CD₃-Ar are compared. The two transitions occur over the same range of impact

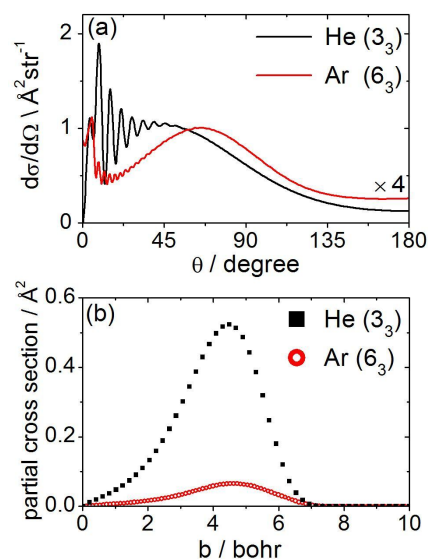


Figure 5.14: (a) Computed state-to-state DCSs and (b) corresponding partial cross sections for inelastic scattering of CD_3 with He for the 1_0 to 3_3 transition, and with Ar for the 1_0 to 6_3 transition at a collision energy of 440 cm^{-1} . The DCS for CD_3 -Ar was multiplied by factor of 4 to assist the comparison.

parameters, which peak at around $4.5 a_0$. The resulting DCSs are indeed very similar. Note that the DCS for CD_3 -Ar was multiplied by a factor of 4 for the purposes of the comparison, and that both transitions involve $\Delta k = 3$. According to our calculations, the lowest final rotational level produced by collisions of CD_3 (1_0) with Ar at a collision energy of 440 cm^{-1} for which backward scattering dominates is $n'_{k'} = 8_3$. For CD_3 (1_0) with He, it is $n'_{k'} = 5_0$. The maximum in the PCS distribution for this CD_3 -Ar transition is at an impact parameter of $b = 2.5 a_0$.

5.5 Conclusions

Experimentally determined differential cross sections for the rotationally inelastic scattering of methyl radicals by He and Ar compare very favorably with theoretical predictions obtained from close-coupling scattering calculations on *ab initio* potential energy surfaces. The experimental measurements are resolved at the level of the final rotational angular momentum of the CD_3 radical (n') but are averaged over some or all of

the final k' levels corresponding to projection of the angular momentum on the symmetry axis of the radical.

The results from close-coupling scattering calculations can be examined at the full state-to-state level to examine trends in the scattering dynamics that depend on the magnitudes of the collision-induced changes Δn and Δk . The scattering calculations also reveal pronounced diffraction oscillations at scattering angles $\theta < 45^\circ$ that are averaged out under the experimental conditions.

The flux of CD_3 scattered by Ar peaks strongly in the forward direction, with little or no amplitude at $\theta > 60^\circ$ for the final states $n' = 2-5$ probed. This behavior contrasts with the broad angular scattering observed in CD_3 -He collisions. The PES of the latter system has a less steep repulsive wall and a shallower well. The greater propensity for forward scattering in the case of CD_3 -Ar is a consequence of the greater importance of long-range attractive interactions which induce changes in the rotational angular momentum of the CD_3 even for glancing (large impact parameter) collisions. In contrast to CD_3 -He scattering, the DCSs for CD_3 -Ar at our chosen collision energy show only a weak dependence on the final values of n' and k' quantum numbers.

Chapter 6

Rotationally Inelastic Scattering of Methyl Radicals with H₂ and D₂

This chapter contains long excerpts of a paper “Differential and integral cross sections for the rotationally inelastic scattering of methyl radicals with H₂ and D₂” by Ondřej Tkáč, Qianli Ma, Cassandra A. Rusher, Stuart J. Greaves, Andrew J. Orr-Ewing, and Paul J. Dagdigian, originally published on *J. Phys. Chem.* [137], and is presented with permission of the American Institute of Physics.

6.1 Introduction

The potential energy surface (PES) is a key theoretical concept in the field of molecular reaction dynamics [248]. Modern quantum chemistry provides methods to compute *ab initio* PESs within the Born-Oppenheimer approximation, while measurement of state-to-state differential cross sections (DCSs) provide an excellent experimental test of the accuracy of the PES since the DCSs are sensitive to both attractive and repulsive parts of the potential [2]. The accuracy of a computed PES can hence be tested by comparing theoretical DCSs, calculated from quantum scattering theory, with experimentally measured DCSs. If theory and experiment are found to be in good agreement, robust deductions can be drawn about the collision dynamics, including the relationship between experimental measurables (e.g. angular distributions and state propensities) and features of the PES

controlling the collision dynamics.

We focus here on DCSs involving the inelastic scattering of methyl radicals with molecular hydrogen. Studies of collisions of several important species (e.g. H_2O , OH , NH_3 , and CH_3) with molecular hydrogen are motivated by astrophysical applications, because of the high abundance of H_2 in the universe. Collisions involving methyl radicals are of particular interest for the hydrocarbon chemistry of the atmospheres of the outer planets in the solar system [204–206], as well as Titan [207]. Methyl radical chemistry is important in the combustion of hydrocarbons [5, 201] and chemical vapor deposition of diamond films [202, 203]. In addition, methyl radicals may be an integral part of a catalytic cycle for partial oxidation of methane to formaldehyde or methanol for chemical feedstocks [249].

From a theoretical perspective, accurate close-coupling DCSs for methyl scattering are computationally tractable for collisions involving the H_2 or D_2 molecule because their large rotational constants ($B_{\text{H}_2} = 60.853 \text{ cm}^{-1}$ and $B_{\text{D}_2} = 30.443 \text{ cm}^{-1}$) [250] mean that only a few rotational levels of the collision partner need to be included in quantum scattering calculations. Although D_2 has the same mass as a He atom, collisions involving the diatomic molecule can change the internal state of both collision partners, along with the relative kinetic energy. Comparison of inelastic DCSs for collisions of methyl radicals with He, H_2 , and D_2 might therefore distinguish the consequences of the additional molecular rotational degrees of freedom from purely mass related effects.

The inelastic scattering of labile free radicals was extensively reviewed in the mid 1990s [9, 74, 208], with a focus on state-resolved integral cross sections (ICSs). Since then, experimental studies using velocity map imaging (VMI) [14, 15] and laser spectroscopic detection have revolutionized measurement of state-resolved DCSs, for which the most extensively studied molecules are the NO [19, 23, 214–216, 218–221] or OH [96, 100, 103, 112, 222–226] diatomic radicals. To date, the only reported measurement of DCSs for inelastic scattering of polyatomic free radicals is our recent study of methyl

radical scattering by He (Chapter 5). We found excellent agreement between experimental measurements and DCSs calculated using the recent PES of Dagdigian and Alexander [81]. The inelastic scattering of closed-shell polyatomic molecules is more extensively illustrated by determinations of DCSs for scattering of ammonia [232–234] and deuterated ammonia [17, 138] with rare gases and molecular hydrogen, and for water with helium [20] and hydrogen [21]. The rotationally inelastic scattering of deuterated methyl radicals and ammonia in collisions with helium were recently compared, using close-coupling quantum-mechanical scattering calculations performed with accurate *ab initio* PESs [243].

Dagdigian’s review of quantum scattering calculations of collisional energy transfer in small hydrocarbon intermediates provides a current perspective on polyatomic radical scattering [27] and highlights studies involving methylene (CH_2) [235, 236] and methyl [81, 152]. The energy transfer dynamics for a polyatomic species like the methyl radical are more complicated than for collisions of a diatomic molecule with an atom. In the latter case, the cylindrical symmetry limits the anisotropy to that associated with the polar angle away from the molecular axis. In contrast, for collisions of methyl radicals, anisotropies must be considered that are associated with the polar angle (away from the C_3 symmetry axis) and the azimuthal angle about this axis.

In the work reported here, DCSs for collisions of CH_3 and CD_3 with H_2 and D_2 were experimentally determined using crossed molecular beam (CMB) and VMI methods. However, we concentrate on the DCSs for collisions of CD_3 since only a few CH_3 levels can be cleanly detected because of predissociation of the excited-state used for spectroscopic detection. We compare the measured DCSs with results from quantum close-coupling scattering calculations performed using a newly computed *ab initio* PES.

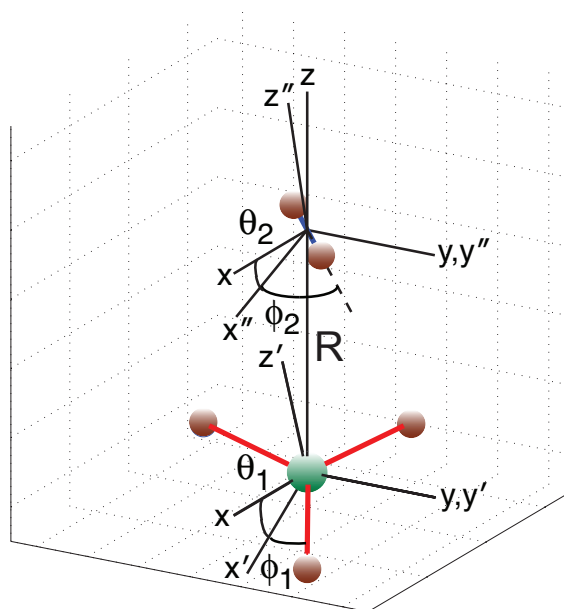


Figure 6.1: Body-frame coordinate system to specify the geometry of the $\text{CH}_3\text{-H}_2$ complex. The Jacobian R vector lies along the z axis. The CH_3 and H_2 molecule-frame axes are denoted by (x', y', z') and (x'', y'', z'') , respectively.

6.2 Method

6.2.1 Experimental Apparatus

Measurement of the DCSs for the inelastic scattering of CD_3 with H_2 and D_2 used a CMB instrument with VMI. The final levels of CD_3 were detected with the resonance-enhanced multiphoton ionization (REMPI) technique. Details of the apparatus are described in Ref. [137] and will not be presented here.

The rotational levels of CD_3 , as well as the details on the REMPI detection of CD_3 , are described in Sec. 5.2.

6.2.2 Potential Energy Surface

The geometry of the $\text{CH}_3\text{-H}_2$ rigid-rotor complex can be described by five coordinates, similar to those used in earlier work by Rist *et al.* on the $\text{NH}_3\text{-H}_2$ system [135]. These include the intermolecular separation R and four angles (θ_1, ϕ_1) and (θ_2, ϕ_2) de-

scribing the orientations of the CH₃ and H₂ collision partners, respectively, relative to the Jacobian vector R connecting the two molecules. This body-frame coordinate system is illustrated in Fig. 6.1.

Following the derivation in Sec. 1.3.1, we can expand the angular dependence of the CH₃-H₂ PES as:

$$V(\mathbf{R}, \Omega_{1S}, \Omega_{2S}) = \sum_{l_1 l_2 l \mu_1 \mu_2} B_{l_1 l_2 l \mu_1 \mu_2}(R) \sum_{m_1 m_2 m} \langle l_1 m_1, l_2 m_2 | l m \rangle \times D_{m_1 \mu_1}^{l_1*}(\Omega_{1S}) D_{m_2 \mu_2}^{l_2*}(\Omega_{2S}) C_{lm}^*(\Omega_{BS}), \quad (6.1)$$

where the B terms are radial expansion coefficients, with

$$B_{l_1 l_2 l \mu_1 \mu_2}(R) = \sum_{ij} \int \int \psi_1^*(\rho_1) \psi_2^*(\rho_2) A_{l_1 l_2 l}(\rho_i, \rho_j, R) C_{l_1 \mu_1}(\rho_i) C_{l_1 \mu_2}(\rho_j) \times \psi_1(\rho_1) \psi_2(\rho_2) d\rho_1 d\rho_2. \quad (6.2)$$

Since V is independent of the choice of the space frame, we align the space frame with the body frame (i.e., we align \mathbf{R} along the space frame z axis). In this case, only $m = 0$ terms contribute to the potential. Also, only $\mu_2 = 0$ terms contribute since the electronic wave function of H₂ is cylindrically symmetric. From Fig. 6.1 we define the orientation between CH₃ and H₂ with four angles: $\Omega_{B1} \equiv (\phi_1, \theta_1, 0)$ defines the Euler angles to rotate the the CH₃ molecule frame to the body frame, and $\Omega_{2B} \equiv (\phi_2, \theta_2, 0)$ that rotates the body frame to the H₂ molecule frame. The third Euler angles can be zero here because structures in the target frames (\mathbf{R} and the H₂ molecule) are cylindrically symmetric. Note that it is not correct to assume the body frame can be rotated to the CH₃ molecule frame with the third

Euler angle be zero. With these considerations, we can rewrite Eq. (6.1) as

$$\begin{aligned}
V(R, \theta_1, \phi_1, \theta_2, \phi_2) &= \sum_{l_1 l_2 l \mu_1} B_{l_1 l_2 l \mu_1}(R) \\
&\times \sum_{m_1} \langle l_1 m_1, l_2, -m_1 | l 0 \rangle D_{m_1 \mu_1}^{l_1^*}(0, -\theta_1, -\phi_1) D_{-m_1, 0}^{l_2^*}(\phi_2, \theta_2, 0).
\end{aligned} \tag{6.3}$$

The expansion coefficient is related to that defined by Eq. (14) of Ref. [135] by

$$B_{l_1 l_2 l \mu_1}(R) = (-1)^{l_1 + l_2} [l]^{-\frac{1}{2}} u_{l_1 l_2 l \mu_1}(R). \tag{6.4}$$

Symmetry considerations restrict the allowed terms in Eq. 6.3. The three-fold symmetry of CH₃ requires that μ_1 be a multiple of 3. The potential is invariant to exchange of the hydrogen nuclei in H₂, hence l_2 must be even. Since V is real, it can be shown that

$$B_{l_1 l_2 l \mu_1}(R) = (-1)^{l_1 + l_1 - l + \mu_1} B_{l_1 l_2 l, -\mu_1}^*(R). \tag{6.5}$$

Since V must be invariant to reflection of H₂ through the xz plane of the CH₃ molecule frame, we have

$$B_{l_1 l_2 l, -\mu_1}(R) = (-1)^{l_1 + l_2 + l + \mu_1} B_{l_1 l_2 l \mu_1}(R). \tag{6.6}$$

Equations (6.5) and (6.6) imply that the B coefficients in Eq. (6.3) are real. In addition, V is invariant to reflection of H₂ through the xy plane of the CH₃ molecule frame since CH₃ is planar. It can be shown that this property restricts $l_2 + l + \mu_1$ to be even. The potential should also be invariant with respect to inversion of all coordinates; this parity invariance restricts the $l_1 + l_2 + l$ to even values [135]. However, this symmetry can be broken for the interaction of a nonlinear molecule with a diatomic [65, 251].

Substituting Eq. (6.6) into Eq. (6.3) and resolving the rotation matrix elements in Eq. (6.3) into products of complex exponentials and reduced rotation matrix elements, $d_{m' m}^j$

[68], we obtain

$$V(R, \theta_1, \phi_1, \theta_2, \phi_2) = \sum_{l_1 l_2 l, \mu_1 \geq 0} B_{l_1 l_2 l \mu_1}(R) (1 + \delta_{\mu_1 0})^{-1} \sum_m \langle l_1 m, l_2, -m | l 0 \rangle \\ \times \left[e^{-i\mu_1 \phi_1} d_{\mu_1 m}^{l_1}(\theta_1) + (-1)^{l_1 + l_2 + l + \mu_1} e^{i\mu_1 \phi_1} d_{-\mu_1, m}^{l_1}(\theta_1) \right] e^{-im\phi_2} d_{-m, 0}^{l_2}(\theta_2). \quad (6.7)$$

The PES was fitted with a modified version of Eq. (6.7)

$$V(R, \theta_1, \phi_1, \theta_2, \phi_2) = \sum_{l_1 l_2 l, \mu_1 \geq 0} C_{l_1 l_2 l \mu_1}(R) \bar{t}(\theta_1, \phi_1, \theta_2, \phi_2), \quad (6.8)$$

with

$$\bar{t}(\theta_1, \phi_1, \theta_2, \phi_2) = \frac{1}{2\pi} \left(\frac{[l_1][l_2]}{2} \right)^{\frac{1}{2}} \sum_{m \geq 0} (1 + \delta_{m 0})^{-1} \langle l_1 m, l_2, -m | l 0 \rangle d_{-m, 0}^{l_2}(\theta_2) \\ \times \left[\cos(\mu_1 \phi_1 + m \phi_2) d_{\mu_1 m}^{l_1}(\theta_1) + (-1)^{l_1 + l_2 + l + \mu_1} \cos(\mu_1 \phi_1 - m \phi_2) d_{-\mu_1, m}^{l_1}(\theta_1) \right], \quad (6.9)$$

where $[x] = 2x + 1$, and

$$C_{l_1 l_2 l \mu_1}(R) = \frac{4\pi}{1 + \delta_{\mu_1 0}} \left(\frac{2}{[l_1][l_2]} \right)^{\frac{1}{2}} B_{l_1 l_2 l \mu_1}(R). \quad (6.10)$$

The angular expansion in Eq. (6.9) is normalized so that the significance of individual terms can be evaluated directly.

We performed the explicitly correlated restricted coupled-cluster calculations with full inclusion of single and double excitations and perturbative inclusion of triple excitations [RCCSD(T)-F12a] [51, 53] of the $\text{CH}_3\text{-H}_2$ PES. We employed the aug-cc-pVTZ correlation-consistent basis sets [192, 240], with aug-cc-pVTZ/MP2FIT and cc-pVTZ/JKFIT as the density fitting basis and the resolution of identity basis, respectively [252, 253]. A counterpoise correction was applied to correct for basis-set superposition error [57]. All calculations were carried out with the MOLPRO 2010.1 suite of programs

[113].

The CH₃-H₂ interaction energies were determined on a five-dimensional grid of 33 values of the intermolecular separation R [R (in a_0) = 3–8 in steps of 0.25; 8.5, 9, 9.5, 10, 11, 12, 13, 14, 15, 16, 18, 20]. The interaction energy was computed over a random angular grid [254] of 1,600 orientations, consisting of uniform distributions of both $\cos \theta_1$ and $\cos \theta_2$ over $[-1, 1]$ and both ϕ_1 and ϕ_2 over $[0, 2\pi]$. The total number of nuclear geometries for which the interaction potential was computed was 52,800. The interaction energies for an additional 1,400 orientations at $R = 5a_0$ were also computed to choose statistically important terms in Eq. (6.9) to be used in the final fit.

These (l_1, l_2, l, μ_1) terms were chosen by the following method. We first performed a least-squares fit of the 3000 geometries at $R = 5a_0$ to a large 418-term angular basis consisting of all symmetry-allowed terms with $l_1 \leq 12$ and $l_2 \leq 6$ to obtain estimated expansion coefficients for all these terms. We started from a minimal angular basis with only the isotropic term, fit the *ab initio* points, and computed the estimated fitting error e_i with a Monte Carlo error estimator¹ [254]. We then iteratively added terms whose estimated expansion coefficients have an absolute value greater than $8e_i$, and recomputed

¹To estimate the expansion error, we first calculate the overlap \mathbf{S} matrix with elements

$$S_{ij} = \frac{16\pi^2}{N} \sum_{k=1}^N \bar{t}_i^*(\hat{\alpha}_k) \bar{t}_j(\hat{\alpha}_k),$$

where N is the number of orientations used in the fit, i and j are indices of the expansion terms, and $\hat{\alpha}_k$ represents $(\theta_1, \phi_1, \theta_2, \phi_2)$ for the k -th orientation. The norm of the inverse \mathbf{S} matrix can be used as an indicator whether the angular sampling is sufficient. A good angular sampling should give $\|\mathbf{S}^{-1}\| \sim 1$. $\|\mathbf{S}^{-1}\|$ can be estimated with

$$\|\mathbf{S}^{-1}\| \approx \min(\lambda_i)^{-1},$$

where λ_i represents the eigenvalues of the \mathbf{S} matrix. The estimated expansion error is given by

$$e_i \approx \sqrt{\frac{16\pi^2}{N}} \sigma \|\mathbf{S}^{-1}\| [1 - \rho(n, N)]^{-\frac{1}{2}},$$

with

$$\rho(n, N) = \frac{(|\|\mathbf{S}^{-1}\||n - 1|)}{N}.$$

In the above equations, n is the number of terms in the expansion, and σ is the root mean squares (RMS) from a least squares fit.

e_i with this new angular basis until no extra terms could be included with this criterion. The total number of terms included was 55. Unlike several other PESs describing the interaction of a symmetric or an asymmetric top with a linear molecule [65, 255], all terms in our PES have even $l_1 + l_2 + l$, and none of the odd $l_1 + l_2 + l$ terms is statistically important.

The *ab initio* points were fitted using this 55-term angular basis and the least-squares method. The root mean squares (RMS) of the fit [65] increases with decreasing R but is $< 0.1\%$ of the average of the absolute value $|V|$ of the potential for $R \geq 4.75 a_0$ ($|V| = 2500 \text{ cm}^{-1}$). Using the Monte Carlo error estimator [254], we found the norm for our randomly generated orientations and angular basis is 1.52. A value of close to 1 indicates sufficient angular sampling.

Figure 6.2 presents a plot of the larger expansion coefficients as a function of the intermolecular separation R in the region of the van der Waals well. For the terms involving the interaction with spherically averaged H_2 (i.e. $l_2 = 0$), shown in the upper panel of Fig. 6.2, the largest coefficients are the same as for $\text{CH}_3\text{-He}$ [81], namely $(l_1, \mu_1) = (3, 3)$ and $(2, 0)$. These reflect the leading anisotropies involving approach of the collision partner within and perpendicular to the plane of the methyl radical, as discussed previously for $\text{CH}_3\text{-He}$ [81]. The lower panel of Fig. 6.2 displays the larger coefficients with $l_2 = 2$, which reflect the molecular nature of the collision partner. The plotted coefficients are direct analogs of the $l_2 = 0$ coefficients plotted in the upper panel, namely $(l_1, \mu_1) = (0, 0)$, $(3, 3)$, $(2, 0)$, and $(5, 3)$, with $l = l_1 + l_2$.

The global minimum of the PES has $D_e = 99.0 \text{ cm}^{-1}$, at a geometry of $R = 6.57 a_0$, $\theta_1 = 0^\circ$, $\theta_2 = 0^\circ$ (the ϕ angles are meaningless here). The H_2 molecule thus lies along the C_3 axis of the methyl radical above (or below, by symmetry) the molecular plane. The well depth D_e is thus significantly larger than that for $\text{CH}_3\text{-He}$ (27.0 cm^{-1} [81]). The equilibrium geometry differs from that of the global minimum for $\text{CH}_3\text{-He}$ [81], for which the He atom lies in the molecular plane and bisects two C-H bonds.

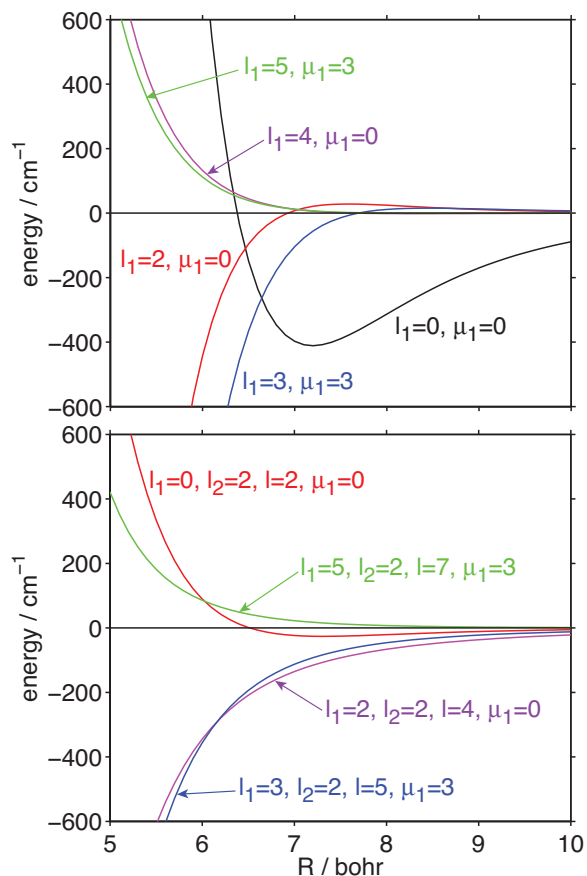


Figure 6.2: Dependence of the larger expansion coefficients [defined in Eq. (6.8)] upon the $\text{CH}_3\text{-H}_2$ separation R . Upper panel: coefficients with $l_2 = 0$ (and hence $l = l_1$); lower panel: coefficients with $l_2 = 2$. The expansion coefficients are the same for the interaction of CH_3 or CD_3 with D_2 since the centers of mass of the hydrogen molecule and methyl radical do not change under isotopic substitution.

Figure 6.3 presents contour plots of the dependence of the potential upon the orientation of the methyl radical for two orientations of H_2 for $R = 6.5 a_0$. For $\theta_2 = 0^\circ$ (left-hand panel of Fig. 6.3) the CH_3 orientation for the most attractive interaction is the same as that of the global minimum. In this case the maximum repulsion occurs for $\theta_1 = 90^\circ$ and $\phi_1 = 0^\circ, 120^\circ, 240^\circ$; this corresponds to approach of one end of the H_2 molecule in the CH_3 plane toward one of the C-H bonds. The right-hand panel of Fig. 3 displays a contour plot of the potential for $\theta_2 = 90^\circ, \phi_2 = 0^\circ$. In this case, the most attractive CH_3 orientation ($\theta_1 = 90^\circ$ and $\phi_1 = 60^\circ, 180^\circ, 300^\circ$) corresponds to approach of the center of the H_2 molecule in the molecular plane and bisecting two C-H bonds, with the H_2

internuclear axis lying perpendicular to the CH₃ plane. The new PES can be used without modification in scattering calculations on CD₃-H₂ and CD₃-D₂ collisions since the centers of mass are unaffected for both molecules upon isotopic substitution.

6.2.3 Quantum Scattering Calculations

State-to-state DCSs and ICSs for collisions of CD₃ with H₂ and D₂ were calculated using the HIBRIDON suite of programs [31] and the PES described in Sec. 6.2.2. Rotational energies for CD₃ were computed with a rigid rotor symmetric top Hamiltonian using rotational constants from spectroscopic study by Sears *et al.* [242]. Separate calculations were carried out for each nuclear spin modification of both CD₃ and H₂/D₂ since they are not interconverted in molecular collisions. The close-coupling channel basis consisted of CD₃ rotational levels whose energies were less than 960 cm⁻¹ and H₂/D₂ rotational levels with $j_2 \leq 2$, and the calculations included total angular momenta $J \leq 100$. Convergence of the DCSs to within $\sim 5\%$ was checked with respect to the size of the rotational basis and the number of partial waves in the calculation. The scattering calculations used up to 5366 channels.

For the collision between CH₃ and H₂, the close-coupling basis can be written as

$$|JMj_1k\varepsilon j_2j_{12}L\rangle = [2(1 + \delta_{k0})]^{-\frac{1}{2}} (|JMj_1kj_2j_{12}L\rangle + \varepsilon |JMj_1, -k, j_2j_{12}L\rangle), \quad (6.11)$$

where

$$|JMj_1kj_2j_{12}L\rangle = \sum_{m_1m_2m_{12}m_L} \langle j_1m_1, j_2m_2 | j_{12}m_{12} \rangle \langle j_{12}m_{12}, Lm_L | JM \rangle \\ \times |j_1km_1\rangle |j_2m_2\rangle |Lm_L\rangle. \quad (6.12)$$

In Eq. (6.12), $|j_1km_1\rangle$ is a symmetric top wave function in the CH₃ molecule frame, $|j_2m_2\rangle$ is the rotational wave functions of H₂ in its molecular frame, and $|Lm_L\rangle$ is the wave function

for end-over-end rotation of the CH₃-H₂ complex. CH₃ rotational wave functions with proper inversion symmetries are expressed as [195]

$$|j_1 k m_1 \varepsilon\rangle = [2(1 + \delta_{k0})]^{-\frac{1}{2}} (|j_1 k m_1\rangle + \varepsilon |j_1, -k, m_1\rangle). \quad (6.13)$$

The close-coupling potential matrix elements can be computed from

$$\begin{aligned} & \langle JM j_1' k' \varepsilon' j_2' j_{12}' L' | V | JM j_1 k \varepsilon j_2 j_{12} L \rangle \\ &= \sum_{l_1 l_2 l \mu_1 \geq 0} B_{l_1 l_2 l \mu_1}(R) (1 + \delta_{\mu_1 0})^{-1} [(1 + \delta_{k'0})(1 + \delta_{k0})]^{-\frac{1}{2}} (-1)^{J+l_1-l_2+j_1-j_2+j_{12}'-L-L'-k-\mu_1} \\ & \times \frac{1}{2} [1 + \varepsilon' \varepsilon (-1)^{j_1'+j_1+l_2+l+\mu_1}] ([j_1'] [j_2'] [j_{12}'] [L'] [j_1] [j_2] [j_{12}] [L] [l])^{\frac{1}{2}} \\ & \times \begin{pmatrix} j_2' & l_2 & j_2 \\ 0 & 0 & 0 \end{pmatrix} \begin{pmatrix} L' & l & L \\ 0 & 0 & 0 \end{pmatrix} \begin{Bmatrix} j_{12} & L & J \\ L' & j_{12}' & l \end{Bmatrix} \begin{Bmatrix} j_1 & j_2 & j_{12} \\ j_1' & j_2' & j_{12}' \\ l_1 & l_2 & l \end{Bmatrix} \\ & \times \left[\begin{pmatrix} j_1' & l_1 & j_1 \\ -k' & \mu_1 & k \end{pmatrix} + \varepsilon' \varepsilon \begin{pmatrix} j_1' & l_1 & j_1 \\ k' & \mu_1 & -k \end{pmatrix} \right. \\ & \quad \left. + \varepsilon' \begin{pmatrix} j_1' & l_1 & j_1 \\ k' & \mu_1 & k \end{pmatrix} + \varepsilon \begin{pmatrix} j_1' & l_1 & j_1 \\ -k' & \mu_1 & -k \end{pmatrix} \right], \quad (6.14) \end{aligned}$$

where (\dots) , $\{\dots\}$, and $\{\dots\}$ are Wigner 3- j , 6- j , and 9- j symbols, respectively [28].

Since the CD₃ incident beam contained several rotational levels, DCSs for formation of a specific final rotational level n_k were determined by weighting the computed state-to-state DCSs at the experimental collision energy by the experimentally determined incident beam rotational level populations presented in Table 1 of Ref. [200]. Since the k projection number is not resolved in the REMPI spectra, computed DCSs for comparison with the experimental measurements were weighted according to the 2-photon line strengths factors for the given detection line. We assume the H₂/D₂ incident beam contains a statistical mixture of $j_2 = 0$ and 1 rotational levels and did not consider initial levels with $j_2 \geq 2$. The

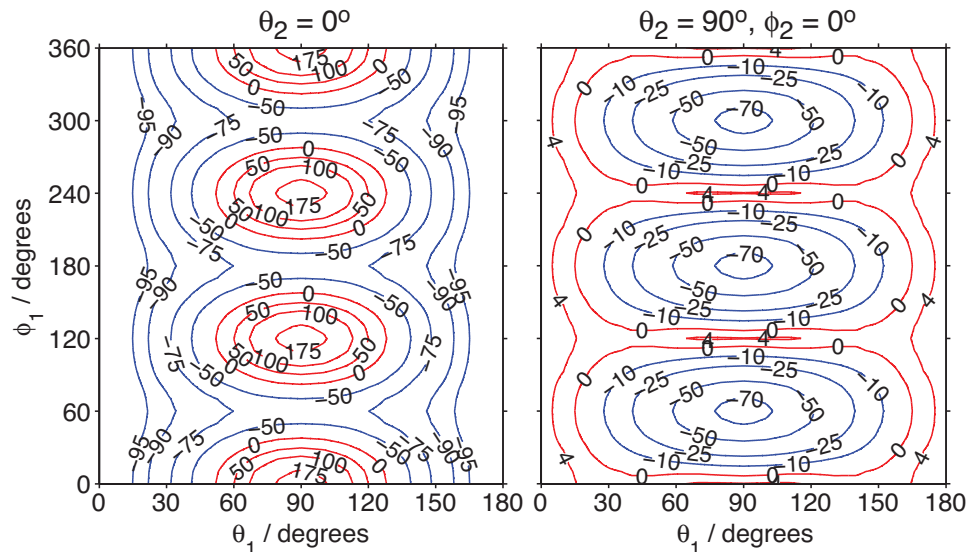


Figure 6.3: Dependence of the potential energy (in cm^{-1}) on the orientation (θ_1, ϕ_1) of the methyl radical for two orientations (θ_2, ϕ_2) of the H_2 collision partner for an intermolecular separation $R = 6.5 a_0$. The ϕ_2 angle is meaningless in the left-hand panel, with $\theta_2 = 0^\circ$.

only j_2 -changing transition included in our DCS calculations was $j_2 = 0 \rightarrow 2$. Including both the $j_2 = 0 \rightarrow 0$ and $j_2 = 0 \rightarrow 2$ transitions changes the averaged DCSs by $< 10\%$ (except for $\theta < 20^\circ$, an angular range obscured by the incident beam) compared to including $j_2 = 0 \rightarrow 0$ transitions alone. We expect the DCSs of other j_2 -changing transitions to be even less significant due to larger energy gaps.

6.3 Results

6.3.1 Integral Cross Sections

In previous work [27, 81, 138], our group examined propensities caused by the leading angular expansion coefficients of the PES in the ICSs for CH_3 and CD_3 transitions induced by collision with He. We briefly explore here these propensities for collisions of CD_3 with D_2 . Figure 6.4 presents computed state-resolved ICSs for collision of the CD_3 1_0 level, the lowest level of A_1 nuclear spin modification, with the D_2 $j_2 = 0$ and 1 rotational levels for which j_2 is the same after the collision. These cross sections were calculated for a

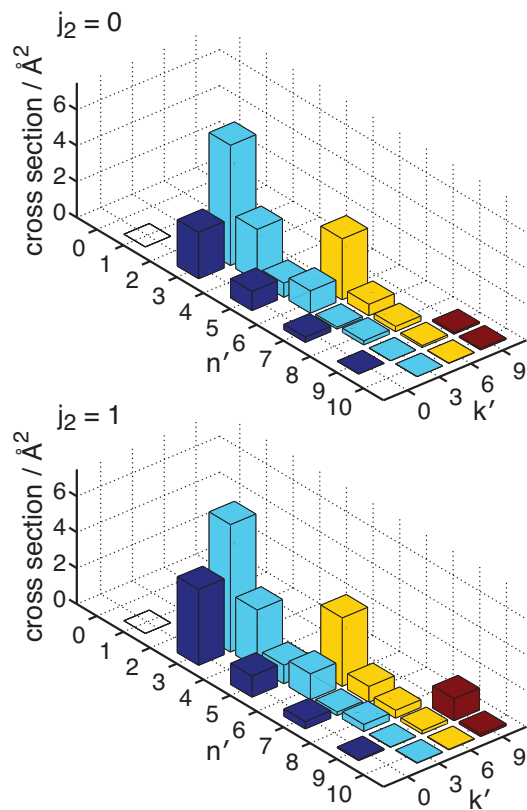


Figure 6.4: ICSs for transitions out of the CD_3 1_0 level (the lowest level of the A_1 nuclear spin modification) in collisions with D_2 at a relative translational energy of 640 cm^{-1} . The rotational level of the collision partner is $j_2 = 0$ (upper panel) and $j_2 = 1$ (lower panel). The initial level is indicated with an open square. Since the cross sections for transitions to CD_3 high n levels are small, the plots show cross sections for final levels with $n' \leq 10$.

collision energy of 640 cm^{-1} . ICSs for transitions out of the lowest rotational levels of the A_2 and E nuclear spin modifications can be found from the supplementary materials of Ref. [137].

We see in Fig. 6.4 that for most CD_3 transitions the ICSs for $j_2 = 1$ are only slightly larger than for $j_2 = 0$. The major exception is for the $1_0 \rightarrow 3_0$ transition, for which the cross section for $j_2 = 1$ is $\sim 70\%$ larger than for $j_2 = 0$, and this increase is seen in DCS for $\theta \leq 45^\circ$. In some other molecule- H_2 systems, e.g. $\text{OH}-\text{H}_2$ [144], $\text{H}_2\text{O}-\text{H}_2$ [145], NH_3-H_2 [72], the cross sections for the $j_2 = 1$ initial level are much larger than for $j_2 = 0$. In these systems, the collision partners of H_2 have nonzero dipole moments so that the leading electrostatic term is the dipole-quadrupole interaction. This interaction corresponds to

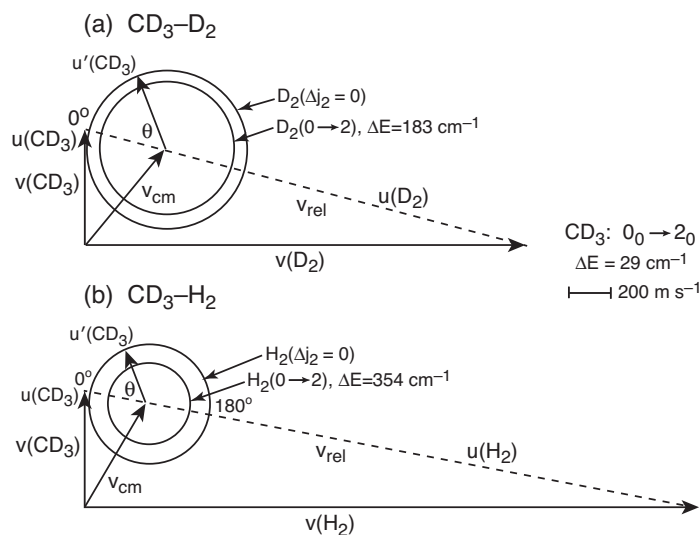


Figure 6.5: Newton diagrams for inelastic scattering of CD_3 with (a) D_2 and (b) H_2 . The Newton spheres are drawn for inelastic scattering of CD_3 from the initial state $n_k = 0_0$ to the final state $n_{k'} = 2_0$, which corresponds to an energy transfer of $\Delta E = 29.0 \text{ cm}^{-1}$ and for $\Delta j_2 = 0$ and $j_2 = 0$ to $j_2' = 2$ transitions between rotational levels of D_2 and H_2 .

the $\{l_1 l_2 l\} = \{1, 2, 3\}$ terms and could contribute to the cross sections for the $j_2 = 1$ but not $j_2 = 0$ initial level. Since methyl has no dipole moment, this interaction is missing for $\text{CD}_3\text{-H}_2/\text{D}_2$. For both these systems, the transitions with the largest cross sections are to the 3_3 and 3_0 levels; the same propensities were found for collisions with He [138]. These final levels are directly coupled by the $(l_1, \mu_1) = (3, 3)$ and $(2, 0)$ terms, respectively, of the PES.

6.3.2 Differential Cross Sections

Newton diagrams for inelastic scattering of CD_3 with D_2 and H_2 are shown in Fig. 6.5 and illustrate the laboratory frame velocities of CD_3 [$v(\text{CD}_3) = 550 \pm 30 \text{ m s}^{-1}$], D_2 and H_2 [$v(\text{D}_2) = 2090 \pm 210 \text{ m s}^{-1}$ and $v(\text{H}_2) = 2950 \pm 320 \text{ m s}^{-1}$], and the pre- and post-collision center-of-mass (CM) frame velocities of the methyl radical $u(\text{CD}_3)$ and $u'(\text{CD}_3)$, respectively. The CM-frame scattering angle θ is defined as the angle between the CM-frame velocities of CD_3 before and after a collision. The displayed Newton spheres correspond to a CD_3 transition from initial level $n_k = 0_0$ into final level $n_{k'} = 2_0$, with an

associated energy transfer of $\Delta E = 29 \text{ cm}^{-1}$, and to $\Delta j_2 = 0$ and $j_2 = 0 \rightarrow j'_2 = 2$ transitions between rotational levels of D_2 and H_2 .

Collision energies for inelastic scattering of CD_3 with D_2 and H_2 were 640 ± 60 and $680 \pm 75 \text{ cm}^{-1}$, respectively. Raw images for detection of CD_3 after collision with H_2 and D_2 can be found from Ref. [137] and its supplementary materials. In most cases, more than one spectroscopic branch was probed for a given final n' , giving different contributions of the unresolved k' projections with weighting according to the 2-photon line strength factors.

The Newton diagrams shown in Fig. 6.5 demonstrate that the Newton spheres for the rotational transition of D_2 from $j_2 = 0$ to $j'_2 = 0$ and 2 would not be distinguishable in the measured images. Comparison of measured images for H_2 as a collision partner with the Newton diagram indicates that transitions involving rotational excitation of H_2 in a collision do not contribute significantly to the scattering, as also found in the scattering calculations (see Sec. 6.2.3). DCSs are different for a given final level n' of CD_3 but different changes of the H_2 and D_2 rotational angular momentum; however, it is not possible to separate these types of Newton spheres from the measured images. The reason is that the experimental images result from superposition of many Newton spheres differing slightly in the magnitude and direction of the initial velocities of the collision partners and these Newton spheres are not perfectly concentric.

The recorded images were corrected with the density-to-flux transformation in order to derive the DCSs. Figure 6.6 displays the determined DCSs for $\text{CD}_3\text{-D}_2$ for final levels $n' = 2\text{-}4$, while Fig. 6.7 presents the DCSs for $n' = 5\text{-}7$. Also plotted in Figs. 6.6 and 6.7 are the theoretical DCSs. The experimental and calculated DCSs for the $\text{CD}_3\text{-H}_2$ system are shown in Fig. 6.8 for final levels $n' = 2\text{-}4$ and in Fig. 6.9 for $n' = 5\text{-}8$. For quantitative comparison with the theoretical calculations, the experimental DCSs were normalized by scaling the experimental value at 60° scattering angle to match the theoretical value at that angle. Since the scattering is mainly into the backward hemisphere for large Δn

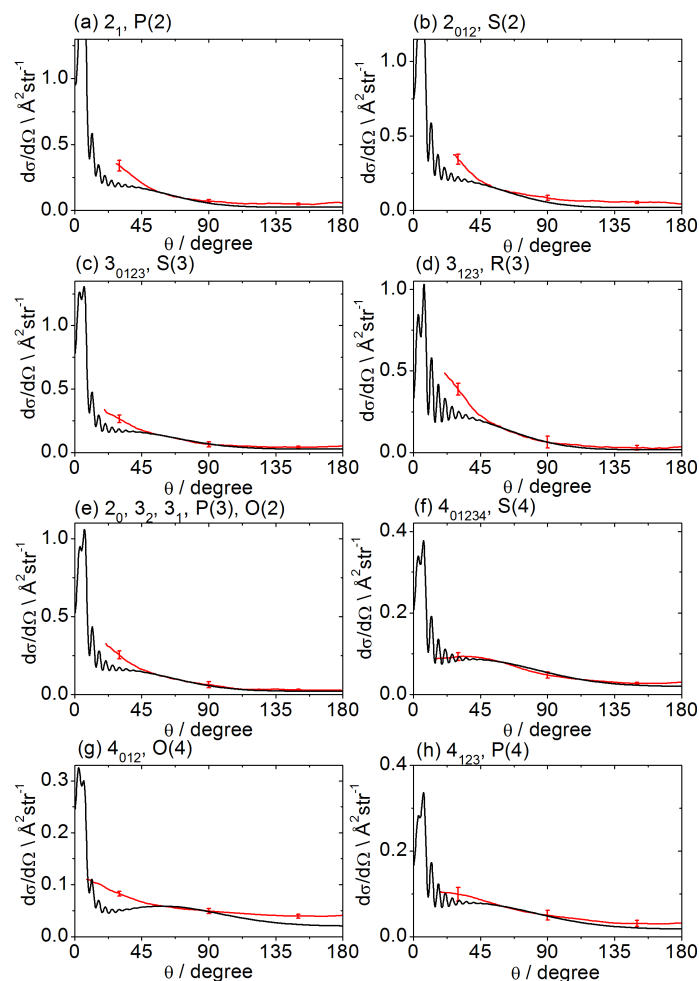


Figure 6.6: Experimental (red) and theoretical (black) DCSs for inelastic scattering of CD_3 radicals by D_2 at a collision energy of $640 \pm 60 \text{ cm}^{-1}$ into final rotational levels $n' = 2-4$. The REMPI line employed for detection is indicated, along with the range of k' projection levels contributing to the scattering. The method of normalization of the experimental DCSs is described in the main text.

transitions, the DCSs for the $R(7)$ and $P(8)$ lines for collision with H_2 were normalized at 90° .

The experimental DCSs are not shown for $\theta < 30^\circ$ for final levels with $n' = 2$ and 3 and for $\theta < 20^\circ$ for final levels with higher n' because of contributions to these angles from unscattered radicals in the parent beam. The calculated DCSs show pronounced diffraction oscillations in this strongly forward scattered region, but the angular resolution of the experiments is insufficient to resolve these structures clearly, even with greater initial state purity. The angular resolution is limited by the velocity and angular spreads of the

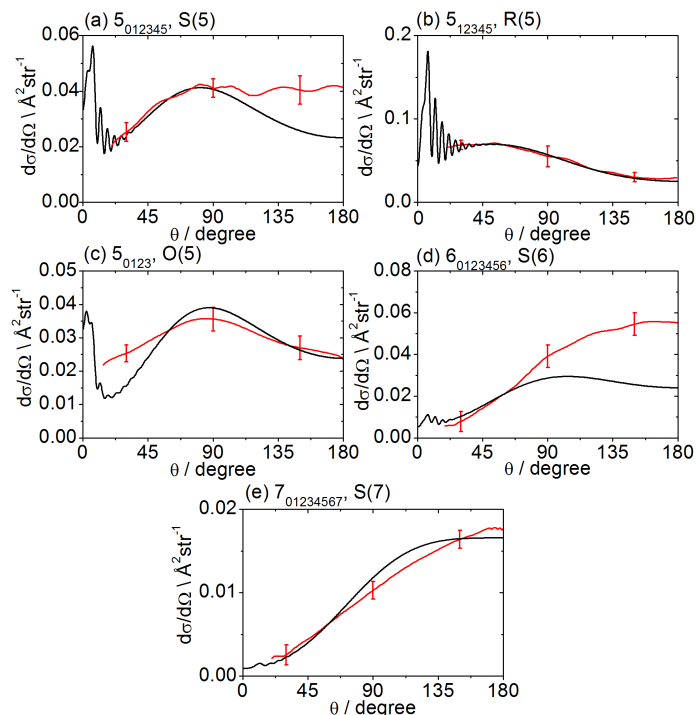


Figure 6.7: Experimental (red) and theoretical (black) DCSs for inelastic scattering of CD_3 radicals by D_2 at a collision energy of $640 \pm 60 \text{ cm}^{-1}$ into final rotational levels $n' = 5-7$. The REMPI line employed for detection is indicated, along with the range of k' projection levels contributing to the scattering. The method of normalization of the experimental DCSs is described in the main text.

two molecular beams, and for the current experiments on the $\text{CD}_3 + \text{D}_2/\text{H}_2$ systems, varies from 3° to 18° depending on the scattering angle [200].

The error bars associated with the experimental DCSs were determined by combining the standard deviation determined from comparison of several measured images for a single final state with the uncertainty introduced by application of the density-to-flux transformation. The latter factor was quantified by comparing DCSs extracted from the two halves of the image separated by the relative velocity vector (which should be symmetric after perfect transformation).

There is generally quantitative agreement between the (normalized) experimental and computed DCSs, although some small discrepancies are evident for scattering angles $< 45^\circ$ for some probe transitions with $n' \leq 4$. Here, the experimental DCSs are slightly larger than the computed DCSs, which could be a consequence of our limited experimental

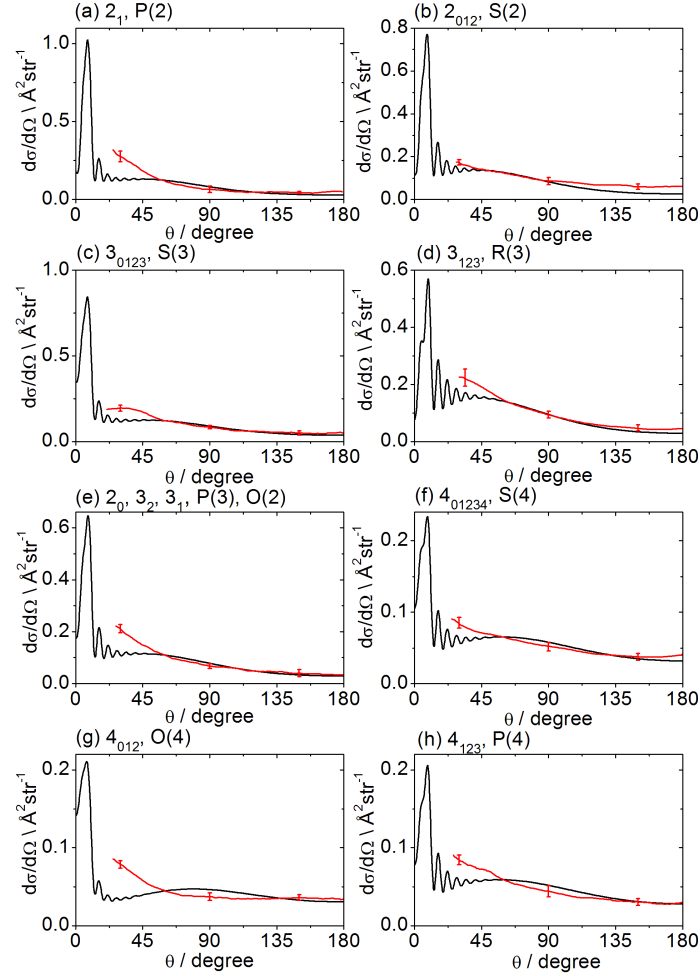


Figure 6.8: Experimental (red) and theoretical (black) DCSs for inelastic scattering of CD_3 radicals by H_2 at a collision energy of $680 \pm 75 \text{ cm}^{-1}$ into final rotational levels $n' = 2-4$. The REMPI line employed for detection is indicated, along with the range of k' projection levels contributing to the scattering. The method of normalization of the experimental DCSs is described in the main text.

angular resolution or imperfect background subtraction. There may also be contributions to the scattering signals from initial levels with higher initial n present at low density in our $\sim 15 \text{ K}$ beam, because elastic scattering events will give strong forward scattering with high integral cross sections. The only significant differences between the experimental and computed DCSs are for detection of some high- n' final rotational levels, in particular via the $S(5)$ and $S(6)$ lines in collisions with D_2 and the $R(5)$ and $S(5)$ lines in collisions with H_2 . Even for these cases, there is satisfactory qualitative agreement between the shapes of the experimental and computed DCSs.

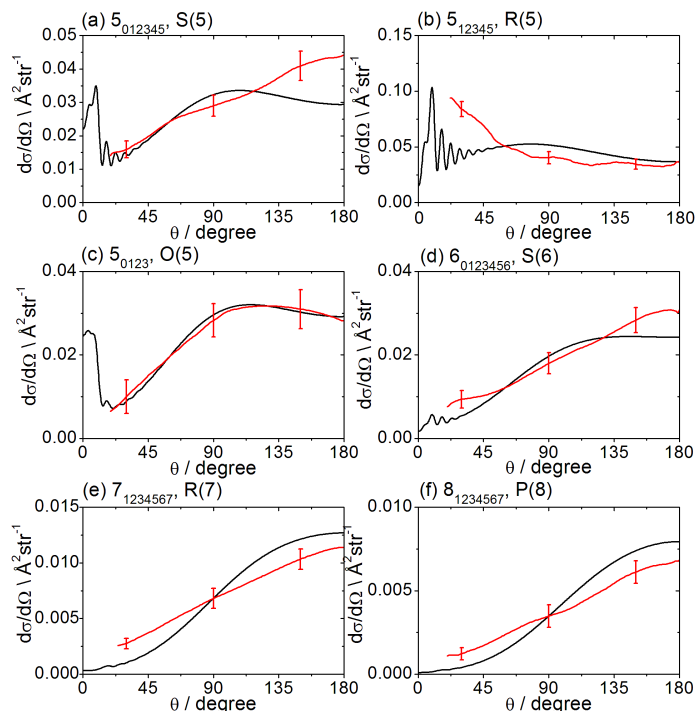


Figure 6.9: Experimental (red) and theoretical (black) DCSs for inelastic scattering of CD_3 radicals by H_2 at a collision energy of $680 \pm 75 \text{ cm}^{-1}$ into final rotational levels $n' = 5-8$. The REMPI line employed for detection is indicated, along with the range of k' projection levels contributing to the scattering. The method of normalization of the experimental DCSs is described in the main text.

6.4 Discussion

Although the focus of our study is on inelastic scattering, the collision of a methyl radical with molecular hydrogen can also follow a reactive pathway. However, the vibrationally adiabatic barrier height on the potential energy surface for reactive formation of methane and atomic hydrogen has been computed to be 3847 cm^{-1} [256]. This energy barrier is much higher than the collision energy in our experiments and calculations so the reactive path is closed. Moreover, the PES was computed with the assumption of rigid molecular geometries. Our comparisons of experimental and computed DCSs therefore test the quality of the *ab initio* PES and the accuracy of the scattering calculation methods in regions of the global PES below the transition state for reaction.

For both D_2 and H_2 as collision partners, the measured images and the corresponding DCSs directly reveal the dependence of the scattering upon CD_3 final rotational angular

momentum n' . The DCSs peak in the forward hemisphere for $n' = 2-4$ and shift more to sideways and backward scattering for $n' = 5$. For $n' = 6-8$, the DCSs are dominated by backward scattering. A similar trend was observed for scattering of methyl radicals with He, and we discussed the origins of this behavior in terms of partial cross sections (or impact-parameter dependence of the scattering) in a recent paper [200]. DCSs were measured for different spectroscopic branches to probe a given methyl rotational level n' , but a different subset of the k' -projection quantum numbers. These DCSs differ, especially for $n' = 5$, demonstrating the sensitivity of scattering to the k' value, even if it is not fully resolved in the current experiments.

With inspection of Figs. 6.6–6.9, we see that there are a few clear differences between DCSs measured for H_2 and D_2 as collision partners with CD_3 , the most apparent being that the DCSs for the CD_3 – D_2 system decrease more sharply from a maximum at small scattering angles towards larger angles. In view of the good agreement between the experimental and computed DCSs, we can compare in detail computed state-resolved DCSs for the two systems. It should be noted that we have no clear experimental information on the rotational inelasticity of the D_2/H_2 collision partner.

Figure 6.10 compares the DCSs for transitions from the CD_3 1_0 rotational level, the lowest level of A_1 nuclear spin modification, into selected final levels in collisions with D_2 and H_2 at relative translational energies of 640 and 680 cm^{-1} , respectively. State-to-state ICSs corresponding to the DCSs plotted in Fig. 6.10 are displayed in Fig. 6.6 for D_2 as a collision partner. DCSs for transitions involving other final levels and for collisions out of the 0_0 and 1_1 rotational levels, the lowest levels of the A_2 and E nuclear spin modifications, respectively, can be found online from the supplementary materials of Ref. [137].

We see in Fig. 6.10 that DCSs for the same transitions have a similar angular dependence for the D_2 and H_2 collision partners. For final levels $n' \leq 4$, the DCSs for the D_2 collision partner are larger for small angles, while the DCSs for H_2 extend to larger scattering angles than do the DCSs for D_2 . For intermediate states ($n' = 5$ and 6), the

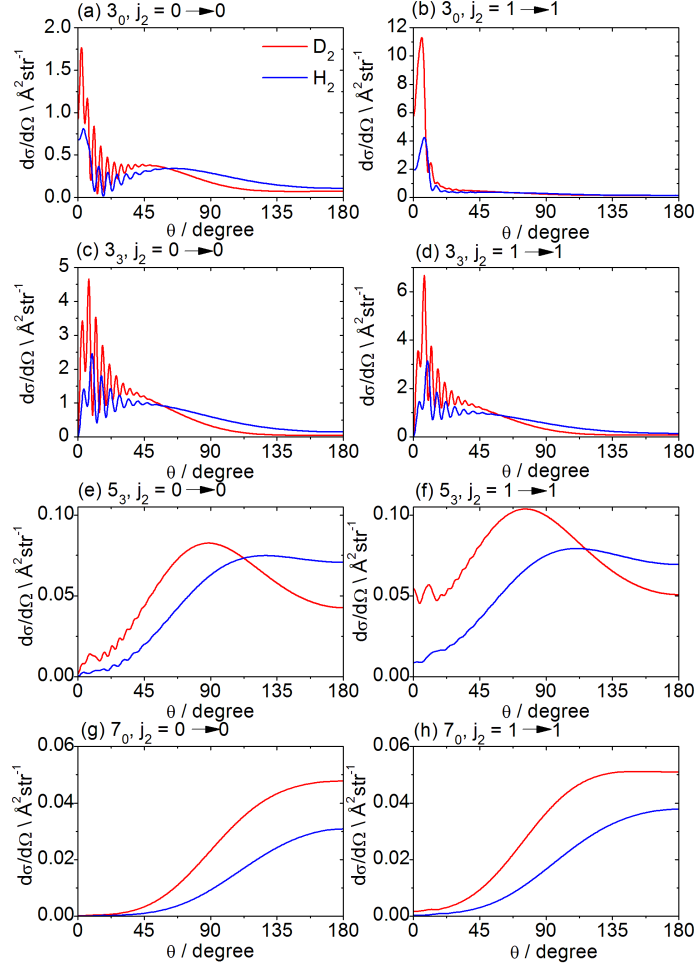


Figure 6.10: Computed state-to-state DCSs for inelastic scattering of CD_3 , initially in the 1_0 rotational level, with D_2 (red) and H_2 (blue) into selected final rotational levels at collision energies of 640 and 680 cm^{-1} , respectively. The left and right panels are DCSs for which the initial rotational level j_2 of the collision partner equals 0 and 1 , respectively, and is the same after the collision.

DCSs for D_2 are dominated by sideways scattering with peaks around $\theta \sim 90^\circ$, whereas the DCSs for H_2 are shifted more to backward hemisphere. The DCSs for higher final levels are dominated by backward scattering for both collision partners as demonstrated in Fig. 6.10 by DCSs for the 7_0 final level. We notice that the CD_3 - D_2 DCSs are very similar for the D_2 $j_2 = 0$ and 1 initial rotational levels. The DCSs for the $j_2 = 0 \rightarrow 2$ transition (not plotted) are in general more backward scattered for H_2 than for D_2 for small Δn changes ($n' \leq 5$) and have the same angular dependence for larger Δn changes. In addition, for a given CD_3 transition, the ratio of the ICSs for the $j_2 = 0 \rightarrow 2$ to the $j_2 = 0 \rightarrow 0$ transition is

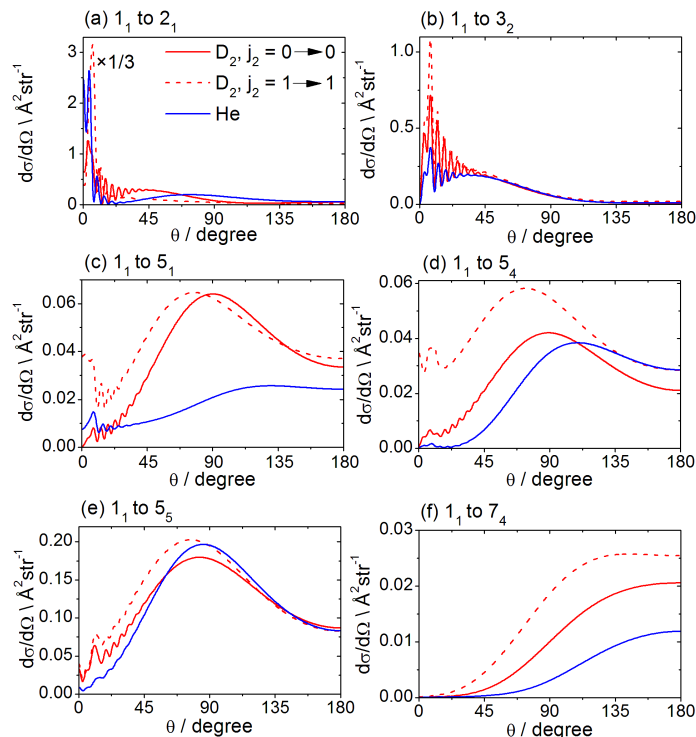


Figure 6.11: Computed state-to-state DCSs for inelastic scattering of CD_3 from the 1_1 rotational level into various final rotational levels in collisions with D_2 (red) and He (blue) at a collision energy of 640 cm^{-1} . The solid and dashed red curves are CD_3 - D_2 DCSs for which the initial rotational level j_2 of the D_2 collision partner equals 0 and 1, respectively, and is the same after the collision. In panel (a), the $j_2 = 1 \rightarrow 1$ DCS has been multiplied by a factor of $1/3$.

much smaller for the H_2 collision partner than for D_2 ; this is presumably due to the larger energy gap for $\Delta j_2 = 2$ transition in H_2 . The PESs for CD_3 - D_2 and CD_3 - H_2 scattering are identical, so observed differences in DCSs must be attributed to the effects of different masses of the collider, and any associated changes to the quantized rotational energy levels of H_2 and D_2 .

Conversely, collisions of CD_3 with D_2 and He have the same reduced mass, but are governed by different PESs. A further difference between He and D_2 collision partners is that D_2 has a rotational degree of freedom, so can be rotationally excited or de-excited in a collision, and collisions can also occur with an initially rotationally excited molecule. In our experiments (present work and Ref. [200]), the D_2 molecular beam has a larger mean speed than does the He beam [because of the larger heat capacity ratio for a monatomic

gas ($\gamma = 5/3$) than for a diatomic gas ($\gamma = 7/5$]. To make a clear comparison of these two systems, we have calculated $\text{CD}_3\text{-He}$ DCSs at the same collision energy (and hence relative velocity) as the present experiments on $\text{CD}_3\text{-D}_2$. Figure 6.11 presents computed DCSs for selected transitions from the 1_1 rotational level, the lowest level of the E nuclear spin modification, for CD_3 in collisions with D_2 and He at a collision energy of 640 cm^{-1} . Each DCS depicted represents an example of a transition directly coupled by one of the largest expansion coefficients of the PES for the $\text{CD}_3\text{-He}$ system (see Fig. 3 in Ref. [81]). For the D_2 collision partner, DCSs are presented for initial rotational levels $j_2 = 0$ and 1, with no collision-induced change in j_2 . DCSs for a wider range of CD_3 initial and final rotational levels can be found online from the supplementary materials of Ref. [137]. The DCSs for initial $j_2 = 1$ of D_2 are often larger, in particular in the forward direction [note the scaling of the $j_2 = 1 \rightarrow 1$ DCS in Fig. 6.11(a)].

The $\text{CD}_3\text{-D}_2$ DCSs show similar propensities for changes in the CD_3 rotational quantum numbers n and k as for $\text{CD}_3\text{-He}$ collisions [200]. For small changes Δn in the rotational angular momentum, the DCSs for $\Delta k = 0$ transitions have fairly sharp forward peaks and broad, lower intensity peaks in the backward hemisphere [Fig. 6.11(a)]. These transitions are enabled mainly by the $(l_1, \mu_1) = (2, 0)$ terms, in a similar fashion to the role of the V_{20} term for $\text{CD}_3\text{-He}$ [138]. The $\Delta k \neq 0$ transitions for small Δn changes display broad DCSs extending over the entire angular range, with oscillations for angles $\theta \leq 45^\circ$ [Fig. 6.11(b)]. Such transitions involve direct coupling through the $(l_1, \mu_1) = (3, 3)$ terms, in analogy to the role of the V_{33} term for $\text{CD}_3\text{-He}$ [138]. The $\Delta k = 1$ transitions for the E nuclear spin modification, e.g. the $1_1 \rightarrow 3_2$ transition in panels (b), have DCSs very similar in shape to those for $\Delta k = 3$ transitions for A_1 and A_2 levels, e.g. the $0_0 \rightarrow 3_3$ transition. As discussed in detail previously for $\text{CD}_3\text{-He}$ [81, 138, 200], these $\Delta k \neq 0$ transitions for E levels are also enabled by the $(l_1, \mu_1) = (3, 3)$ terms. For transitions with larger changes in the rotational quantum number n , the DCSs shift toward the backward hemisphere, as can be seen in the comparison of experimental and computed DCSs displayed in Figs. 6.7

and 6.9 for D₂ and H₂ collision partners, respectively.

6.5 Conclusions

The experimental measurements reported here of inelastic scattering of CD₃ radicals with H₂ and D₂ molecules represent the first DCSs obtained for collisions of a polyatomic radical with a diatomic molecule. We have compared these experimental DCSs with the outcomes of close coupling quantum-mechanical calculations performed using a newly determined *ab initio* PES computed at the RCCSD(T)-F12a level of theory. We find good agreement between the experimental and calculated DCSs, with the exception of scattering into the $n' = 5$ and 6 levels of CD₃, as probed by the $S(5)$ and $S(6)$ REMPI lines in collisions with D₂ and the $R(5)$ and $S(5)$ lines in collisions with H₂. This agreement suggests that the PES and the scattering calculations provide an accurate description of the interaction of CD₃ with these diatomic molecules, at least at energies around 600–700 cm⁻¹ corresponding to our experimental conditions.

The DCSs for inelastic scattering of CD₃ with H₂ and D₂ peak in the forward hemisphere for $n' = 2-4$ and shift more to sideways and backward scattering for $n' = 5$. As the energy transfer in a collision increases, the DCSs are increasingly dominated by backward scattering ($n' = 6-8$). This same behavior is recognized for inelastic scattering of diatomic and polyatomic molecules and it is also consistent with our prior report [200] of inelastic scattering of CD₃ with He. DCSs for a given $n_k \rightarrow n'_{k'}$ transition show similar angular dependences for D₂ and H₂ as collision partners. Since CD₃-D₂ and CD₃-H₂ interactions are described by the same PES, small differences between DCSs or ICSs for D₂ and H₂ collision partners can be attributed to mass effects, or, in the case of transitions involving a change in the rotational angular momentum of the diatomic collider, to mass-related changes in the quantized energy level structure.

We also computed rotational-level resolved integral cross sections for collision of CD₃ with D₂ and H₂. The ICSs for inelastic scattering of CD₃ with D₂ and H₂ $j_2 = 1$ are

larger than for $j_2 = 0$, indicating that an initially rotating D_2 or H_2 molecule increases the probability of a given CD_3 transition. The ratio of ICSs for $j_2 = 0 \rightarrow 2$ to $j_2 = 0 \rightarrow 0$ transitions in the diatomic, for a particular change in the CD_3 angular momentum, is much smaller for H_2 than for D_2 because of the larger energy gap between rotational levels of the lighter isotopologue. CD_3 - D_2 DCSs are very similar for collisions with D_2 initially in $j_2 = 0$ and 1 rotational levels.

We also compared the DCSs for CD_3 - D_2 with CD_3 -He measured previously [200]. Comparison of these systems is interesting because they have the same reduced mass, but the scattering dynamics of CD_3 with D_2 and He is governed by different PESs, and thus the forces acting between the collision partners. For example, the global minimum of the CD_3 - D_2 PES has $D_e = 99.0 \text{ cm}^{-1}$, which is significantly larger than for CD_3 -He [27.0 cm^{-1} (Ref. [138])]. The equilibrium geometry for CD_3 - D_2 is $R = 6.57 a_0$, $\theta_1 = 0^\circ$, $\theta_2 = 0^\circ$. The D_2 molecule thus lies along the C_3 axis of the methyl radical as opposed to the equilibrium geometry of the global minimum for CD_3 -He, for which the He atom lies in the molecular plane and bisects two C-H bonds at $R = 6.52 a_0$.

When comparisons are made between computed DCSs for CD_3 - D_2 and CD_3 -He scattering at the same collision energy, we find a similar dependence on scattering angle. This observation is particularly the case for transitions directly coupled by terms representing the three-fold anisotropy associated with the azimuthal angle about the C_3 symmetry axis of the radical. The ICSs for CD_3 -He and CD_3 - D_2 , in which the D_2 is in an initial level with $j_2 = 0$, are of comparable magnitudes.

Chapter 7

OH–H₂ Potential Energy Surfaces and Bound States

This chapter contains long excerpts of an unpublished manuscript titled “The interaction of OH($X^2\Pi$) with H₂: *Ab initio* potential energy surfaces and bound states”, by Qianli Ma, Jacek A. Kłos, Millard H. Alexander, Ad van der Avoird, and Paul J. Dagdigian.

The majority of the *ab initio* calculations in this work were performed by Jacek A. Kłos.

7.1 Introduction

There has been considerable interest in the dynamics of the OH–H₂ system. One important reason is that the OH + H₂ → H₂O + H reaction is one of the simplest four-atom reactions [127, 257]. The OH($X^2\Pi$)–H₂ system is also of astrophysical importance [258, 259].

Loomis and Lester have stabilized the weakly-bound OH($X^2\Pi$)··H₂/D₂ complexes [260], reporting binding energies of, for H₂, 54 cm^{−1} and, for D₂, > 66 cm^{−1}, which they assigned to the OH-*ortho*-H₂ and OH-*para*-D₂ complexes, respectively [261]. Subsequently, Lester and coworkers have observed and analyzed the rotational structure of these complexes [262–264].

Andresen *et al.* [265, 266] first determined relative inelastic cross sections of OH $j = 3/2 F_1$ (with equal populations in both Λ -doublet levels) in collisions with H₂ and D₂.

Later, Schreel and ter Meulen [144] measured Λ -doublet resolved inelastic cross sections for OH-H₂, using an electrostatic hexapole as a state selector for OH. Recently Kirste *et al.* [96] used a Stark decelerator [267] to measure the energy dependence of inelastic cross sections for transitions out of the upper $j = 3/2 F_1$ Λ -doublet level in collisions with D₂.

Here we report two accurate sets of OH(X²Π)-H₂ potential energy surface (PESs) for the study of both bound states and inelastic collisions. Because of its orbital degeneracy, two potential energy surfaces (PESs) are needed to describe the interaction of OH with a closed-shell collision partner [268].

To treat the dynamics of the OH-H₂ system, it is most convenient to describe the interaction of the collision partner with the two ($\Lambda = \pm 1$) components of the Π state of OH. Here, $\Lambda = \pm 1$ is the body-frame projection of the electronic orbital angular momentum. These “definite- Λ ” states are linear combinations of Cartesian basis functions, $|\Pi_x\rangle$ (with electronic occupancy $\dots \pi_x \pi_y^2$) and $|\Pi_y\rangle$ (with electronic occupancy $\dots \pi_x^2 \pi_y$). The Cartesian states are eigenfunctions of the operator corresponding to the reflection of the spatial coordinates of all the electrons in a plane through the OH axis.

In this Cartesian basis, the wave functions for the supermolecular system of OH and a structureless atom are eigenfunctions of the same reflection operator, and correspond to two states of differing reflection symmetry (A' and A''). The electronic energies of these two states correspond to interaction potentials which are conventionally labeled $V_{A'}$ and $V_{A''}$. In the definite- Λ basis, the matrix of the electronic Hamiltonian is a full 2×2 matrix, with matrix elements which are the sum and difference of $V_{A'}$ and $V_{A''}$ [106].

In general the tetratomic OH-H₂ system is nonplanar. There will be still two electronic states, which we can express as linear combinations of the two Cartesian basis functions $|\Pi_x\rangle$ and $|\Pi_y\rangle$. The matrix of the electronic Hamiltonian can be diagonalized in this “adiabatic” basis, at each geometry, by a rotation of the adiabatic wave functions through a single “mixing angle”.

Two strategies have been previously employed to treat this: The first is to sample

only OH-H₂ geometries that have a plane of symmetry, in which case the wave functions for the two electronic states have differing reflection symmetries. This allows the two PESs, which correspond to the lowest states of A' and A'' symmetry, to be calculated separately using conventional quantum chemical approaches. This strategy was adopted by Kochanski and Flower (KF) [269], who used self-consistent field (SCF) calculations with a perturbation theory approximation to include electron correlations, and later by Miller *et al.* (MCKW) [148] in coupled electron pair approximation (CEPA) calculations.

Alternatively, one can obtain the mixing angle directly in the *ab initio* calculations. This strategy was implemented by Offer and van Hemert (OvH) [268], using the multi-configuration self-consistent field (MCSCF) method with corrections for the dispersion interaction.

The PESs mentioned above have been tested by comparison with experimental studies of rotationally inelastic scattering and the determination of OH-H₂ bound-states. Both the KF and MCKW PESs gave state-to-state inelastic cross sections in good agreement with the experiments by Andresen *et al.*, although the agreement was better for cross sections in which OH remains in its initial (F_1) spin-orbit manifold [148, 270, 271]. Cross sections computed from the OvH PESs agree well with the later scattering experiments of Schreel and ter Meulen [144, 272]. The KF and MCKW PESs predict dissociation energies (D_0'') of the OH-*ortho*-H₂ complex of 42.2 and 85.4 cm⁻¹, respectively [148, 273]. These numbers are only in semi-quantitative agreement with the experimental value of 54 cm⁻¹ [261].

It is probable that these disagreements reflect inaccuracies in the PESs, either because the *ab initio* calculations sampled a small number of geometries, or because of a simplistic (by today's standards) treatment of electron correlation.

The two strategies mentioned above have their own shortcomings. In the first approach one samples very limited number of orientations. The second tack requires *ab initio* methods that can compute excited-state energies accurately, which is less cost-

effective. In this paper, we present two high-quality sets of OH-H₂ PESs, one based on a multi-reference configuration interaction [MRCISD+Q(Davidson)] method and the other based on an explicitly correlated coupled cluster method with single-, double-, and (pertubatively) triple-excitations [CCSD(T)-F12a].

This chapter is organized as follows: We present in Sec. 7.2 the theory for the analytical expansion of the OH-H₂ PESs in a definite- Λ basis. In Sec. 7.3 we describe our treatment in developing the PESs. We show that despite its incomplete angular sampling, the CCSD(T) PESs are more accurate. Features of the PESs and comparison with previous PESs are also illustrated in Sec. 7.3. We present bound-state calculations for the OH-H₂ complex with our PESs in Sec. 7.4. A discussion in Sec. 7.5 concludes this paper.

7.2 Theory

The theoretical framework for the PESs describing the interaction of a diatomic molecule in a $^2\Pi$ electronic state, like OH($X^2\Pi$), and another diatomic molecule in a $^1\Sigma$ electronic state has been described previously [69, 268, 270]. In this section we summarize and clarify the previous treatments. More technical details on the theory can be found in Appendix A.

7.2.1 Interaction Potential

We use the coordinate system of Fig. 7.1 to describe the OH-H₂ system. The OH moiety lies in the XZ plane. We shall keep the OH and HH bond distances frozen. The interaction then depends on the two polar angles θ_O and θ_H , the azimuthal angle ϕ_H of the HH moiety, and the distance R between the centers-of-mass of the OH and HH moieties. We define the orientation of the OH so that $\theta_O = 0$ corresponds to the H-atom of the OH pointing toward the H₂ moiety.

To intuit a suitable expansion for the interaction potential, we write the wave function for the OH-H₂ system as a product of a definite- Λ function on OH multiplied by the

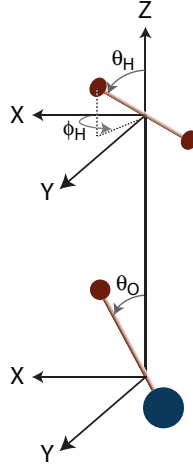


Figure 7.1: The definition of the coordinate system describing the interaction between OH and H₂. The OH moiety lies in the XZ plane, with $\theta_O = 0$ corresponding to the H-atom of the OH pointing toward the H₂ moiety.

non-degenerate wave function for H₂ in its $^1\Sigma^+$ electronic ground state, namely

$$\Psi_{\text{OH}(\Lambda)\text{-H}_2} \equiv |\Lambda\rangle = \psi_\Lambda \psi_{\text{H}_2}$$

As discussed in Appendix A, we follow earlier work on the interaction between a $^2\Pi$ molecule and a closed shell atom [106]. For the more general case of a $^2\Pi$ molecule and a closed shell diatom the elements of the 2×2 matrix of interaction potential in the definite- Λ basis can be expressed in the body frame (BF) expansion

$$\begin{aligned} V_{\Lambda',\Lambda}(R, \theta_O, \theta_H, \phi_H) &= \sum_{l_1 l_2 l} V_{l_1 l_2 l}^{(\Lambda'-\Lambda)}(R) \sum_m \langle l_1 m, l_2, -m | l 0 \rangle \\ &\times d_{m, \Lambda'-\Lambda}^{l_1}(\theta_O) D_{-m, 0}^{l_2*}(\phi_H, \theta_H, 0), \end{aligned} \quad (7.1)$$

where $\langle l_1 m_1, l_2 m_2 | l m \rangle$ is a Clebsch-Gordan coefficient, and $d_{m, m'}^l$ and $D_{m, m'}^l$ are reduced and full Wigner rotation matrices [28]. This equation is equivalent to Eq. (27) of Wormer and co-workers [69] under the assumption that the OH molecule lies in the XZ plane.

Rist, Alexander, and Valiron have shown [135] that the symmetry of the Hamiltonian

with respect to inversion of all the coordinates

$$\hat{P} \equiv \{\theta_O, \theta_H, \phi_H, Z\} \rightarrow \{\pi - \theta_O, \pi - \theta_H, \pi + \phi_H, -Z\}, \quad (7.2)$$

restricts $(l_1 + l_2 + l)$ to even values. Wormer and co-workers have used time-reversal invariance of the Hamiltonian to make the same argument [69]. Also, the potential must be symmetric with respect to interchange of the two identical H atoms. This forces l_2 to be even.

7.2.2 Diagonal ($\Lambda' = \Lambda$) Matrix Elements

Since the Hamiltonian is invariant with respect to the chirality of a rotation around \vec{R} , the summation over m in Eq. (7.1) must be independent of the sign of m . Consequently, we can restrict the sum over m to positive semi-definite values and use a symmetry property of the Clebsch-Gordan coefficient to write the diagonal matrix elements V_d as

$$V_d = \sum_{l_1 l_2 l} V_{l_1 l_2 l}^{(0)}(R) \sum_{m \geq 0} \langle l_1 m, l_2, -m | l 0 \rangle (1 + \delta_{m0})^{-1} \\ \times [e^{-im\phi_H} + (-1)^{l_1+l_2-l} e^{im\phi_H}] d_{m0}^{l_1}(\theta_O) d_{-m,0}^{l_2}(\theta_H), \quad (7.3)$$

Since for the diagonal potential the sum is limited to even values of $(l_1 + l_2 + l)$, the electronic Hamiltonian will be invariant with respect to a reflection in the XZ plane in Fig. 7.1 ($\phi_H \rightarrow -\phi_H$). Under this constraint the sum of exponentials in Eq. (7.3) is proportional to $\cos(m\phi_H)$, which allows us to write V_d as

$$V_d = \sum_{l_1 l_2 l} V_{l_1 l_2 l}^{(0)}(R) \sum_{m \geq 0} \langle l_1 m, l_2, -m | l 0 \rangle (2 - \delta_{m0}) \\ \times d_{m0}^{l_1}(\theta_O) d_{-m,0}^{l_2}(\theta_H) \cos(m\phi_H). \quad (7.4)$$

Since the diagonal elements of a Hermitian matrix must be real, and since all the terms

in this equation except the $V_{l_1 l_2 l}^{(0)}$ expansion coefficients are real, it follows that the these coefficients must also be real.

7.2.3 Off-Diagonal ($\Lambda' \neq \Lambda$) Matrix Elements

The reader can easily deduce from the work of Wormer and co-workers [69] [see their Eqs. (30) and (31)] that the V expansion coefficient of Eq. (7.1) obey the symmetry relation

$$V_{l_1 l_2 l}^{(-2)}(R) = (-1)^{l_1 + l_2 + l} V_{l_1 l_2 l}^{(2)}(R). \quad (7.5)$$

Because the off-diagonal matrix elements of the Hamiltonian must be Hermitian, Eq. (7.5) implies that the $V_{l_1 l_2 l}^{(\pm 2)}(R)$ expansion coefficients must be real.

We designate the off-diagonal $V_{\Lambda'=1, \Lambda=-1}(R, \theta_O, \theta_H, \phi_H)$ PES as V_o ,

$$V_o = \sum_{l_1 l_2 l} V_{l_1 l_2 l}^{(2)}(R) \sum_m \langle l_1 m, l_2, -m | l 0 \rangle e^{-im\phi_H} d_{m2}^{l_1}(\theta_O) d_{-m,0}^{l_2}(\theta_H), \quad (7.6)$$

7.2.4 Restriction on $(l_1 + l_2 + l)$

As discussed already, the requirement of inversion symmetry and time reversal invariance forces the sum $(l_1 + l_2 + l)$ expansion indices to be even [135]. Strictly speaking, however, this is limited to the expansion of the Coulomb interaction r_{ij}^{-1} . The interaction of linear molecule in a Π electronic state with a closed-shell diatomic exhibits the same lowering of an underlying symmetry as the interaction of a non-linear triatomic with a closed-shell diatomic. Consequently, the question of the role of $(l_1 + l_2 + l)$ =odd terms applies to the angular expansion of the intermolecular interaction involving non-linear triatomic molecules [65, 251].

Green [251] has investigated various model potentials for interactions involving a non-linear molecule. He concluded that odd $(l_1 + l_2 + l)$ terms “cannot be excluded on the grounds of the underlying symmetry of space itself”. Consequently, in fitting our ab

initio interaction energies, we did include the flexibility of both even and odd values of $(l_1 + l_2 + l)$ for the off-diagonal matrix elements.

7.2.5 Normalization

The individual $\{l_1, l_2, l\}$ basis functions in the expansions in Eqs. (7.3) and (7.6) are not normalized with respect to integration over θ_O , θ_H , and ϕ_H . Comparable expansions in orthonormal bases are

$$V_d = (8\pi)^{-1/2} \sum_{l_1 l_2 l} B_{l_1 l_2 l}(R) [(2l_1 + 1)(2l_2 + 1)]^{\frac{1}{2}} \\ \times \sum_{m \geq 0} \langle l_1 m, l_2, -m | l 0 \rangle (2 - \delta_{m0})^{1/2} d_{m0}^{l_1}(\theta_O) d_{-m,0}^{l_2}(\theta_H) \cos m \phi_H, \quad (7.7)$$

and

$$V_o = (8\pi)^{-1/2} \sum_{l_1 l_2 l} F_{l_1 l_2 l}(R) [(2l_1 + 1)(2l_2 + 1)]^{\frac{1}{2}} \\ \times \sum_m \langle l_1 m, l_2, -m | l 0 \rangle e^{-im\phi_H} d_{m0}^{l_1}(\theta_O) d_{-m,0}^{l_2}(\theta_H). \quad (7.8)$$

Examination of the magnitude of these $B_{l_1 l_2 l}$ and $F_{l_1 l_2 l}$ coefficients will provide the most meaningful insight into the importance of individual terms. Note that the earlier treatment of collisions between a $^2\Pi$ molecule and a structureless atom [106, 274] used an unnormalized basis.

7.2.6 Adiabatic and Quasi-Diabatic Bases

Ab initio calculations give electronically adiabatic states. For a four-atom $^2\Pi^{-1}\Sigma^+$ system in geometries in which there is a reflection plane that lies in the XZ or YZ plane, the electronic wave functions will belong to different irreducible representations A' and A'' in C_s symmetry. We will designate these states as $|\Pi_x\rangle$ and $|\Pi_y\rangle$, in which the Cartesian index designates the singly-filled π lone-pair orbitals on the OH molecule, *i.e.* $|\Pi_x\rangle \sim \pi_x^1 \pi_y^2$

and $|\Pi_y\rangle \sim \pi_x^2 \pi_y^1$. Because these two Cartesian states belong to different irreducible representations, they are not mixed by the OH-H₂ interaction. In these geometries, the Cartesian states are then the electronically adiabatic states and their energies, the electronically adiabatic energies.

Consider now an arbitrary OH-H₂ geometry, in which there are no symmetry elements save the identity operator (C₁ symmetry). In an *ab initio* calculation it is possible to rotate the orthogonal π molecular orbitals so that one lies in the *XZ* plane and the other, perpendicular to this plane. In our specific application, the molecular orbitals from a complete active space, self-consistent field (CASSCF) calculation are rotated to achieve maximum overlap with the CASSCF orbitals for the OH-H₂ system at the same geometry except for $\phi_H = 0$.

We use these rotated orbitals to define two state functions $\pi_x^1 \pi_y^2$ and $\pi_x^2 \pi_y^1$. These will be mixed by the Hamiltonian. Diagonalization will give rise to two electronically adiabatic states, which we designate as $|u\rangle$ (upper) and $|l\rangle$ (lower). These are 2×2 linear transformations of the two Cartesian states, namely

$$\begin{pmatrix} |u\rangle \\ |l\rangle \end{pmatrix} = \begin{pmatrix} \cos \chi & \sin \chi \\ -\sin \chi & \cos \chi \end{pmatrix} \begin{pmatrix} |\Pi_x\rangle \\ |\Pi_y\rangle \end{pmatrix} = \mathbf{C}^T \begin{pmatrix} |\Pi_x\rangle \\ |\Pi_y\rangle \end{pmatrix}, \quad (7.9)$$

where χ is the so-called “mixing angle”. This latter depends on the OH-H₂ geometry, just as the potential energy surfaces.

The 2×2 basis in terms of the rotated π orbitals defines what are called “quasi-diabatic” states (or, more simply, “diabatic” states) [143, 275]. In this diabatic basis the

matrix of the interaction Hamiltonian is [69, 268]

$$\begin{aligned} \begin{pmatrix} V_{xx} & V_{xy} \\ V_{yx} & V_{yy} \end{pmatrix} &= \mathbf{C} \begin{pmatrix} V_u & 0 \\ 0 & V_l \end{pmatrix} \mathbf{C}^T \\ &= \begin{pmatrix} V_u \cos^2 \chi + V_l \sin^2 \chi & \frac{1}{2}(V_u - V_l) \sin 2\chi \\ \frac{1}{2}(V_u - V_l) \sin 2\chi & V_u \sin^2 \chi + V_l \cos^2 \chi \end{pmatrix}, \end{aligned} \quad (7.10)$$

where $V_{q'q}$ is a shorthand notation for $\langle \Pi_{q'} | \hat{H}_{int} | \Pi_q \rangle$, and V_l and V_u are the adiabatic interaction energies. This equation should be compared to Eq. (3) of Ref. [268], which gives the relation between the definite- Λ diabatic and adiabatic states.

As with the one-electron molecular orbitals, the definite- Λ states are linear combinations of the Cartesian states, namely

$$|\Pi_{\pm 1}\rangle = \mp 2^{-\frac{1}{2}} (|\Pi_x\rangle \pm i |\Pi_y\rangle), \quad (7.11)$$

Wormer and co-workers have shown (see Eq. (4) of Ref. [69]) that in the definite- Λ basis the diagonal potential is

$$V_d = \frac{1}{2}(V_l + V_u), \quad (7.12)$$

and the off-diagonal potential is

$$V_o = \frac{1}{2}(V_l - V_u)(\cos 2\chi - i \sin 2\chi). \quad (7.13)$$

For any OH-H₂ geometry in which the XZ plane is a plane of reflection symmetry V_{xy} and V_{yx} vanish. For these geometries, the diagonal potentials are identical to the adiabatic potentials V_l and V_u , and it follows that

$$V_d = \frac{1}{2}(V_{yy} + V_{xx}), \quad (7.14)$$

and

$$V_o = \frac{1}{2}(V_{yy} - V_{xx}). \quad (7.15)$$

Equations (7.14) and (7.15) are equivalent to the “sum” and “difference” PESs usually used in describing the interaction between a $^2\Pi$ atom and a structureless atom [106, 107, 274].

7.2.7 Symmetry Restrictions

The symmetry of the potential with respect to interchange of the two hydrogen atoms and to reflection in the XZ plane (Fig. 7.1) allows us to restrict the *ab initio* calculations to a subspace of the complete coordinate space grid. As a consequence, in the *ab initio* calculation of the potential energy surfaces, we can restrict ourselves to the subspace $0 \leq \theta_H \leq \pi/2$ and $0 \leq \phi_H \leq \pi$.

7.2.8 Limiting Geometries

When the OH molecule lies along the Z axis, $\theta_O = 0$ or π . The two adiabatic potential energies, V_l and V_u , will obviously be independent of ϕ_H .

When the H_2 molecule is in the XZ plane, *i.e.*, $\phi_H = 0$, or $\theta_H = 0$ or π , $|\Pi_x\rangle$ and $|\Pi_y\rangle$ will be symmetric and antisymmetric to reflection in the XZ plane. Since the identification of V_l and V_u with V_{xx} and V_{yy} is different for $\theta_H = 0$ and π , we have $\chi = 0$ and $\pi/2$ for these two values of θ_H . For both cases, the off-diagonal potential V_o is real.

When the OH molecule lies along the Z axis, the OH-HH system is always planar. However, the CASSCF orbitals are rotated to achieve maximum overlap with those from a calculation in which the XZ plane (Fig. 7.1) defines the plane of reflection symmetry. Because the system is planar, there is no additional coupling between the two states. In the case where $\theta_O = 0$ the mixing angle χ is equal to ϕ_H , while for $\theta_O = \pi$ we have $\chi = -\phi_H$ [69, 268].

Finally, in linear geometries (both polar angles 0 or π), the degeneracy of the two Π states of OH is not lifted. The two adiabatic states of the complex are degenerate.

7.3 Potential Energy Surfaces

7.3.1 MRCI Calculations

We used the MOLPRO program suite [151] to determine the two lowest adiabatic energies of the OH-H₂ complex, E_l and E_u , as well as the mixing angle χ . For each geometry, we first performed a CASSCF calculation, with 1 core orbital and 7 active orbitals, and the augmented correlation-consistent polarized quadruple zeta (aug-cc-pVQZ) basis [240]. As discussed in Sec. 7.2.6, the resulting orbitals were rotated to maximize the overlap with CASSCF orbitals from a calculation with $\phi_H = 0$ and the other coordinates unchanged.

With configuration state functions built from these diabatic orbitals, we then performed an internally-contracted, multi-reference configuration interaction calculation including all single and double excitations (IC-MRCISD) to determine the two adiabatic energies. The CI calculation included 7 active orbitals and 210 external orbitals. We used the cluster corrected energies of Davidson [59]. These MRCI calculations were carried out on a four-dimensional grid (R , θ_O , θ_H), and ϕ_H (Fig. 7.1).

We assumed that the OH and HH bond distances remain fixed at the average value of r in the $v=0$ vibrational levels (1.8509 a_0 for OH [276] and 1.448736 a_0 for H₂ [277]). The MRCISD method is not size-extensive, i.e., the calculated energy of the OH-H₂ complex does not precisely equal the sum of the energies of OH and H₂ when the distance R goes to infinity. Therefore, we obtained the interaction energy at a given geometry from the expression

$$V_{\text{MRCI}}(R, \Omega) = E_{\text{MRCI}}(R, \Omega) - E_{\text{MRCI}}(R = 100 a_0, \Omega) \quad (7.16)$$

where Ω denotes the three angles. Finally, the quasi-diabatization procedure in MOLPRO was used to compute $\chi(R, \Omega)$ from analysis of the CI coefficients [278, 279].

The angular grid included 845 orientations, with 11 values of θ_O defined by $\cos \theta_O =$

−1 to 1 in steps of 0.2, 6 values of θ_{H} defined by $\cos \theta_{\text{H}} = 0$ to 1 in steps of 0.2, and 13 values of ϕ_{H} from 0 to π in steps of $\pi/12$. This choice of grid provides a uniform sampling of the differential solid angle $\sin \theta_1 d\theta_1 \sin \theta_2 d\theta_2 d\phi_2$ [254]. The OH-H₂ distance was spanned by 32 values of R ranging from $3.5a_0$ to $16a_0$.

We found that the angular dependence of the computed interaction energy is not smooth beyond $R = 16a_0$. We discarded 112 of the 27456 points, corresponding to small values of R , for which there was unacceptable scatter in the calculated values of V_o .

7.3.2 CCSD(T) Calculations

We also carried out restricted explicitly correlated coupled-cluster calculations with all single- and double-, and (perturbatively) triple-excitations [RCCSD(T)-F12a] [51, 53]. The advantage of a coupled-cluster method is that one can recover more of the correlation energy. The disadvantage is that it is difficult to determine the energy of the second adiabatic state, except in high-symmetry geometries where the wave functions for the two states belong to different irreducible representations.

We performed RCCSD(T)-F12a calculations with the augmented correlation-consistent triple-zeta basis [240, 252, 253] supplemented with mid-bond functions (*3s3p2d2f1g1h*) at the following high-symmetry OH-H₂ geometries: (1) $\phi_{\text{H}} = 0$ or 180° , and a grid including 11 values of θ_{O} ($0^\circ, 20^\circ, 40^\circ, 60^\circ, 80^\circ, 90^\circ, 100^\circ, 120^\circ, 140^\circ, 160^\circ$, and 180°) and 7 values of θ_{H} ($0^\circ, 22.5^\circ, 30^\circ, 45^\circ, 60^\circ, 67.5^\circ$, and 90°); (2) $\phi_{\text{H}} = 90^\circ$, $\theta_{\text{O}} = 0^\circ$ or 180° , and θ_{H} with each of the 7 values listed above; and (3) $\phi_{\text{H}} = 90^\circ$, $\theta_{\text{H}} = 0^\circ$ or 90° , and θ_{O} with each of the 11 values listed above excluding 0° and 180° . This choice of angles gives rise to 186 orientations, of which 131 are unique.

For all these geometries the existence of a plane of symmetry allows us to determine RCCSD(T) energies for the lowest states of both A' and A'' symmetry. These energies correspond to V_{xx} and V_{yy} depending on the chosen plane of symmetry. The potential in the definite- Λ basis was computed with Eqs. (7.14) and (7.15). The grid in the OH-HH

distance consisted of 39 values ranging from $3.5 a_0$ to $30 a_0$.

We used the scaled triples correction as implemented in MOLPRO [151]. In these RCCSD(T) calculations we used the counterpoise method to estimate the basis set superposition error (BSSE) [57], in which we subtract the energies of the fragments computed in the (supermolecular) atomic orbital basis. The interaction energy is

$$V_{\text{CCSD(T)}}(R, \Omega) = E_{\text{CCSD(T)}}^{(\text{OH-HH})}(R, \Omega) - E_{\text{CCSD(T)}}^{(\text{OH})}(R, \Omega) - E_{\text{CCSD(T)}}^{(\text{HH})}(R, \Omega). \quad (7.17)$$

7.3.3 Fitting the Potential Energy Surfaces

The phase of the CI wave functions is not defined uniquely in the CI calculation. Consequently the signs of the the mixing angle χ as well as of the real and/or imaginary part of the off-diagonal potential may vary inconsistently from point to point. To compensate for this uncertainty in sign, we first fitted our CCSD(T) *ab initio* potential to a small set of angular basis functions. This fitted potential was then used to resolve ambiguities in the signs of the MRCI off-diagonal potentials. Manual inspection confirmed smoothness in the off-diagonal PES. Unfortunately, for a few geometries, V_o is very close to zero ($|V_o| < 0.05 \text{ cm}^{-1}$), preventing the determination of a consistent sign for these points.

The fitting procedure was as follows: We first set upper limits of 9 and 6 for, respectively, l_1 and l_2 . The subsequent expansion contains 126 terms for V_d and 198 terms for V_o . We then carried out a least-squares fit of the sign-corrected MRCI interaction energies at $R = 5 a_0$ (a point in the repulsive region of the PES where we don't anticipate that the important expansion coefficients will be changing sign) to Eqs. (7.7) and (7.8). All terms with expansion coefficients of absolute value greater than 1.5 cm^{-1} were retained. This corresponds to 39 terms for V_d and 15 terms for V_o . In the latter case, 3 of the terms have odd values of $(l_1 + l_2 + l)$.

We used this (39/15)-term fitting scheme and Eqs. (7.7) and (7.8) to fit both the MRCI and the CCSD(T) PESs. Figure 7.2 displays the root-mean-square (RMS) deviation of the

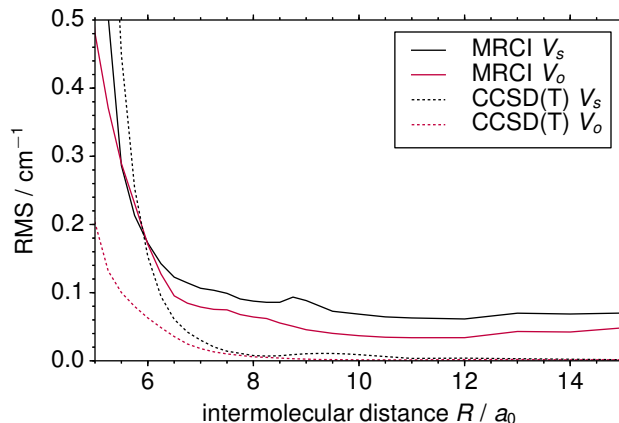


Figure 7.2: Root mean squares (RMS) as a function of intermolecular distance between the fitted potential and the *ab initio* potential for the MRCI and CCSD(T) PESs.

fits to V_d and V_o as a function of R .

Overall, we see the fit is good, and the RMS is well below 1 cm^{-1} for $R \geq 6a_0$. Because the off-diagonal potential is overall smaller in magnitude, the RMS for V_o is smaller. We will discuss this further in Sec. 7.3.5.

At short range, V_d of the CCSD(T) potential has a larger RMS. This is reasonable since the terms we used in the fit were optimized for the MRCI PESs. For V_o and V_d at long range, the CCSD(T) PESs have smaller RMS. The RMS for the MRCI PESs generally remains a constant ($0.05 \sim 0.1 \text{ cm}^{-1}$) for $R \geq 8a_0$. This is a measure of the precision of our MRCI calculations.

To estimate the systematic error of the CCSD(T) PESs due to the restriction of the angular sampling to high symmetry points, we also created a test V_d and V_o PES using only the MRCI points whose molecular geometry has a plane of symmetry [referred to in the following as the MRCI-HS (high-symmetry) PESs]. Out of the 858 orientations for each R , there are 153 that have a plane of symmetry. Fitting just these points, by means of the same procedure as described above, we obtain the MRCI-HS PESs.

7.3.4 Extrapolation of the Potential Energy Surfaces

Short Range

The calculated PES was limited to $R \geq 3.5 a_0$, which is sufficiently small for scattering and bound-state calculations. Inside this value of R , the expansion coefficients are held constant to their values at $3.5 a_0$. We note that a few expansion coefficients, of relatively small magnitude, do not vary smoothly for $R \leq 4.25 a_0$.

Long Range

The CCSD(T) PESs were extrapolated by a least-squares fit of a few *ab initio* points at large R to the form

$$V_{l_1 l_2 l}^{\text{ext}}(R) = \sum_i C_i R^{-n_i}. \quad (7.18)$$

Here V^{ext} represents an extrapolated B or F coefficient, C_i is a fitted parameter, and n_i is the appropriate power in the standard long-range expansion of the multipole-multipole electrostatic, the dispersion, and the induction interactions [66, 73]. We included only the smallest one or two values of $n_i \leq 11$ in modeling the induction and dispersion terms. Care was taken to choose a proper range of R values for this long-range fit so that none of the expansion coefficient would be artificially large at $R = 200 a_0$.

The MRCI PESs were extrapolated by a slightly different method since the *ab initio* points are less precise at long-range. We employed a multipole expansion method similar to that described in Ref. [69] to model the long-range electrostatic interaction in terms of the multipole moments of the separate OH and H₂ molecules. We used the distributed multipole [70] capability of MOLPRO to determine from MRCI calculations the multipole moments of the isolated OH and H₂ molecules. For these calculations we used a larger active space as well as an augmented correlation consistent sextuple zeta (aug-cc-pV6Z) basis set [280]. As in the calculations of the full OH-H₂ PESs, the OH and H₂ bond distances were held fixed at their average value in the $v=0$ vibrational level. In Table 7.1

Table 7.1: Multipole moments (in atomic units) of OH($X^2\Pi$) and H₂ from the calculations described in the text. Previously published experimental and theoretical values are given in parentheses.

l	m	q_{lm}
OH		
1	0	0.6442 (0.6512 ^a , 0.6512 ^b , 0.6545 ^c , 0.6472 ^d)
2	0	1.2913 (1.3939 ^c , 1.2709 ^d)
2	2	-1.1948 (-1.1825 ^c , -1.1589 ^d)
3	0	2.3494 (2.6691 ^c , 2.3023 ^d)
3	2	-0.0615 (0.7986 ^c , -0.0289 ^d)
H ₂		
2	0	0.5235 (0.4852 ^e)

^a Experimental value for the ground ro-vibrational level (Ref. [281]).

^b Theoretical value averaged over the $v=0$ vibrational distribution $\langle q_{lm} \rangle_{v=0}$ (Ref. [282]).

^c Theoretical value for $r_0(\text{OH})$ (Ref. [69]).

^d Theoretical value for $r_0(\text{OH})$ (Ref. [12]).

^e Theoretical value averaged over the $v=0$ vibrational distribution $\langle q_{lm} \rangle_{v=0}$ (Ref. [283]).

we compare our calculated values of the lower multipole moments of the OH and H₂ fragments with experiment and previous theoretical predictions.

We included in this expansion only the dipole, quadrupole, and octupole moments of OH, and the quadrupole moment of H₂. For the diagonal PES, we can thus estimate the OH-dipole/H₂-quadrupole (B_{123}, R^{-4}), the quadrupole-quadrupole (B_{224}, R^{-5}), and the OH-octupole/H₂ quadrupole (B_{325}, R^{-6}) interactions. Since there is no dipole moment between the $\Lambda = \pm 1$ and $\Lambda = \mp 1$ states of OH, for the off-diagonal PES we included just the quadrupole-quadrupole (F_{224}, R^{-5}) and the OH-octupole/H₂ quadrupole (F_{325}, R^{-6}) terms.

For these multipole-multipole interactions, the $V_{l_1 l_2 l}^{(\Lambda' - \Lambda)}$ expansion coefficients are proportional to the products of the corresponding OH and H₂ moments, multiplied by R^{-l-1} . We then subtracted these electrostatic expansion coefficients from the coefficients obtained by fitting the MRCI *ab initio* points to Eq. (7.18). The difference potential was then extrapolated to long range with Eq. (7.18), using the same method as used in extrapolating the CCSD(T) PESs. The values of n_i in Eq. (7.18) corresponding to the already modeled electrostatic interaction were excluded.

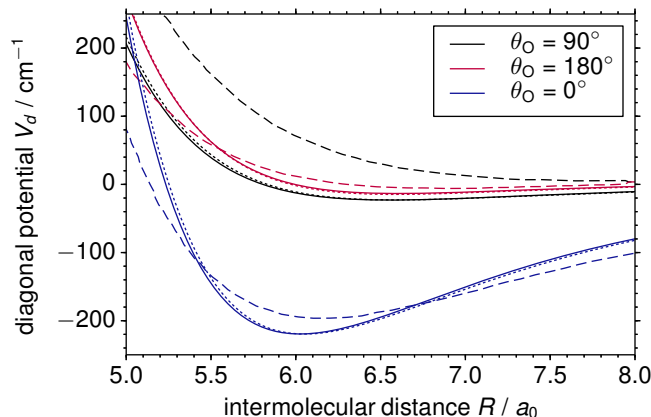


Figure 7.3: The diagonal potential V_d as a function of intermolecular distance for various θ_O with $\theta_H = 90^\circ$ and $\phi_H = 0^\circ$, obtained from the CCSD(T) PESs (solid lines), the MRCI PESs (dotted lines), and the MCKW PES (dashed lines). The MRCI and CCSD(T) curves are nearly identical to within the resolution of the plot.

We obtain the final MRCI expansion coefficients by smoothly switching, as R approaches $16a_0$, between the fit to the *ab initio* points at short range and the extrapolated expansion coefficients at long range, for the $\{l_1 l_2 l_3\} = 123, 224$ and 325 terms. For the other $\{l_1 l_2 l\}$ terms with known inverse R dependences we extrapolated by smoothly switching at $R = 16a_0$ to Eq. (7.18), or, if not, to an exponential decay.

In the case of the CCSD(T) expansion coefficients, which are smoothly varying out to $R = 30a_0$, we did not switch to the known multipole-multipole terms. For $R > 30a_0$ we just extrapolated by Eq. (7.18) for the terms with a known inverse R dependence, or by an exponential decay.

The MRCI-HS PESs were extrapolated with the same procedure and parameters as for the full MRCI PESs.

7.3.5 Fitted Potential Energy Surfaces

Expansion Coefficients

Figure 7.3 shows several radial cuts of V_d for the MRCI and CCSD(T) PESs at $\theta_H = 90^\circ$ and $\phi_H = 0^\circ$. These correspond to planar geometries with H_2 perpendicular to \mathbf{R} . Three values of θ_O (0° , 90° , and 180°) were chosen. For comparison, we also show

Table 7.2: Predicted and experimental OH-H₂ equilibrium separation (R_e) and dissociation energies for the OH-H₂ complex.

PES	$R_e(a_0)$	$D_e(\text{cm}^{-1})$	$D_0(\text{cm}^{-1})$			
			OH-H ₂		OH-D ₂	
			<i>para</i>	<i>ortho</i>	<i>para</i>	<i>ortho</i>
KF ^a	5.90	248.8	53.7	85.4		
MCKW ^b	6.08	188.1	28.6	42.2		
MRCI ^c	6.05	219.6	38.7	55.8	69.5	53.8
MRCI-HS ^c	6.05	219.6	38.5	55.5	69.2	53.5
CCSD(T) ^c	6.02	219.5	36.1	53.7	67.5	51.4
Experiment ^d				54	> 66	

^a PESs described in Ref. [269], and bound states in Ref. [273].

^b Ref. [148].

^c This work.

^d Ref. [261].

comparable radial cuts of the CEPA MCKW PESs (adapted from Ref. [148]).

The MRCI and the CCSD(T) PESs agree very well. Of the three orientations plotted, only the $\theta_{\text{O}} = 0$ curve shows a significant well, which corresponds to a T-shaped geometry with the H-end of the OH pointing to H₂. The minima on these curves are also the global minima of V_d , whose positions and depths are tabulated in Table 7.2. The geometry of these global minima are a consequence of both the dipole-quadrupole interaction and the quadrupole-quadrupole interaction. The signs of both quadrupole moments are positive, which implies that there is an excess of positive charge at both ends of each molecule and of negative charge in the middle. Therefore, the quadrupole-quadrupole interaction favors T-shaped geometry.

Both minima are significantly more attractive than predicted by the MCKW PESs (see Table 7.2). This is not unexpected, since the MCKW *ab initio* calculations were based on the CEPA method which gives a less complete recovery of electron correlation and, hence, a shallower van der Waals well. Secondly, the monomer bond lengths were slightly different. Here, for both OH and H₂ we used the average value of r in the ground vibrational level, namely, $\langle r \rangle_{v=0}$ for both OH and H₂, as recommended by Faure *et al.*

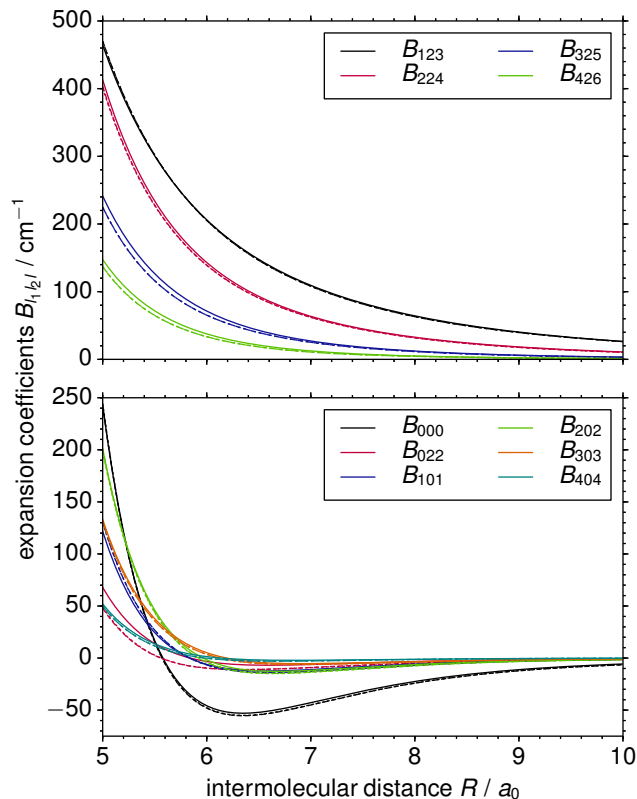


Figure 7.4: Larger $B_{l_1 l_2 l}$ expansion coefficients for the diagonal potential V_d as a function of intermolecular distance R for the CCSD(T) (solid lines) and MRCI (dashed lines) PESs. The corresponding expansion coefficients for the MRCI-HS PES are indistinguishable from the dashed lines. The upper panel shows the $B_{l_1 l_2 l}$ terms which go asymptotically to multipole-multipole electrostatic interactions; the lower panel displays other coefficients.

[64]. Since $\langle r \rangle_{v=0}$ is larger than r_e , the polarizability and the electrostatic moments of the monomer fragments will be larger, so that the long-range interaction will be stronger.

We display the larger fitted expansion coefficients as a function of R in Figs. 7.4 and 7.5 for the MRCI, MRCI-HS, and CCSD(T) PESs. The difference between the expansion coefficients of the MRCI PESs and MRCI-HS PESs are insignificant. Consequently, restricting the angular sampling in the CCSD(T) *ab initio* calculations to geometries with a plane of symmetry will not lead to significant error in the fitted CCSD(T) PES.

As a justification of the use of only the points with high symmetry, we performed some full close-coupling scattering calculations for several rotationally inelastic transitions of OH in collisions of H_2 $j = 0$, $j = 1$, and $j = 2$, at collision energies ranging from 70

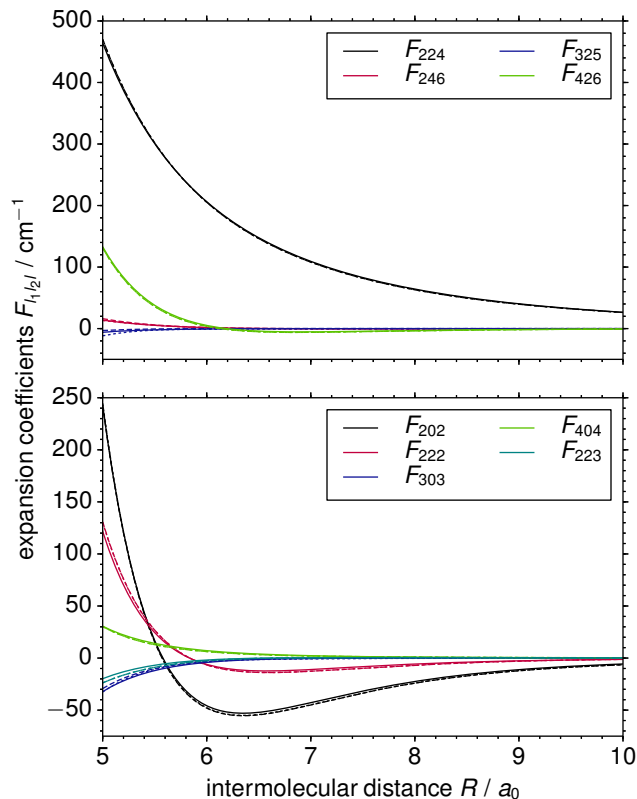


Figure 7.5: Larger $F_{l_1 l_2 l}$ expansion coefficients for the off-diagonal potential V_o as a function of intermolecular distance R for the CCSD(T) PESs (solid lines), MRCI PESs (dashed lines), and the MRCI-HS PES (dotted lines, barely visible due to the overlap with the dashed lines). The top panel shows $F_{l_1 l_2 l}$ coefficients that have contributions from multipole-multipole interactions; the bottom panel displays other coefficients.

to 150 cm^{-1} . We found that the state-to-state cross sections computed with the MRCI and the MRCI-HS PESs differ by no more than $\sim 2\%$, comparable to the precision of the scattering calculations ($\sim 1\%$). For calibration, the maximum difference between cross sections computed on the MRCI and CCSD(T) PESs is 8% . Detailed results on the OH-H₂ scattering calculations are presented in Chapter 8. Also, we see from Table 7.2 that OH \cdots H₂ dissociation energies computed with MRCI and MRCI-HS PESs differ by only $\sim 0.3 \text{ cm}^{-1}$. We will further show the OH \cdots H₂ bound state energies and spectroscopic constants computed from these two sets of PESs in Sec. 7.4.

We thus assert that our CCSD(T) set of PESs, determined at the points with a plane of symmetry, is the most accurate currently available for OH-H₂. Inclusion of

triple excitations allows a more complete recovery of electron correlation than in the MRCISD+Q calculations. Use of the CCSD(T)-F12a method with an aug-cc-pVTZ basis is expected to be more accurate than a standard (without explicit correlation) CCSD(T) calculation with a larger aug-cc-pVQZ basis [53]. The CCSD(T) calculations are faster than the MRCISD+Q calculations. Also, whenever there is a plane of symmetry, the diabatic coupling V_{xy} vanishes, so that the determination of the diagonal V_d and off-diagonal V_o PESs from the V_{xx} and V_{yy} Cartesian PESs is straightforward by means of Eqs. (7.14) and (7.15).

The top panels of Figs. 7.4 and 7.5 show coefficients with $l = l_1 + l_2$, $l_1 \geq 1$, and $l_2 \geq 2$, to which the multipole-multipole electrostatic interactions make significant contributions at long range. For the diagonal potential, the B_{123} (OH-dipole/H₂-quadrupole, R^{-4} dependence) and the B_{224} (quadrupole-quadrupole, R^{-5} dependence) terms dominate the PES at medium to long range. In this range the only comparable non-multipole contribution is the isotropic B_{000} term, which is a reflection of the R^{-6} dispersion interaction. As seen in the lower panel of Fig. 7.5, the largest non-multipole contribution is the F_{202} term, which is a difference between the dispersion interaction between H₂ and OH in its $\pi_x^2\pi_y$ and $\pi_x\pi_y^2$ Cartesian states.

We discussed in Sec. 7.2.4 the appearance of terms in the expansion of the off-diagonal potential V_o corresponding to an odd sum of the indices $\{l_1, l_2, l\}$. For the electrostatic interactions between the two fragments, the indices obey the relation $l_1 + l_2 = l$, so they do not give rise to terms in the expansion with odd $(l_1 + l_2 + l)$. The induction, dispersion, and overlap interactions do not obey this relation, however, so there are also terms with $l_1 + l_2 \neq l$, both with odd and even $(l_1 + l_2 + l)$. For this reason, and guided by Green's investigation of similar terms in the expansion of the interaction between a non-linear polyatomic and a diatomic [251], we included terms with odd $(l_1 + l_2 + l)$ in our fit. The largest of these was the F_{223} term (see Fig. 7.5). As can be seen, this term is quite small except at small values of R .

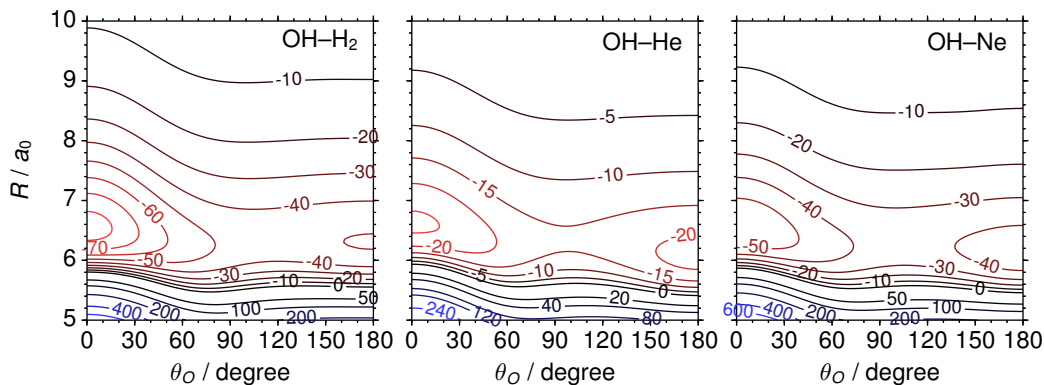


Figure 7.6: Contour plots (in cm^{-1}) of the CCSD(T) V_d PES (left panel) averaged over all orientations of H_2 compared to the V_{sum} PES for OH-He (middle panel) from Ref. [83] and for OH-Ne (right panel) from Ref. [111].

Anisotropies

At small R , the anisotropy of both the diagonal and the off-diagonal PESs is more complex than predicted by a simple multipole-multipole model. A number of expansion terms make important contributions. When H_2 is in the lowest rotational level ($j = 0$), its wave function is spherically symmetric. The OH- $\text{H}_2(j = 0)$ PES is a function of only R and θ_O , and can be obtained by an equal-weight averaging over all orientations (θ_H and ϕ_H) of the H_2 moiety. Figure 7.6 compares the OH- $\text{H}_2(j = 0)$ V_d PES with the V_{sum} PESs for OH-He [83] and OH-Ne [111].

The anisotropies of these PESs are very similar. All three have global minima at $\theta_O = 0$ and $R \sim 6.5 a_0$. Although OH- H_2 is isoelectronic with OH-He, the OH- $\text{H}_2(j = 0)$ minimum is more than three times deeper than the OH-He minimum, and the interaction is more repulsive at short range. Both differences are reasonable. For H_2 in $j = 0$, the charge distribution is spherical so that there will be no multipole moments. Hence, the dominant attractive contribution is the dispersion interaction. Because the charge distribution of H_2 is more polarizable than that of He, the OH- H_2 attractive interaction will be larger. Similarly the size of an H_2 molecule, even averaged over orientation, will be larger than that of the isoelectronic He atom. Thus, we expect a somewhat steeper repulsive wall. In

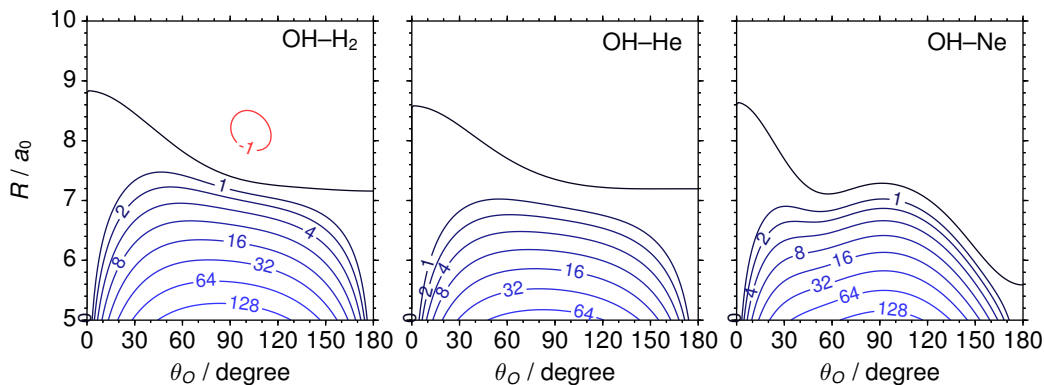


Figure 7.7: Contour plots (in cm^{-1}) of the (left panel) CCSD(T) V_o PES averaged over the orientation of H_2 in its $j = 0$ rotational level compared to the V_{dif} PES for OH-He (middle panel) from Ref. [83], and for OH-Ne (right panel) from Ref. [111].

reality, the OH- $\text{H}_2(j = 0)$ PESs appears more similar to that of OH-Ne.

Figure 7.7 displays contour plots of the off-diagonal OH- $\text{H}_2(j = 0)$ PES and the V_{dif} PESs for OH-He and OH-Ne. The V_o (or V_{dif}) PESs are the half difference between the PESs corresponding to interaction of a collision partner with OH ($\pi_x^2 \pi_y^1$) and ($\pi_x^1 \pi_y^2$). This will vanish in linear geometry, where the two electron occupancies are degenerate, and reach a maximum at $\theta_O \sim 90^\circ$ where the spherical partner is pointed at either a singly-filled or doubly-filled OH π orbital. Overall, V_o is smaller magnitude than V_d . We thus expect it to play a less important role in scattering and bound-state calculations.

Figure 7.8 presents contour plots of V_d and V_o in the OH molecule frame similar to plots given by OvH (Fig. 3a of Ref [268]). In these plots, the center of mass of the OH molecule defines the origin. The OH molecule lies on the z axis with the H atom on the positive direction. The OH- H_2 separation is $\sqrt{x^2 + z^2}$, and the orientation of the OH molecule in the space-fixed frame defined in Fig. 7.1 is $\theta_O = \tan^{-1}(-x/z)$. The orientation of the H_2 molecule is fixed at $\{\theta_{\text{H}}, \phi_{\text{H}}\} = \{27.464^\circ, 45^\circ\}$. Overall, our PESs and those of OvH [268] show a very similar dependence on the OH-HH distances and on the orientation of the OH moiety. For both sets of PESs, V_d has an attractive well on the oxygen side of OH, and $|V_o|$ is slightly asymmetric about the $x = 0$ axis.

Our CCSD(T) calculations sampled only high-symmetry geometries while the OvH

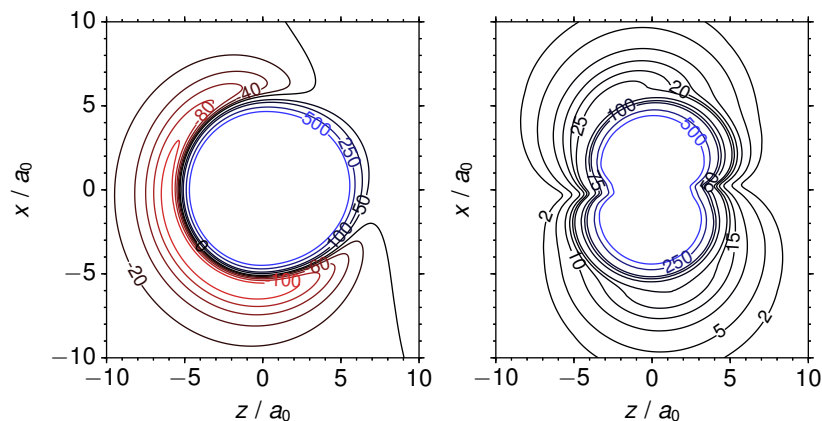


Figure 7.8: Contour plots showing the variation of V_d (left panel) and $|V_o|$ (right panel) in the OH molecule frame. The OH molecules lies on the z axis. The orientation of OH in the space-fixed frame defined in Fig. 7.1 is $\theta_O = \tan^{-1}(-x/z)$. The OH- H_2 separation is $\sqrt{x^2 + z^2}$. The orientation of H_2 in the space-fixed frame is fixed at $\{\theta_H, \phi_H\} = \{27.464^\circ, 45^\circ\}$. Contour labels in cm^{-1} .

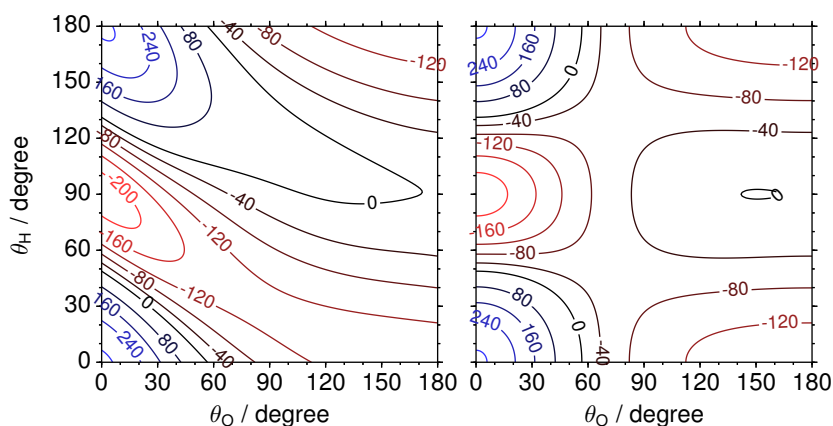


Figure 7.9: Contour plots of the diagonal CCSD(T) PESs V_d (in cm^{-1}) as a function of θ_O and θ_H when $\phi_H = 0$ (coplanar geometry; left panel) and $\phi_H = 90^\circ$ (right panel). In both cases $R = 6a_0$.

PESs are fits to *ab initio* calculations which sampled non-planar geometries. Thus the great qualitative similarity in the OvH and CCSD(T) PESs confirms that sampling only high-symmetry geometries will provide an excellent description of the OH- H_2 system. The OvH PESs were computed with a SCF + dispersion method, which yields a deeper well at this H_2 orientation compared with our more accurate method.

Contour plots showing the dependence of V_d and V_o on θ_O and θ_H for $\phi_H = 0^\circ$ and 90° at $R = 6a_0$ are presented in Figs. 7.9 and 7.10, respectively. At medium to long range, the interaction between the OH dipole (negative at the O end) and the HH quadrupole

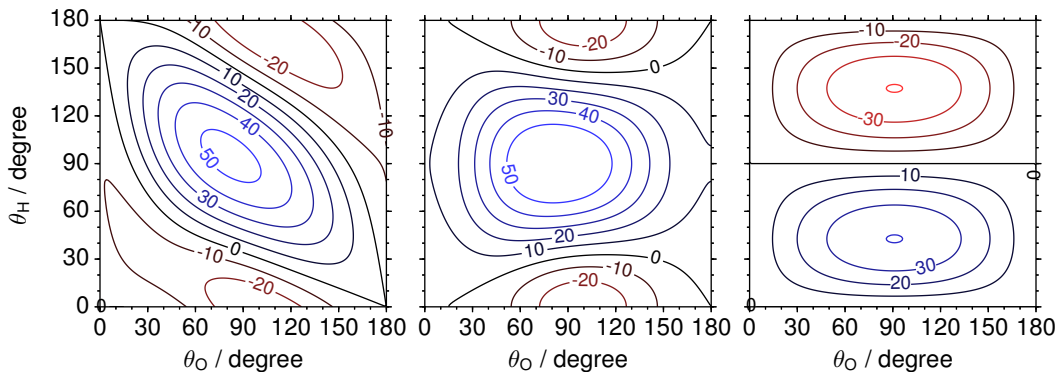


Figure 7.10: Contour plots of V_o of the CCSD(T) PESs (in cm^{-1}) as a function of θ_O and θ_H when $\phi_H = 0$ (left panel) and $\phi_H = 90^\circ$ (middle panel and right panel, for the real and the imaginary part, respectively). When $\phi_H = 0$, V_o is purely real.

(positive at the ends, negative in the middle) will dominate the interaction. The interaction will be most attractive when the OH approaches the H_2 in T-shaped geometry with the H-end of the OH closer to the H_2 ($\theta_O = 0$, $\theta_{r,mH} = 90^\circ$, T-shaped OH-HH). In addition to this global minimum, there are local minima in linear HO-HH geometry, in which the negative end of the OH dipole approaches the positive ends of the HH quadrupole ($\theta_O = 180^\circ$, $\theta_H = \pi/2$, linear HO-HH).

Figure 7.10 presents contour plots of the off-diagonal potential V_o . The minima and the maxima of $\Re(V_o)$ and $\Im(V_o)$ are all located at $\theta_O = 90^\circ$. At this value of θ_O , one lobe of the π_x orbital of OH points to H_2 , and thus will maximize the difference between the energies of the $\pi_x^2\pi_y$ and $\pi_x\pi_y^2$ electron occupancies. When $\phi_H = 0^\circ$, $\Im(V_d)$ vanishes by symmetry, while the real and imaginary parts of V_d have comparable magnitudes when $\phi_H = 90^\circ$.

When $\phi_H = 90^\circ$, $\exp(im\phi_H) = i^m$, and $\cos(m\phi_H)$ vanishes unless m is even. Since the index l_2 is also even (because of the permutation symmetry of the HH moiety), one can show that the diagonal potential [Eq. (7.4)] and the real part of the off-diagonal potential [Eq. (7.6)] is unchanged when θ_H is replaced by $\pi - \theta_H$. In contrast, the imaginary part of the off-diagonal potential changes sign when $\theta_H \rightarrow \pi - \theta_H$. Thus V_d and $\Re(V_o)$ should be symmetric, while $\Im(V_o)$ should be antisymmetric, about $\theta_H = 90^\circ$. This prediction is

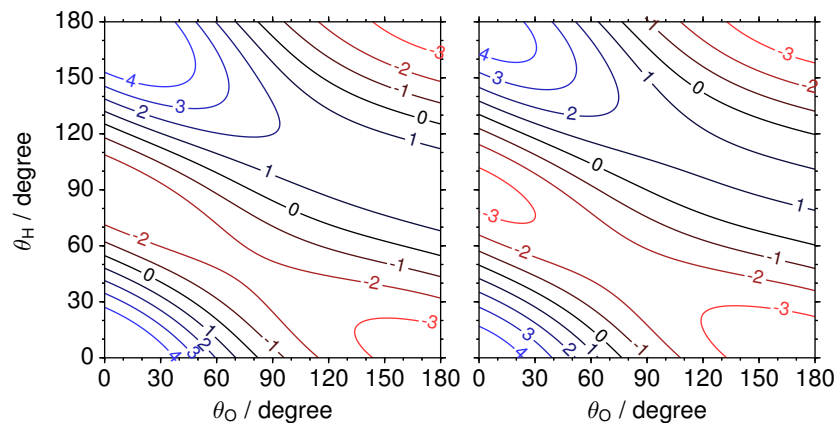


Figure 7.11: Contour plots showing the variation of V_o of the electrostatic interactions (left panel) and the CCSD(T) PESs (right panel) as a function of θ_O and θ_H when $\phi_H = 0$; $R = 15 a_0$. Contour labels in cm^{-1} .

borne out by the right panel of Fig. 7.9, and the middle and right panels of Fig. 7.10.

Finally we compare in Fig. 7.11 at $R = 15 a_0$ contour plots of the contribution to V_d of just the terms which correlate at long-range to the lower-order multipole-multipole interactions (B_{123} , B_{224} , and B_{325}) and the full fitted CCSD(T) PESs. The electrostatic interactions were computed from the multipole moments listed in Table 7.1. Overall, consideration of just the electrostatic interactions represents well the angular dependence and magnitude of the PES. Notwithstanding, the CCSD(T) PESs are less repulsive at all orientations than that predicted by with the electrostatic interactions alone. We infer that there are still non-trivial contributions from induction and dispersion at this large value of R . We thus believe that a full calculation of the long-range potential will be more accurate than relying on electrostatics alone.

We note that Wormer *et al.* [69] used electrostatic interactions only in extrapolating their OH-HCl PES. However, the OH-HCl PES is dominated by the strong R^{-3} dipole-dipole interaction which is absent for OH-H₂.

Although we did not use the multipole moments in extrapolating the CCSD(T) PES, fits of the CCSD(T) *ab initio* points at large R actually give quite similar results. For example, from the multipole moments listed in Table 7.1, we predict $B_{123} = 2.86 \times$

$10^5(R/a_0)^{-4} \text{ cm}^{-1}$, compared to a coefficient of 2.66 obtained by direct fit of the *ab initio* points. This good agreement justifies our direct fit of the CCSD(T) points to Eq. (7.18).

7.4 Bound-state Calculations

7.4.1 Theory and Method

The Hamiltonian for the OH-H₂ system with fixed bond lengths can be written as

$$\hat{H} = -\frac{1}{2\mu R} \frac{\partial}{\partial R^2} R + \hat{H}_O + \hat{H}_H + \frac{\hat{L}^2}{2\mu R^2} + V(R, \theta_O, \theta_H, \phi_H), \quad (7.19)$$

where μ is the OH-H₂ reduced mass, \hat{H}_O and \hat{H}_H are the rotational Hamiltonians of OH and H₂, respectively, \hat{L} is the orbital angular momentum of the complex, and V is the interaction potential.

We construct a set of basis functions from the product of stretching functions and angular functions and use a set of distributed Gaussians to span the R -space [284]. The construction of the rotational basis functions, which can also be used for scattering calculations, is discussed in detail in Appendix A.

We employed the following parameters for \hat{H}_O : the rotational constant B , the spin-orbit constant A , and Λ doubling parameters p and q for the $v = 0$ level of OH. The values of these parameters were taken from Mélen *et al.* [285], and the matrix elements of \hat{H}_O were defined by Kotlar *et al.* [286]. For \hat{H}_H we use the rotational constants B of H₂ and D_2 averaged over the $v = 0$ probability distributions (59.322 and 29.9043 cm⁻¹, respectively).

The expression for the matrix elements of the interaction potential in this angular basis is given in Appendix A. We used our Hibridon [31] suite of programs, recently extended to handle the OH-H₂ system, to construct and diagonalize the Hamiltonian matrix to determine the energies of the OH-H₂ bend-stretch states.

Table 7.3: $J = 1/2$ bound levels (in cm^{-1}) of OH-H₂ for the CCSD(T) PESs. Also shown are assignments of the stretching quantum numbers.^a

n	$\rho = +1^b$		$\rho = -1^b$	
	Energy	v_s	Energy	v_s
OH- <i>para</i> -H ₂				
1	-29.01	0	-26.93	0
2	-20.55	0	-22.43	0
OH- <i>ortho</i> -H ₂				
1	-53.14	0	-53.73	0
2	-41.72	0	-41.02	0
3	-33.16	0	-32.83	0
4	-25.08	0	-25.17	0
5	-9.48	0	-11.82	0
6	-7.43	0	-7.20	1
7	-6.52	1	-5.39	0
8	-3.74	1	-3.18	1
9	-1.42	1	-1.34	1

^a The zero of energy is the energy of separated OH(² Π , $j = 3/2$ F_1e) + H₂(j), where $j = 0$ and 1 for *para*- and *ortho*-H₂, respectively. Levels with energy $> -1 \text{ cm}^{-1}$ are not listed.

^b Symmetry index for the complex. The overall parity of the bend-stretch wave function equals $\rho(-1)^{j-1/2}$.

7.4.2 Results

We list in Tables 7.3 and 7.4 the energies of the bend-stretch levels of the OH-H₂ complex calculated with the CCSD(T) PESs for total angular momenta $J = 1/2$ and $3/2$. In computing these energies, we included all angular basis functions with $j_1 \leq 6$, and $j_2 \leq 5$ and ≤ 4 for *ortho* and *para* H₂, respectively. The stretch basis (the expansion in the OH-H₂ distance) was 41 equally spaced Gaussian functions spanning the range $4a_0 \leq R \leq 16a_0$. The computed bound state energies are converged to $\sim 0.01 \text{ cm}^{-1}$.

We have inspected the wave functions for each bound level and assigned OH-H₂ stretching quantum numbers v_s and the body-fixed projection P of the angular momentum of the complex J . P was assigned using the vector model of angular momenta similar to the method described in Ref. [273].

Overall, we find that the computed bound level energies are in qualitative agreement with the values reported by Miller *et al.* [148, 273]: The number of bound states are similar,

Table 7.4: $J = 3/2$ bound levels (in cm^{-1}) of OH- H_2 predicted the CCSD(T) PESs. Also shown are assignments of the stretching quantum numbers and approximate values of P .^a

n	$\rho = -1^{\text{b}}$			$\rho = +1^{\text{b}}$		
	Energy	v_s	P	Energy	v_s	P
OH- <i>para</i> - H_2						
1	-36.12	0	3/2	-36.09	0	3/2
2	-28.00	0	1/2	-24.23	0	1/2
3	-20.89	0	1/2	-22.47	0	1/2
4	-16.48	0	1/2	-18.32	0	3/2
5	-1.51	1	3/2	-1.48	1	3/2
OH- <i>ortho</i> - H_2						
1	-51.22	0	1/2	-52.36	0	1/2
2	-43.10	0	3/2	-42.51	0	— ^c
3	-38.66	0	— ^c	-38.09	0	3/2
4	-36.49	0	3/2	-36.36	0	3/2
5	-30.83	0	1/2	-30.16	0	1/2
6	-23.00	0	1/2	-23.30	0	— ^c
7	-16.54	0	3/2	-16.45	0	— ^c
8	-8.21	0	— ^c	-11.24	0	1/2
9	-6.88	0	1/2	-7.14	1	— ^c
10	-5.82	0	— ^c	-5.83	0	3/2
11	-4.62	1	— ^c	-4.10	1	— ^c
12	-3.45	0	— ^c	-2.80	1	— ^c
13	-2.12	1	— ^c	-2.07	1	— ^c
14	-2.08	1	1/2			

^a The zero of energy is the energy of separated OH($^2\Pi, j = 3/2 F_1e$) + $\text{H}_2(j)$, where $j = 0$ and 1 for *para*- and *ortho*- H_2 , respectively. Levels with energy $> -1 \text{ cm}^{-1}$ are not listed.

^b Symmetry index for the complex. The overall parity of the bend-stretch wave function is $\rho(-1)^{j-1/2}$.

^c Strong Coriolis coupling prevents the assignment of the body-frame projection P .

the zero point energies are large, and for both $J = 1/2$ and $3/2$ the binding energies for OH-*ortho*- H_2 are greater than for the *para*- H_2 complex. The stronger binding with *ortho*- H_2 is a general phenomenon for all H_2 complexes [146–150, 273]. The *para*- H_2 molecule is spherically symmetric and cannot orient to sample the most attractive orientations (at least without mixing in the higher $j = 2$ rotational level).

In Sec. 7.3.5, we discussed whether restricting the angular sampling to geometries with a plane of symmetry would lead to significant error in the fitted PESs. The difference between the expansion coefficients for the MRCI and MRCI-HS PESs were found to be

Table 7.5: The lower $J = 1/2$ and $3/2$ bound levels (in cm^{-1}) of OH-H₂ predicted the MRCI and MRCI-HS PESs.^a

n	$\rho = +1^b$		$\rho = -1^b$	
	MRCI	MRCI-HS	MRCI	MRCI-HS
OH- <i>para</i> -H ₂ $J = 1/2$				
1	-30.62	-30.28	-28.60	-28.28
2	-22.24	-21.96	-24.07	-23.78
OH- <i>para</i> -H ₂ $J = 3/2$				
1	-38.74	-38.52	-38.72	-38.50
2	-29.64	-28.31	-25.99	-25.70
3	-22.79	-22.59	-24.25	-24.00
OH- <i>ortho</i> -H ₂ $J = 1/2$				
1	-55.21	-54.96	-55.79	-55.54
2	-44.26	-43.90	-43.54	-43.18
3	-35.17	-34.81	-34.96	-34.60
OH- <i>ortho</i> -H ₂ $J = 3/2$				
1	-53.31	-53.06	-54.42	-54.17
2	-46.12	-45.82	-45.63	-45.35
3	-41.27	-40.94	-40.46	-40.13

^a The zero of energy is the energy of separated OH(²Π, $j = 3/2 F_1e$) + H₂(j), where $j = 0$ and 1 for *para*- and *ortho*-H₂, respectively.

^b Symmetry index for the complex. The overall parity of the bend-stretch wave function is $\rho(-1)^{j-1/2}$.

insignificant. Moreover, there were only minimal differences between state-to-state cross sections computed with these two PESs. As a further check on the validity of considering interaction energies only for geometries with a plane of symmetry, we compare the energies of bend-stretch levels computed with these two PESs. Table 7.5 presents comparison of the energies of the lower $J = 1/2$ and $3/2$ bound levels computed with the MRCI and MRCI-HS PESs. We see that the energies computed with the MRCI PESs are slightly lower than the MRCI-HS values. However, the differences in energies are quite small, $< 0.3 \text{ cm}^{-1}$. This provides additional justification for using only geometries that have a plane of symmetry in our fit, and hence allowing the use of RCCSD(T) theory in computing the interaction energies.

We see in Tables 7.3, 7.4, and 7.5 that there are significant parity splittings in the energies of the bend-stretch levels. Green and Lester [287] and Dubernet *et al.* [288]

have employed a perturbation theory to determine the J -dependence of the bend-stretch energies and parity splittings, which can be expressed for $P = 1/2$ bend levels as

$$BJ(J + 1) + \frac{\rho}{2}p(J + 1/2) \quad (7.20)$$

where B is the rotational constant of the complex and p is the parity splitting parameter of that particular bend level. As expected from the analysis in the above cited studies [287, 288], the parity splittings are much larger for $P = 1/2$ levels than for $P = 3/2$ levels.

We have fit the J and parity dependence of the computed energy of the lowest bend-stretch level ($P = 1/2$) of OH-*ortho*-H₂ to Eq. (7.20). Table 7.6 compares the rotational constant and parity splitting parameter for this bend-stretch level, determined both experimentally and theoretically. As expected from the small differences between the MRCI and MRCI-HS bend-stretch energies, the derived spectroscopic constants computed with these two PES's are in good agreement. We also see that there are only slight differences in the parameters computed with the CCSD(T) and MRCI PES's. By contrast, the agreement of our computed spectroscopic constants with those reported experimentally [262], which were obtained from fitting $J = 1/2$ and $J = 3/2$ level energies derived from the spectrum, is less satisfactory. Our values for B and p are, respectively, smaller and larger than the experimental values. The differences lie outside the experimental error bars. Curiously, the spectroscopic constants computed with the less sophisticated MCKW PES are in better agreement with experiment. We note that the Coriolis coupling in the $J = 3/2$, $P = 1/2$ levels we used in deriving spectroscopic constants are weak.

Calculation of the bend-stretch energies allows us to predict the zero-point corrected dissociation energy D_0 . These values are presented in Table 7.2. Our predicted well depths (D_e) are $\approx 31 \text{ cm}^{-1}$ larger than predicted for the MCKW PESs. However, this difference is compensated somewhat by the larger curvature of our PESs in the region of the well (see the blue lines in Fig. 7.3). Thus the zero-point-corrected dissociation energies (D_0)

Table 7.6: Predicted and experimental spectroscopic constants for the lowest bend-stretch level of the OH-*ortho*-H₂ complex. Unless otherwise stated, the theoretical constants were determined by fitting $J = 1/2$ and $J = 3/2$ energies.

PES	B (cm ⁻¹)	p (cm ⁻¹)
MCKW ^a	0.660(2)	0.452(2)
MRCI ^b	0.543(1)	0.558(2)
MRCI-HS ^b	0.545(1)	0.560(2)
CCSD(T) ^{b,c}	0.554(1)	0.552(2)
Experiment ^d	0.633(25)	0.498(39)

^a Reported in Ref. [262].

^b This work.

^c Constants determined by fitting the $J = 1/2, 3/2$ and $5/2$ energies.

^d OH($X^2\Pi, v = 0$). Ref. [262].

are only 8 cm⁻¹ (MRCI) and 11 cm⁻¹ [CCSD(T)] larger than the values computed for the MCKW PESs.

The D_0 values obtained from our CCSD(T) PESs, 36.1 cm⁻¹ and 53.7 cm⁻¹ for OH-*para*-H₂ and OH-*ortho*-H₂, respectively, are both in good agreement with the MRCI values (Table 7.2). We note that our computed D_0 for OH-*ortho*-H₂ is in excellent agreement with the experimental value of 54 cm⁻¹ [261]. We have also computed the bound states for OH-*ortho*-D₂ and OH-*para*-D₂ with the CCSD(T) PESs, and obtained D_0 values of 51.4 cm⁻¹ and 67.5 cm⁻¹. These values are ~ 7 cm⁻¹ larger than those obtained with the MCKW PES [264]. The lower limit of the OH-*para*-D₂ binding energy determined via electronic spectroscopy is 66 cm⁻¹ [261], which is again in excellent agreement with our prediction.

7.5 Discussion and Conclusions

We have presented here two sets of OH($X^2\Pi$)-H₂ PESs, calculated using the MR-CISD+Q (Davidson) and the CCSD(T)-F12a methods. Comparison of the full MR-CISD+Q PES with a fit to a subset of points determined at geometries with at least one plane of reflection symmetry, shows that sampling based on this subset of points provides

a very accurate, but much less computationally demanding, representation of the OH-H₂ PES. For these points with symmetry we can then use the CCSD(T)-F12a method, which is more accurate and, in addition, computationally faster. We expect this strategy to be useful in developing PESs for similar systems involving a ²Π molecule and a ¹Σ molecule, such as NO(*X*²Π)-H₂.

We have performed calculations of the bend-stretch levels of the binary OH-H₂ complex for both the *para* and *ortho* nuclear spin modifications. The dissociation energies (*D*₀) predicted by fits to the MRCI and the CCSD(T) points differ by less than 2 cm⁻¹, and agree extremely well with the experimental estimate [261]. This agreement is a measure of the accuracy of our PESs, especially for the depth and shape of the attractive well.

Comparison of inelastic OH-H₂ scattering cross sections with experiment would constitute a further test of our PESs. This comparison would be most sensitive to the PESs near the onset of the repulsive well. Collisions of OH with H₂ have been well studied [144, 263]. Most recently, use of a Stark decelerator [82, 96] has permitted the determination of the relative magnitude of state-resolved OH(*j* → *j'*) transitions in collisions with D₂ and H₂ over a wide range of collision energies. Comparable scattering calculations will be reported in Chapter 8.

Chapter 8

Rotationally Inelastic Scattering of OH and H₂

The work described in this chapter has not been published. The additional *ab initio* calculations described in Sec. 8.5 were performed by Jacek A. Kłos. Paul J. Dagdigian, Millard H. Alexander, and Ad van der Avoird have directed/participated in this work. Christian Schewe and Nicholas Vanhaecke have also provided useful discussion.

8.1 Introduction

In the preceding chapter, we have presented two sets of *ab initio* diabatic potential energy surfaces (PESs) describing the interaction between OH($X^2\Pi$) and H₂. The first set of PESs (the MRCI PESs) used an internally-contracted, multi-reference configuration interaction (IC-MRCI) method, with a direct computation of the non-adiabatic coupling matrix elements. The second set of the PESs [the CCSD(T) PESs] used a restricted open-shell explicitly correlated coupled-cluster [RCCSD(T)-F12a] method, circumventing the non-adiabatic coupling problem by sampling high-symmetry geometries only. We have, in addition, created another set of PESs (the MRCI-HS PESs) by fitting the high-symmetry points of the MRCI PESs. From inspecting these PESs, we discussed our preference of the CCSD(T) PESs.

Our new PESs gave the dissociation energies (D_0) of the OH($X^2\Pi$) \cdots H₂/D₂ bound complex in nearly perfect agreement with those obtained from spectroscopic studies

by Loomis and Lester [261, 262]. This agreement confirmed the accuracy of our PESs. However, the energies of the bound levels are mainly sensitive to the attractive part of the PESs. The energy dependence of the state-to-state inelastic cross sections from crossed beam molecular experiments would provide a more critical test of the PESs.

In the present work, we perform fully quantum close-coupling calculations with our new PESs, and compare the cross sections with earlier experiments by Schreel and ter Meulen [144], and by Kirste *et al.* [96]. In the study of Schreel and ter Meulen, state-to-state OH-H₂ cross sections were measured at a collision energy of 595 cm⁻¹. In the Kirste *et al.* experiment, the state-to-state energy dependent OH-D₂ cross sections at collision energies of 100–500 cm⁻¹ were measured. For a more thorough investigation, we also computed the state-to-state rotationally inelastic cross sections of OH with both normal and *para*-H₂ at a collision energy of 68–150 cm⁻¹. In our study we will focus on the transitions out of the $j = 1/2, F_1, f$ level of OH, whose molecular beam can be manipulated by a state-of-the-art Stark decelerator [267].

We found our computed cross sections are in reasonably good agreement with experimental results, although some discrepancies remain. However, when investigating the low-energy (≤ 150 cm⁻¹) collisions, we found the cross sections for the $j = 1/2, F_1, f \rightarrow j = 1/2, F_1, e$ and the $j = 1/2, F_1, f \rightarrow j = 3/2, F_1, e$ transitions are very sensitive to the PESs used. In this work we will also check the accuracy of our *ab initio* calculations and attempt to identify the properties of the PESs that would lead to the discrepancies between theory and experiments.

This chapter is organized as follows: Section 8.2 describes the detail of our quantum scattering calculations. In Secs. 8.3 and 8.4 we show our computed scattering cross sections for OH-H₂ and OH-D₂ collisions, respectively. In these sections we also compare our cross sections with the experimental values and discuss the correlation between the collision dynamics and the PESs. We discuss the accuracy of our PESs and scattering calculations in Sec. 8.5, and Sec. 8.6 summarizes this work.

8.2 Quantum Scattering Calculations

The theory of scattering between a molecule in a $^2\Pi$ electronic state with a molecule in a $^1\Sigma$ state has been described in previous publications [69, 268, 270], as well as in Appendix A. Close-coupling calculations were performed both with the HIBRIDON suite of programs [31], recently modified to support the collision between a $^2\Pi$ molecule and a $^1\Sigma$ molecule. Some of the cross sections are also checked with a second independent scattering program for scattering described in Ref. [94]. Care was taken to check the consistency of the results from the two scattering programs and the convergence of the cross sections.

In all the calculations, the rotational constant B , the spin-orbit constant A , and the Λ doubling parameters p and q for the $v = 0$ level of OH were taken from Ref. [285]. The rotational constant B used for H_2 and D_2 were 59.322 and 29.9043 cm^{-1} , respectively. The close coupling basis used varies upon the collision energy and the initial rotational level of H_2/D_2 , and will be described in subsequent sections.

8.3 Collisions of OH with H_2

8.3.1 OH- H_2 Collisions at 595 cm^{-1} Collision Energy

We first consider the OH- H_2 collision at a relatively high collision energy, and compare our computed cross sections with the experimental results of Schreel and ter Meulen [144], as well as theoretical results obtained using the OvH PES [268, 272]. The scattering dynamics in this case would be mostly sensitive to the repulsive wall of the PESs, which has not been tested in our previous bound-state calculations.

In the experiments, the cross sections for the the inelastic scattering of OH, with and without using a electrostatic hexapole to select the $j_1 = 3/2, F_1, f$ level, in collisions with H_2 at a collision energy of 595 cm^{-1} were measured. State-to-state cross sections were

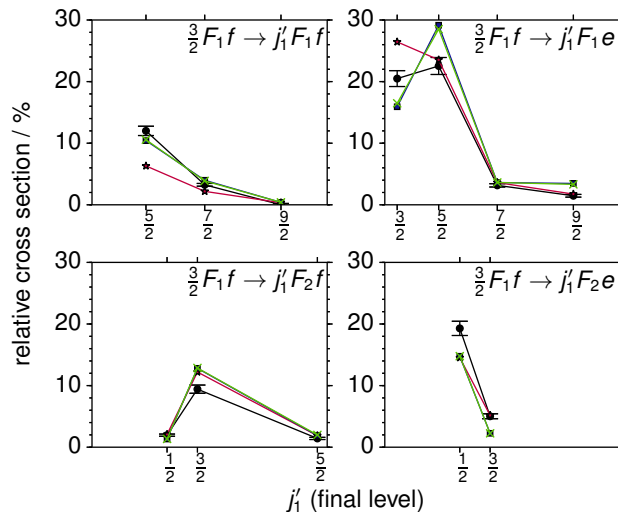


Figure 8.1: Experimental and theoretical cross sections for the scattering of $\text{OH}(X^2\Pi, j = 3/2, F_1, f)$ with “cold” *para*- H_2 at 595 cm^{-1} . The experimental cross sections (black lines) and the theoretical values computed with the OvH PESs (red lines) are taken from Ref. [144]. The theoretical values computed with the CCSD(T) PESs and the MRCI PESs are shown as blue and green lines (indistinguishable on the plots), respectively.

then derived for transitions out of the $\text{OH } j_1 = 3/2, F_1, e$ and the $j_1 = 3/2, F_1, f$ levels. The H_2 beam used in the experiment consisted of a mixture of H_2 in various rotational levels. The population of each level depends on the temperature (“cold” or “warm”) of the beam and whether the beam was *para*-converted. For a comparison, we performed close-coupling calculations at this collision energy, considering the scattering of OH with H_2 in the $j_2 = 0-3$ initial levels. All channels with $j_1 \leq 13/2$ and $j_2 \leq 4$ were included in the channel basis. The cross sections obtained were then averaged according to the initial population distribution of H_2 , shown in Table II of Ref. [144].

Figures 8.1 and 8.2 shows the cross sections for “cold” *para*- and normal H_2 collisions, respectively. In these figures, the relative cross sections, obtained from dividing the state-to-state cross section by the total inelastic cross section, are plotted. Given the similarity between our CCSD(T) PESs and the MRCI PESs (discussed in Chapter 7) it is not surprising to see that the relative cross sections obtained from the two sets of PESs (blue and green lines, respectively) are practically indistinguishable. By contrast, these cross sections are slightly different from those obtained from the OvH PESs, in particular the transitions to

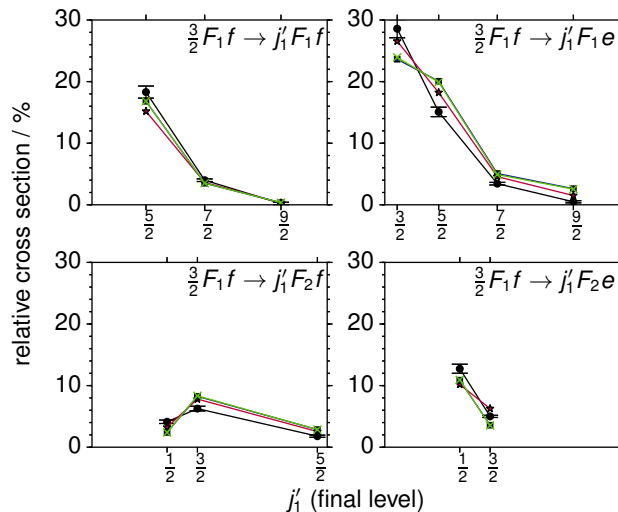


Figure 8.2: Experimental and theoretical cross sections for the scattering of $\text{OH}(X^2\Pi, j = 3/2, F_1, f)$ with “cold” normal H_2 at 595 cm^{-1} . The experimental cross sections (black lines) and the theoretical values computed with the OvH PESs (red lines) are taken from Ref. [144]. The theoretical values computed with the CCSD(T) PESs and the MRCI PESs are shown as blue and green lines (indistinguishable on the plots), respectively.

other low-lying F_1 levels. Aside from the differences between the PESs, the cross sections for the OvH PESs were computed using the coupled stated approximation. From our bound state calculations (Chapter 7), we see that the Coriolis coupling can be strong for this system. The coupled state calculations ignore Coriolis coupling completely and may leads to some error in the cross sections.

We see the agreement between theoretical and experimental cross sections is good, which validates our PESs. The largest deviations are for the $j_1 = 3/2, F_1, f \rightarrow j_1 = 3/2, F_1, e$ and the $j_1 = 3/2, F_1, f \rightarrow j_1 = 5/2, F_1, e$ transitions, which are unfortunately the two with the largest cross sections. We will discuss these transitions further in Sec. 8.3.2 that these transitions are very sensitive to the PESs.

Comparing Figures 8.1 and 8.2, we see that the *para*- and normal H_2 scattering show roughly the same behavior. Initially, this looks surprising given that many larger coefficients of the PESs have $l_2 \neq 0$, which do not couple channels with $j_2 = 0$ directly. However, we note that significant amount of H_2 is in the $j_2 = 2$ rotational level (48.3% in the “warm” beam, or 30.8% in the “cold” beam) in the beam used in the Schreel and ter

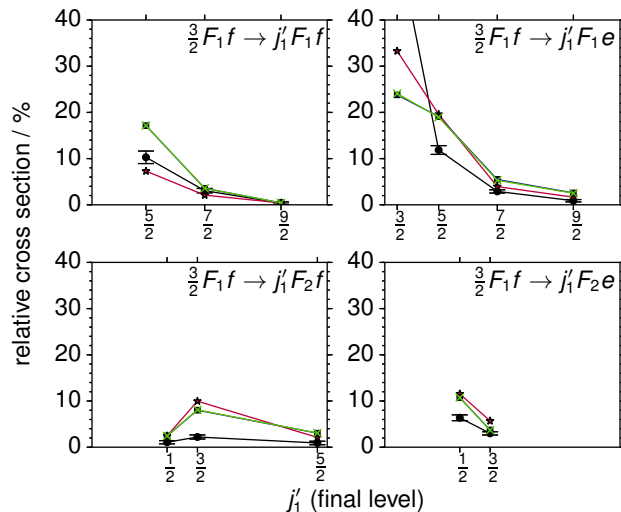


Figure 8.3: Experimental and theoretical cross sections for the scattering of $\text{OH}(X^2\Pi, j = 3/2, F_1, f)$ with “warm” *para*- H_2 at 595 cm^{-1} . The experimental cross sections (black lines) and the theoretical values computed with the OvH PESs (red lines) are taken from Ref. [144]. The theoretical values computed with the CCSD(T) PESs and the MRCI PESs are shown as blue and green lines (indistinguishable on the plots), respectively.

Meulen experiments. This will make the propensities in the *para*- and normal H_2 scattering similar. We will discuss this phenomenon further in Sec. 8.4.

We show in Fig. 8.3 the cross sections for the collision of $\text{OH}(j_1 = 3/2, F_1, f)$ with “warm” *para*- H_2 . Clearly, the agreement between theory and experiment is worse than that for the collision with “cold” H_2 , and our cross sections do not show better agreement than those from OvH PESs. One can expect this deviation suggests lesser quality in the calculations for the collisions with $\text{H}_2 j_2 = 2$. However, our PESs used significant higher level of theory than the OvH PESs, and we have performed converged close coupling calculations. Given that the experiment is at a single collision energy and the state purity of the beams is limited, no hard conclusions can be drawn from this deviation between theory and experiment.

8.3.2 Cold Collisions of OH with H_2

To investigate further the collision dynamics between OH and H_2 , we computed the state-to-state cross sections for this system at collision energies between 70 and 155

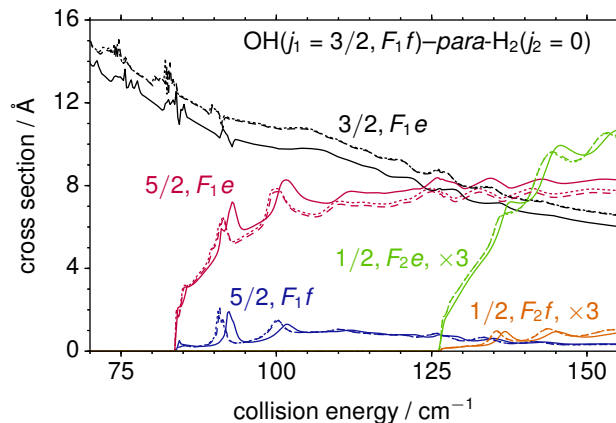


Figure 8.4: Theoretical state-to-state integral cross section as a function of collision energy for transitions out of the OH $j_1 = 3/2, F_1, f$ level in collisions with H₂ in $j_2 = 0$ level. The cross sections were computed with the CCSD(T) PESs (solid lines), the MRCI PESs (dotted lines), and the MRCI-HS PESs (dashed lines, overlap significantly with the dotted lines). The final level of the transitions are indicated on the plots. For clarity, the transitions to the F_2 levels are multiplied by 3.

cm^{-1} . We will focus on the transition out of the $j_1 = 3/2, F_1, f$ level, which can be Stark-decelerated in a crossed molecular beam experiment. For these calculations, we included all channels with $j_1 \leq 11/2$ and $j_2 \leq 4$ in the channel basis.

We first show in Fig. 8.4 the energy dependent cross sections of OH out of the $j_1 = 3/2, F_1, f$ level in collisions with *para*-H₂ ($j_2 = 0$). In the collision energy range considered, all possible inelastic transitions with j_2 unchanged are shown. We see that the $j_1 = 3/2, F_1, f \rightarrow j_1 = 3/2, F_1, e$ transition dominates at low collision energies, but its cross section becomes comparable to that of the $j_1 = 3/2, F_1, f \rightarrow j_1 = 5/2, F_1, e$ transition at $\sim 120 \text{ cm}^{-1}$. The latter transition will eventually dominate at higher collision energies. For the transitions shown, there is a strong propensity toward the formation of *e*-parity levels in the Λ -doublets. These propensities are surprisingly similar to those for the OH-Ne collision [83, 112] (see also Fig. 2.13). Although the masses of Ne and H₂ are very different, we have shown that the PESs for OH-H₂($j_2 = 0$) are very similar to those for OH-Ne (see Figs. 7.6 and 7.7). This similarity in PESs in turn leads to similar collision dynamics. We do note that the $j_2 = 2$ channels are not unimportant in a proper description of the OH-H₂($j_2 = 0$) collisions. Including these channels would make the anisotropies of OH-H₂

PESs that are absent from the OH-Ne PESs accessible indirectly in scattering calculations.

The low-energy collision dynamics is quite sensitive to the PESs. The cross sections computed from the CCSD(T) PESs and the MRCI PESs in Fig. 8.4 show some differences, particularly for the two transitions with larger cross sections. The agreement between the MRCI and MRCI-HS cross sections is excellent, showing that sampling high-symmetry geometries is a good approximation for OH-H₂. The sensitivity of the computed cross sections to the PESs indicates the importance of retrieving electron correlation energies in *ab initio* calculations.

The peaks shown in the energy dependent cross sections are scattering resonances and are also very sensitive to the PESs. Using a wave function analysis as described in Chapter 3, we were able to identify the two major peaks located at $\sim 93 \text{ cm}^{-1}$ and $\sim 102 \text{ cm}^{-1}$ in the $j_1 = 3/2, F_1, f \rightarrow j_1 = 5/2, F_1, e$ transition are primarily shape resonances arising from the quasibound states related to the final level of the transition. The two peaks for the $j_1 = 3/2, F_1, f \rightarrow j_1 = 5/2, F_1, f$ transition at similar collision energies are also shape resonances. While these peaks are broad which would facilitate the experimental observation, the resonance peaks do not show significant increase over the background cross section. Therefore, the unambiguous observation of these peaks in a crossed molecular beam experiment would be difficult.

In Fig. 8.5 we show the computed state-to-state cross sections for OH in collisions with *ortho*-H₂ in the $j_2 = 1$ level. We see the propensities of the inelastic transitions are quite different from the collision with H₂ ($j_2 = 0$). The transition between the Λ -doublets, $j = 3/2, F_1, f \rightarrow j = 3/2, F_1, e$ dominates at all energies considered, and its cross sections are much larger than when the collision partner is H₂ ($j_2 = 0$) (note the cross section for this transition is divided by 2 in Fig. 8.5). Also, for the collision with H₂ ($j_2 = 1$), the preference to the *e*-parity no longer exists.

These changes in the propensities originates from the $l_2 > 0$ terms of the PESs, which can couple directly $j_2 = 1 \rightarrow 1$ transitions but no $j_2 = 0 \rightarrow 0$ transitions. The difference in

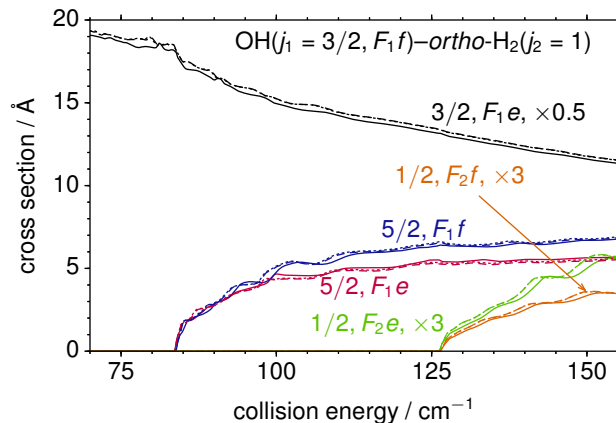


Figure 8.5: Theoretical state-to-state integral cross section as a function of collision energy for transitions out of the OH $j_1 = 3/2, F_1, f$ level in collisions with H₂ in $j_2 = 1$ level. The cross sections were computed with the CCSD(T) PESs (solid lines), the MRCI PESs (dotted lines), and the MRCI-HS PESs (dashed lines, overlap significantly with the dotted lines). The final level of the transitions are indicated on the plots. For clarity, the cross sections for the transitions to the F_2 levels are multiplied by 3, and that for the transition to the $j = 3/2, F_1, e$ level is divided by 2.

cross sections obtained from the CCSD(T) PESs and the MRCI PESs are smaller in Fig. 8.5. This is surprising since the collision dynamics here depends heavily on the ϕ_H -dependent $l_2 = 2$ terms of the PESs, and CCSD(T) calculations can only deal with special values of ϕ_H . This again validates our approach in creating the CCSD(T) PESs.

8.4 Collisions of OH with D₂

In this section we consider the collision between OH and D₂. Comparing with the OH-H₂ collision, OH-D₂ is of less astrophysical importance, and probably show less quantum properties of the molecules.¹ However, Kirste *et al.* [96] has recently carried out a molecular beam experiment on OH-D₂ using a Stark decelerator. In the experiment, state-to-state cross sections as a function of collision energy were measured. Comparing the computed cross sections with their experimental results would provide a stronger test of our newly developed PESs.

In Figs. 8.6 and 8.7 we show the state-to-state cross sections out of the $j_1 = 3/2, F_1, f$

¹Chapter 3 presents a comparison of the scattering resonance for the collision of NH₃ with H₂ and D₂, which is an analogy to the OH-H₂/D₂ system.

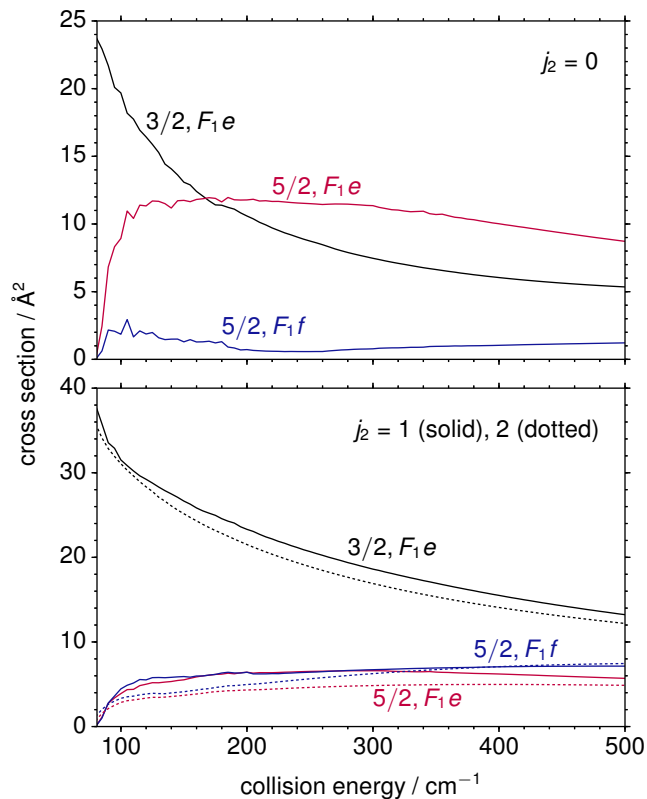


Figure 8.6: State-to-state integral cross section as a function of collision energy for transition from the $j_1 = 3/2, F_1, f$ level of OH to other F_1 levels in collisions with D_2 . The final levels are indicated for each transition for which the cross section is plotted. The initial rotational quantum number j_2 is labeled on each subplot. Cross sections to various final rotational levels of D_2 are summed up.

level of OH in collisions of D_2 in $j_2 = 0, 1$, and 2 levels. Figure 8.6 shows the cross sections of the spin-orbit conserving ($F_1 \rightarrow F_1$) transitions. As expected, for the collisions with *ortho*- D_2 ($j_2 = 0$), the transition between the Λ -doublet dominates at lower collision energies while the transition to the $j_1 = 5/2, F_1, e$ level becomes significant at higher energies. A strong preference to the $j_1 = 5/2, F_1, e$ final level over the $j_1 = 5/2, F_1, f$ level is observed with *ortho*- D_2 ($j_2 = 0$) as the collision partner, but not with *para*- D_2 ($j_2 = 1$). Overall the spin-orbit changing ($F_1 \rightarrow F_2$) transitions shown in Fig. 8.7 have smaller cross sections. These propensity rules are similar to what we observe for OH- H_2 .

We see the cross sections for the collisions with D_2 in the $j_2 = 1$ and $j_2 = 2$ initial levels are very similar for the larger $F_1 \rightarrow F_1$ transitions. This is reasonable considering that both collisions allows direct access to the parts of PESs related to the quadrupole moment

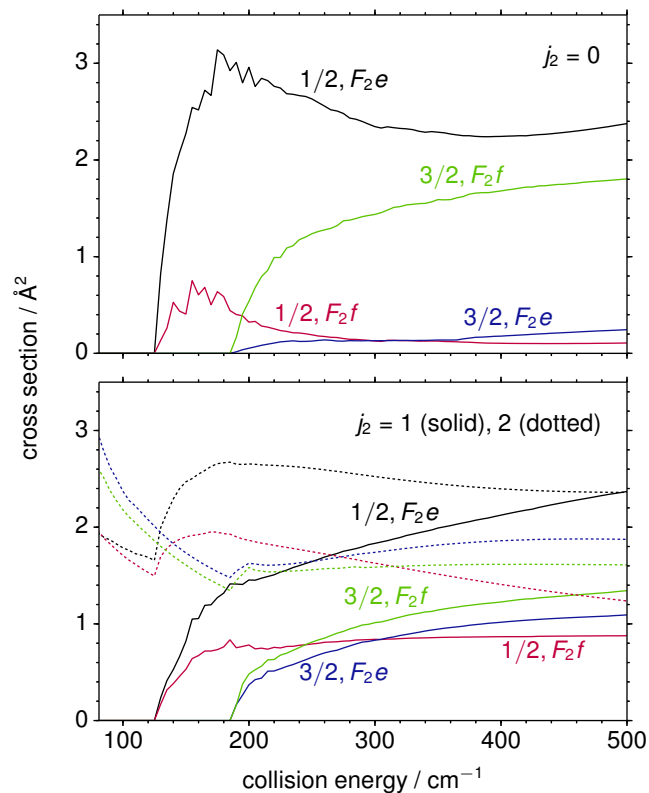


Figure 8.7: State-to-state integral cross section as a function of collision energy for transition from the $j_1 = 3/2, F_1, f$ level of OH to other F_2 levels in collisions with D_2 . The final levels are indicated for each transition for which the cross section is plotted. The initial rotational quantum number j_2 is labeled on each subplot. Cross sections to various final rotational levels of D_2 are summed up.

of D_2 (or $l_2 = 2$ expansion coefficients). For the $F_1 \rightarrow F_2$ transitions, collisions with D_2 in the $j_2 = 1$ and $j_2 = 2$ initial levels show cross sections of distinctly different magnitude. A primary reason for this difference is the presence of $j_2 = 2 \rightarrow 0$ transitions, which has cross sections comparable to the smaller $j_2 = 2 \rightarrow 2, F_1 \rightarrow F_2$ transitions at lower collision energies. The $j_2 = 2 \rightarrow 0$ transitions are also responsible for the non-zero cross sections below the threshold.

Figure 8.8 shows the comparison between our computed state-to-state relative cross sections with the experimental results by Kirste *et al.* [96]. Unfortunately the rotational temperature of the D_2 beam, which is important in making a fair comparison between theory and experiment was not reported in Ref. [96]. The authors stated that six temperatures ranging from 93 K to 293 K were used for the valve producing the D_2 beam. Here

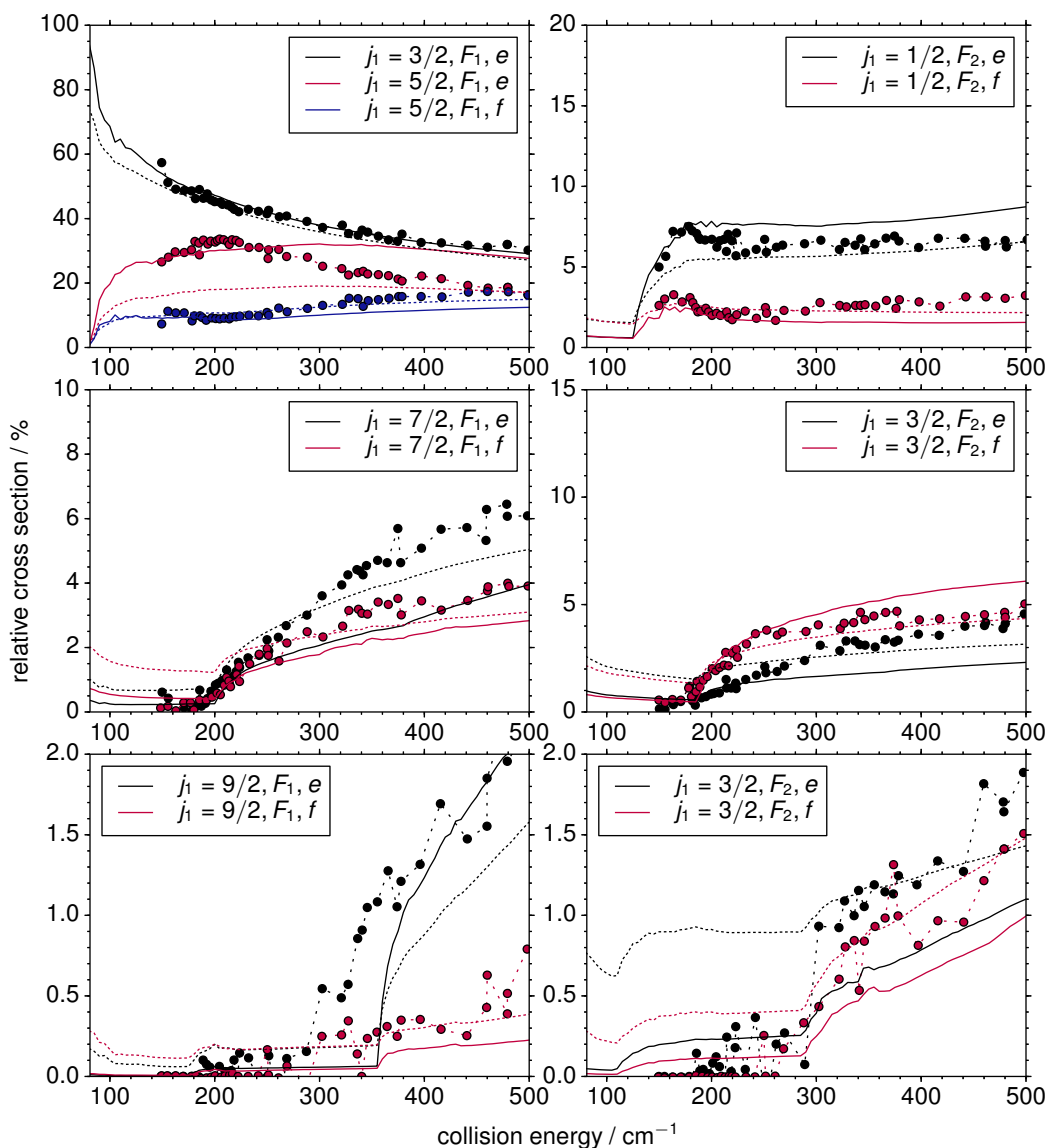


Figure 8.8: Experimental and theoretical relative state-to-state inelastic scattering cross section of as a function of collision energy for transition out of the $j_1 = 3/2, F_1, f$ level of OH. The experimental data, taken from Ref. [96], are shown as dots. The theoretical results computed using the CCSD(T) PESs assuming the temperature of the D₂ beam be 93 K and 293 K are plotted in solid lines and dotted lines, respectively. These two temperatures are the lower and upper limits of the D₂ beam temperature in the experiment. The final levels are indicated for each transition for which the cross section is plotted.

Table 8.1: Populations (in percent) of the lower D₂ rotational levels at various temperatures, assuming Boltzmann distribution and a rotational constant of 29.322 cm⁻¹.

D ₂ initial level	$T = 93$ K	$T = 133$ K	$T = 173$ K	$T = 213$ K	$T = 253$ K	$T = 293$ K
$j = 0$	52.1	38.6	30.5	25.2	21.4	18.6
$j = 1$	31.0	30.3	27.8	25.2	22.9	20.8
$j = 2$	16.2	27.7	34.3	37.4	38.6	38.6
$j = 3$	0.7	2.8	5.4	7.8	9.7	11.2
$j = 4$	0.0	0.5	1.9	4.0	6.4	8.9
$j = 5$	0.0	0.0	0.1	0.3	0.7	1.3

we assume the D₂ beam is in thermal equilibrium (rotational level distribution of D₂ at various rotational temperatures are shown in Table 8.1). To make a reasonable comparison between theory and experiment, we computed the two sets of relative cross sections (up to the $j_2 = 3$ initial level of D₂ considered) assuming that the initial level of D₂ is at thermal equilibrium at 93 K (solid lines in Fig. 8.8) and 293 K (dotted lines in Fig. 8.8). These two sets of theoretical cross sections would give an indication of the variation in relative cross sections due to the unknown beam temperature. In addition, we could probably assume that the experimental cross sections for lower energies are taken with a lower D₂ beam temperature. Thus, if the theoretical and experimental results were to match perfectly, in Fig. 8.8 the dots representing the experimental cross sections would overlap with the solid lines at the lowest collision energies, and gradually move toward and eventually overlap with the dotted lines as the collision energy increases.

Using this criterion, we see the agreement between theory and experiment is excellent. Most of the experimental cross sections lie close to the range we predicted. For some of the transitions, e.g., the $j_1 = 3/2, F_1, f \rightarrow j_1 = 5/2, F_1, e$ transition, we could even observe the experimental cross sections agree with the theoretical results at 93 K and eventually move towards those at 293 K at the collision energy increases. Given this excellent agreement, we believe that the loss of preference for the e -symmetry levels for the transition to the $j_1 = 5/2, F_1$ state at higher energies is actually due to the increased rotational temperature of the D₂ beam, rather than the increased collision energy, as presumed in Ref. [96]. In addition, we note that the relative cross section for the dominating

transition, $j_1 = 3/2, F_1, f \rightarrow j_1 = 3/2, F_1, e$, does not vary significantly for the two D_2 rotational temperature considered. For this transition the agreement between theory and experiment is excellent.

We see our CCSD(T) PESs are successful in predicting the spin-orbit changing ($F_1 \rightarrow F_2$) transitions as well. In the Hund's case (a) limit, these transitions are coupled directly by the off-diagonal V_o PES only. Although OH cannot be described by a pure case (a) coupling scheme, we could expect V_o plays a more significant role in the $F_1 \rightarrow F_2$ transitions. This agreement between theory and experiment again validates our approach by sampling only the high symmetry geometries.

Still, we notice that our predicted cross sections to the $j_1 = 7/2, F_1$ levels are much smaller than the experimental values, and at $\sim 200 \text{ cm}^{-1}$ collision energy the experimental cross sections for the transition to the $j_1 = 5/2, F_1, e$ level is noticeably larger than our prediction. These discrepancies may come from the inaccuracy of our PESs.

8.5 The Quality of the PESs

We have shown in Sec. 8.3.2 that the OH- H_2 scattering dynamics is very sensitive to the accuracy of the PESs. To further check the accuracy of our *ab initio* calculations, we performed extra calculations for the potential for the T-shaped geometry ($\theta_O = 0^\circ$, $\theta_H = 90^\circ$, $\phi_H = 0^\circ$) of OH- H_2 at three values of intermolecular distances ($5, 5.25$, and $6a_0$). At $5a_0$, the potential is repulsive with a value of $\sim 300 \text{ cm}^{-1}$, close to the classical turning point in the cold collisions. At $5.25a_0$, the potential is close to zero and is very sensitive to the level of theory. The potential at $R = 6a_0$ is a good indicator of the well depth of the PESs as it is close to the geometry at which the global minimum is found.

Our results are listed in Table 8.2. First, we notice that all the methods give consistent values for the off-diagonal V_o potential, which at this OH- H_2 orientation is proportional to the difference between the interaction energy of OH in $|\Pi_x\rangle$ and $|\Pi_y\rangle$ states with H_2 . For the diagonal V_d potential, the CCSD(T)-F12a values agree reasonably very

Table 8.2: Comparison of the computed OH-H₂ diagonal V_d and off-diagonal V_o potential at three intermolecular separations for the T-shaped ($\theta_O = 0^\circ$, $\theta_H = 90^\circ$, $\phi_H = 0^\circ$) geometry.^a In this table aVnZ represent the correlation consistent aug-cc-pVnZ basis set. The last two lines represent results obtained by averaging CCSD(T)-F12a/aVTZ+BF^b potential computed with various bond lengths of OH or H₂ over the ground-state vibrational wave function of the molecule.

Method	V_d (cm ⁻¹)			V_o (cm ⁻¹)		
	$R = 5 a_0$	$5.25 a_0$	$6 a_0$	$R = 5 a_0$	$5.25 a_0$	$6 a_0$
MRCISD+Q/aVQZ ^b	268.6	1.8	-218.9	-34.7	-25.8	-12.1
CCSD(T)-F12a/aVTZ+BF ^{c,d}	243.8	-13.4	-219.6	-34.3	-25.3	-11.6
CCSD(T)/aVTZ+BF ^d	280.0	12.5	-210.2	-34.6	-25.6	-11.7
CCSDT/aVTZ+BF ^d	271.8	6.0	-213.4	-34.9	-25.8	-11.7
CCSD(T)/CBS[345] ^e	255.8	-4.2	-215.1	-34.0	-25.1	-11.5
averaged over $\chi_0(r)$ of H ₂	243.1	-13.4	-219.2	-34.5	-25.4	-11.6
averaged over $\chi_0(r)$ of OH	263.5	-1.9	-219.8	-34.5	-25.5	-11.6

^a See Chapter 7 for the definition of V_d , V_o and the angles.

^b The method used in creating the MRCI PESs.

^c The method used in creating the CCSD(T) PESs.

^d BF indicates the addition of mid-bond functions.

^e CBS limit extrapolated from CCSD(T) calculations using the aVTZ, aVQZ, and aV5Z basis.

well with the CBS values, showing that the CCSD(T)-F12a method is a good approximation to improve the basis-set convergence. Using the aug-cc-pVTZ basis with mid-bond functions (aVTZ+BF), the close coupling calculations with full triples (CCSDT) [289] gives results very similar to those with the perturbative inclusion of triples [CCSD(T)], and the difference between these results are much less than the difference between the CCSD(T)/aVTZ+BF and the CBS results. The CCSD(T)-F12a calculations are much cheaper, and more accurate, than the CCSDT calculations when the aug-cc-pVTZ basis is used. Hence the CCSD(T)-F12a/aVTZ+BF calculations we used for the CCSD(T) PESs are of good accuracy.

We used a rigid rotor model in creating PESs and performing scattering calculations. Full-dimensional dynamics study is not possible presently using the close-coupling method. For the PESs, a better treatment would be to calculate the PESs at various values of O-H and H-H bond lengths and then average over the ground vibrational wave function $\chi_0(r)$ for both species. The last two lines in Table 8.2 show the effect of vibrational averaging on

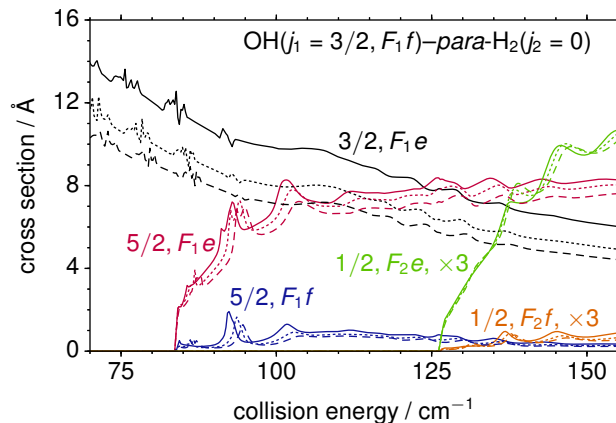


Figure 8.9: Comparison of the theoretical state-to-state OH-H₂ ($j_2 = 0$) integral cross section computed from potential energy surfaces generated using different monomer bond lengths. Cross section as a function of collision energy for transitions out of the OH $j_1 = 3/2, F_1, f$ are shown. The cross sections were computed with the CCSD(T) PESs (using r_0 of OH and H₂, solid lines), a CCSD(T)/aVTZ+BF PES using r_e of OH and r_0 of H₂ (dotted lines), and a CCSD(T)/aVTZ+BF PES using r_e of OH and r_e of H₂ (dashed lines). The final level of the transitions are indicated on the plots. For clarity, the transitions to the F_2 levels are multiplied by 3.

the potential. We see the averaging over $\chi_0(r)$ of H₂ has little effect on the potential of the T-shaped geometry, while the averaging over $\chi_0(r)$ of OH leads to a $\sim 8\%$ change in V_d at $R = 5 a_0$.

To gain more insight on the effect of the vibrational averaging on the cross sections, we computed two extra sets of PESs, at a slightly lower level of theory [CCSD(T)/aVTZ+BF], by using the equilibrium bond lengths (r_e) instead of vibrationally averaged bond lengths (r_0) of OH and/or H₂. We then computed the state-to-state cross sections for the cold collisions of OH with H₂ with these new PESs. Our results are shown in Fig. 8.9. Again, the cross section for the $j_1 = 3/2, F_1, f \rightarrow j_1 = 3/2, F_1, e$ (black lines in Fig. 8.9) appears to be most sensitive to the PESs. For this transition, the bond lengths of OH and H₂ may have a significant impact on the cross sections, and our simplified treatment may be a source of deviations between theory and experiments.

In our scattering calculations the reaction (OH+H₂ \rightarrow H₂O+H) channel is ignored. The experimental value for the activation energy was reported to be $1380 \pm 240 \text{ cm}^{-1}$ [290], which is much higher than the collision energies considered in our calculations.

8.6 Conclusions

In this chapter we have presented computed cross sections for the rotationally inelastic scattering of OH out of the $j_1 = 3/2, F_1, f$ level with H₂ and D₂, using our recently developed CCSD(T) and MRCI PESs (Chapter 7) and the close coupling method. Specifically, we have computed OH-H₂ cross sections at 595 cm⁻¹ collision energy and OH-D₂ cross sections at 100–500 cm⁻¹. These results are compared to the experimental values by Schreel and ter Meulen [144] and by Kirste [96], respectively. The agreement between theory and experiments is satisfactory, signifying the accuracy of our PESs.

In addition, we present cross sections for the cold collisions of OH-H₂ at 70–150 cm⁻¹. We found that the cross sections are very sensitive to the PESs, especially for the $j_1 = 3/2, F_1, f, j_2 = 0 \rightarrow j_1 = 3/2, F_1, e, j_2 = 0$ transition. The collision dynamics for the OH-H₂/D₂ system depends heavily on the initial rotational level of H₂/D₂. In particular, the quadrupole of H₂/D₂ does not play a direct role in the collisions with H₂ or D₂ in the $j_2 = 0$ initial level, which leads to distinct dynamics. The existing experimental cross sections were measured with relative high-temperature H₂/D₂ beams. In this case the measured cross sections are less dependent upon the $j_2 = 0 \rightarrow 0$ cross sections, which is more sensitive to the accuracy of PESs. We encourage further experimental study on this system, which will provide more strict tests to our PESs.

We also performed extra *ab initio* calculations to justify our PESs. We believe the CCSD(T)-F12a/aug-cc-pVTZ+BF method we used in generating the PESs is accurate and cost-effective. Still, we ignored the vibrational motion of the collision partners in creating the PESs and in the scattering calculations. This may lead to some error in our description of the scattering dynamics.

Appendix A

Theory on the OH–H₂ Potential Energy Surfaces, and Bound-State and Scattering Calculations

A.1 Expansion of the Potential

To suggest a functional form for the OH–H₂ interaction we use the two-center multipolar expansion of the Coulomb interaction, namely [66, 135]

$$r_{ij}^{-1} = \sum_{l_1 l_2 l m_1 m_2 m} \langle l_1 m_1, l_2 m_2 | l m \rangle A_{l_1 l_2 l}(r_i, r_j, \mathbf{R}) C_{l_1 m_1}(\omega_i) C_{l_2 m_2}(\omega_j) C_{l m}^*(\Omega). \quad (\text{A.1})$$

Here, ω_i and ω_j are the space-frame polar angles of vectors centered, respectively, at the centers-of-mass of the OH and HH moieties, and Ω denotes the polar coordinates of the OH–HH Jacobi vector \mathbf{R} which joins these two centers of mass.

We define a body frame where the Z axis lies along \mathbf{R} . In this frame, the orientations of the OH and H₂ molecular frames (in which the internuclear axes define the z axes) are defined by, respectively, the angles $(0, \theta_O, 0)$ and $(\phi_H, \theta_H, 0)$. In the OH molecule frame, \vec{z} points from O to H, so that $\theta_O = 0$ corresponds to the H nucleus lying along the $+z$ direction. The body-frame expansion in Eq. (A.1) can then be written as

$$r_{ij}^{-1} = \sum_{l_1 l_2 l m} \langle l_1 m, l_2, -m | l 0 \rangle A_{l_1 l_2 l}(r_i, r_j, \mathbf{R}) C_{l_1 m}(\hat{r}_i) C_{l_2, -m}(\hat{r}_j). \quad (\text{A.2})$$

In Eqs. (A.1) and (A.2) \hat{r}_i and \hat{r}_j are the orientations of the vectors describing the position of the i -th OH electron (referred to the coordinate system fixed at the OH center of mass) and the j -th H₂ electron (referred to the coordinate system fixed at the HH center of mass). Specifically, the operator involves a product of a one-electron operator in the space of the OH electrons and a one-electron operator in the space of the H₂ electrons.

To investigate the symmetry of the OH-HH potential, it is sufficient to express the electronic wave function as a product of a definite- Λ function on OH multiplied by the non-degenerate wave function for H₂ in its $^1\Sigma^+$ electronic state, namely

$$\Psi_{\text{OH}(\Lambda)\text{-H}_2} \equiv |\Lambda\rangle = \psi_\Lambda \psi_{\text{H}_2}$$

Following an earlier work on interactions of a molecule in a $^2\Pi$ electronic state with an atom[106], in this two-fold ($\Lambda = \pm 1$) basis we can express the matrix elements of the electronic Hamiltonian as

$$V_{\Lambda\Lambda}^{(el)} = \langle \psi_\Lambda \psi_{\text{H}_2} | \hat{H}_{el} | \psi_\Lambda \psi_{\text{H}_2} \rangle \quad (\text{A.3})$$

To obtain a formal expansion of these $V_{\Lambda\Lambda}$ potential energy surfaces, we can replace \hat{H}_{el} by \hat{V} , where

$$\hat{V} = \sum_{i,j>i} r_{ij}^{-1}$$

We then use the multipolar expansion of Eq. (A.2). It is then necessary to integrate over the electronic coordinates. The electronic wave functions of the diatomic moieties are conventionally defined in molecular frames, in which the z axes lie along the OH or HH bonds. Thus, to integrate over the electronic coordinates, it is first necessary to transform from the body frame to the molecular frame.

In the OH molecular frame the first spherical harmonic in Eq. (A.2) transforms as

[68]

$$C_{l_1 m}(\hat{r}_i) = \sum_{\mu_1} D_{m\mu_1}^{l_1*}(0, \theta_O, 0) C_{l_1 \mu_1}(\hat{\rho}_i) = \sum_{\mu_1} d_{m\mu_1}^{l_1}(\theta_O) C_{l_1 \mu_1}(\hat{\rho}_i), \quad (\text{A.4})$$

where $\hat{\rho}_i \equiv \theta_i, \phi_i$ is the orientation of the i -th OH electron in the OH molecular frame, and $d_{m\mu}^l$ is a reduced rotation matrix [68]. Similarly, in the H₂ molecular frame the second spherical harmonic in Eq. (A.2) transforms as [68]

$$\begin{aligned} C_{l_2, -m}(\hat{r}_j) &= \sum_{\mu_2} D_{-m\mu_2}^{l_2*}(\phi_H, \theta_H, 0) C_{l_2 \mu_2}(\hat{\rho}_j) \\ &= \sum_{\mu_2} d_{-m\mu_2}^{l_2}(\theta_H) \exp(-im\phi_H) C_{l_2 \mu_2}(\hat{\rho}_j), \end{aligned} \quad (\text{A.5})$$

We now wish to determine the dependence of the interaction potential on the angular momentum projection Λ . To do so, it is simplest to write the OH electronic wave function as a Slater determinant built of the $\pi_{\pm 1}$ molecular orbitals of the OH moiety,

$$\psi_{\Lambda} \equiv |\dots \pi_{\lambda} \bar{\pi}_{\lambda} \pi_{-\lambda}| \quad (\text{A.6})$$

We choose these definite- Λ π orbitals to have the same reflection symmetry in the xz -plane as the spherical harmonics with $m_L = \lambda$ namely

$$\hat{\sigma}_{xz} \pi_{\lambda} = -\pi_{-\lambda}$$

The OH wave function will then have the same symmetry, namely

$$\hat{\sigma}_{xz} \psi_{\Lambda} = -\psi_{-\Lambda}$$

Formally, we can expand the OH molecular orbitals in single-center expansions. In particular,

$$|\pi_{\lambda}\rangle = \sum_L g_L(\rho_i, \theta_i) C_{L\lambda}(\hat{\rho}_i), \quad (\text{A.7})$$

Consequently, in the integration over the angular coordinates of electron i we have

$$\begin{aligned} & \int C_{L'\lambda'}^*(\theta_i, \phi_i) C_{l_1\mu_1}(\theta_i, \phi_i) C_{L\lambda}(\theta_i, \phi_i) \sin\theta_i d\theta_i d\phi_i \\ &= 4\pi \begin{pmatrix} L' & l_1 & L \\ 0 & 0 & 0 \end{pmatrix} \begin{pmatrix} L' & l_1 & L \\ -\lambda' & \mu_1 & \lambda \end{pmatrix}. \end{aligned} \quad (\text{A.8})$$

This vanishes unless

$$\mu_1 = \lambda' - \lambda. \quad (\text{A.9})$$

For the OH component of the diagonal $\langle \Lambda | \hat{V} | \Lambda \rangle$ matrix element, both the bra and the ket correspond to the same Slater determinant, so that the one-electron integral over each π_λ spin-orbital corresponds to $\lambda' = \lambda$, so that μ_1 must equal 0.

For the OH component of the off-diagonal $\langle \Lambda' | \hat{V} | \Lambda \rangle$ matrix element, the bra and the ket differ in one spin orbital. In the $\langle +1 | \hat{V} | -1 \rangle$ matrix element this one-electron integral is of the form

$$\langle |\dots\pi_1\bar{\pi}_1\pi_{-1}| | \hat{V} | |\dots\pi_{-1}\bar{\pi}_{-1}\pi_1| \rangle = -\langle \bar{\pi}_1 | \hat{V} | \bar{\pi}_{-1} \rangle$$

so that $\mu_1 = +2$. Similarly for the $\langle -1 | \hat{V} | +1 \rangle$ matrix element,

$$\langle |\dots\pi_{-1}\bar{\pi}_{-1}\pi_1| | \hat{V} | |\dots\pi_1\bar{\pi}_1\pi_{-1}| \rangle = -\langle \bar{\pi}_{-1} | \hat{V} | \bar{\pi}_1 \rangle$$

so that $\mu_1 = -2$.

The electronic wave function of the H_2 moiety is cylindrically symmetric, so that regardless of the value of Λ , the integration of Eq. (A.5) over the azimuthal coordinate of electron j will vanish unless $\mu_2 = 0$.

Using this analysis, we can expand the $V_{\Lambda\Lambda}$ interaction potential [Eq. (A.3)] as

$$V_{\Lambda',\Lambda}(R, \theta_O, \theta_H, \phi_H) = \sum_{l_1 l_2 l} V_{l_1 l_2 l}^{(\Lambda'-\Lambda)}(R) \sum_m \langle l_1 m, l_2, -m | l 0 \rangle \\ \times d_{m, \Lambda'-\Lambda}^{l_1}(\theta_O) d_{-m, 0}^{l_2}(\theta_H) e^{-im\phi_H} \quad (\text{A.10})$$

The potential must be invariant with respect to interchanging the two hydrogen nuclei in the H_2 moiety. The corresponding operator, \hat{P}_{HH} , involves a rotation around the Z -axis by π followed by a reflection in the XY -plane, in other words

$$\{\theta_H, \phi_H\} \rightarrow \{\pi - \theta_H, \pi + \phi_H\} \quad (\text{A.11})$$

Applying this operation to Eq. (A.10) gives

$$\hat{\Pi}_{\text{H}_2} V_{\Lambda',\Lambda}(R, \theta_O, \theta_H, \phi_H) = \sum_{l_1 l_2 l} V_{l_1 l_2 l}^{(\Lambda'-\Lambda)}(R) \sum_m \langle l_1 m, l_2, -m | l 0 \rangle \\ \times d_{m, \Lambda'-\Lambda}^{l_1}(\theta_O) d_{-m, 0}^{l_2}(\pi - \theta_H) (-1)^m e^{-im\phi_H} \quad (\text{A.12})$$

Now, we can use the relations $d_{m 0}^{l_2}(\pi - \theta) = (-1)^{l_2+m} d_{-m, 0}^{l_2}(\theta)$ to obtain

$$\hat{\Pi}_{\text{H}_2} V_{\Lambda',\Lambda}(R, \theta_O, \theta_H, \phi_H) = \sum_{l_1 l_2 l} V_{l_1 l_2 l}^{(\Lambda'-\Lambda)}(R) \sum_m \langle l_1 m, l_2, -m | l 0 \rangle \\ \times d_{m, \Lambda'-\Lambda}^{l_1}(\theta_O) d_{-m, 0}^{l_2}(\theta_H) (-1)^{l_2} e^{-im\phi_H} \quad (\text{A.13})$$

By symmetry this expression should equal Eq. (A.12). Thus l_2 must be even.

A.2 Long-Range Multipole-Multipole Expansion of the PESs

At long-range, most of the expansion terms in Eq. (A.10) go to zero exponentially. The exception are terms which correspond to the electrostatic interactions between the multipoles which arise in the expansion of the the OH and H₂ electron densities (or, for OH, in the expansion of the overlap density between the $\Lambda = 1$ and $\Lambda = -1$ electronic wave functions. For these terms, the expansion index l in Eq. (A.10) takes on its “stretched” value of $l = l_1 + l_2$.

For these multipole-multipole terms the $V_{l_1 l_2 l}(R)$ terms in Eq. (A.10) are [66]

$$V_{l_1 l_2 l}^{|\Lambda' - \Lambda|}(R) = \delta_{l, l_1 + l_2} A_{l_1 l_2} R^{-l-1} q_{l_1, |\Lambda' - \Lambda|}^O q_{l_2, 0}^H, \quad (\text{A.14})$$

where

$$A_{l_1 l_2} = (-1)^{l_2} \left[\frac{(2l_1 + 2l_2)!}{(2l_1)!(2l_2)!} \right]^{\frac{1}{2}}.$$

Here $q_{l_2, 0}^H$ is the l^{th} electrostatic definite- Λ multiple moment of the H₂ molecule

$$q_{l_2, 0}^H = \int |\Psi_{\text{H}_2}|^2 \sum_j e_j r_j^{l_2} C_{l_2, 0}(\omega_j) d\tau_j. \quad (\text{A.15})$$

The integration extends over the coordinates of the j^{th} electron of the H₂ moiety. For OH, there are two sets of definite- Λ multipole moments: a diagonal set comparable to Eq. (A.15)

$$q_{l_1, 0}^O = \int |\Psi_{\Lambda_2}|^2 \sum_i e_i r_i^{l_1} C_{l_1, 0}(\omega_i) d\tau_i, \quad (\text{A.16})$$

and an off-diagonal set ($|\Lambda' - \Lambda| = 2$)

$$q_{l_1, 2}^O = \int \Psi_1^* \left[\sum_i e_i r_i^{l_1} C_{l_1, 2}(\omega_i) \right] \Psi_{-1} d\tau_i. \quad (\text{A.17})$$

Most *ab initio* packages yield real multipole moments

$$Q_{lx} = \langle \psi | \hat{R}_{lx} | \psi \rangle \quad (\text{A.18})$$

The definition of \hat{R}_{lx} can be found in Table E.1 of Stone [71]. The index x can be 0, 1c, 1s, 2c, 2s, We use upper case Q to distinguish these from the definite- Λ moments q_{lm} .

The relationship between the Q_{lx} and q_{lm} is

$$Q_{l0} = q_{l0}, \quad (\text{A.19})$$

$$Q_{lmc} = \sqrt{2} \Re(q_{lm}), \quad (\text{A.20})$$

and

$$Q_{lms} = \sqrt{2} \Im(q_{lm}). \quad (\text{A.21})$$

Since, for OH

$$|\Pi_{\pm 1}\rangle = \mp 2^{-\frac{1}{2}} (|\Pi_x\rangle \pm i |\Pi_y\rangle), \quad (\text{A.22})$$

we find

$$q_{l_1 0}^{\text{O}} = \langle \Pi_1 | \hat{q}_{l_1 0} | \Pi_1 \rangle = \langle \Pi_{-1} | \hat{q}_{l_1 0} | \Pi_{-1} \rangle = \langle \Pi_x | \hat{q}_{l_1 0} | \Pi_x \rangle = \langle \Pi_x | R_{l_1 0} | \Pi_x \rangle, \quad (\text{A.23})$$

and

$$\begin{aligned} q_{l_1 2}^{\text{O}} &= q_{l_1, -2}^{\text{O}} = \langle \Pi_1 | \hat{q}_{l_1 2} | \Pi_{-1} \rangle = \langle \Pi_{-1} | \hat{q}_{l_1, -2} | \Pi_1 \rangle \\ &= -2 \langle \Pi_x | \hat{q}_{l_1 2} | \Pi_x \rangle = -\sqrt{2} \langle \Pi_x | R_{l_1 2c} | \Pi_x \rangle. \end{aligned} \quad (\text{A.24})$$

Equation (A.14) was employed in Sec. 7.3.4 in the long-range extrapolation of the OH-H₂ PESs.

A.3 Matrix Elements of the Potential in an OH–H₂ Rotational Basis

By defining a complete coupled rotational basis, built of products of the rotational wave functions of the OH and H₂ moieties, we can describe both scattering of OH by H₂, as well as the bend-stretch levels of the OH···H₂ complex. We follow earlier work by Miller and Clary [273], and Offer and van Hemert [268], in using a Hund's case (a) basis for the OH(*X*²Π) rotational wave function.

$$|j_1 m_1 \omega \varepsilon\rangle = 2^{-\frac{1}{2}} (|j_1 m_1 \omega\rangle |\Lambda \Sigma\rangle + \varepsilon |j_1 m_1, -\omega\rangle |-\Lambda, -\Sigma\rangle), \quad (\text{A.25})$$

where $\varepsilon = \pm 1$, and j_1 , m_1 , ω , and Σ designate the total angular momentum of OH, the space-frame projection of j_1 , the absolute value of the molecule-frame projection of j_1 , and the molecule-frame projection of the electron spin, respectively. The OH rotational wave function in Eq. (A.25) is

$$|j_1 m_1 \omega\rangle = [(2j_1 + 1)/4\pi]^{\frac{1}{2}} D_{m_1 \omega}^{j_1*}(\phi_O, \theta_O, 0). \quad (\text{A.26})$$

Similarly, the rotational wave function of H₂ is

$$|j_2 m_2\rangle = [(2j_2 + 1)/4\pi]^{\frac{1}{2}} D_{m_2 0}^{j_2*}(\phi_H, \theta_H, 0), \quad (\text{A.27})$$

and the wave function for end-over-end rotation of the OH–H₂ complex is

$$|LM_L\rangle = [(2L + 1)/4\pi]^{\frac{1}{2}} D_{M_L 0}^{L*}(\Phi, \Theta, 0), \quad (\text{A.28})$$

where $(\Phi, \Theta, 0)$ is the space-frame orientation of **R**.

The close-coupling basis is then

$$\begin{aligned}
|JMj_1\omega j_2j_{12}L\rangle &= \sum_{m_1m_2m_{12}M_L} \langle j_1m_1, j_2m_2 | j_{12}m_{12}\rangle \\
&\times \langle j_{12}m_{12}, LM_L | JM\rangle |j_1m_1\omega\rangle |j_2m_2\rangle |LM_L\rangle. \tag{A.29}
\end{aligned}$$

The rotational levels of the isolated OH radical are described in mixed Hund's case coupling. The lower and higher energy fine-structure levels for each j_1 are designated F_1 and F_2 . Expressing the wave function of OH as a linear combination of Hund's case (a) wave functions. Thus the full close-coupled angular basis is

$$|JMj_1\varepsilon F_i j_2 j_{12} L\rangle = c_{1/2} |JMj_1, \omega = \frac{1}{2}, \varepsilon j_2 j_{12} L\rangle + c_{3/2} |JMj_1, \omega = \frac{3}{2}, \varepsilon j_2 j_{12} L\rangle. \tag{A.30}$$

Making use of the above equations, we find the following expression for the potential matrix elements in the $\{JMj_1\varepsilon F_i j_2 j_{12} L\}$ basis

$$\begin{aligned}
&\langle JMj_1'\varepsilon' F_i' j_2' j_{12}' L' | V | JMj_1\varepsilon F_i j_2 j_{12} L\rangle \\
&= \sum_{l_1 l_2 l} \frac{1}{2} \left[1 - \varepsilon' \varepsilon (-1)^{j_1' + j_1 + l_1} \right] (-1)^{j_1' + l_1 - l_2 + j_1 - j_2 + j_{12}' - L - L' - \frac{1}{2}} \\
&\times ([j_1'] [j_2'] [j_{12}'] [L'] [j_1] [j_2] [j_{12}] [L] [l])^{\frac{1}{2}} \\
&\times \begin{pmatrix} j_2' & l_2 & j_2 \\ 0 & 0 & 0 \end{pmatrix} \begin{pmatrix} L' & l & L \\ 0 & 0 & 0 \end{pmatrix} \begin{Bmatrix} j_{12} & L & J \\ L' & j_{12}' & l \end{Bmatrix} \begin{Bmatrix} j_1 & j_2 & j_{12} \\ j_1' & j_2' & j_{12}' \\ l_1 & l_2 & l \end{Bmatrix} \\
&\times \left\{ \left[c'_{1/2} c_{1/2} \begin{pmatrix} j_1' & l_1 & j_1 \\ -\frac{1}{2} & 0 & \frac{1}{2} \end{pmatrix} - c'_{3/2} c_{3/2} \begin{pmatrix} j_1' & l_1 & j_1 \\ -\frac{3}{2} & 0 & \frac{3}{2} \end{pmatrix} \right] B_{l_1 l_2 l}(R) \right. \\
&\left. + \varepsilon \left[c'_{1/2} c_{3/2} \begin{pmatrix} j_1' & l_1 & j_1 \\ -\frac{1}{2} & 2 & -\frac{3}{2} \end{pmatrix} - c'_{3/2} c_{1/2} \begin{pmatrix} j_1' & l_1 & j_1 \\ -\frac{3}{2} & 2 & -\frac{1}{2} \end{pmatrix} \right] F_{l_1 l_2 l}(R) \right\}, \tag{A.31}
\end{aligned}$$

where $[J] \equiv (2J + 1)$, and (\vdots) , $\{\vdots\}$, and $\{\vdots\}$ are Wigner 3- j , 6- j , and 9- j symbols, respectively [28]. Equation (A.31) can be used in both bound-state and scattering calculations.

The phase factor in Eq. (A.31) is different from that in Eq. (A15) of Ref. [273]. We believe the latter value is incorrect, although, this difference in phase does not affect the computed bound-state energies or state-to-state cross sections.

Bibliography

- [1] J. I. Steinfeld, J. S. Francisco, and W. L. Hase, *Chemical Kinetics and Dynamics* (Prentice Hall, Upper Saddle River, New Jersey, 1998).
- [2] M. S. Child, *Molecular Collision Theory* (Academic, London/New York, 1974).
- [3] R. B. Bernstein, in *Atom-Molecule Collision Theory: A Guide for the Experimentalist*, edited by R. B. Bernstein (Plenum, New York, 1979) Chap. 1, pp. 1–44.
- [4] R. P. Wayne, *Chemistry of Atmospheres* (Oxford University Press, Oxford, 2000).
- [5] J. A. Miller, R. J. Kee, and C. K. Westbrook, *Annu. Rev. Phys. Chem.* **41**, 345 (1990).
- [6] A. M. Shaw, *Astrochemistry: From Astronomy to Astrobiology* (John Wiley & Sons Inc., 2006).
- [7] Y. T. Lee, *Science* **236**, 793 (1987).
- [8] A. G. Suits and Y. T. Lee, in *Springer Handbook of Atomic, Molecular, and Optical Physics*, edited by G. W. F. Drake (Springer, 2005) Chap. 66, pp. 967–982.
- [9] P. J. Dagdigian, in *The Chemical Dynamics and Kinetics of Small Radicals*, Advanced Series in Physical Chemistry, edited by K. Liu and A. Wagner (World Scientific Publishing Co. Pte. Ltd., 1996) Chap. 8, pp. 315–364.
- [10] R. W. Gentry, in *Atomic and Molecular Beam Methods*, edited by G. Scoles (Oxford University Press, New York, Oxford, 1988) pp. 54–82.
- [11] S. Y. T. van de Meerakker, H. L. Bethlem, and G. Meijer, *Nat. Phys.* **4**, 595 (2008).
- [12] M. Kirste, X. Wang, H. C. Schewe, G. Meijer, K. Liu, A. van der Avoird, L. M. C. Janssen, K. B. Gubbels, G. C. Groenenboom, and S. Y. T. van de Meerakker, *Science* **338**, 1060 (2012).
- [13] S. Chefdeville, Y. Kalugina, S. Y. T. van de Meerakker, C. Naulin, F. Lique, and M. Costes, *Science* **341**, 1094 (2013).
- [14] D. W. Chandler and P. L. Houston, *J. Chem. Phys.* **87**, 1445 (1987).
- [15] A. T. J. B. Eppink and D. H. Parker, *Rev. Sci. Instrum.* **68**, 3477 (1997).

- [16] N. T. Goldberg, J. Zhang, K. Koszinowski, F. Bouakline, S. C. Althorpe, and R. N. Zare, *Proc. Natl. Acad. Sci.* **105**, 18194 (2008).
- [17] J. J. Kay, S. Y. T. van de Meerakker, E. A. Wade, K. E. Strecker, and D. W. Chandler, *J. Phys. Chem. A* **113**, 14800 (2009).
- [18] J. J. Kay, G. Paterson, M. L. Costen, K. E. Strecker, K. G. McKendrick, and D. W. Chandler, *J. Chem. Phys.* **134**, 091101 (2011).
- [19] J. J. Kay, J. D. Steill, J. Kłos, G. Paterson, M. L. Costen, K. E. Strecker, K. G. McKendrick, M. H. Alexander, and D. W. Chandler, *Mol. Phys.* **110**, 1693 (2012).
- [20] C.-H. Yang, G. Sarma, J. J. ter Meulen, D. H. Parker, U. Buck, and L. Wiesenfeld, *J. Phys. Chem. A* **114**, 9886 (2010).
- [21] C.-H. Yang, G. Sarma, D. H. Parker, J. J. ter Meulen, and L. Wiesenfeld, *J. Chem. Phys.* **134**, 204308 (2011).
- [22] A. von Zastrow, J. Onvlee, S. N. Vogels, G. C. Groenenboom, A. van der Avoird, and S. Y. T. van de Meerakker, *Nat. Chem.* **6**, 216 (2014).
- [23] C. J. Eyles, M. Brouard, C.-H. Yang, J. Kłos, F. J. Aoiz, A. Gijsbertsen, A. E. Wiskerke, and S. Stolte, *Nat. Chem.* **3**, 597 (2011).
- [24] A. M. Arthurs and A. Dalgarno, *Proc. R. Soc. London. Ser. A* **256**, 540 (1960).
- [25] D. Secrest, in *Atom-Molecule Collision Theory: A Guide for the Experimentalist*, edited by R. B. Bernstein (Plenum, New York, 1979) Chap. 8, pp. 265–299.
- [26] J. Lester, William A., in *Atomic and Molecular Scattering*, *Methods in Computational Physics: Advances in Research and Applications*, Vol. 10, edited by B. Alder, S. Fernbach, and M. Rotenberg (Elsevier, 1971) pp. 211 – 241.
- [27] P. J. Dagdigian, *Int. Rev. Phys. Chem.* **32**, 229 (2013).
- [28] R. N. Zare, *Angular Momentum: Understanding Spatial Aspects in Chemistry and Physics* (John Wiley & Sons, Inc., 1988).
- [29] M. H. Alexander, *J. Chem. Phys.* **81**, 4510 (1984).
- [30] L. D. Thomas, M. H. Alexander, B. R. Johnson, W. A. Lester, Jr., J. C. Light, K. D. McLenithan, G. A. Parker, M. J. Redmon, T. G. Schmalz, D. Secrest, and R. B. Walker, *J. Comput. Phys.* **41**, 407 (1981).
- [31] HIBRIDON is a package of programs for the time-independent quantum treatment of inelastic collisions and photodissociation written by M. H. Alexander, D. E. Manolopoulos, H.-J. Werner, B. Follmeg, P. J. Dagdigian, and others. More information and/or a copy of the code can be obtained from the website <http://www2.chem.umd.edu/groups/alexander/hibridon>.

- [32] B. R. Johnson, *J. Comput. Phys.* **13**, 445 (1973).
- [33] D. E. Manolopoulos, *J. Chem. Phys.* **85**, 6425 (1986).
- [34] R. G. Gordon, *J. Chem. Phys.* **51**, 14 (1969).
- [35] M. H. Alexander and D. E. Manolopoulos, *J. Chem. Phys.* **86**, 2044 (1987).
- [36] J. M. Hutson and S. Green, "Molscat computer code, version 14," (1994), distributed by Collaborative Computational Project No. 6 of the Engineering and Physical Sciences Research Council (UK).
- [37] B. R. Johnson, *J. Chem. Phys.* **67**, 4086 (1977).
- [38] B. R. Johnson, *J. Chem. Phys.* **69**, 4678 (1978).
- [39] D. J. Kouri, in *Atom-Molecule Collision Theory: A Guide for the Experimentalist*, edited by R. B. Bernstein (Plenum, New York, 1979) Chap. 9, pp. 301–358.
- [40] M. H. Alexander, S. Gregurick, P. J. Dagdigian, G. W. Lemire, M. J. McQuaid, and R. C. Sausa, *J. Chem. Phys.* **101**, 4547 (1994).
- [41] M. H. Alexander, S. Gregurick, and P. J. Dagdigian, *J. Chem. Phys.* **101**, 2887 (1994).
- [42] S. Y. Lin and H. Guo, *J. Chem. Phys.* **117**, 5183 (2002).
- [43] F. Otto, F. Gatti, and H.-D. Meyer, *Mol. Phys.* **110**, 619 (2012).
- [44] G. Chałasiński and M. M. Szczyński, *Chem. Rev.* **100**, 4227 (2000).
- [45] P. E. S. Wormer and A. van der Avoird, in *Theory and Application of Computational Chemistry: The First Forty Years*, edited by C. E. Dykstra, F. Gernot, K. S. Kim, and G. E. Scuseria (Elsevier, 2005) Chap. 37, pp. 1047–1091.
- [46] A. J. Misquitta, in *Handbook of Computational Chemistry*, edited by J. Leszczynski (Springer, 2012) Chap. 6, pp. 157–194.
- [47] F. Jensen, *Introduction to Computation Chemistry*, 2nd ed. (John Wiley & Sons, Ltd., 2007).
- [48] T. Helgaker, in *Modern Electronic Structure Theory*, edited by D. R. Yarkony (World Scientific Publishing Co. Pte. Ltd., 1995) Chap. 12, pp. 725–856.
- [49] H. Koch, B. Fernandez, and O. Christiansen, *J. Chem. Phys.* **108**, 2784 (1998).
- [50] F.-M. Tao and Y.-K. Pan, *J. Chem. Phys.* **97**, 4989 (1992).
- [51] T. B. Adler, G. Knizia, and H.-J. Werner, *J. Chem. Phys.* **127**, 221106 (2007).
- [52] G. Knizia and H.-J. Werner, *J. Chem. Phys.* **128**, 154103 (2008).

- [53] G. Knizia, T. B. Adler, and H.-J. Werner, *J. Chem. Phys.* **130**, 054104 (2009).
- [54] F. Lique, J. Kłos, and M. Hochlaf, *Phys. Chem. Chem. Phys.* **12**, 15672 (2010).
- [55] K. B. Gubbels, S. Y. T. van de Meerakker, G. C. Groenenboom, G. Meijer, and A. van der Avoird, *J. Chem. Phys.* **136**, 074301 (2012).
- [56] S. F. Boys and F. Bernardi, *Mol. Phys.* **19**, 553 (1970).
- [57] F. B. van Duijneveldt, J. G. C. M. van Duijneveldt-van de Rijdt, and J. H. van Lenthe, *Chem. Rev.* **94**, 1873 (1994).
- [58] M. Rode, J. Sadlej, R. Moszynski, P. E. S. Wormer, and A. van der Avoird, *Chem. Phys. Lett.* **314**, 326 (1999).
- [59] S. R. Langhoff and E. R. Davidson, *Int. J. Quantum Chem.* **8**, 61 (1974).
- [60] B. Jeziorski and K. Szalewicz, in *Handbook of Molecular Physics and Quantum Chemistry*, Vol. 8, edited by S. Wilson (Wiley, 2002) Chap. 8, pp. 37–83.
- [61] K. Szalewicz, K. Patkowski, and B. Jeziorski, in *Intermolecular Forces and Clusters II*, Structure and bonding, Vol. 116, edited by D. J. Wales (Springer, Berlin, 2005) pp. 43–117.
- [62] A. J. Misquitta, R. Podeszwa, B. Jeziorski, and K. Szalewicz, *J. Chem. Phys.* **123**, 214103 (2005).
- [63] P. Jankowski and K. Szalewicz, *J. Chem. Phys.* **123**, 104301 (2005).
- [64] A. Faure, P. Valiron, M. Wernli, L. Wiesenfeld, C. Rist, J. Noga, and J. Tennyson, *J. Chem. Phys.* **122**, 221102 (2005).
- [65] P. Valiron, M. Wernli, A. Faure, L. Wiesenfeld, C. Rist, S. Kedzuch, and J. Noga, *J. Chem. Phys.* **129**, 134306 (2008).
- [66] C. G. Gray, *Can. J. Phys.* **54**, 505 (1976).
- [67] H. J. Silverstone, in *Proceedings of MEST 2012: Electronic Structure Methods with Applications to Experimental Chemistry*, Advances in Quantum Chemistry, Vol. 68, edited by P. Hoggan (Academic Press, 2014) pp. 3–18.
- [68] D. Brink and G. Satchler, *Angular Momentum* (Clarendon, Oxford, 1968).
- [69] P. E. S. Wormer, J. A. Kłos, G. C. Groenenboom, and A. van der Avoird, *J. Chem. Phys.* **122**, 244325 (2005).
- [70] A. J. Stone, *Chem. Phys. Lett.* **83**, 233 (1981).
- [71] A. J. Stone, *The Theory of Intermolecular Forces*, 2nd ed. (Oxford University Press, 2013).

- [72] S. Maret, A. Faure, E. Scifoni, and L. Wiesenfeld, *Mon. Not. R. Astron. Soc.* **399**, 425 (2009).
- [73] R. P. Leavitt, *J. Chem. Phys.* **72**, 3472 (1980).
- [74] J. C. Whitehead, *Rep. Prog. Phys.* **59**, 993 (1996).
- [75] H. Kohguchi and T. Suzuki, *Annu. Rep. Prog. Chem., Sect. C: Phys. Chem.* **98**, 421 (2002).
- [76] P. T. P. Ho and C. H. Townes, *Annu. Rev. Astron. Astrophys.* **21**, 239 (1983).
- [77] D. R. Flower, *Phys. Rep.* **174**, 1 (1989).
- [78] J. Lequeux and E. Roueff, *Phys. Rep.* **200**, 241 (1991).
- [79] E. Roueff, D. C. Lis, F. F. S. van der Tak, M. Gerin, and P. F. Goldsmith, *Astron. Astrophys.* **438**, 585 (2005).
- [80] P. Casavecchia and M. H. Alexander, *Science* **341**, 1076 (2013).
- [81] P. J. Dagdigian and M. H. Alexander, *J. Chem. Phys.* **135**, 064306 (2011).
- [82] C. Schewe, N. Vanhaecke, and G. Meier, private communication (2013).
- [83] K. B. Gubbels, Q. Ma, M. H. Alexander, P. J. Dagdigian, D. Tanis, G. C. Groenenboom, A. van der Avoird, and S. Y. T. van de Meerakker, *J. Chem. Phys.* **136**, 144308 (2012).
- [84] R. B. Bernstein, ed., *Atom-Molecule Collision Theory: A Guide for the Experimentalist* (Plenum, New York, 1979).
- [85] Z. Bačić and R. E. Miller, *J. Phys. Chem.* **100**, 12945 (1996).
- [86] P. E. S. Wormer and A. van der Avoird, *Chem. Rev.* **100**, 4109 (2000).
- [87] F. Lique, G. Li, H.-J. Werner, and M. H. Alexander, *J. Chem. Phys.* **134**, 231101 (2011).
- [88] D. W. Chandler, *J. Chem. Phys.* **132**, 110901 (2010).
- [89] A. Schutte, D. Bassi, F. Tommasini, and G. Scoles, *Phys. Rev. Lett.* **29**, 979 (1972).
- [90] A. Schutte, D. Bassi, F. Tommasini, and G. Scoles, *J. Chem. Phys.* **62**, 600 (1975).
- [91] J. P. Toennies, W. Welz, and G. Wolf, *J. Chem. Phys.* **71**, 614 (1979).
- [92] M. Qiu, Z. Ren, L. Che, D. Dai, S. A. Harich, X. Wang, X. Yang, C. Xu, D. Xie, M. Gustafsson, R. T. Skodje, Z. Sun, and D. H. Zhang, *Science* **311**, 1440 (2006).
- [93] R. B. Bernstein, ed., *Molecular Reaction Dynamics and Chemical Reactivity* (Oxford University Press, New York, 1979).

- [94] L. Scharfenberg, J. Kłos, P. J. Dagdigian, M. H. Alexander, G. Meijer, and S. Y. T. van de Meerakker, *Phys. Chem. Chem. Phys.* **12**, 10660 (2010).
- [95] J. J. Gilijamse, S. Hoekstra, S. Y. T. van de Meerakker, G. C. Groenenboom, and G. Meijer, *Science* **313**, 1617 (2006).
- [96] M. Kirste, L. Scharfenberg, J. Kłos, F. Lique, M. H. Alexander, G. Meijer, and S. Y. T. van de Meerakker, *Phys. Rev. A* **82**, 042717 (2010).
- [97] L. Scharfenberg, S. Y. T. van de Meerakker, and G. Meijer, *Phys. Chem. Chem. Phys.* **13**, 8448 (2011).
- [98] W. Erlewein, M. Seggern, and J. P. Toennies, *Z. Physik* **211**, 35 (1968).
- [99] M. Seggern and J. P. Toennies, *Z. Physik* **218**, 341 (1969).
- [100] M. C. van Beek, J. J. ter Meulen, and M. H. Alexander, *J. Chem. Phys.* **113**, 637 (2000).
- [101] M. C. van Beek, J. J. ter Meulen, and M. H. Alexander, *J. Chem. Phys.* **113**, 628 (2000).
- [102] J. Kłos, F. Lique, and M. H. Alexander, *Chem. Phys. Lett.* **445**, 12 (2007).
- [103] Z. Pavlovic, T. V. Tscherbul, H. R. Sadeghpour, G. C. Groenenboom, and A. Dalgarno, *J. Phys. Chem. A* **113**, 14670 (2009).
- [104] P. J. Dagdigian and M. H. Alexander, *J. Chem. Phys.* **130**, 164315 (2009).
- [105] P. J. Dagdigian and M. H. Alexander, *J. Chem. Phys.* **130**, 094303 (2009).
- [106] M. H. Alexander, *Chem. Phys.* **92**, 337 (1985).
- [107] H.-S. Lee, A. B. McCoy, R. R. Toczyłowski, and S. M. Cybulski, *J. Chem. Phys.* **113**, 5736 (2000).
- [108] J. Han and M. C. Heaven, *J. Chem. Phys.* **123**, 064307 (2005).
- [109] S. L. Holmgren, M. Waldman, and W. Klemperer, *J. Chem. Phys.* **67**, 4414 (1977).
- [110] F. T. Smith, *Phys. Rev.* **118**, 349 (1960).
- [111] Y. Sumiyoshi, I. Funahara, K. Sato, Y. Ohshima, and Y. Endo, *Phys. Chem. Chem. Phys.* **12**, 8340 (2010).
- [112] L. Scharfenberg, K. B. Gubbels, M. Kirste, G. C. Groenenboom, A. van der Avoird, G. Meijer, and S. Y. T. van de Meerakker, *Eur. Phys. J. D* **65**, 189 (2011).
- [113] H.-J. Werner, P. J. Knowles, F. R. Manby, M. Schütz *et al.*, MOLPRO, version 2010.1, a package of ab initio programs, see <http://www.molpro.net>.

- [114] A. van der Avoird, P. E. S. Wormer, F. Mulder, and R. M. Berns, in *Van der Waals Systems*, Topics in Current Chemistry, Vol. 93 (Springer, Berlin/Heidelberg, 1980) pp. 1–51.
- [115] K. T. Tang and J. P. Toennies, *J. Chem. Phys.* **80**, 3726 (1984).
- [116] T.-S. Ho and H. Rabitz, *J. Chem. Phys.* **104**, 2584 (1996).
- [117] G. C. Groenenboom and N. Balakrishnan, *J. Chem. Phys.* **118**, 7380 (2003).
- [118] M. P. J. van der Loo and G. C. Groenenboom, *J. Chem. Phys.* **126**, 114314 (2007).
- [119] G. C. Groenenboom and D. T. Colbert, *J. Chem. Phys.* **99**, 9681 (1993).
- [120] P. J. Dagdigian, A. Khachatryan, and V. I. Babushok, *Appl. Opt.* **49**, C58 (2010).
- [121] D. T. Colbert and W. H. Miller, *J. Chem. Phys.* **96**, 1982 (1992).
- [122] L. Tao and M. H. Alexander, *J. Chem. Phys.* **127**, 114301 (2007).
- [123] E. P. Wigner, *Phys. Rev.* **98**, 145 (1955).
- [124] J. F. Castillo, D. E. Manolopoulos, K. Stark, and H.-J. Werner, *J. Chem. Phys.* **104**, 6531 (1996).
- [125] F. M. H. Crompvoets, R. T. Jongma, H. L. Bethlem, A. J. A. van Roij, and G. Meijer, *Phys. Rev. Lett.* **89**, 093004 (2002).
- [126] J. M. Beames, F. Liu, M. I. Lester, and C. Murray, *J. Chem. Phys.* **134**, 241102 (2011).
- [127] J. Z. H. Zhang, *Theory and Application of Quantum Molecular Dynamics* (World Scientific Publishing Co. Pte. Ltd., 1999).
- [128] S. Klaiman and I. Gilary (Academic Press, 2012) Chap. 1, pp. 1–31.
- [129] G. C. Schatz, *Science* **288**, 1599 (2000).
- [130] P. S. Żuchowski and J. M. Hutson, *Phys. Rev. A* **79**, 062708 (2009).
- [131] D. Pentlehner, R. Riechers, B. Dick, A. Slenczka, U. Even, N. Lavie, R. Brown, and K. Luria, *Rev. Sci. Instrum.* **80**, 043302 (2009).
- [132] G. Danby, D. R. Flower, P. Valiron, P. Schilke, and C. M. Walmsley, *Mon. Not. R. Astron. Soc.* **235**, 229 (1988).
- [133] A. Offer and D. R. Flower, *J. Phys. B: At. Mol. Opt. Phys.* **22**, L439 (1989).
- [134] A. Offer and D. R. Flower, *J. Chem. Soc., Faraday Trans.* **86**, 1659 (1990).
- [135] C. Rist, M. H. Alexander, and P. Valiron, *J. Chem. Phys.* **98**, 4662 (1993).

- [136] L. Wiesenfeld, E. Scifoni, A. Faure, and E. Roueff, *Mon. Not. R. Astron. Soc.* **413**, 509 (2011).
- [137] O. Tkáč, Q. Ma, C. A. Rusher, S. J. Greaves, A. J. Orr-Ewing, and P. J. Dagdigian, *J. Chem. Phys.* **140**, 204318 (2014).
- [138] O. Tkáč, A. K. Saha, J. Onvlee, C.-H. Yang, G. Sarma, C. K. Bishwakarma, S. Y. T. van de Meerakker, A. van der Avoird, D. H. Parker, and A. J. Orr-Ewing, *Phys. Chem. Chem. Phys.* **16**, 477 (2014).
- [139] C. H. Townes and A. L. Schawlow, *Microwave Spectroscopy* (Dover, New York, 1975).
- [140] L. Fusina and S. N. Murzin, *J. Mol. Spectrosc.* **167**, 464 (1994).
- [141] C. Léonard, S. Carter, and N. C. Handy, *Chem. Phys. Lett.* **370**, 360 (2003).
- [142] T. R. Phillips, S. Maluendes, A. D. McLean, and S. Green, *J. Chem. Phys.* **101**, 5824 (1994).
- [143] D. R. Yarkony, in *Conical Intersections: Electronic Structure, Dynamics & Spectroscopy*, edited by W. Domcke, D. R. Yarkony, and H. Köppel (World Scientific Publishing Co. Pte. Ltd., 2004) Chap. 2, pp. 41–128.
- [144] K. Schreel and J. J. ter Meulen, *J. Chem. Phys.* **105**, 4522 (1996).
- [145] A. Faure, N. Crimier, C. C., P. Valiron, L. Wiesenfeld, and M. L. Dubernet, *Astron. Astrophys.* **472**, 1029 (2007).
- [146] C. M. Lovejoy, D. D. Nelson, and D. J. Nesbitt, *J. Chem. Phys.* **87**, 5621 (1987).
- [147] D. C. Clary and P. J. Knowles, *J. Chem. Phys.* **93**, 6334 (1990).
- [148] S. M. Miller, D. C. Clary, A. Kliesch, and H.-J. Werner, *Mol. Phys.* **83**, 405 (1994).
- [149] X. Yang, E. Hwang, and P. J. Dagdigian, *J. Chem. Phys.* **104**, 8165 (1996).
- [150] X. Tan, P. J. Dagdigian, and M. H. Alexander, *Faraday Discuss.* **118**, 387 (2001).
- [151] H.-J. Werner, P. J. Knowles, G. Knizia, F. R. Manby, M. Schütz, *et al.*, “Molpro, version 2012.1, a package of ab initio programs,” (2012), see <http://www.molpro.net>.
- [152] Q. Ma, P. J. Dagdigian, and M. H. Alexander, *J. Chem. Phys.* **138**, 104317 (2013).
- [153] E. Weitz and G. Flynn, *Annu. Rev. Phys. Chem.* **25**, 275 (1974).
- [154] D. C. Tardy and B. S. Rabinovitch, *Chem. Rev.* **77**, 369 (1977).
- [155] D. J. Krajnovich, C. S. Parmenter, and D. L. Catlett, *Chem. Rev.* **87**, 237 (1987).
- [156] I. Oref and D. C. Tardy, *Chem. Rev.* **90**, 1407 (1990).

- [157] R. E. Weston and G. W. Flynn, *Annu. Rev. Phys. Chem.* **43**, 559 (1992).
- [158] G. W. Flynn, C. S. Parmenter, and A. M. Wodtke, *J. Phys. Chem.* **100**, 12817 (1996).
- [159] A. S. Mullin and G. C. Schatz, eds., *Highly Excited Molecules: Relaxation, Reaction, and Structure*, ACS Symposium Series, Vol. 678 (American Chemical Society, Washington, DC, 1997).
- [160] M. H. Alexander, *J. Chem. Phys.* **59**, 6254 (1973).
- [161] J. Schaefer and W. A. Lester, Jr., *J. Chem. Phys.* **62**, 1913 (1975).
- [162] R. Ramaswamy and H. Rabitz, *J. Chem. Phys.* **66**, 152 (1977).
- [163] J. A. Kłos, F. Lique, M. H. Alexander, and P. J. Dagdigian, *J. Chem. Phys.* **129**, 064306 (2008).
- [164] G. Lendvay, G. C. Schatz, and L. B. Harding, *Faraday Discuss.* **102**, 389 (1995).
- [165] V. Bernshtein and I. Oref, *J. Phys. Chem. A* **105**, 10646 (2001).
- [166] V. Bernshtein and I. Oref, *J. Chem. Phys.* **125**, 133105 (2006).
- [167] C. Higgins, Q. Ju, N. Seiser, G. W. Flynn, and S. Chapman, *J. Phys. Chem. A* **105**, 2858 (2001).
- [168] Z. Li, R. Sansom, S. Bonella, D. F. Coker, and A. S. Mullin, *J. Phys. Chem. A* **109**, 7657 (2005).
- [169] G. C. Schatz and G. Lendvay, *J. Chem. Phys.* **106**, 3548 (1997).
- [170] M. V. Ivanov, S. Y. Grebenshchikov, and R. Schinke, *J. Chem. Phys.* **130**, 174311 (2009).
- [171] K. M. Christoffel and J. M. Bowman, *J. Chem. Phys.* **112**, 4496 (2000).
- [172] R. Valero and G.-J. Kroes, *J. Phys. Chem. A* **108**, 8672 (2004).
- [173] D. C. Clary, R. G. Gilbert, V. Bernshtein, and I. Oref, *Faraday Discuss.* **102**, 423 (1995).
- [174] D. C. Clary and A. J. H. M. Meijer, *J. Chem. Phys.* **116**, 9829 (2002).
- [175] A. B. Callear and H. E. van den Bergh, *Chem. Phys. Lett.* **5**, 23 (1970).
- [176] S. L. Baughcum and S. R. Leone, *J. Chem. Phys.* **72**, 6531 (1980).
- [177] S. L. Baughcum and S. R. Leone, *Chem. Phys. Lett.* **89**, 183 (1982).
- [178] D. J. Donaldson and S. R. Leone, *J. Phys. Chem.* **91**, 3128 (1987).

- [179] R. N. Rudolph, G. E. Hall, and T. J. Sears, *J. Chem. Phys.* **105**, 7889 (1996).
- [180] H. W. Hermann and S. R. Leone, *J. Chem. Phys.* **76**, 4766 (1982).
- [181] G. E. Hall, T. J. Sears, and J. M. Frye, *J. Chem. Phys.* **90**, 6234 (1989).
- [182] G. E. Hall, D. V. Bout, and T. J. Sears, *J. Chem. Phys.* **94**, 4182 (1991).
- [183] T. Suzuki and E. Hirota, *J. Chem. Phys.* **98**, 2387 (1993).
- [184] N. E. Triggs, M. Zahedi, J. W. Nibler, P. DeBarber, and J. J. Valentini, *J. Chem. Phys.* **96**, 1822 (1992).
- [185] M. E. Jacox, *J. Phys. Chem. Ref. Data* **27**, 115 (1998).
- [186] J. O. Chu, G. W. Flynn, C. J. Chen, and R. M. Osgood, Jr., *Chem. Phys. Lett.* **119**, 206 (1985).
- [187] J. T. Yardley, *Introduction to Molecular Energy Transfer* (Academic Press, New York, 1980).
- [188] C. Yamada, E. Hirota, and K. Kawaguchi, *J. Chem. Phys.* **75**, 5256 (1981).
- [189] C. Hampel, K. A. Peterson, and H.-J. Werner, *Chem. Phys. Lett.* **190**, 1 (1992).
- [190] P. J. Knowles, C. Hampel, and H.-J. Werner, *J. Chem. Phys.* **99**, 5219 (1993).
- [191] P. J. Knowles, C. Hampel, and H.-J. Werner, *J. Chem. Phys.* **112**, 3106 (2000).
- [192] R. A. Kendall, T. H. Dunning, and R. J. Harrison, *J. Chem. Phys.* **96**, 6796 (1992).
- [193] F. Driessler, R. Ahlrichs, V. Staemmler, and W. Kutzelnigg, *Theor. Chim. Acta* **30**, 315 (1973).
- [194] J. W. I. van Bladel, A. van der Avoird, and P. E. S. Wormer, *Chem. Phys.* **165**, 47 (1992).
- [195] S. Green, *J. Chem. Phys.* **64**, 3463 (1976).
- [196] S. Davis, D. T. Anderson, G. Duxbury, and D. J. Nesbitt, *J. Chem. Phys.* **107**, 5661 (1997).
- [197] H. W. Kroto, *Molecular Rotation Spectra* (John Wiley & Sons, 1975).
- [198] M. Zahedi, J. A. Harrison, and J. W. Nibler, *J. Chem. Phys.* **100**, 4043 (1994).
- [199] T. Amano, P. F. Bernath, C. Yamada, Y. Endo, and E. Hirota, *J. Chem. Phys.* **77**, 5284 (1982).
- [200] O. Tkáč, A. G. Sage, S. J. Greaves, A. J. Orr-Ewing, P. J. Dagdigian, Q. Ma, and M. H. Alexander, *Chem. Sci.* **4**, 4199 (2013).

- [201] W. C. Gardiner, Jr., ed., *Gas-phase Combustion Chemistry* (Springer, New York, 2000).
- [202] P. W. May, N. L. Allan, M. N. R. Ashfold, J. C. Richley, and Y. A. Mankelevich, *J. Phys.: Condens. Matter* **21**, 364203 (2009).
- [203] S. J. Harris, *Appl. Phys. Lett.* **56**, 2298 (1990).
- [204] B. Bézard, H. Feuchtgruber, J. I. Moses, and T. Encrenaz, *Astron. Astrophys.* **334**, L41 (1998).
- [205] B. Bézard, P. N. Romani, H. Feuchtgruber, and T. Encrenaz, *Astrophys. J.* **515**, 868 (1999).
- [206] J. I. Moses, B. Bézard, E. Lellouch, G. Gladstone, H. Feuchtgruber, and M. Allen, *Icarus* **143**, 244 (2000).
- [207] Y. L. Yung and W. B. DeMore, *Photochemistry of Planetary Atmospheres* (Oxford University Press, New York, Oxford, 1997).
- [208] A. Schiffman and D. W. Chandler, *Int. Rev. Phys. Chem.* **14**, 371 (1995).
- [209] P. Andresen, H. Joswig, H. Pauly, and R. Schinke, *J. Chem. Phys.* **77**, 2204 (1982).
- [210] A. G. Suits, L. S. Bontuyan, P. L. Houston, and B. J. Whitaker, *J. Chem. Phys.* **96**, 8618 (1992).
- [211] J. J. van Leuken, J. Bulthuis, S. Stolte, and J. G. Snijders, *Chem. Phys. Lett.* **260**, 595 (1996).
- [212] M. J. L. de Lange, M. Drabbels, P. T. Griffiths, J. Bulthuis, S. Stolte, and J. G. Snijders, *Chem. Phys. Lett.* **313**, 491 (1999).
- [213] J. I. Cline, K. T. Lorenz, E. A. Wade, J. W. Barr, and D. W. Chandler, *J. Chem. Phys.* **115**, 6277 (2001).
- [214] H. Kohguchi, T. Suzuki, and M. H. Alexander, *Science* **294**, 832 (2001).
- [215] J. Kłos, F. J. Aoiz, J. E. Verdasco, M. Brouard, S. Marinakis, and S. Stolte, *J. Chem. Phys.* **127**, 031102 (2007).
- [216] F. J. Aoiz, J. E. Verdasco, M. Brouard, J. Kłos, S. Marinakis, and S. Stolte, *J. Phys. Chem. A* **113**, 14636 (2009).
- [217] G. Paterson, A. Relf, M. L. Costen, K. G. McKendrick, M. H. Alexander, and P. J. Dagdigian, *J. Chem. Phys.* **135**, 234304 (2011).
- [218] C. J. Eyles, M. Brouard, H. Chadwick, F. J. Aoiz, J. Kłos, A. Gijsbertsen, X. Zhang, and S. Stolte, *Phys. Chem. Chem. Phys.* **14**, 5420 (2012).

- [219] C. J. Eyles, M. Brouard, H. Chadwick, B. Hornung, B. Nichols, C.-H. Yang, J. Kłos, F. J. Aoiz, A. Gijsbertsen, A. E. Wiskerke, and S. Stolte, *Phys. Chem. Chem. Phys.* **14**, 5403 (2012).
- [220] M. Brouard, H. Chadwick, C. J. Eyles, B. Hornung, B. Nichols, F. J. Aoiz, P. G. Jambrina, S. Stolte, and M. P. de Miranda, *J. Chem. Phys.* **138**, 104309 (2013).
- [221] M. Brouard, H. Chadwick, C. J. Eyles, B. Hornung, B. Nichols, F. J. Aoiz, P. G. Jambrina, and S. Stolte, *J. Chem. Phys.* **138**, 104310 (2013).
- [222] K. Schreel, J. Schleipen, A. Eppink, and J. J. ter Meulen, *J. Chem. Phys.* **99**, 8713 (1993).
- [223] S. Marinakis, G. Paterson, J. Kłos, M. L. Costen, and K. G. McKendrick, *Phys. Chem. Chem. Phys.* **9**, 4414 (2007).
- [224] G. Paterson, S. Marinakis, M. L. Costen, K. G. McKendrick, J. Kłos, and R. Toboła, *J. Chem. Phys.* **129**, 074304 (2008).
- [225] M. Brouard, A. Bryant, Y.-P. Chang, R. Cireasa, C. J. Eyles, A. M. Green, S. Marinakis, F. J. Aoiz, and J. Kłos, *J. Chem. Phys.* **130**, 044306 (2009).
- [226] M. Brouard, H. Chadwick, C. J. Eyles, F. J. Aoiz, and J. Kłos, *J. Chem. Phys.* **135**, 084305 (2011).
- [227] G. Sarma, S. Marinakis, J. J. ter Meulen, D. H. Parker, and K. G. McKendrick, *Nat. Chem.* **4**, 985 (2012).
- [228] R. G. Macdonald and K. Liu, *J. Chem. Phys.* **97**, 978 (1992).
- [229] R. G. Macdonald and K. Liu, *J. Chem. Phys.* **98**, 3716 (1993).
- [230] L. Lai, Y. Chiu, and K. Liu, *J. Chem. Phys.* **103**, 8492 (1995).
- [231] P. J. Dagdigian, *J. Chem. Phys.* **90**, 2617 (1989).
- [232] G. Ebel, R. Krohne, H. Meyer, U. Buck, R. Schinke, T. Seelemann, P. Andresen, J. Schleipen, J. J. ter Meulen, and G. H. F. Diercksen, *J. Chem. Phys.* **93**, 6419 (1990).
- [233] H. Meyer, *J. Chem. Phys.* **101**, 6686 (1994).
- [234] H. Meyer, *J. Phys. Chem.* **99**, 1101 (1995).
- [235] L. Ma, M. H. Alexander, and P. J. Dagdigian, *J. Chem. Phys.* **134**, 154307 (2011).
- [236] L. Ma, P. J. Dagdigian, and M. H. Alexander, *J. Chem. Phys.* **136**, 224306 (2012).
- [237] I. Powis and J. F. Black, *J. Phys. Chem.* **93**, 2461 (1989).
- [238] J. F. Black and I. Powis, *J. Chem. Phys.* **89**, 3986 (1988).

- [239] PGOPHER is a program for simulating rotational structure written by C. M. Western of University of Bristol. See <http://pgopher.chm.bris.ac.uk>.
- [240] T. H. Dunning, Jr., *J. Chem. Phys.* **90**, 1007 (1989).
- [241] D. E. Woon and T. H. Dunning, Jr., *J. Chem. Phys.* **98**, 1358 (1993).
- [242] T. J. Sears, J. M. Frye, V. Spirko, and W. P. Kraemer, *J. Chem. Phys.* **90**, 2125 (1989).
- [243] O. Tkáč, A. J. Orr-Ewing, P. J. Dagdigan, M. H. Alexander, J. Onvlee, and A. van der Avoird, *J. Chem. Phys.* **140**, 134308 (2014).
- [244] A. Gijsbertsen, H. Linnartz, G. Rus, A. E. Wiskerke, S. Stolte, D. W. Chandler, and J. Kłos, *J. Chem. Phys.* **123**, 224305 (2005).
- [245] M. S. Westley, K. T. Lorenz, D. W. Chandler, and P. L. Houston, *J. Chem. Phys.* **114**, 2669 (2001).
- [246] U. Buck, F. Huisken, and J. Schleusener, *J. Chem. Phys.* **68**, 5654 (1978).
- [247] S. Bosanac, *Phys. Rev. A* **26**, 816 (1982).
- [248] M. Brouard and C. Valance, eds., *Tutorials in Molecular Reaction Dynamics* (Royal Society of Chemistry, Cambridge, 2010).
- [249] H. F. Liu, R. S. Liu, K. Y. Liew, R. E. Johnson, and J. H. Lunsford, *J. Am. Chem. Soc.* **106**, 4117 (1984).
- [250] K. P. Huber and G. Herzberg, *Constants of Diatomic Molecules: Spectra, Molecular and Molecular Structure Vol. IV* (Van Nostrand Reinhold, New York, 1979).
- [251] S. Green, *J. Chem. Phys.* **103**, 1035 (1995).
- [252] F. Weigend, *Phys. Chem. Chem. Phys.* **4**, 4285 (2002).
- [253] F. Weigend, A. Köhn, and C. Hättig, *J. Chem. Phys.* **116**, 3175 (2002).
- [254] C. Rist and A. Faure, *J. Math. Chem.* **50**, 588 (2012).
- [255] A. Spielfiedel, M.-L. Senent, F. Dayou, C. Balanca, L. Cressiot-Vincent, A. Faure, L. Wiesenfeld, and N. Feautrier, *J. Chem. Phys.* **131**, 014305 (2009).
- [256] D. Wang, *J. Chem. Phys.* **117**, 9806 (2002).
- [257] D. C. Clary, *J. Phys. Chem.* **98**, 10678 (1994).
- [258] M. Alagia, N. Balucani, L. Cartechini, P. Casavecchia, and G. G. Volpi, in *Molecules in Astrophysics: Probes and Processes*, Vol. 178, edited by E. F. van Dishoeck (IAU, 1997) pp. 271–280.
- [259] E. Roueff and F. Lique, *Chem. Rev.* **113**, 8906 (2013).

- [260] R. A. Loomis and M. I. Lester, *J. Chem. Phys.* **103**, 4371 (1995).
- [261] R. A. Loomis, R. L. Schwartz, and M. I. Lester, *J. Chem. Phys.* **104**, 6984 (1996).
- [262] R. L. Schwartz, D. T. Anderson, M. W. Todd, and M. I. Lester, *Chem. Phys. Lett.* **273**, 18 (1997).
- [263] D. T. Anderson, R. L. Schwartz, M. W. Todd, and M. I. Lester, *J. Chem. Phys.* **109**, 3461 (1998).
- [264] M. W. Todd, D. T. Anderson, and M. I. Lester, *J. Phys. Chem. A* **104**, 6532 (2000).
- [265] P. Andresen, D. Häusler, and H. W. Lülf, *J. Chem. Phys.* **81**, 571 (1984).
- [266] P. Andresen, N. Aristov, V. Beushausen, D. Häusler, and H. W. Lülf, *J. Chem. Phys.* **95**, 5763 (1991).
- [267] L. Scharfenberg, H. Haak, G. Meijer, and S. Y. T. van de Meerakker, *Phys. Rev. A* **79**, 023410 (2009).
- [268] A. R. Offer and M. C. van Hemert, *J. Chem. Phys.* **99**, 3836 (1993).
- [269] E. Kochanski and D. R. Flower, *Chem. Phys.* **57**, 217 (1981).
- [270] A. Offer and D. R. Flower, *J. Phys. B: At. Mol. Opt. Phys.* **23**, L391 (1990).
- [271] A. R. Offer and E. F. van Dishoeck, *Mon. Not. R. Astron. Soc.* **257**, 377 (1992).
- [272] A. R. Offer, M. C. van Hemert, and E. F. van Dishoeck, *J. Chem. Phys.* **100**, 362 (1994).
- [273] S. M. Miller and D. C. Clary, *J. Chem. Phys.* **98**, 1843 (1993).
- [274] M. H. Alexander, *J. Chem. Phys.* **76**, 5974 (1982).
- [275] F. T. Smith, *Phys. Rev.* **179**, 111 (1969).
- [276] T. D. Varberg and K. M. Evenson, *J. Mol. Spectrosc.* **157**, 55 (1993).
- [277] P. Jankowski and K. Szalewicz, *J. Chem. Phys.* **108**, 3554 (1998).
- [278] H.-J. Werner, B. Follmeg, and M. H. Alexander, *J. Chem. Phys.* **89**, 3139 (1988).
- [279] D. Simah, B. Hartke, and H.-J. Werner, *J. Chem. Phys.* **111**, 4523 (1999).
- [280] A. K. Wilson, T. van Mourik, and T. H. Dunning, Jr., *J. Mol. Struct.: Theochem* **388**, 339 (1996).
- [281] K. I. Peterson, G. T. Fraser, and W. Klemperer, *Can. J. Phys.* **62**, 1502 (1984).
- [282] S. R. Langhoff, C. W. Bauschlicher, Jr., and P. R. Taylor, *J. Chem. Phys.* **86**, 6992 (1987).

- [283] J. D. Poll and L. Wolniewicz, *J. Chem. Phys.* **68**, 3053 (1978).
- [284] I. P. Hamilton and J. C. Light, *J. Chem. Phys.* **84**, 306 (1986).
- [285] F. Mélen, A. J. Sauval, N. Grevesse, C. B. Farmer, Ch. Servais, L. Delbouille, and G. Roland, *J. Mol. Spectrosc.* **174**, 490 (1995).
- [286] A. J. Kotlar, R. W. Field, J. I. Steinfeld, and J. A. Coxon, *J. Mol. Spectrosc.* **80**, 86 (1980).
- [287] W. H. Green, Jr. and M. I. Lester, *J. Chem. Phys.* **96**, 2573 (1992).
- [288] M.-L. Dubernet, P. A. Tuckey, and J. M. Hutson, *Chem. Phys. Lett.* **193**, 355 (1992).
- [289] M. Kállay and P. R. Surján, *J. Chem. Phys.* **115**, 2945 (2001).
- [290] A. R. Ravishankara, J. M. Nicovich, R. L. Thompson, and F. P. Tully, *J. Phys. Chem.* **85**, 2498 (1981).

Qianli Ma

Curriculum Vitae

Education

- 2009–2014 **Graduate**, *The Johns Hopkins University*, Baltimore, Maryland, USA, GPA 3.96/4.00.
M.A. Degree in Chemistry: December 2011
- 2007–2009 **Graduate**, *Nanjing University*, Nanjing, Jiangsu, China, GPA 86.3/100.
- 2003–2007 **Undergraduate**, *Nanjing University*, Nanjing, Jiangsu, China, GPA 87.2/100.
B.S. Degree in Chemistry: June 2007

Experience

Research

- 2010–2014 **Research Assistant**, *The Johns Hopkins University*, Baltimore, Maryland, USA, under Dr. Paul J. Dagdigian and Dr. Millard H. Alexander.
- Created non-reactive atom-molecule and molecule-molecule potential energy surfaces and studied scattering dynamics
 - Made significant modifications to Millard Alexander's Hibridon software package for time-independent scattering calculations
 - Performed experimental and theoretical study into the kinetics in laser-induced breakdown spectroscopy
- 2007–2009 **Research Assistant**, *Nanjing University*, Nanjing, Jiangsu, China, under Dr. Xuefeng Guo.
- Synthesized and characterized functional inorganic nanomaterials

Teaching

- 2009–2012 **Teaching Assistant**, *The Johns Hopkins University*, Baltimore, Maryland, USA.
Teaching assistant of *Introductory Chemistry* (three semesters), *Physical Chemistry* (one semester), and *Spectroscopy* (one semester)
- 2007–2008 **Teaching Assistant**, *Nanjing University*, Nanjing, Jiangsu, China.
Teaching assistant of *Experiments in Physical Chemistry* (one semester)

Awards

- 2013 Dr. Eugene W. and Susan C. Zeltmann Fellowship, the Johns Hopkins University

- 2010 H. A. B. Dunning Fellowship, the Johns Hopkins University
2007 Fu Xiancai Award in Physical Chemistry, Nanjing University
2004–2006 People’s Fellowship Award, Nanjing University (three times)

Publications

- 6 Ondřej Tkáč, **Qianli Ma** (马千里), Cassandra A. Rusher, Stuart J. Greaves, Andrew J. Orr-Ewing, and Paul J. Dagdigian, *Differential and integral cross sections for the rotationally inelastic scattering of methyl radicals with H_2 and D_2* , *J. Chem. Phys.*, **140**, 204318 (2014)
- 5 Ondřej Tkáč, Alan G. Sage, Stuart J. Greaves, Andrew J. Orr-Ewing, Paul J. Dagdigian, **Qianli Ma**, and Millard H. Alexander, *Rotationally inelastic scattering of CD_3 and CH_3 with He: comparison of velocity map-imaging data with quantum scattering calculations*, *Chem. Sci.*, **4**, 4199 (2013)
- 4 **Qianli Ma** (马千里), Paul J. Dagdigian, and Millard H. Alexander, *Theoretical study of the vibrational relaxation of the methyl radical in collisions with helium*, *J. Chem. Phys.*, **138**, 104317 (2013)
- 3 Koos B. Gubbels, **Qianli Ma** (马千里), Millard H. Alexander, Paul J. Dagdigian, Dick Tanis, Gerrit C. Groenenboom, Ad van der Avoird, and Sebastiaan Y. T. van de Meerakker, *Resonances in rotationally inelastic scattering of $OH(X^2\Pi)$ with helium and neon*, *J. Chem. Phys.*, **136**, 144308 (2012)
- 2 **Qianli Ma** and Paul J. Dagdigian, *Kinetic model of atomic and molecular emissions in laser-induced breakdown spectroscopy of organic compounds*, *Anal. Bioanal. Chem.*, **400**, 3193 (2011)
- 1 Xiangke Guo, **Qianli Ma**, Xuefeng Guo, Weiping Ding, and Yi Chen, *Biomimetic synthesis of aluminophosphate nanorolls induced by mixed organoamines*, *Chem. Commun.*, page 3443 (2009)

Background

- Born on Aug 22, 1985 in Luoyang, Henan, China; Chinese citizenship